I. HETEROEPITAXY ON SI

II. ION IMPLANTATION IN SI AND HETEROSTRUCTURES

Thesis by

Gang Bai

In Partial Fulfillment of the Requirements

for the Degree of

Doctor of Philosophy

California Institute of Technology

Pasadena, California

1991

(Submitted May 14, 1991)

To my parents

ACKNOWLEDGEMENTS

First and foremost, I wish to express my sincere gratitute to Professor Marc-A. Nicolet for making my graduate study at Caltech a very rewarding experience. His support, encouragement, inspiration, and guidance are truly appreciated. I am also deeply indebted to Professor Thad Vreeland, Jr., whose advice has been extremely valuable.

I would like to thank Professor K.L. Wang at UCLA and Professor J.E. Mahan at CSU. Part of the work described here was completed by fruitful collaboration with their research groups. Special thanks go to Dr. Y.C. Kao, C.H. Chern, Q. Ye, and Dr. V. Mii at UCLA, and Dr. K.M. Geib at CSU, for their efficient cooperation.

Particular acknowledgements are due to Dr. D.N. Jamieson, Dr. K.H. Kim, Dr. S.J. Kim, A. Venezia, C.J. Tsai, Dr. B. Paine, and Dr. A. Dormman at Caltech, Dr. J.L. Tandon at McDonnel Douglas Aeronautics Company, and Dr. A. Venezia in Israel, who have also contributed to the completion of this thesis through collaboration.

I am especially indebted to R. Gorris and B. Stevens for their expert technical assistance, and to R. Sampley for her outstanding secretarial work.

I would also like to thank members of Professor Nicolet's group, Dr. E. Ma, T. Workman, J. Reid, Dr. Q.T. Vu, Dr. E. Kolawa, J.S. Chen, Dr. S. Nieh, W.S. Liu, Dr. C.K. Kwok, Dr. P. Pokela, Dr. J.M. Pereda, Dr. Y.T. Cheng, Dr. F. So, E. Pan, B. Flick, and Dr. X.A. Zhao, for their generous help and friendship.

Special thanks are due to Dr. A.E. White at Bell Labs, Dr. S. Akbar at IBM, Dr. D.E. Holmes at Rockwell, for providing some of the samples. Financial support of this work has been provided by the Semiconductor Research Corporation and the National Science Foundation.

PREFACE

The themes of this thesis, heteroepitaxy and ion implantation, are two areas that have been very actively researched in the last two decades.

Heterostructures made of III-V compound semiconductors by MBE and OMVPE have been used extensively in the fabrication of optoelectronics devices such as high-speed transistors and semiconductor lasers. Heterostructures on Si, which is the focus of part I of this thesis, have the advantage of compatibity with Si-based VLSI and promise to have impact on the microelectronics industry. Studies on the structural, elastic, thermal, and electrical properties of heteroepitaxial $CoSi_2$, $ReSi_2$, and GeSi films grown on Si constitute the backbone of this thesis. Some new characteristics of heterosetructures were discovered as a result of this investigation. Among them are the observation and modeling of misorientation effects on an epitaxial film grown on a vicinal substrate; the misorientation induced by interfacial misfit dislocation arrays; the experimental measurements and phenomenological analysis of thermal strain, dislocation generation, and strain relaxation; and illustrative measurements of elastic, thermal, and structural properties of epitaxial films.

Ion implantation is an important process in the fabrication of integrated circuits. The second part of this thesis deals with the production and annealing of damage produced by ion implantation in semiconductors. The defect production, stability, microstructure, and the induced strain in implanted bulk Si crystals were quantitatively investigated as a function of ion species, dose, and implantation temperature. Many new features, such as the rapid rise of damage near the amorphization threshold, the correlation between the strain and defect concentration, and the scaling behavior of the damage with ion species and implantation temperature, are revealed.

The last chapter concerns the effects of ion implantation in $CoSi_2$, $ReSi_2$, and GeSi/Si heterostrcutures, which is a marriage of heteroepitaxial and of ion implantation studies. Some interesting phenomena, such as the selective damage of the film and the substrate, the superposition of the intrinsic and the induced strain, are observed, and some preliminary results are obtained. Many interesting questions remain, and there are great research opportunities in this relatively unexplored area.

CONTENTS

ACKNOWLEDGEMENTS iii

PREFACE iv

CONTENTS v

LIST OF TABLES vii

LIST OF FIGURES viii

Part I Heteroepitaxy on Si

Chapter 1 Heteroepitaxy on Si 2

Chapter 2 Epitaxial $CoSi_2$ Films on Si 9

2.1 Introduction 9

2.2 Growth and characterization of $CoSi_2$ on Si(111) 10

2.3 Growth and characterization of $CoSi_2$ on vicinal Si(111) 17

2.4 Critical thickness and strain relaxation 22

2.5 Thermal strain and its inference for pseudomorphic growth 25

2.6 Elastic and thermal properties of mesotaxial $CoSi_2$ films on Si 31

Chapter 3 Epitaxial $ReSi_2$ Films on Si 43

3.1 Semiconducting silicides 43

3.2 Growth and characterization of $ReSi_2$ on Si(100) 44

3.3 Channeling of MeV ions in polyatomic crystals 49

Chapter 4 GeSi Films on Si(100) 59

4.1 Introduction 59

4.2 Properties of GeSi films grown at 550°C 59

4.3 Pseudomorphic GeSi films and superlattices on vicinal Si(100) 66

4.4 Strain relaxation of pseudomorphic GeSi films grown at 300°C 73

4.5 Asymmetrical tilt boundary in GeSi/Si(001) heterostructures 79

Chapter 5 Porous Si and Its Properties 86

5.1 Introduction 86

5.2 Strain and stress in porous Si(100) 87

5.3 Epitaxial films of GeSi and $CoSi_2$ on porous Si 96

Part II Ion Implantation in Si and Heterostructures

Chapter 6 Ion-Solid Interaction 102

Chapter 7 Damage Production and Annealing in Si(100) 105

7.1 Introduction 105

7.2 Damage by self-implantation at room temperature 106

7.3 Damage by ^{19}F, ^{40}Ar, and ^{131}Xe implantation at room temperature 118

7.4 Damage by ion implantation at liquid nitrogen temperature 124

Chapter 8 Ion Implantation in Heterostructures 130

8.1 Introduction 130

8.2 Damage production and annealing in ^{28}Si implanted $CoSi_2$ films 131

8.3 Radiation damage in $ReSi_2$ by an MeV ^4He beam 141

8.4 Amorphization and recrystallization of epitaxial $ReSi_2$ films 148

8.5 Strain induced by ion implantation in GeSi films 154

Appendix I Some Studies of Compound Semiconductors 163

Appendix II List of Publications 165

LIST OF TABLES

Table 2.6-I Lattice distortion of $CoSi_2$ films on (100) and (111) oriented Si substrates. Data for Si/$CoSi_2$/Si samples are from Ref. 49 of Chapter 2 and those for B-type sample are from Ref. 7 of Chapter 2. 33

Table 2.6-II Ratios and elastic constants (in units of GPa) of cubic $CoSi_2$ from strain and curvature measurements. Data for Si are from Ref. 51 of Chapter 2 and are listed for comparison. 33

Table 3.3-I Calculated values of the characteristic and critical angles, measured values of half angles, and the calculated and measured minimum yields, for the [100] axial channeling of 1.4 MeV ^4He beam in an epitaxial $ReSi_2$ film. 54

Table 4.3-I The strain obtained from rocking curve analyses and the biaxial stress model of the single layer Ge_xSi_{1-x} films, and the superlattice with the average Ge composition of 0.07, grown on vicinal Si(100) substrates at 550°C. 72

LIST OF FIGURES

FIG. 1 An artist's view of total integration: a multiple heterostructure where the logic is fabricated on Si, while all other functions are designed on the optimum choice of materials epitaxially grown on a Si substrate (from Fig. 1 of Ref. 6 of Chapter 1). 5

FIG. 2.2-1 2 MeV ^{4}He: (a) backscattering spectra of a $CoSi_2$/Si(111) heterostructure for a beam incident along a random (solid line) and the [111] axial direction (dotted line); (b) an angular scan about the [111] axis of the same sample; the Si and Co signal in the film were taken at 1.53 and 1.13 MeV, respectively, and the substrate signal was taken at 1.05 MeV. 12

FIG. 2.2-2 A Fe K_{α_1} x-ray ($\lambda = 0.1936$ nm) rocking curve from the (111) symmetrical diffraction of the same $CoSi_2$/Si(111) sample shown in Fig. 2-2-1. 14

FIG. 2.2-3 Transmission electron micrographs of $CoSi_2$/Si(111) samples: (a) a cross-sectional high resolution lattice image of the interface (from Ref. 12 of Chapter 2); (b) a weak-beam dark-field plane-view ([0$\overline{2}$2] beam) micrograph showing a hexagonal misfit dislocation network (from Ref. 24 of Chapter 2); (c) a plane-view morié pattern caused by the lattice mismatch between the layer and the substrate (from Ref. 12 of Chapter 2). 16

FIG. 2.3-1 Fe K_{α_1} x-ray (111) symmetrical diffraction from a 100 nm thick $CoSi_2$ film on a vicinal Si(111) substrate (offset angle $\phi_s = 16^o$): (a) diffraction geometry, n is the surface normal; (b) the Bragg peak position of the substrate versus the azimuthal angle; (c) the separation between the Bragg peaks of the film and the substrate versus the azimuthal angle. 18

FIG. 2.3-2 The misorientation angle α of (a) the $CoSi_2$/Si(111) samples of various film thickness versus the substrate offset angle ϕ_s; (b) the sample shown in Fig. 2.3-1 ($\phi_s = 16^o$, 100 nm thick) versus the perpendicular strain. 20

FIG. 2.3-3 (a) Schematical diagram of the interface between a $CoSi_2$ film and a vicinal Si(111) substrate along the [11$\overline{2}$] tilt direction, and the proposed geometrical model on the misorientation between the film and the substrate; (b) the geometrical model that predicts $\alpha = \epsilon^{\perp} \tan\phi_s$ agrees excellently with the least-squares fit to the experimental data of epitaxial $CoSi_2$ films grown on vicinal Si(111) substrates. 21

FIG. 2.4-1 Perpendicular strain in an epitaxial $CoSi_2$ film as a function of film thickness for a $CoSi_2$/Si(111) heterostructure. The solid line is the strain relaxation behavior predicted by Matthews

and Blakeslee's minimum energy model. The dashed line is the average of the experimentally measured strain value on samples of various film thickness, substrate offset angle, and growth condition. 24

FIG. 2.5-1 Perpendicular x-ray strain $\epsilon^{\perp}$ as a function of sample temperature T for two 100 nm thick $CoSi_2$ films on (i) a Si substrate whose surface is offset from the [111] direction by 16° towards the $[1\bar{1}0]$ direction of the substrate (•), and (ii) a Si substrate whose surface is aligned with the (111) planes ($\triangle\bigtriangledown$). All strain values are reversible below 490^oC. When the latter sample was heated above that temperature up to 650^oC and then cooled, a reduced strain was measured ($\bigtriangledown$), again reversible below 500^oC. The solid lines are linear fits to the data (omitting the two highest temperature points). The strain for a coherent interface is calculated with the Poisson ratio $\nu = 1/3$ (lower dashed line). At the temperature at which the samples were grown ($\sim 600^oC$), the measured strain is that predicted for an elastically relaxed film (upper dashed line). 27

FIG. 2.5-2 Three x-ray rocking curves diffracted from symmetrical (111) planes measured at room temperature on sample #1 as-grown, vacuum-annealed, and air-annealed. The curve of the as-grown sample is indistinguishable from that measured after annealing *in vacuum* at 700^oC for 40 min (solid line). Annealing *in air* at 650^oC induces an irreversible reduction of the strain in the epitaxial $CoSi_2$ film as indicated by the shift and the broadening of the diffraction peak (dotted line). 29

FIG. 2.6-1. Fe K_{α_1} x-ray ($\lambda = 0.1932$ nm) rocking curves of symmetrical (400) and asymmetrical (311) diffractions from a mesotaxial $CoSi_2$/Si(100) sample. The diffraction geometry and direction of x-ray incidence are shown in the inset above the corresponding Bragg peaks from the $CoSi_2$ film. 33

FIG. 2.6-2. The lattice mismatch, $\epsilon^{\perp}$ (square), $\epsilon^{\parallel}$ (triangle), and f (circle), as a function of the measurement temperature for both (a) the $CoSi_2$/Si(100) and (b) the $CoSi_2$/Si(111) mesotaxial samples. Open (filled) symbols are for the measurements when the temperature was raised (lowered). 38

FIG. 2.6-3. Schematics of the proposed model showing how an epitaxial $CoSi_2$ film relaxes to an equilibrium strain state at T_R and above, and that misfit dislocations are locked-in below T_R. T_M is the melting temperature of $CoSi_2$, and T_O is the hypothetical temperature at which the lattice mismatch between $CoSi_2$ and Si becomes zero. 38

FIG. 3.2-1 2 MeV ^4He minimum channeling yields of Re and Si for $ReSi_2$ films grown on Si(100) by reactive deposition epitaxy as a function of substrate temperature during deposition. 45

FIG. 3.2-2 Epitaxial relationship between a $ReSi_2$ film and a Si(100) substrate: (a) transmission electron diffraction pattern of the Si[100] zone and the $ReSi_2$[010] zone (from Ref. 14 of Chapter 3). The bright spots are Si diffractions. The faint spots are $ReSi_2$ diffractions (note their fourfold symmetry). (b) Schematical drawing of two equivalent common unit meshes (from Ref. 15 of Chapter 3). The dots are Si atoms in the substrate. The crosses are Re atoms in the film. The actual atomic positions are unknown and assumed. 47

FIG. 3.2-3 Transmission electron micrograph of a 150 nm thick $ReSi_2$ film grown on Si(100) at 650°C (from Ref. 15 of Chapter 3): (a) plane-view dark-field image with a beam diffraction vector of $ReSi_2$(002); (b) cross-sectional bright-field image with a beam incident along Si[022]. 48

FIG. 3.3-1 Backscattering spectra of 1.4 MeV ^{4}He incident along a random direction (solid line) and a [100] aligned axial direction (dotted line). 51

FIG. 3.3-2 A plot of normalized backscattering yield versus tilt angle. The normalization is performed with respect to the backscattering yield of a random incident beam. The half angle is the half of the full width of the angular dip. 51

FIG. 3.3-3 A cross-sectional schematic diagram showing the [100] axial channel of $ReSi_2$. 54

FIG. 4.2-1 The lattice mismatch between epitaxial Ge_xSi_{1-x} alloy and Si, f, as a function of Ge composition. The data agree well with the Vegard law over the entire composition range ($0 \leq x \leq 1$). 61

FIG. 4.2-2 Ge composition—film thickness plot of epitaxial Ge_xSi_{1-x} films on Si(100): dotted line is the equilibrium critical thickness from Matthews and Blakeslee's model; $\triangle$ is the measured critical thickness of films grown at $\sim 550^\circ$C by Bean et al., and $\bullet$ is from our work. The number associated with each datum point is the normalized parallel strain $\epsilon^{\parallel}/f$. 61

FIG. 4.2-3 Channeling characteristics vs x-ray diffraction of epitaxial GeSi films grown on Si(100) at 550°C: (a) dechanneling probability of an aligned MeV ^{4}He beam across the interface as a function of parallel strain $\epsilon^{\parallel}$ of the film; (b) the difference of the minimum channeling yield between a relaxed and a coherent GeSi film as function of the square of the x-ray peak broadening caused by threading dislocations in the film. 64

FIG. 4.2-4 Thermal properties of a metastable coherent Ge_xSi_{1-x} film grown on Si(100) at 550°C: (a) the lattice mismatch (dotted line) and the strains (solid lines) as a function of temperature; dashed lines are for a film with rigid interface; (b) Fe K_{α_1} x-ray rocking curves diffracted from (400)

planes of of sample before (solid line) and after (dotted line) thermal annealing at 630°C for 2h in ambient air. 65

FIG. 4.3-1 (a) The angular position of the (400) peak diffracted from the substrate and (b) the difference of the peaks from the film and the substrate versus the azimuthal angle of the sample configuration. (c) Schematics of the results from analysis of the x-ray rocking curve data (a) and (b). 67

FIG. 4.3-2 Schematics of one symmetrical (400) and four asymmetrical {311} diffracting planes of vicinal samples. The surface normal is taken as Z-axis. 68

FIG. 4.3-3 (a) The mismatch in interplanar spacing and (b) the misorientation angle as a function of diffracting planes of a $Ge_{0.05}Si_{0.95}$ film 100 nm thick on a vicinal Si(100). The solid line is the prediction of the biaxial stress model with $\epsilon^{XX} = \epsilon^{YY} = 0$, $\epsilon^{ZZ} = 0.52\%$, and $\phi_s = 3.1^o$. 70

FIG. 4.3-4 Fe K_{α_1} ($\lambda = 0.1932$ nm) x-ray rocking curves diffracted from the (400) symmetrical planes of the GeSi superlattice on vicinal Si(100): (a) two diffraction geometries corresponding to a rotation of 180° of the incident x-ray about the surface normal; (b) the corresponding diffraction spectra. 72

FIG. 4.4-1 The strain relaxation of a highly metastable GeSi strained layer grown on Si(100) at ~ 300°C as a function of temperature upon isochronal annealing for 30 min in vacuum. The strain relaxes sharply at 375 ± 25°C. 75

FIG. 4.4-2 Parallel strain $\epsilon^{\parallel}$ of 570 nm thick epitaxial $Ge_{0.3}Si_{0.7}$ layers grown on Si(100) at ~ 300°C obtained from (400) diffraction x-ray rocking curve measurements vs duration of *ex situ* thermal annealing in vacuum ($\sim 5 \times 10^{-7}$ Torr) at various temperatures. 75

FIG. 4.4-3 Relaxation rate measured by the rate of increasing parallel strain with increasing time at modest relaxation level vs the inverse of the temperature at which the relaxation proceeds (see Fig. 4.4-2). The data follow an Arrhenius behavior with a slope of 2.1 ± 0.2 eV. 78

FIG. 4.4-4 X-ray peak broadening of (400) diffraction from 570 nm thick epitaxial $Ge_{0.3}Si_{0.7}$ layers grown at ~ 300°C caused by imperfections in the layers versus the strain relaxation. 78

FIG. 4.5-1 Schematic representation of parallel strain and misorientation in a heterostructure. 80

FIG. 4.5-2 Four different types of dislocation arrangements at heterointerfaces: (I) mismatch relieving dislocations; (II) asymmetrical low angle tilt boundary; (III) mixed dislocations with a

non-zero parallel strain and a zero misorientation angle; (IV) mixed dislocations with both non-zero net mismatch-relieving and tilt components. 80

FIG. 4.5-3 Schematic representation of a 60°-mixed dislocation in a GeSi/Si(001) structure. 82

FIG. 4.5-4 Misorientation angle vs parallel strain of $\sim$ 570 nm thick $Ge_{0.3}Si_{0.7}$ films grown on Si(001) substrates at 300-500°C. Most samples (A) analyzed have zero misorientation angles regardless of the value of the parallel strain. Samples B and C are initially pseudomorphic and have a zero misorientation angle. They relax upon thermal annealing and develop finite misorientation angles. Sample D is relaxed initially and has a non-zero misorientation angle. It relaxes further upon annealing. After amorphization of the entire film and solid phase epitaxial regrowth, the misorientation becomes zero. 82

FIG. 5.2-1 Backscattering spectra of porous Si and bulk Si: (a) a 2 MeV ^{4}He beam incident along a near-normal random direction (solid lines) and along the [100] aligned direction (dotted lines); (b) 3.05 MeV oxygen resonance of a bulk Si, of a porous Si after storage of 18 months in air at 23°C, and of a thermally oxidized Si wafer ($\sim$ 1 μm SiO_2/Si). 88

FIG. 5.2-2 Auger electron spectroscopy depth profile of oxygen and silicon in porous Si of the sample that had been stored in air at room temperature for $\sim$ 18 months after the formation of porous Si. 90

FIG. 5.2-3 Perpendicular strain $\epsilon^{\perp}$ of porous Si aged for 18 months in air at 23°C and then annealed in vacuum for 30 min, measured immediately after annealing ($\circ$), after storage in air at room temperature for about 1 month ($\bullet$) and 7 months (filled triangle). 90

FIG. 5.2-4 Decreasing rate of perpendicular strain in porous Si upon vacuum annealing: (a) $\epsilon^{\perp}$ versus annealing duration at 300, 400, and 600°C; (b) Arrhenius plot of the time constant τ of the decrease of the perpendicular strain. 92

FIG. 5.2-5 Time evolution of the perpendicular strain $\epsilon^{\perp}$ of the porous Si stored at room temperature in different ambient gases after being annealed in vacuum at 500°C for 30 min (see the point marked by star in Fig. 5.2-3). 93

FIG. 5.2-6 Schematic representation of porous Si and of the evolution of the perpendicular strain as a function of the sample history given on the abscissa. The upwards (downwards) arrows in the silicon rods indicate the positive (negative) perpendicular strain; their length suggests the magnitude

of the strain. The perpendicular strain evolves as a result of absorption by and their desorption from the native oxide. 93

FIG. 5.3-1 Illustration of a heteroepitaxial Ge film on a Si substrate of seed pads with lateral dimension l. The strain energy profile, $\omega(0, z)$, for the pad mid-cross section is shown on the left (from Ref. 24 of Chapter 5). 97

FIG. 5.3-2 Schematic drawings of (a) a patterned substrate as used in Luryi and Suhir's model (Fig. 5.3-1), and (b) a porous Si substrate (from Ref. 26 of Chapter 5). 97

Fig. 5.3-3 Perpendicular strain $\epsilon^{\perp}$ of $CoSi_2$-capped porous Si(111) aged for 18 months in air and then annealed in vacuum for 30 min, measured immediately after annealing (∘), and after storage in air at room temperature for 1 month (•). The figure has identical scales as those of Fig. 5.2-3 for comparison. 97

FIG. 7.2-1 Fe K_{α_1} x-ray (wavelength=0.1936 nm) rocking curves diffracted from the symmetrical (400) planes of the Si(100) samples implanted at room temperature by 230 keV ^{28}Si ions to the doses of (a) 1×, (b) 3.5×, (c) 4.3×, (d) $4.8 \times 10^{14}/cm^2$. 107

FIG. 7.2-2 The maximum perpendicular strain (∘) extracted from dynamical x-ray diffraction simulations of the experimental rocking curves as a function of the ^{28}Si implantation dose. The solid line is to stress the trend. The filled circles correspond to the samples for which the x-ray rocking curves are shown in Fig. 7.2-1. 107

FIG. 7.2-3 2 MeV ^4He backscattering (filled triangle) and channeling spectra (solid line) of the set of the samples shown in Fig. 7.2-1. Also plotted are the channeling spectra (dotted line) of a virgin Si sample and a sample implanted 7.7×10^{14} $^{28}Si/cm^2$ in which a continuous amorphous layer forms. 109

FIG. 7.2-4 The maximum defect concentration extracted from channeling spectra such as those of Fig. 7.2-3 as a function of the ^{28}Si dose. The solid line is to highlight the trend. The filled circles correspond to the samples (a-d) shown in Fig. 7.2-3. The dashed line is the maximum value in the concentration profile of the Frenkel pair predicted by the TRIM88 simulation code of 230 keV ^{28}Si implantation in an amorphous Si target. 109

FIG. 7.2-5 The measured maximum defect concentration as a function of dose (∘ of Fig. 7.2-4) is compared with that predicted from the phenomenological model of the accelerated damage growth in a predamaged crystal (solid line, see text). The dashed lines are the fraction of the amorphous zones calculated from Gibbson's overlap model with various (m,A_i) parameters. 112

FIG. 7.2-6 The depth profile of the Frenkel pair concentration from TRIM88 simulation (dashed line), the defect concentration from the channeling measurements of the sample (c) (solid line), and the perpendicular strain from the dynamical x-ray diffraction simulation of the rocking curve (dotted line). The vertical scale is in an arbitrarily normalized unit. 112

FIG. 7.2-7 The relationship between the maximum values of the perpendicular strain from x-ray diffraction measurements and the defect concentration from 2 MeV ^{4}He channeling measurements. The solid line is the least-squares fit of the data (○) to a linear function. 115

FIG. 7.2-8 The isochronal annealing characteristics of the perpendicular strain in the implanted layers as a function of the annealing temperature. All annealings were performed in a vacuum of $\sim 7 \times 10^{-7}$ Torr for a duration of 30 min. The data are from the four samples for which the x-ray rocking curves are shown in Fig. 7.2-1 and the channeling spectra in Fig. 7.2-3. 115

FIG. 7.3-1 The maximum defect concentration extracted from channeling spectra similar to those of Fig. 7.2-3 as a function of the ^{19}F dose. The solid line is to highlight the trend. The dashed line is the maximum value in the depth profile of the Frenkel pair concentration predicted by the TRIM88 simulation of 230 keV ^{19}F implantation into an amorphous Si target. 119

FIG. 7.3-2 The relationship between the maximum values of the perpendicular strain from x-ray diffraction measurements and the defect concentration from 2 MeV ^{4}He channeling measurements. The solid line is the least-squares fit to the data (•) of a linear function. 119

FIG. 7.3-3 The maximum perpendicular strain obtained by fitting the dynamical x-ray diffraction simulations to the experimental rocking curves as a function of the implantation dose for four different ions. The solid line is to stress the trend. 121

FIG. 7.3-4 The initial (regime I) slope of the maximum perpendicular strain vs dose as a function of the Frenkel pair concentration per unit dose for various incident ions. 121

FIG. 7.4-1 The maximum perpendicular strain extracted from the dynamical x-ray diffraction simulations of experimental rocking curves as a function of the 250 keV ^{40}Ar dose of implantations at 100K ($\triangledown$) and at 300K ($\triangle$) into Si(100). The solid line is to stress the trend. The modified data points (filled inverse triangle) are obtained by multiplying the dose of the data $\triangledown$ by a factor of 3.5. 125

Fig. 7.4-2 The cross-sectional TEM (from Ref. 40 of Chapter 7) of the sample implanted by 250 keV 5×10^{13} ^{40}Ar/cm^2 into Si(100) at 100K ($\epsilon^{\perp}_{max} \sim 0.4\%$, see Fig. 7.4-1). A heavily damaged layer is located from a depth of 120 nm to 240 nm. 125

FIG. 8.2-1 2 MeV ^{4}He backscattering spectra with a beam incident along a random (•) and a [111] axial channel orientation of the as-grown $CoSi_2$(50 nm)/Si(111) (solid line); and the samples implanted at room temperature by 150 keV ^{28}Si to doses of 2× ($\bigtriangledown$), 5× (∘), 30 × $10^{14}/cm^2$ ($\triangle$). The detected ^{4}He particles exit at an angle of 82° from the line of the incident beam. 132

FIG. 8.2-2 The defect concentration in the $CoSi_2$ films extracted from the channeling yields of Fig. 8.2-1 vs the Si dose, for the as-implanted samples (•), and those annealed for 60 min at 400°C (∘), 600°C ($\triangle$), 800°C (square). The Frenkel pair concentration as a function of dose, predicted from TRIM88, is also shown (dashed line). 132

FIG. 8.2-3 Fe K_{α_1} x-ray rocking curves diffracted from the symmetrical (111) planes of (a) as-grown $CoSi_2$/Si(111); and the samples implanted to doses of (b) 0.5×, (c) 1×, (d) 2×, (e) 5 × $10^{14}/cm^2$. Bragg peak from the bulk Si substrate is $\theta_B = 18^o$. 135

FIG. 8.2-4 The static atomic displacement induced by the defects in the $CoSi_2$ films vs the Si dose, for the as-implanted sample (•), and for those annealed in vacuum for 60 min at 250°C ($\bigtriangledown$) and 400°C (∘). The shaded area represents the error in estimating the displacement of a perfect $CoSi_2$ film. 135

FIG. 8.2-5 The resistivity difference between the implanted and as-grown $CoSi_2$ films vs the dose, for the as-implanted sample (•), and for those annealed in vacuum for 60 min at 250°C ($\bigtriangledown$), 400°C (∘), 600°C ($\triangle$), 800°C (square). 139

FIG. 8.2-6 The resistivity difference vs the static displacement of the lightly damaged $CoSi_2$ films ($c_D \leq 4\%$ or $\phi \leq 5 \times 10^{14}/cm^2$). The approximately linear relationship indicates a good correlation between the concentration of the carrier scatterers and the structural defects in such films. .. 139

FIG. 8.3-1 1.4 MeV ^{4}He backscattering and channeling spectra of a 150 nm thick epitaxial $ReSi_2$ layer grown on a Si(100) substrate. All four spectra were taken at room temperature and are plotted by normalizing incident doses to a common value. The solid line is the spectrum for random incidence. The three [100] channeling spectra are for samples irradiated at room temperature with doses of (a) $\sim 10^{14}/cm^2$, $\sim 10^{17}/cm^2$ (b) in a [100] aligned direction and (c) in a random direction. 143

FIG. 8.3-2 The normalized backscattering yield of the Re signal versus angle of tilt between the incident beam and the [100] direction of the sample for the three damage stages of Fig. 8.3-1. 143

FIG. 8.3-3 The minimum channeling yields of the Si and Re signals for an epitaxial $ReSi_2$ film as a function of the 1.4 MeV ^4He irradiation dose for both a random and a [100] aligned incidence. 145

FIG. 8.3-4 Comparison of the measured defect concentration versus irradiation dose in $ReSi_2$ produced by 1.4 MeV ^4He ion beams of random (∘) and [100] aligned (•) incidence at 300K, and one calculated (dashed line) by a TRIM88 computer simulation of a beam of random incidence at 0K. 145

FIG. 8.4-1 X-ray diffraction spectra of epitaxial $ReSi_2$/Si(100) samples: (a) as-grown; and implanted by 300 keV ^{28}Si to doses of (b) $10^{13}/cm^2$, (c) $10^{14}/cm^2$, and (d) $5 \times 10^{14}/cm^2$. A Cu x-ray source and θ–2θ geometry were used. 149

FIG. 8.4-2 Resistivity of the samples shown in Fig. 8.4-1, measured at temperatures ranging from 90K to 330K in the dark. 150

FIG. 8.4-3 Changes of the minimum yield for Re upon thermal annealing in vacuum at 500°C, 600°C and 700°C for 30 min for the samples shown in Fig 8.4-1. 150

FIG. 8.5-1 X-ray rocking curves diffracted from the (400) symmetrical planes of the as-grown $Ge_{0.09}Si_{0.91}$/Si(100) sample (solid line), and of those implanted at room temperature with 320 keV ^{28}Si to 2× (•), $5 \times 10^{14}/cm^2$ (∘). 156

FIG. 8.5-2 The strain induced by 320 keV ^{28}Si implantation into pseudomorphic GeSi layers vs the Ge composition. The dashed lines are the strains predicted from a linear interpolation model of Eq. (8.5-2). 156

FIG. 8.5-3 (400) x-ray rocking curves of a pseudomorphic $Ge_{0.09}Si_{0.91}$/Si(100) implanted at room temperature (RT) by 320 keV 5×10^{14} $^{28}Si/cm^2$ and annealed for 30 min at various temperatures. The spectrum of the 700°C annealed sample (solid line) is indistinguishable from that of the as-grown sample (Fig. 8.5-1). 159

FIG. 8.5-4 The strain in the Ge_xSi_{1-x} layer vs the annealing temperature. The square, triangle, and circle are for the samples with $x = 0.04$, 0.09, and 0.13, respectively. The filled symbols represent the unimplanted samples. The small (big) open symbols represent the samples implanted by 320 keV 1.2× (2×) 10^{14} $^{28}Si/cm^2$. 159

Part I

Heteroepitaxy on Si

Chapter 1 Heteroepitaxy on Si

Heteroepitaxy is oriented overgrowth of a thin layer of material A on a substrate of material B. The key concept of pseudomorphic growth, where the overlayer is in perfect atomic registry with the substrate, was first introduced by Frank and van der Merwe in 1949.[1] They also showed that with a given lattice mismatch there exists a critical layer thickness for pseudomorphic growth.

Heteroepitaxial growth can be achieved in vapor, liquid, or solid phase. To date, most studies have focused on vapor phase deposition, such as molecular beam epitaxy (MBE) or organometallic vapor phase epitaxy (OMVPE). Growth of a thin film by vapor deposition proceeds in three different modes:[2]

1. layer growth (Frank-van der Merwe);
2. island growth (Volmer-Weber);
3. layer plus subsequent island growth (Stranski-Krastanov).

Using molecular dynamics simulation, Grabow and Gilmer[3] showed that the equilibrium morphology of a heteroepitaxial layer is that of islands (growth mode 2 or 3). In an actual growth, kinetic processes such as surface diffusion as well as energetics such as surface energy[4] determine the growth mode. Indeed, one of the key problems of heteroepitaxy is how to control the kinetics to promote layer growth. Another fundamental issue[5] is what ultimately limits heteroepitaxial growth. The understanding of such issues and the eventual ability to manipulate heteroepitaxial growth are the key for realizing heterostructure-based devices.

Silicon microelectronics lies at the heart of information technology. Silicon has many superior physical properties, such as its almost perfectly passivating oxide, high mechanical strength, thermal stability and conductivity. Unfortunately, having an indirect bandgap, Si cannot be used for light sources. Heteroepitaxy on Si opens new possibilities for Si-based optoelectronics. This approach attempts to combine the best properties of individual materials. Figure 1 is an example of that "total integration" concept.[6] The key is the ability to grow functionally desirable materials in high quality, single crystalline form on a Si substrate.

There exist two broad configurations of heteroepitaxial devices. In one, physical properties of heterointerfaces determine the device performance. Examples are metal-base transistors and heterojunction bipolar transitors. The interface has to be free of defects such as misfit dislocations for good device performance. In another, the Si is used only as a substrate to support a heterostructural device, such as laser diodes fabricated from GaAs epilayers grown on Si. The interface becomes irrelevent in this case so long as the near-surface region is of high crystalline quality. However, the

crystalline perfection near the surface is closely related to the defects at the interface. The control of interfacial defects is therefore important even in this configuration.

Most studies of heteroepitaxy on Si focus on MBE growth where precise atomic control and *in situ* monitoring of the growth process are possible. Many materials have been grown on Si substrates and various properties studied.[6,7] Single crystalline epitaxial silicides of $CoSi_2$ and $NiSi_2$ were successfully grown on Si(111) by MBE in 1982.[8,9] Both silicides have cubic CaF_2 structure. A $NiSi_2$ overlayer on Si(111) can have two different orientations, type-A, where the layer is fully aligned with the substrate, and type-B, where the layer is rotated by 180 degree about the [111] axis with respect to the substrate.[9] Tung observed that the Schottky barrier height between $NiSi_2$ and Si differs for type-A and type-B heterostructures.[10] A $CoSi_2$ overlayer always has type-B orientation.[8] Transisitor action has been demonstrated for Si/$CoSi_2$/Si(111) permeable-base transistors.[11] Recently, pinhole free $CoSi_2$ layers were grown on Si(111) by low temperature deposition and annealing.[12] Single crystalline $CoSi_2$ and $NiSi_2$ layers were also successfully grown on Si(100) and (110) substrates by the template technique and low temperature deposition.[13] High quality single crystalline buried $CoSi_2$ layers were also fabricated by high dose ^{59}Co implantation into Si(100), (110), and (111) substrates, followed by thermal annealing.[14]

Single crystalline rare-earth metal silicides of YSi_{2-x} and $ErSi_{2-x}$ were grown on Si(111) recently.[15,16]

Some silicides such as $FeSi_2$, $CrSi_2$, and $ReSi_2$, are narrow-gap semiconductors. They have potential applications as infrared light sources and detectors. The key is the growth of an epitaxial silicide/Si heterostructure of high perfection and a defect-free interface. Recently, some progress has been made in growing epitaxial semiconducting $ReSi_2$,[17] $FeSi_2$,[18,19] and $CrSi_2$[20–22] films on Si substrates.

By employing MBE deposition at relatively low temperature ($\sim 550°C$), pseudomorphic GeSi alloys over the entire composition range can be grown on Si.[23] The low temperature growth produces metastable strained layers because of energy barriers for dislocation generations.[24] The nucleation and propagation of dislocations have been examined by transmission electron microscopy.[25] Motivated by potential device applications, both the band alignment at the Ge/Si interface[26] and the bandgap of coherently strained GeSi alloys[27] were studied. Devices such as infrared waveguide photodetectors,[28] n-channel[29] and p-channel[30] modulation-doped SiGe/Si field-effect transistors, and Si/GeSi/Si heterojunction bipolar transistors by MBE[31] and chemical vapor deposition (CVD[32]) have been demonstrated.

Photonic devices are made from direct bandgap III-V semiconductors. Successful growth of high quality GaAs[33,34] and InP[35] layers on Si substrates opens the possibilties for application of Si-based, optoelectronic integrated circuits in optical interchip connection and lightwave communication.

Current integrated circuits are based on 2-dimensional planar architecture. Growth of single crystalline insulators such as CaF_2, BaF_2 on Si[36] makes it possible to build 3-dimensional integrated circuits, which enable one to multiply the device elements in one chip. This approach also provides an opportunity to fabricate novel electronic devices.[37] Single crystalline insulating films can also be used as buffer layers (e.g., between GaAs epilayers and Si substrates) to relieve stress in epilayers.[38]

3C-SiC is a semicondcutor with zinc-blende structure. Its wide bandgap and high thermal conductivity and stability are ideal for high-temperature and high-power device applications.[39,40] Since the growth of single crystalline 3C-SiC films on Si by CVD was demonstrated in 1983,[41] significant progress in improvement of film quality and reduction of defects has been made. Prototype devices such as p-n junction and field-effect transistors have been demonstrated.[39,40]

As the device size shrinks to a submicron regime, electrical resistence in interconnections becomes the limiting factor for high-speed performance. Superconductors therefore become the ideal candidate. Growth of high-T_C superconductor films on Si by various deposition techniques has been demonstrated.[42–44] Highly epitaxial layers with high critical currents were successfully grown on Si with buffer layers.[45]

In the following chapters, we present some results from experimental investigations on epitaxial films of metallic $CoSi_2$, semiconducting $ReSi_2$ silicides, and GeSi alloys grown on Si. Many properties found are generic and apply to other epitaxial films on Si, and to other heterostructures.

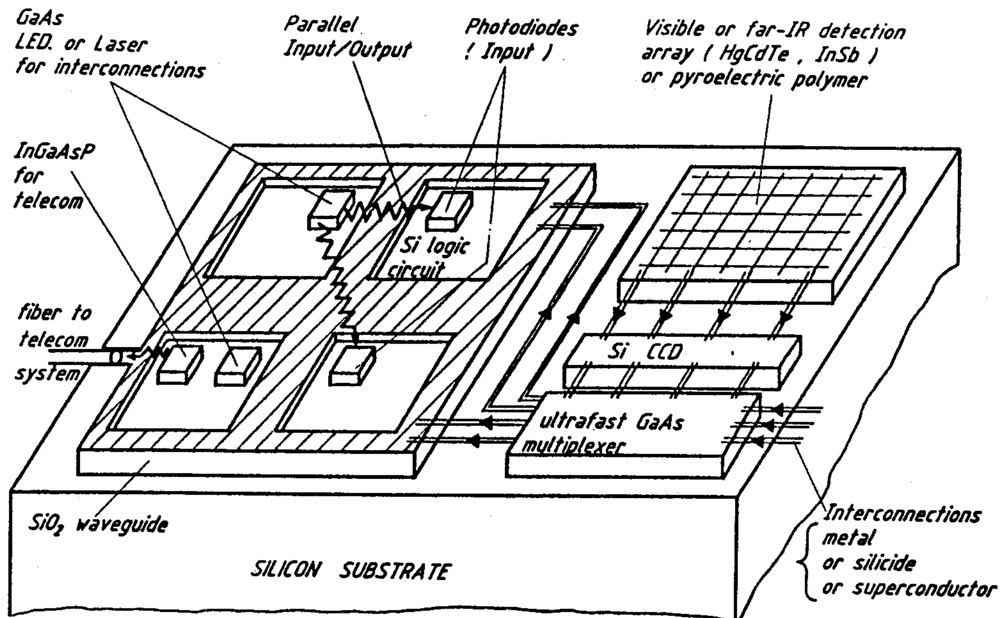

FIG. 1 An artist's view of total integration: a multiple heterostructure where the logic is fabricated on Si, while all other functions are designed on the optimum choice of materials epitaxially grown on a Si substrate (from Fig. 1 of Ref. 6).

References

1. F.C. Frank and J.H. van der Merwe, Proc. Roy. Soc. A198, 216 (1949).
2. J.A. Venables, G.D.T. Spiller, and M. Hanbücken, Rep. Prog. Phys. 47, 399 (1984).
3. M.H. Grabow and G.H. Gilmer, Mat. Res. Soc. Proc. 56, 13 (1984).
4. E. Bauer, Z. Krist 110, 372 (1958).
5. E.G. Bauer, B.W. Dodson, D.J. Ehrlich, L.C. Feldman, C.P. Flynn, M.W. Geis, J.P. Harbison, R.J. Matyi, P.S. Peercy, P.M. Petroff, J.M. Phillips, G.B. Stringfellow, A. Zangwill, J. Mater. Res. 5, 852 (1990).
6. *Proc. of the NATO Adv. Res. Workshop on Heterostructures on Silicon*, eds. E. Rosencher and Y. Nissim, Kluwer Academic, Norwell, 1988.
7. Mat. Res. Soc. Symp. Proc. 116, *Heteroepitaxy on Silicon: Fundamentals, Structures, and Devices*, eds. H.K. Choi, R. Hull, H. Ishiwara, R.J. Nemanich, Materials Research Society, Pittsbugh, 1988.
8. R.T. Tung, J.C. Bean, J.M. Gibson, J.M. Poate, and D.C. Jacobson, Appl. Phys. Lett. 40, 684 (1982).
9. R.T. Tung, J.M. Gibson, and J.M. Poate, Phys. Rev. Lett. 50, 429 (1983).
10. R.T. Tung, Phys. Rev. Lett. 52, 461 (1984).
11. J.C. Hensel, A.F.J. Levi, R.T. Tung, and J.M. Gibson, Appl. Phys. Lett. 47, 151 (1985).
12. H. von Känel, J. Henz, M. Ospelt, J. Hugi, E. Müller, N. Onda, and A. Gruhle, Thin Solid Films 184, 295 (1990).
13. R.T. Tung, F. Schrey, and S.M. Yalisove, Appl. Phys. Lett. 55, 2005 (1989).
14. A.E. White, K.T. Short, R.C. Dynes, J.P. Garno, and J.M. Gibson, Appl. Phys. Lett. 50, 95 (1987).
15. M.P. Siegal, F.H. Kaatz, W.R. Graham, J.J. Santiago, and J.V.D. Spiegel, Appl. Surf. Sci. 38, 162 (1989).
16. J.Y. Duboz, P.A. Badoz, A. Perio, J.C. Oberlin, F. Arnaud D'Avitaya, Y. Campidelli, and J.A. Chroboczek, Appl. Surf. Sci. 38, 171 (1989).
17. J.E. Mahan, K.M. Geib, G.Y. Robinson, R.G. Long, X.H. Yan, G. Bai, M-A. Nicolet, M. Nathan, Appl. Phys. Lett. 56, 2439 (1990).
18. N. Cherief, C.D'Anterroches, R.C. Cinti, T.A. Nguyen Tan, and J. Derrien, Appl. Phys. Lett. 55, 1671 (1989).

19. J.E. Mahan, K.M. Geib, G.Y. Robinson, R.G. Long, X.H. Yan, G. Bai, M-A. Nicolet, M. Nathan, Appl. Phys. Lett. 56, 2126 (1990).

20. L. Haderbache, P. Wetzel, C. Pirri, J.C. Peruchetti, P. Bolmont, and G. Gewinner, Surf. Sci. 209, L139 (1989).

21. R.W. Fathauer, P.J. Grunthaner, T.L. Lin, K.T. Chang, J.H. Mazur, D.N. Jamieson, J. Vac. Sci. Technol. B6, 708 (1988).

22. J.E. Mahan, K.M. Geib, G.Y. Robinson, G. Bai, and M-A. Nicolet, J. Vac. Sci. Technol. B9, 64 (1991).

23. J.C. Bean, L.C. Feldman, A.T. Fiory, S. Nakahara, and I.K. Robinson, J. Vac. Sci. Technol. A2, 436 (1984).

24. B.W. Dodson and J.Y. Ysao, Appl. Phys. Lett. 51, 1325 (1987).

25. R. Hull, J.C. Bean, D.J. Werder, and R.E. Leibenguth, Phys. Rev. B40, 1681 (1989).

26. C.G. Van de Walle, R.M. Martin, J. Vac. Sci. Technol. B3, 1256 (1985).

27. R. People, Phys. Rev. B32, 1405 (1985).

28. H. Temkin, T.P. Pearsall, J.C. Bean, R.A. Logan, and S. Luryi, Appl. Phys. Lett. 48, 963 (1986).

29. H. Daembkes, H-J. Herzog, H. Jorke, H. Kibbel, and E. Kaspar, IEEE Trans. Electron Devices, ED-33, 633 (1986).

30. T.P. Pearsall, J.C. Bean, IEEE Electron Device Lett. EDL-7, 308 (1986).

31. T. Tatsumi, H. Hirayama, and N. Aizaki, Appl. Phys. Lett. 52, 895 (1988).

32. C.A. King, J.L. Hoyt, C.M. Gronet, J.F. Gibbons, M.P. Scott, and J. Turner, IEEE Electron Device Lett. ED-34, 52 (1989).

33. S.F. Fang, K. Adomi, S. Iyer, H. Morkoc, H. Zabel, C. Choi, and N. Otsuka, J. Appl. Phys. 68, R31 (1990).

34. D.W. Shaw, in *Proc. of the NATO Adv. Res. Workshop on Heterostructures on Silicon* (Kluwer Academic, Norwell, 1988), p. 61.

35. A. Yamamoto and M. Yamaguchi, Mat. Res. Soc. Symp. Proc. 116, 285 (1988).

36. J.M. Phillips, Mat. Res. Soc. Symp. Proc. 71, 97 (1986).

37. L.J. Schowalter, R.W. Fathauer, F.A. Ponce, G. Anderson, and S. Hashimoto, Mat. Res. Soc. Symp. Proc. 67, 125 (1986).

38. H. Zogg, Appl. Phys. Lett. 49, 933 (1986).

39. H. Matsunami, Mat. Res. Soc. Symp. Proc. 116, 325 (1988).

40. R.F. Davis, Thin Solid Films 181, 1 (1989).

41. S. Nishino, J.A. Powell, and H.A. Will, Appl. Phys. Lett. 42, 460 (1983).

42. T. Venkatesan, E.W. Chase, X.D. Wu, A. Inam, C.C. Chang, F.K. Shokoohi, Appl. Phys. Lett. 53, 243 (1988).

43. R.M. Silver, A.B. Berezin, M. Wendman, A.L. de Lozanne, Appl. Phys. Lett. 52, 2147 (1988).

44. W.Y. Lee, J. Salem, V. Lee, T. Huang, R. Savoy, V. Deline, J. Duran, 52, 2263 (1988).

45. D.K. Fork, D.B. Fenner, R.W. Barton, J.M. Phillips, G.A.N. Connell, J.B. Boyce, and T.H. Geballe, Appl. Phys. Lett. 57, 1161 (1990).

Chapter 2 Epitaxial $CoSi_2$ Films on Si

2.1 Introduction

Thin films of transistion-metal silicides on silicon have important applications in metallization of Si-based VLSI as contacts and interconnections.[1,2] Silicide thin films can be readily formed by solid state reaction between deposited metal films and silicon substrates at temperatures well below the melting point.

$CoSi_2$ has some distinct properties among silicides: high thermal stability and low resistivity. Together with $NiSi_2$, it has a cubic CaF_2 structure with a close lattice match to Si. The lattice mismatch equals -1.2% at room temperature and decreases with rising temperature because of the larger thermal expansion of $CoSi_2$ than that of Si. This small lattice mismatch is important for the growth of high quality epilayers on Si.

Highly oriented $CoSi_2$ film can be formed on Si by conventional solid phase epitaxy (SPE)—deposition of thick cobalt film (> 1 nm) on Si substrate and subsequent thermal annealing.[3] The Co_2Si phase nucleates first at the Co/Si interface upon thermal annealing and grows uniformly until complete consumption of cobalt. The CoSi phase then nucleates and grows at the expense of the Co_2Si phase. Finally the highly oriented $CoSi_2$ phase is formed at $\sim 700^oC$.[3]

Single crystalline $CoSi_2$ films can be grown on atomically clean Si(111) substrates in an ultrahigh vacuum.[4] The crystallographic orientation of the layer is rotated by 180° about the [111] axis with respect to the substrate (type-B).[4] The interface is highly ordered with a cobalt coordination number of 5 (cobalt coordination number in bulk $CoSi_2$ is 8).[5] The critical thickness for coherent growth is 3 nm.[6] For films thicker than the critical thickness, misfit dislocations of pure edge type are generated with Burger's vector $1/6 < 11\bar{2} >$.[4] The average dislocation spacing of all thick films (> 10 nm) is roughly the same, about 30 nm.[7,8] This universal lateral mismatch measured at room temperature is a combined result of strain relaxation at the growth temperature and dislocation locking upon cooling.[7,8] The layers grown on vicinal Si(111) are misoriented with respect to the substrates.[9] The misorientation angle is proportional to the offset angle and the perpendicular lattice mismatch.[9] The growth of $CoSi_2$ layers with a smooth surface morphology and with no pinholes was recently achieved by a low temperature deposition process.[10–12] This approach provides the possibilty for Si overgrowth and fabrication of Si/silicide superlattices.[10] High quality layers were also successfully grown on Si(100), (110) by the template technique.[13]

Following the successful growth of single crystalline $CoSi_2$ layers on Si(111) substrates by molec-

ular beam epitaxy (MBE), A.E. White and her colleagues[14] demonstrated that such layers can also be formed by high dose implantation of ^{59}Co into Si substrates and by subsequent thermal annealing. This "mesotaxy" technique has several advantages over the vacuum deposition. The best mesotaxial layers have a residual resistivity of $\sim 1\mu\Omega$ cm, half of the value of the best MBE-grown films.[15] The mesotaxial layers formed on Si(111) are mostly A-type,[16] while the layers grown on Si(111) by MBE deposition are B-type.

One's ability to fabricate single crystalline metal/semiconductor heterostructures provides opportunities for fundamental research on metal-semiconductor interfaces such as the Schottky barrier formation[17] and for novel device applications such as metal- or permeable-base transistors.[18] Theoretical calculations of the energy-band structure and related electronic properties of $CoSi_2$ show that ballistic electron transmission through $CoSi_2$/Si interfaces is possible for (100) and (110), but not for (111) orientations.[19]

In the following sections, we will focus on the structural, elastic, and thermal properties of single layer $CoSi_2$/Si, discuss experimental results from transmission electron microscopy, double crystal x-ray diffractometry, and MeV backscattering spectrometry, and develop phenomenological models to understand some of the results.

2.2 Growth and characterization of $CoSi_2$ on Si(111)

Single crystalline $CoSi_2$ films of type-B and 20-200 nm thick were grown on Si(111) substrates by molecular beam epitaxy (MBE) at University of California at Los Angeles (UCLA).[20] Cho and Arthur[21] showed that an ultrahigh vacuum environment and an atomically clean wafer surface are paramount for growth of high quality films. The Si wafers used for our epitaxial $CoSi_2$ films were cleaned by the Shiraki method,[22] which consists of repeated oxidation and etching to remove carbon and oxygen (two major contaminations), and then immediately loaded into the MBE chamber (base pressure $\sim 10^{-10}$ Torr). The protective oxide layer was stripped off by flash heating to 900°C.[20] $CoSi_2$ films were grown mostly by codeposition of cobalt (flux rate $\sim$ 0.1 nm/s) and silicon ($\sim$ 0.2 nm/s) on Si substrates at $\sim$ 600°C (growth pressure $\sim 10^{-9}$ Torr).[20] Some samples were also made by solid phase epitaxy of room-temperature-codeposited stoichiometric Co/Si mixtures[23] or by cobalt deposition onto hot Si substrates.

Epitaxial $CoSi_2$/Si(111) samples were characterized at Caltech [7–9,20,24] principally by three analytical techniques: backscattering spectrometry (BS),[25] x-ray double crystal diffractometry (DCD),[26] and transmission electron microscopy (TEM).[27] MeV ^{4}He BS analysis shows that the cobalt and sil-

icon concentrations are uniform through the entire film with correct stoichiometry (Co:Si=1:2±0.2) for all samples.[24] Channeling[28] measurements indicate that most films are of reasonable epitaxial quality, with a minimum channeling yield, χ_{min}, of $\sim 2-10\%$.[24] Fig. 2.2-1(a) displays both 2 MeV He backscattering (solid line) and [111] axial channeling (dotted line) spectrum of a demonstration sample composed of a 100 nm thick single layer of $CoSi_2$ on a Si(111) substrate. The surface peaks (at 1.53 MeV and 1.13 MeV for Co and Si, respectively) of the channeling spectrum are due to direct backscattering of an aligned incident beam from the $CoSi_2$ surface. The minimum channeling yield (counts of the channeling spectrum measured immediately beneath the surface peak normalized against those of the backscattering spectrum at the same energy)[28] is $\sim 2\%$ for both Si and Co in the film of the demonstration sample, indicating that the film is highly epitaxial. Energetic ions can be steered by the crystal potential to follow a channel within an angular divergence measured by a channeling half angle, $\psi_{1/2}$.[28] Fig. 2.2-1(b) plots the normalized backscattering yield versus the angular deviation of the incident He beam direction from the [111] channel of the sample. The half angle $\psi_{1/2}$ is the same for both Si (•) and Co (∘) in the film, $\sim 1.2^o$, and is larger than that of Si (■) in the substrate, $\sim 0.9^o$. All these features can be understood by the phenomenological model of channeling phenomena in polyatomic crystals that we developed recently.[29] The dechanneling near ~ 1.06 MeV may be caused by extended defects such as dislocations at the interface.[28] However, in a heterostructure, the channeling half angle of the film differs from that of the substrate (see Fig. 2.2-1(b)). This also contributes to the change of the channeling yield across the interface.[30] The measured dechanneling is a combined contribution of both factors. Therefore, care must exercised in extracting a defect density from a dechanneling yield.

A thin epitaxial film is usually under uniform strain because of its lattice mismatch to a substrate. DCD is routinely used to measure the lattice dimension of a film and hence its strain.[26] In a heterostructure, one uses lattice mismatch, f, perpendicular and parallel strain, $\epsilon^{\perp}$ and $\epsilon^{\parallel}$, to describe the lattice dimension of a film. If both film and substrate have cubic structure, the above quantities are defined according to

$$f = \frac{a_f - a_s}{a_s}, \qquad (2.2-1)$$

where a_f (a_s) is the lattice constant of an unstrained film (substrate);

$$\epsilon^{\perp} = \frac{d_f^{\perp} - d_s^{\perp}}{d_s^{\perp}}, \qquad (2.2-2)$$

where $d_f^{\perp}$ ($d_s^{\perp}$) is the interplanar spacing of a film (substrate) along the surface normal, and $\epsilon^{\parallel}$ is defined similarly. Both $\epsilon^{\perp}$ and $\epsilon^{\parallel}$ can be extracted from x-ray rocking curve measurements.[26] The

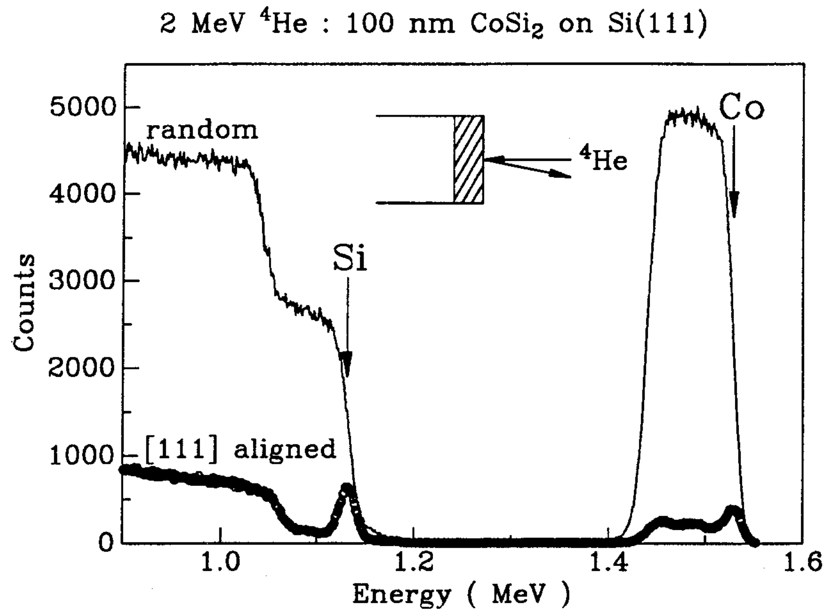

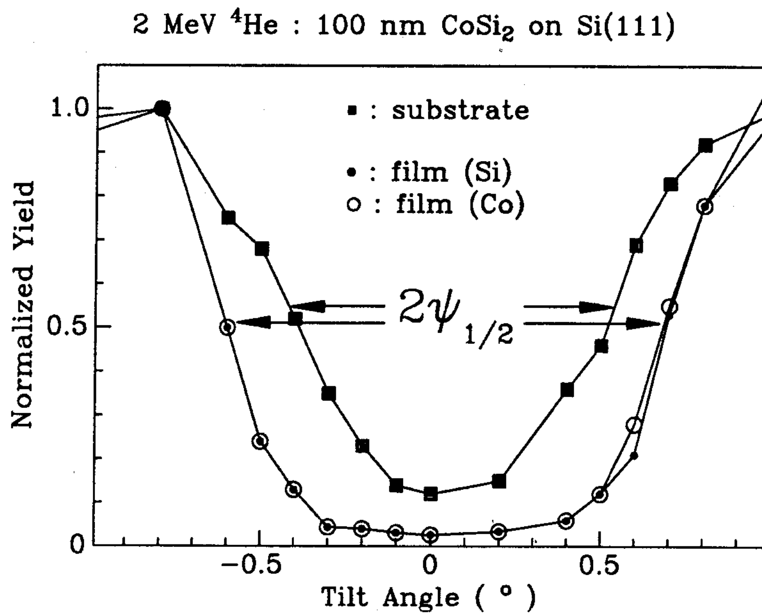

FIG. 2.2-1 2 MeV ^{4}He: (a) backscattering spectra of a $CoSi_2$/Si(111) heterostructure for a beam incident along a random (solid line) and the [111] axial direction (dotted line); (b) an angular scan about the [111] axis of the same sample; the Si and Co signal in the film were taken at 1.53 and 1.13 MeV, respectively, and the substrate signal was taken at 1.05 MeV.

Bragg peak separation between a substrate and a film, $\Delta\theta_B$, is related to $\epsilon^{\perp}$ and $\epsilon^{\parallel}$ by

$$-\Delta\theta_B = k_1\epsilon^{\perp} + k_2\epsilon^{\parallel}, \tag{2.2-3}$$

where k_1 and k_2 are numerical coefficients determined by diffraction geometry.[26] For a symmetrical diffraction, one has

$$k_1 = \tan\theta_B \quad \text{and} \quad k_2 = 0,$$

where θ_B is the Bragg angle of the substrate. Equation (2.2-3) hence simplifies to

$$\epsilon^{\perp} = -\cot\theta_B \Delta\theta_B. \tag{2.2-4}$$

The Fe K_{α_1} x-ray rocking curve from the (111) symmetrical diffraction ($\theta_B = 18^o$) of our demonstration sample is shown in Fig. 2.2-2. The Bragg peak separation, $\Delta\theta_B = 0.33^o$, gives a perpendicular strain of $\epsilon^{\perp} = -1.7\%$ according to Eq. (2.2-4). This is the value for all thick films (> 10 nm).[7,8] Additional information can be extracted from an x-ray rocking curve.[8] A small-amplitude oscillation on either side of the Bragg peak is caused by the finite thickness of the film[26] and is clearly visible in Fig. 2.2-2. This indicates that the film is elastically uniform with few extended defects inside the film, and most dislocations are confined to the interface. The periodicity of the oscillation, $(\delta\theta)_O$, measures the thickness of the film, t_f,[26]

$$t_f = \frac{\lambda}{2(\delta\theta)_O \cos\theta_B}, \tag{2.2-5}$$

where λ is the x-ray wavelength (0.1936 nm). The sample has a periodicity of $(\delta\theta)_O = 0.06^o$ (see Fig. 2.2-2), which gives the film thickness of $t_f = 100\ nm$ according to Eq.(2.2-5). The result agrees well with that obtained from the BS meaurement (see Fig. 2.2-1(a)). The finite film thickness also broadens the diffraction peak, with a full-width at half-maximum intensity (FWHM), W_S, given by the Scherrer equation,[31]

$$W_S = \frac{0.94\lambda}{2t_f \cos\theta_B}. \tag{2.2-6}$$

For a perfect single crystalline film, the measured FWHM, W_θ, is the same as W_S. For a film containing extended defects that produce an imhomogeneous strain, the diffraction peak broadens,

$$W_\theta{}^2 = W_S{}^2 + W_D{}^2,$$

where W_D is the broadening by defects. For a dislocated crystal with a threading dislocation density, ρ, the defect broadening can be estimated by[32]

$$W_D{}^2 = 9b^2\rho, \tag{2.2-7}$$

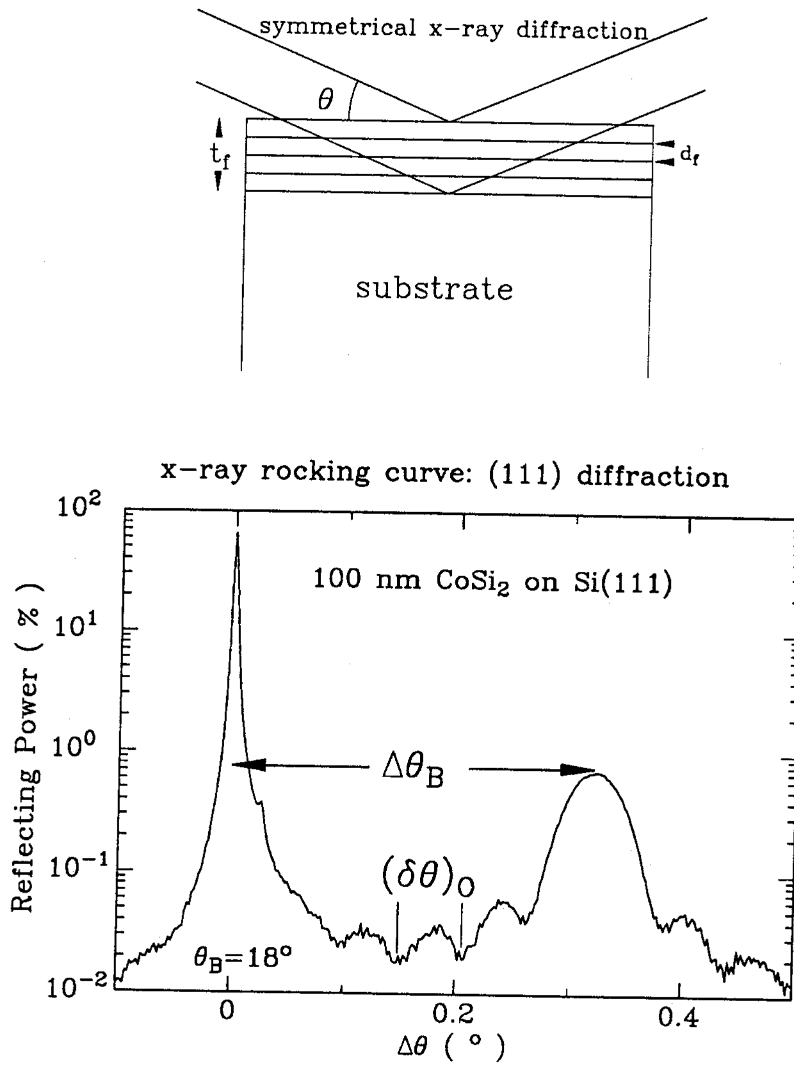

FIG. 2.2-2 A Fe K_{α_1} x-ray ($\lambda = 0.1936$ nm) rocking curve from the (111) symmetrical diffraction of the same $CoSi_2$/Si(111) sample shown in Fig. 2-2-1.

where b is Burger's vector. One could therefore get an estimate of the threading dislocation density in a film from measured FWHM.[8] The measured FWHM of our demonstration sample (see Fig. 2.2-2) is about the same as that caused by finite film thickness, meaning that the threading dislocation density in the film is below the detection limit ($< 10^6/\mathrm{cm}^2$).

Microstructure and extended defects such as dislocations in a crystal can be revealed by TEM.[27] In particular, high-resolution transmission electron microscopy (HRTEM) is capable of direct lattice imaging and has been used to study the atomic structure at the interface in a heterostructure.[33] Fig. 2.2-3(a) is a cross-sectional HRTEM image of the interface for an MBE-grown $CoSi_2$/Si(111) sample,[12] which clearly shows an atomically sharp interface and type-B orientation. Fig. 2.2-3(b) is a weak-beam dark-field plane-view TEM micrograph of a 50 nm thick $CoSi_2$/Si(111) sample prepared by MBE,[24] which illustrates the hexagonal dislocation network at the interface. These misfit dislocations have been identified to be pure edge type with Burger's vertor $\mathbf{b} = 1/6 < 11\bar{2} >$.[4] The average spacing between misfit dislocations, p, is about 30 nm. It is the same for all thick samples (> 10 nm).[8] The parallel strain $\epsilon^{\|}$ is related to dislocation spacing and Burger's vector,

$$\epsilon^{\|} = -\frac{b}{p}. \qquad (2.2-8)$$

For the sample shown in Fig. 2.2-3(b), one has

$$\epsilon^{\|} = -0.7\%.$$

Fig. 2.2-3(c) is the plane-view TEM morié pattern of a 10 nm thick $CoSi_2$/Si(111) sample.[12] The regular morié fringes indicate that the film is uniformly strained. The periodicity of $\sim$ 30 nm (see Fig. 2.2-3(c)) means that the parallel strain of this heterostructure is about -0.6%, about the same as that obtained above for the sample shown in Fig. 2.2-3(b). The termination of the lines (arrowed in Fig. 2.2-3(c)) indicates that a dislocation threads into the film and emerges at the surface. The average spacing between threading dislocations is about 100 nm (see Fig. 2.2-3(c)), meaning that the areal density of threading dislocations in this sample is $10^{10}/\mathrm{cm}^2$. This density is more than 10^4 times greater than that obtained for our demonstration sample, while the average spacing between misfit dislocations is about the same for both samples. This fact means that the threading dislocations in $CoSi_2$ films are not closely related to the misfit dislocations at the interface, and suggests that relaxed epitaxial $CoSi_2$ films free of threading dislocations can be grown.

In this section, we discussed some general properties of epitaxial $CoSi_2$ films on Si(111) and introduced three analytical tools to characterize heteroepitaxial structures. The following sections detail various aspects on the strain state of $CoSi_2$ films.

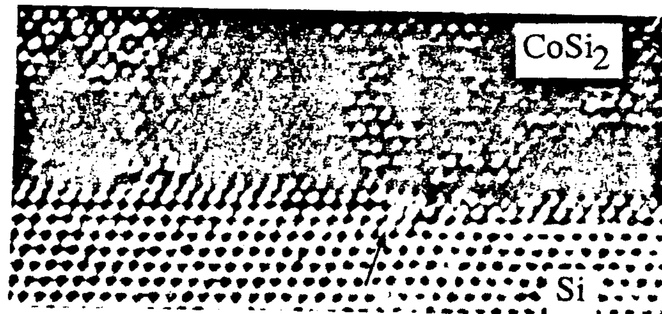

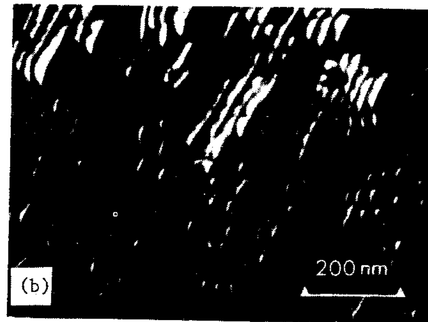

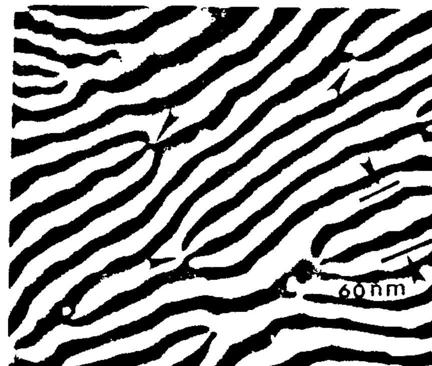

FIG. 2.2-3 Transmission electron micrographs of $CoSi_2$/Si(111) samples: (a) a cross-sectional high resolution lattice image of the interface (from Ref. 12); (b) a weak-beam dark-field plane-view ($[0\bar{2}2]$ beam) micrograph showing a hexagonal misfit dislocation network (from Ref. 24); (c) a plane-view morié pattern caused by the lattice mismatch between the layer and the substrate (from Ref. 12).

2.3 Growth and characterization of $CoSi_2$ on vicinal Si(111)

In this section we study the properties of $CoSi_2$ films grown on Si wafers whose surfaces were tilted away from (111) planes toward $[11\bar{2}]$ direction by an offset angle, ϕ_s, ranging from 0° to 16°.[9] The surface of these vicinal Si(111) substrates consists of wide (111) ledges, and clusters of steps with height $d_{(111)}$ and edges parallel to $[1\bar{1}0]$.[34] Epitaxial B-type $CoSi_2$ films 10-200 nm thick were grown by MBE at UCLA.[20] We used BS and channeling to characterize the stoichiometry, thickness, and epitaxial quality of these films. Some samples were also analyzed by both plane-view and cross-sectional TEM to reveal pinholes, misfit dislocations and interface structure.[20,24] Back-reflection Laue patterns were used to measure the substrate offset angles ϕ_s. DCD shows that there is a misorientation angle, α, between the [111] orientation of the film and of the substrate for the sample with a non-zero offset angle.[9]

All x-ray rocking curves were taken from symmetrical (111) diffractions. For a vicinal substrate with an offset angle ϕ_s, the Bragg peak position, θ_P, is related to the Bragg angle θ_B of the (111) plane and the azimuthal angle, ψ (see Fig. 2.3-1(a)). The relationship can be approximately expressed as[35]

$$\theta_P = \theta_B + \phi_s \cos\psi. \qquad (2.3-1)$$

In particular, at two extreme sample configurations of $\psi = 0^o$ or 180° (see Fig. 2-3-1(a)), the relation is exact and simplifies to

$$\theta_P = \theta_B + \phi_s \text{ or } \theta_P = \theta_B - \phi_s.$$

Fig. 2.3-1(b) shows the measured (111) Bragg peak position θ_P of a vicinal Si(111) substrate with $\phi_s = 16^o$ ($\theta_B = 18^o$) as a function of the sample azimuthal angle ψ. It closely follows the relation dictated by Eq. (2.3-1). Furthermore, the Bragg peak separation between the film (~ 100 nm thick) and the substrate, $\triangle\theta_P$, has a similar functional dependence on ψ (see Fig. 2.3-1(c)). This clearly demonstrates that (a) there is a misorientation angle, α, between the [111] orientation of the film and the substrate; (b) the [111] orientation of the film and the substrate, and the surface normal lie in the same plane.[9] Under such circumstances, only two rocking curve measurements corresponding to $\psi = 0^o$ and 180° are required to extract the misorientation angle α, and the difference of Bragg angles between the film and the substrate $\triangle\theta_B$,[9]

$$\alpha = \frac{\triangle\theta_{P,I} - \triangle\theta_{P,II}}{2}, \qquad (2.3-2a)$$

$$\triangle\theta_B = \frac{\triangle\theta_{P,I} + \triangle\theta_{P,II}}{2}, \qquad (2.3-2b),$$

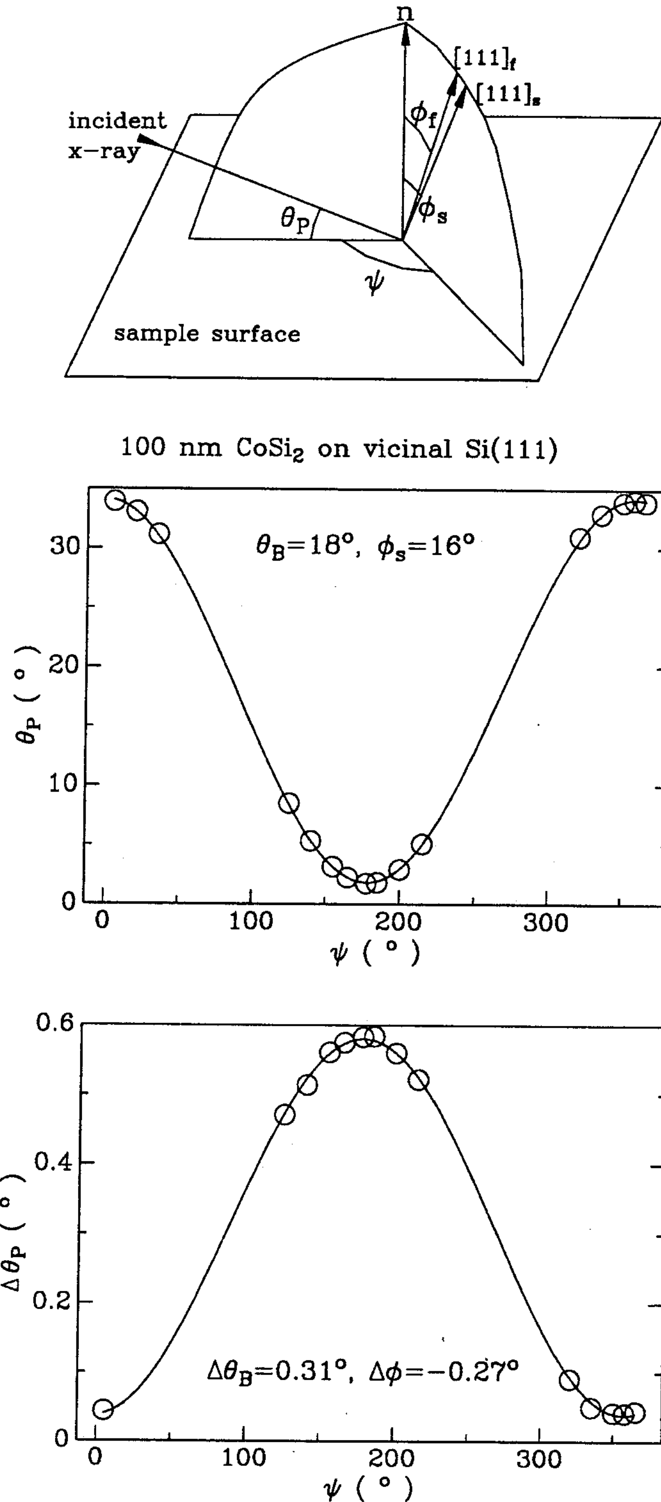

FIG. 2.3-1 Fe K_{α_1} x-ray (111) symmetrical diffraction from a 100 nm thick $CoSi_2$ film on a vicinal Si(111) substrate (offset angle $\phi_s = 16°$): (a) diffraction geometry, n is the surface normal; (b) the Bragg peak position of the substrate versus the azimuthal angle; (c) the separation between the Bragg peaks of the film and the substrate versus the azimuthal angle.

where $\Delta\theta_{P,I}$ ($\Delta\theta_{P,II}$) is the Bragg peak separation obtained for the $\psi = 0^o$ (180°) configuration. For the sample shown in Fig. 2.3-1, we obtain

$$\alpha = -0.27^o \text{ and } \Delta\theta_B = 0.31^o,$$

according to Eq. (2.3-2). The perpendicular strain (defined here as the strain along the [111] direction) $\epsilon^{\perp}$ is therefore $\sim -1.7\%$ according to Eq. (2.2-4).

Our results from back-reflection Laue and DCD analyses of more than 20 samples can be summarized as follows:[9]

(1) The [111] *directions of the substrate and of the film, and the surface normal lie in the same* $(1\bar{1}0)$ *plane (Fig. 2.3-1(*a*)).*[9] *The* [111] *direction of the film lies between the other two directions, and very close to the [111] direction of the substrate at a misorientation angle* α *whose magnitude is much less (about two orders of magnitude) than that of the offset angle itself.*

(2) The misorientation angle α *is proportional to the substrate offset angle* ϕ_s *(Fig. 2.3-2(*a*)). The slope is the same (*$\sim -1.7\%$*) for all samples investigated and is independent of the thickness of the film and the growth processes.*

(3) The perpendicular strain $\epsilon^{\perp}$ *is essentially a constant (*$\sim -1.7\%$*) at room temperature for all the samples.*

These last two facts suggest that the increase of the misorientation angle with an increasing substrate offset angle is given by the perpendicular strain, $\alpha = \epsilon^{\perp}\phi_s$.

To check the validity of this observation, experiments were undertaken to measure the change of the misorientation angle, as the perpendicular strain varies while keeping the substrate offset angle the same. One technique to accomplish this is to perform x-ray rocking curve measurements at different temperatures on the same sample. The strain decreases as the temperature rises because of the difference of thermal expansion coefficients between the film and the substrate,[7,8] but the offset angle does not change. The experimental result of the sample shown in Fig. 2.3-1 ($\phi_s = 16^o$ and film thickness=100 nm) is plotted in Fig. 2.3-2(b). It clearly verifies that the misorientation angle is proportional to the perpendicular strain.

On the basis of the experimental findings and current knowledge about the interfacial structure of $CoSi_2$ films on vicinal Si(111),[36] we propose a simple geometrical model to relate the geometrical quantities of a film and a substrate. For a $CoSi_2$ film on a vicinal Si(111) substrate, the interface consists of evenly distributed, approximately parallel steps of single atomic height $d_{(111)} = 0.314$ nm (see Fig. 2.3-3(a)).[36] In the ideal case of a coherent interface, by imposing "length matching" across

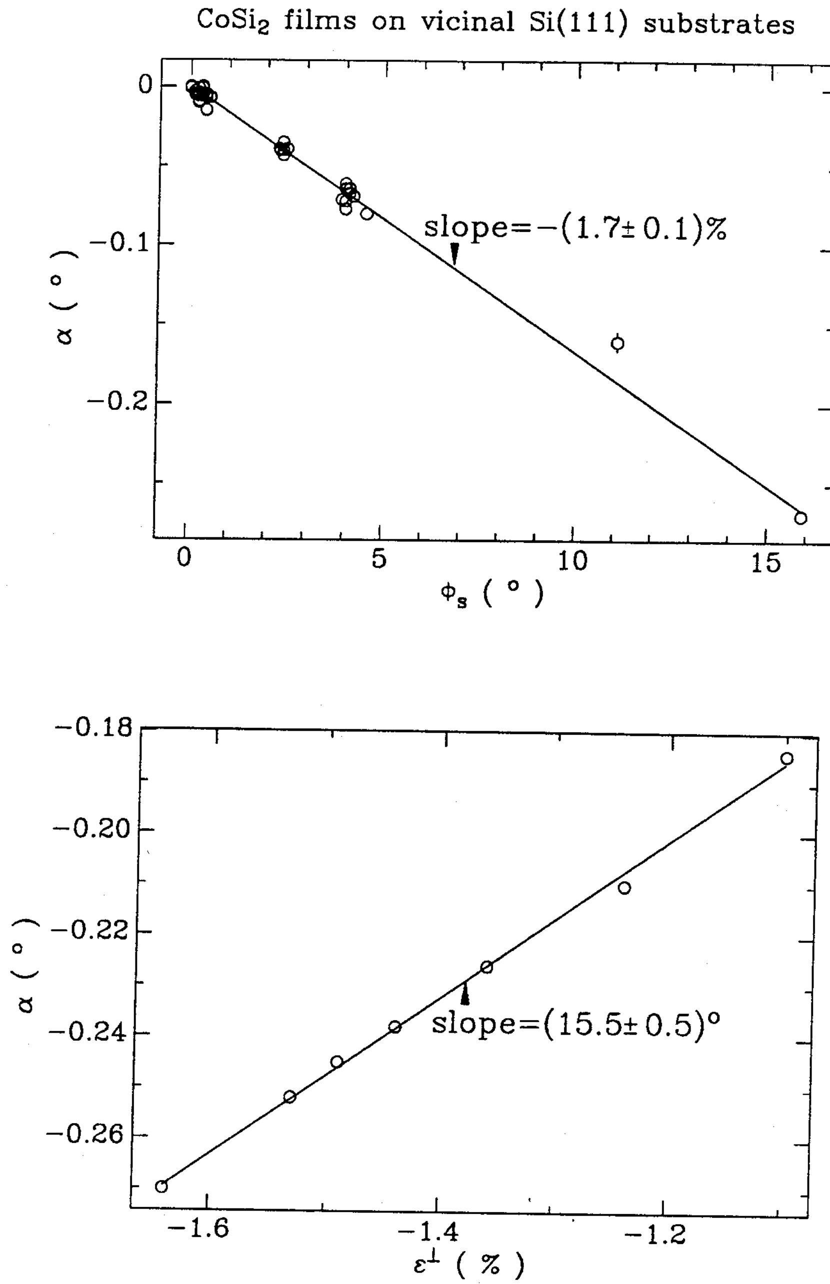

FIG. 2.3-2 The misorientation angle α of (a) the $CoSi_2$/Si(111) samples of various film thickness versus the substrate offset angle ϕ_s; (b) the sample shown in Fig. 2.3-1 (ϕ_s = 16°, 100 nm thick) versus the perpendicular strain.

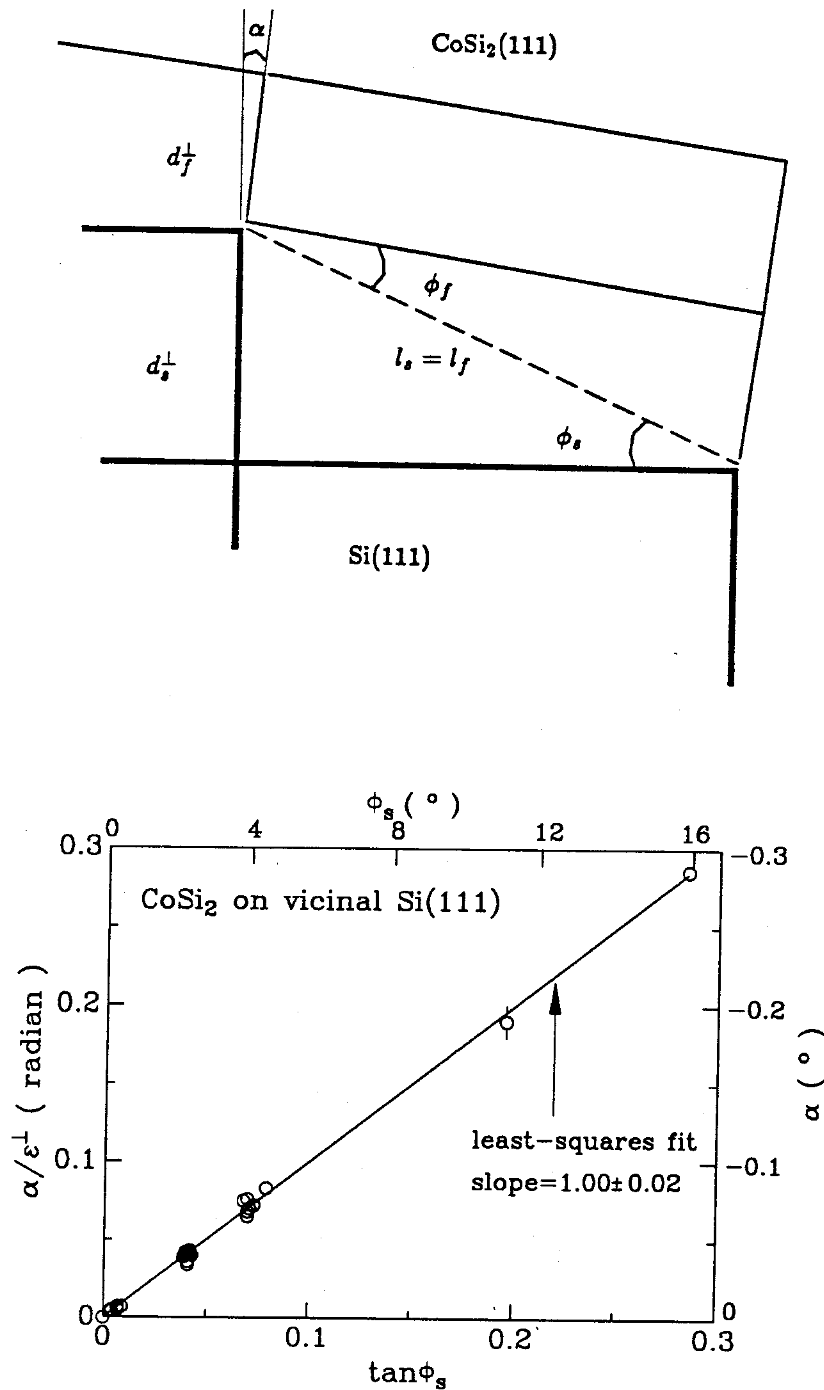

FIG. 2.3-3 (a) Schematical diagram of the interface between a $CoSi_2$ film and a vicinal Si(111) substrate along the $[11\bar{2}]$ tilt direction, and the proposed geometrical model on the misorientation between the film and the substrate; (b) the geometrical model that predicts $\alpha = \epsilon^\perp \tan\phi_s$ agrees excellently with the least-squares fit to the experimental data of epitaxial $CoSi_2$ films grown on vicinal Si(111) substrates.

the interface (Fig. 2.3-3(a)), we obtain the following relations,

$$l_f = \frac{d_f^{\parallel}}{\cos\phi_f} = \frac{d_s^{\parallel}}{\cos\phi_s} = l_s \quad \text{and} \quad l_f = \frac{d_f^{\perp}}{\sin\phi_f} = \frac{d_s^{\perp}}{\sin\phi_s} = l_s. \qquad (2.3-3)$$

After simple algebra, one has

$$\alpha = \epsilon^{\perp}\tan\phi_s \qquad (2.3-4a)$$

and

$$\epsilon^{\parallel} = -\epsilon^{\perp}\tan^2\phi_s, \qquad (2.3-5a)$$

to the first order in α. Non-zero (but very small) $\epsilon^{\parallel}$ from Eq. (2.3-5a) for a coherent interface is caused by misorientation between planes such as $(11\bar{2})$ of the film and the substrate. Along $[1\bar{1}0]$ direction (normal to the paper face in Fig. 2.3-3(a)), there is no misorientation, and hence $\epsilon^{\parallel}{}_{[1\bar{1}0]}$ equals 0 for a coherent interface. In a general case where there exist misfit dislocation arrays at the interface, similar results can be derived,

$$\alpha = \epsilon^{\perp}\tan\phi_s \qquad (2.3-4b)$$

and

$$\epsilon^{\parallel} = -\delta - \epsilon^{\perp}\tan^2\phi_s, \qquad (2.3-5b)$$

where δ is the strain relaxation from the misfit dislocations. This model agrees excellently with the experimental results (see Fig. 2.3-3(b)). A similar model has been proposed by Nagai to explain the observed misorientation effect between a film and a vicinal substrate in a compound semiconductor heterostructure.[37]

2.4 Critical thickness and strain relaxation

We investigate here the (elastic) energetics and (meta-) stability of a $CoSi_2$/Si(111) heterostructure. The material is treated as an elastic continuum. The (elastic) energy is composed of two parts: uniform strain energy and dislocation energy. The equilibrium state of this system corresponds to that of the minimum elastic energy.[38] For a very thin film, the film is strained to match the lattice constants of the substrate. As the film thickens, it becomes energetically favorable to generate misfit dislocations at the interface to relieve the lattice mismatch f between the film and the substrate. Using the minimum energy criterion, Matthews and Blakeslee[38] estimated the critical thickness of a film, t_{cr}, the maximum film thickness above which generation of misfit dislocations is energetically

favored, for a given lattice mismatch f,

$$\frac{t_{cr}}{b} = \frac{1}{8\pi(1+\nu)|f|}(\ln\frac{t_{cr}}{b}+1), \qquad (2.4-1)$$

where ν is Poisson's ratio of the film. For a $CoSi_2$/Si(111) heterostructure, the lattice mismatch at room temperature is $f = -1.2\%$. The critical thickness obtained from Eq. (2.4-1) is $t_{cr} = 1.7$ nm, using $\nu = 1/3$ for $CoSi_2$ on Si(111).[8] The experimental critical thickness determined by plane-view TEM at room temperature is ~ 3 nm,[6] about 80% larger than that from the theoretical estimate. We will explain this discrepency in Ch. 2.6.

For a film thicker than the critical thickness ($t_f > t_{cr}$), misfit dislocations are generated and the elastic strain relaxes. The strain of the film in the equilibrium state is given by[38]

$$\epsilon^{\perp} = f(1 + \frac{2\nu}{1-\nu}\frac{t_{cr}}{t_f}\frac{\ln t_f/b+1}{\ln t_{cr}/b+1}). \qquad (2.4-2)$$

As an example, we considered a $CoSi_2$/Si(111) heterostructure at room temperature, and computed the perpendicular strain $\epsilon^{\perp}$ as a function of film thickness according to Eq. (2.4-2) (solid line in Fig. 2.4-1). We used the measured t_{cr} in the computation (using theoretical t_{cr} gives a similar result beyond critical thickness). The data points in the same figure are from all the $CoSi_2$/Si(111) samples we have analyzed (see Ch. 2.2 and 2.3), grown by MBE or SPE, with film thickness from 10 nm to 230 nm, and with a substrate offset angle from 0° to 16°. It clearly shows that the strain is roughly a constant, $\epsilon^{\perp} \sim -1.7\%$, over the thickness range from 10 nm to 230 nm (Fig. 2.4-1). And the film is more strained than that predicted by Matthews and Blakeslee's model, meaning that the $CoSi_2$/Si(111) samples are metastable at room temperature.

To study the effect of thermal processing on such metastable heterostructures, we annealed the samples in a vacuum ($\sim 5 \times 10^{-7}$ Torr) at 650, 750, 850°C for 30 min and analyzed the structural change of the samples at room temperature after such postgrowth thermal processing. 2 MeV ^{4}He backscattering spectra of both random and aligned incidence remain the same before and after thermal processing, meaning that no significant diffusion or structural reordering occurs.[7,20] Misfit dislocation spacings from plan view TEM remain unchanged, ~ 30 nm,[20] so does the perpendicular strain from DCD measurements, $\sim -1.7\%$.[7,20] These results demonstrate that the $CoSi_2$/Si(111) structures do not change upon annealing at 850°C for 30 min in a vacuum.

To gain insight on such elastic metastability of $CoSi_2$/Si(111) heterostructures at room temperature, we conducted DCD measurements at elevated temperatures on some of these metastable samples. As shown in the next section, we discovered that at their growth temperature, the samples

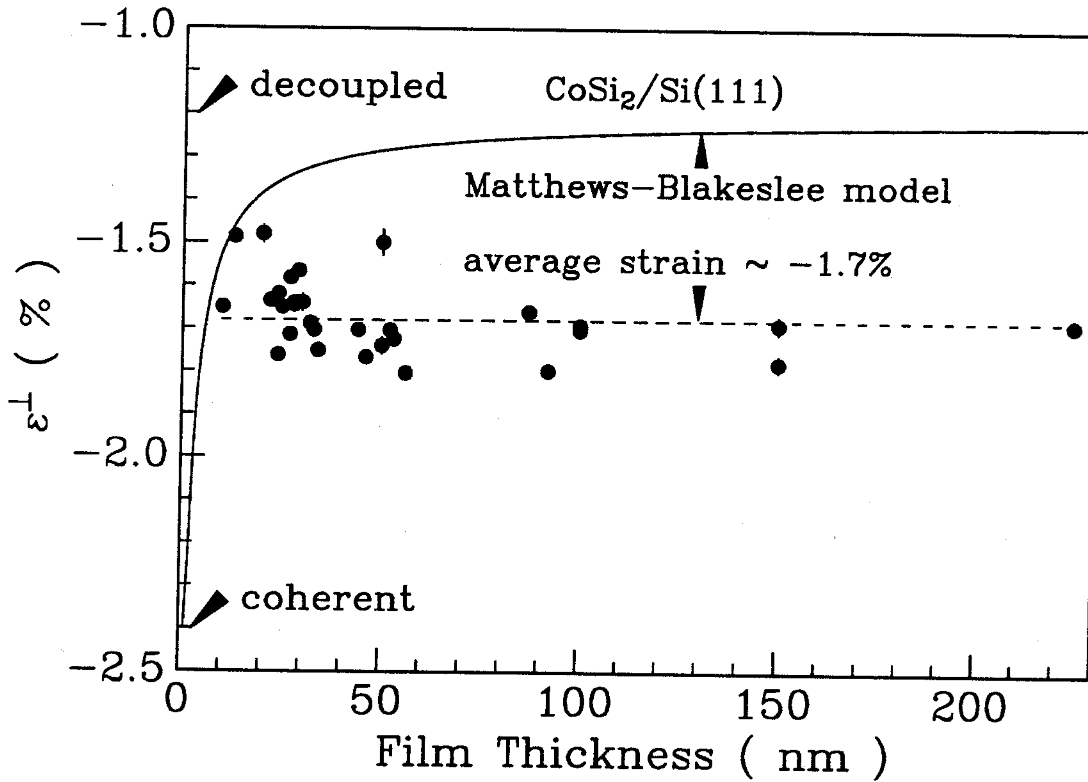

FIG. 2.4-1 Perpendicular strain in an epitaxial $CoSi_2$ film as a function of film thickness for a $CoSi_2$/Si(111) heterostructure. The solid line is the strain relaxation behavior predicted by Matthews and Blakeslee's minimum energy model. The dashed line is the average of the experimentally measured strain value on samples of various film thickness, substrate offset angle, and growth condition.

are relaxed. The strain measured at room temperature is caused by different thermal contractions of $CoSi_2$ and Si upon cooling while the misfit dislocations created during the growth do not shear and no new ones are nucleated.[7]

2.5 Thermal strain and its inference for pseudomorphic growth

We report here a DCD measurement of the perpendicular strain in epitaxial $CoSi_2$ films ~ 100 nm thick (which is much thicker than t_{cr}) formed on Si substrates by codeposition of Co and Si at either $\sim 600^oC$[20] or at room temperature followed by *in situ* annealing.[23] The surfaces of the substrates are tilted from the (111) planes of the Si lattice towards the $[11\bar{2}]$ direction by offset angles ϕ_s ranging from 0° to 16°.

A sample was mounted on a heating stage capable of reaching 650°C in air.[7] The perpendicular strain at temperature, T,

$$\epsilon^{\perp}(T) \equiv \frac{d^{\perp}{}_f(T) - d^{\perp}{}_s(T)}{d^{\perp}{}_s(T)}, \qquad (2.5-1)$$

was extracted from Fe K_{α_1} x-ray rocking curve diffracted from the symmetrical (111) diffraction peaks. The parallel strain $\epsilon^{\parallel}$ defined analogously to $\epsilon^{\perp}$ is related to the lattice mismatch f and $\epsilon^{\perp}$,[7]

$$\epsilon^{\perp} = (\frac{1+\nu}{1-\nu})f - (\frac{2\nu}{1-\nu})\epsilon^{\parallel}. \qquad (2.5-2)$$

The measured perpendicular strain at room temperature is $\epsilon^{\perp}(24^oC) = -1.66 \pm 0.01\%$, a typical value for all thick films ($t_f > t_{cr}$).[7,8] That strain is between that of a fully relaxed film for which $\epsilon^{\perp}{}_{decoupled}(24^oC) = f(24^oC) = -1.23\%$, and that of a pseudomorphic film for which $\epsilon^{\perp}{}_{coherent}(24^oC) = -2.46\%$, obtained from Eq. (2.5-2) with $\epsilon^{\parallel} = 0$ for a coherent film and $\nu = 1/3$ for a $CoSi_2$ film on Si(111).[7] Thus, the thick $CoSi_2$ films ($t_f > t_{cr}$) are elastically strained at room temperature with a common perpendicular elastic strain, $e^{\perp}$, of $e^{\perp}(24^oC) \approx \epsilon^{\perp}(24^oC) - f(24^oC) = -0.43\%$.

Measurements of the perpendicular strain at elevated temperatures provide a clue as to why $\epsilon^{\perp}(24^oC)$ is always nearly -1.66%. Figure 2.5-1 shows two sets of experimental data ($\bullet$ and $\triangle$) for two samples that have slightly different perpendicular strains at room temperature. As the temperature rises, the strain decreases, because $CoSi_2$ expands faster than Si does upon heating. The slopes, $(1.3 \pm 0.1) \times 10^{-5}/^oC$, are twice as large as the difference of the bulk thermal expansion coefficients between $CoSi_2$ ($\alpha_f = 0.94 \times 10^{-5}/^oC$[1]) and Si ($\alpha_s = 0.29 \times 10^{-5}/^oC$[39]), $\alpha_f - \alpha_s = 0.65 \times 10^{-5}/^oC$. All strain values remain reversible after ~ 2 *hr* annealing in air up to 490°C.

This temperature dependence can be explained if it is assumed that the lateral change in the $CoSi_2$ lattice is constrained to follow that of the Si substrate. The slope of the perpendicular strain versus temperature is then given by

$$\frac{\delta\epsilon^{\perp}{}_{constrained}}{\delta T} = (\frac{1+\nu}{1-\nu}) \cdot (\alpha_f - \alpha_s). \qquad (2.5-3)$$

Substituting $\nu = 1/3$,[7,8] the model predicts a slope of $1.3 \times 10^{-5}/^oC$, in excellent agreement with the measured value of $(1.3 \pm 0.1) \times 10^{-5}/^oC$. We thus conclude that *no new misfit dislocations are created by thermal cycling in air up to 490°.*

Figure 2.5-1 also contains the predicted perpendicular strains versus temperature for a fully relaxed (stress-free) film, labeled "decoupled," and a pseudomorphic film, labeled "coherent." At 24°C, these lines have known values of −1.23% (from Eq. (2.5-2) with $\epsilon^{\parallel} = f$, ■) and −2.46% (from Eq. (2.5-2) with $\epsilon^{\parallel} = 0$, open square). The slope for the fully relaxed film is given by

$$\frac{\delta\epsilon^{\perp}{}_{decoupled}}{\delta T} = \frac{\delta f(T)}{\delta T} = (\alpha_f - \alpha_s), \qquad (2.5-4)$$

while that for the coherent film is given by Eq. (2.5-3). The line for the fully relaxed film intercepts the experimental curves near 600°C, which is the nominal growth temperature of the films. This fact says that *within the uncertainties of the experimental data, the epitaxial $CoSi_2$ films grow elastically unstrained at the temperature of their formation.* This fact, combined with the observation that no new misfit dislocations are generated upon subsequent cooling of the sample, explains the common value of strain observed at room temperature for all thick films ($t_f > t_{cr}$). The observed elastic strains originate after the films are formed and are the consequence of the dissimilar thermal contraction of the film and substrate upon cooling.

As a corollary of the above discussion, one can obtain the parallel strain of the $CoSi_2$ films at room temperature in two ways. For a rigid interface, the parallel strain at room temperature must be the same as that at the growth temperature. At the growth temperature, the $CoSi_2$ film is fully relaxed, and hence cubic. The parallel strain $\epsilon^{\parallel}$ at the growth temperature thus equals the perpendicular strain $\epsilon^{\perp}$ at that temperature,

$$\epsilon^{\parallel}(24^oC) = \epsilon^{\parallel}(600^oC) = \epsilon^{\perp}(600^oC) = -0.86\%, \qquad (2.5-5)$$

where the numerical value is obtained from Fig. 2.5-1. On the other hand, $\epsilon^{\parallel}$ can be obtained from Eq. (2.5-2). With $\epsilon^{\perp}(24^oC) = -1.66\%$, $f(24^oC) = -1.23\%$, and $\nu = 1/3$, one finds $\epsilon^{\parallel}(24^oC) = -0.80\%$. This consistency supports the notion that the interface does not shear, and the parallel strain is independent of temperature with zero elastic strain at the growth temperature.

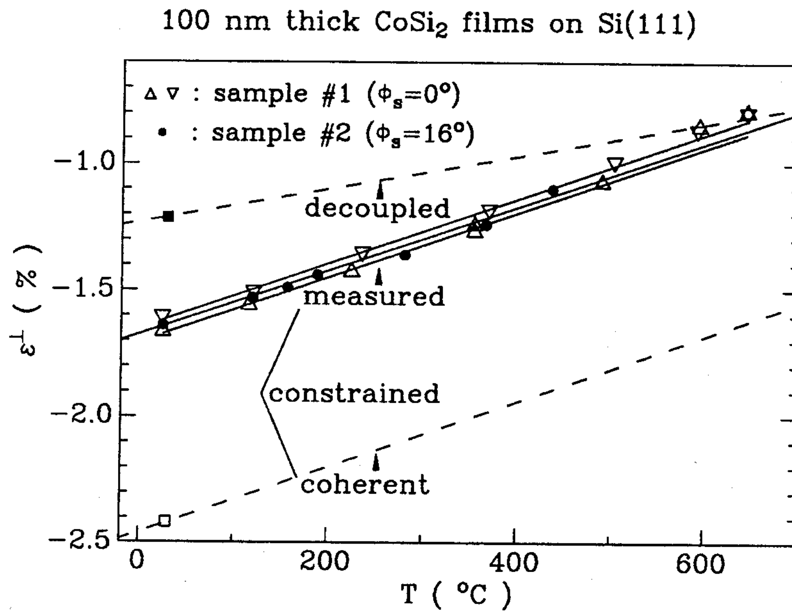

FIG. 2.5-1 Perpendicular x-ray strain $\epsilon^{\perp}$ as a function of sample temperature T for two 100 *nm* thick $CoSi_2$ films on (i) a Si substrate whose surface is offset from the [111] direction by 16° towards the [1$\bar{1}$0] direction of the substrate (•), and (ii) a Si substrate whose surface is aligned with the (111) planes (△▽). All strain values are reversible below 490°C. When the latter sample was heated above that temperature up to 650°C and then cooled, a reduced strain was measured (▽), again reversible below 500°C. The solid lines are linear fits to the data (omitting the two highest temperature points). The strain for a coherent interface is calculated with the Poisson ratio $\nu = 1/3$ (lower dashed line). At the temperature at which the samples were grown ($\sim$ 600°C), the measured strain is that predicted for an elastically relaxed film (upper dashed line).

The estimated average spacing between misfit dislocations from the parallel strain $\epsilon^{\|}$,

$$p = \frac{b}{|\epsilon^{\|}|} \approx 28\ nm,$$

agrees well with the result obtained from the plan view TEM ($\sim$ 30 nm) of the samples produced by the same deposition process (see Fig. 2.2-3(b)).

Furthermore, sample #1 was raised to 600°C and subsequently to 650°C in air, and rocking curves were measured *in situ*. The perpendicular x-ray strains derived from these measurements indicate that the sample is fully relaxed at these temperatures (Fig. 2.5-1). Cooling this sample to room temperature now yields a slightly reduced perpendicular strain (−1.61% instead of −1.66%). Reheating the sample in air then traces a new line for the perpendicular x-ray strain *vs.* temperature (points marked $\bigtriangledown$). That line has the same slope as that measured initially (points marked $\triangle$). This new curve is reproducible up to 550°C. This result shows that maintaining the sample in air near or above 650°C for a sufficient length of time ($\sim$ 40 min) modifies the elastic strain in the film. The x-ray rocking curve of this modified sample (point $\bigtriangledown$ in Fig. 2.5-1) is shown in Fig. 2.5-2 (dotted line). One sees that the interaction of the sample with air at $\sim$ 650°C has reduced the perpendicular x-ray strain and has broadened the diffraction peak from the film when compared with the rocking curve of the as-grown sample (solid line). We conclude therefore that even though the interface does not shear at temperatures below $\sim$ 600°C (the growth temperature) in air, the interfacial registry and the film quality are altered by annealing above $\sim$ 600°C in air.

As an additional experiment, a piece of the same sample #1 was thermally annealed in vacuum at 700°C for 40 min. The rocking curve of the sample was then remeasured at room temperature (solid line in Fig. 2.5-2). The vacuum treatment produces no detectable change, consistent with previous results of Ch. 2.4. This indicates that the strain state of an epitaxial $CoSi_2$ film is not altered by an annealing at temperature higher than the $CoSi_2$ formation temperature in vacuum. The change after annealing in air at temperatures above $\sim$ 600°C then must be the result of reaction of the epitaxial film with the ambient-air. Auger electron spectroscopy of the ambient-air-annealed sample shows that a thin oxide of $\sim$ 10 nm is present on the surface of the silicide but that is absent in the vacuum-annealed sample. An oxidation of the $CoSi_2$ at its surface induces atomic rearrangements at the silicide/silicon interface.[48] All three samples of as-grown, vacuum-annealed, and air-annealed were also analyzed by 2 MeV ^{4}He backscattering and channeling. No significant differences are noted (see Fig. 2.2-1 as an example of the spectra).

The findings reported here have interesting implications that may have very general validity.

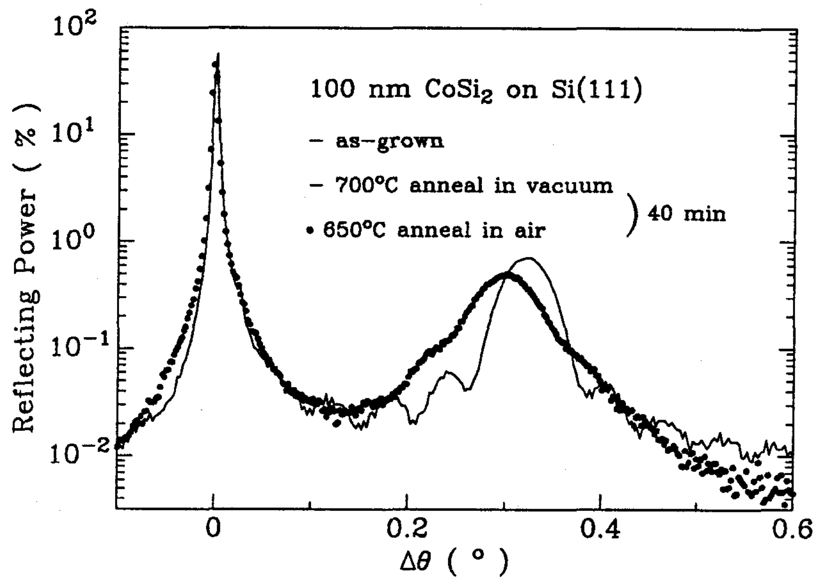

FIG. 2.5-2 Three x-ray rocking curves diffracted from symmetrical (111) planes measured at room temperature on sample #1 as-grown, vacuum-annealed, and air-annealed. The curve of the as-grown sample is indistinguishable from that measured after annealing *in vacuum* at 700°C for 40 *min* (solid line). Annealing *in air* at 650°C induces an irreversible reduction of the strain in the epitaxial $CoSi_2$ film as indicated by the shift and the broadening of the diffraction peak (dotted line).

We note that for an epitaxial GaAs film grown on a Si(100) substrate, findings like ours have recently been reported.[40] There too, the strain observed at room temperature is explainable in terms of the differential thermal contraction of the film and substrate upon cooling after the epitaxial structure was created at an elevated temperature. When two such dissimilar systems behave so similarly, the observation may apply to a large class of epitaxial systems. Generalizing accordingly, we extract the following rules:

— *Differential thermal expansion does not introduce new misfit dislocations in epitaxial $CoSi_2$ films on Si(111), even when the film is thicker than the critical thickness. This statement probably applies to all systems where non-ionic bonding dominates.*

— *For pseudomorphic growth in such systems, it is important to minimize the lattice mismatch at the growth temperature.*

Tabulated lattice constants are usually measured at room temperature. It thus follows that thermal expansion data are also important to consider in optimizing conditions for pseudomorphic growth. The data are, however, often unavailable. The importance of a lattice match at the growth temperature for pseudomorphic growth has already been pointed out in the literature.[41,42]

We note further that when an epitaxial $CoSi_2$ film is exposed to a reactive medium (air), irreversible changes take place in the strain state of the film that do not arise in the absence of a reaction. Similar effects have been reported for different systems. A polycrystalline film of Pd_2Si on an epitaxial Pd_2Si film raised to 275°C in vacuum is stable. The same film undergoes an epitaxial reordering when additional polycrystalline Pd_2Si is formed by a reaction with an overlaid Pd film.[43] The disordering of III-V heterostructures by impurity diffusion is another example where a defect-generating process (here group II lattice vacancies generated by the diffusion of an impurity) destabilizes a structure that is quite (meta)stable in the absence of this process.[44] Yet another example is the epitaxial arrangement of a polycrystalline Ge film on a Si single crystal substrate induced by thermal annealing in oxygen.[45] The feature common to all these examples is the presence of a defect-generating process (diffusion, reaction, irradiation). The defects destabilize a metastable state. We are thus led to conclude that

— *To favor pseudomorphic growth, processes that induce atomic rearrangement should be minimized.*

Procedures advocated in the literature for the successful growth of epitaxial layers are consistent with that conclusion. For example, a successful procedure to grow high quality epitaxial layers

consists of first growing a very thin ($t < t_{cr}$) epitaxial film by solid phase epitaxy, followed by codeposition of a thick layer ($t > t_{cr}$) at low temperature and subsequently inducing epitaxial rearrangement of the full layer at an elevated temperature.[46] This template procedure actually implements the idea of minimizing atomic rearrangement. One also understands why codeposition of a compound in the correct atomic ratio is more likely to result in a pseudomorphic structure than its formation by solid phase reaction if the epitaxial film is strained at the formation temperature, or why deposition at a low temperature followed by high temperature annealing is more likely to result in a pseudomorphic structure than deposition at a high temperature.[47]

The three rules for pseudomorphic growth enunciated here are in the nature of guidelines, as is evident from the way they are deduced. They are nonetheless useful, because they emphasize considerations not previously stressed in the literature (lattice matching at the growth temperature, with the concomitant relevance of knowing thermal expansion behavior for the materials involved; minimizing atomic relocation processes during the film formation).

2.6 Elastic and thermal properties of mesotaxial $CoSi_2$ films on Si

Thin $CoSi_2$ films formed by high dose ^{59}Co implantation are A-type,[14] enabling one to make a high-precision determination of both parallel and perpendicular strains by x-ray rocking curves.[8] With B-type films, the Bragg peaks from asymmetrical diffraction of the films are widely separated from those of the substrates, precluding high-precision measurements of $\epsilon^{\parallel}$. Recognizing this opportunity that mesotaxial A-type $CoSi_2$ films on Si(111) offer, we measured both the perpendicular and the parallel strain in such films, as well as those of mesotaxial films formed on Si(100). These two measurements enable us to extract two ratios of the three independent elastic constants of cubic single crystal $CoSi_2$. We also measured the curvature of one sample to estimate the biaxial stress in the film. These three measurements yield the absolute values of the three elastic constants of $CoSi_2$. We repeated similar measurements up to $\sim$ 500°C. Assuming that the elastic constants do not change between 20°C and 500°C, we are able to extract the linear thermal expansion coefficient for single crystalline $CoSi_2$.

A. Sample Preparation

Single crystalline buried $CoSi_2$ films 110 nm thick were formed at AT&T Bell Laboratories by 200 keV $3 \times 10^{17}/cm^2$ ^{59}Co implantation at $\sim$ 400°C into Si substrates of both (100) and (111) orientation, followed by vacuum annealing at 600°C for 60 min and 1000°C for 30 min.[14] The top Si

layers were then removed by reactive ion etching. Cross-sectional transmission electron microscopy shows that the interfaces between the films and substrates are flat and atomically sharp.[14] MeV ^4He backscattering and channeling spectrometry indicate that the films are stoichiometric and highly oriented, with a minimum yield of $\sim 3\%$.[14]

B. Lattice Mismatch and Misfit Dislocations

We used DCD to measure both $\epsilon^{\perp}$ and $\epsilon^{\parallel}$ between the $CoSi_2$ film and the Si substrate. Figure 2.6-1 shows the Fe K_{α_1} x-ray rocking curves from the symmetrical (400) and asymmetrical (311) diffraction planes of the $CoSi_2$/Si(100) sample. The two curves diffracted from the same (311) planes (A and B in Fig. 2.6-1) correspond to the x-ray incidence of opposite directions. The strain $\epsilon^{\perp}$ and $\epsilon^{\parallel}$ were extracted from the angular separations of the Bragg peaks between the film and the substrate shown in Fig. 2.6-1. The results are listed in the first column of Table 2.6-I. They are very close to those measured for buried $CoSi_2$ mesotaxial layers in the second column of Table 2.6-I.[49] This agreement means that the Si capping layer has little effect on the strain state of the buried $CoSi_2$ layer. Unequal $\epsilon^{\perp}$ and $\epsilon^{\parallel}$ means that the $CoSi_2$ film is distorted tetragonally under the tensile stress imposed by the Si substrate. The relative volume expansion, $\Delta V/V$, is $\sim 0.2\%$, more than 3 times less than the average linear dilatation, $\Delta L/L$, ($\sim 0.7\%$, see Table 2.6-I). This means that the volume is almost conserved under biaxial stress.

The non-zero $\epsilon^{\parallel}$ means that there exist misfit dislocations at the interface to relax strain. Burger's vector of the dislocations for epitaxial $CoSi_2$ films on Si(100) substrates is $\mathbf{b} = 1/4 < 111 >$.[50] The average spacing p between the misfit dislocations is therefore

$$p = \frac{b_e}{|\epsilon^{\parallel}|} = \frac{0.19\ nm}{0.62\%} = 31\ nm,$$

where b_e is the edge component of Burger's vector projected onto the interface plane. This is roughly the same as that of MBE-grown thick ($> 10\ nm$) B-type $CoSi_2$/Si(111) samples ($\sim 30\ nm$).[4]

Single crystalline $CoSi_2$ has three independent elastic constants, C_{11}, C_{12}, C_{44}. Measurements of the lattice distortion of $CoSi_2$ films on Si substrates of two different orientations enable one to extract two ratios, C_{12}/C_{11} and C_{44}/C_{11}. From the definition of the lattice mismatch and the elastic strain, $e^{\perp}$ and $e^{\parallel}$, one has the following relationship,

$$\frac{e^{\perp}}{e^{\parallel}} = \frac{\epsilon^{\perp} - f}{\epsilon^{\parallel} - f}. \quad (2.6-1)$$

Assuming that the film is under biaxial stress in the (100) plane, the relation[51]

$$\frac{e^{\perp}}{e^{\parallel}} = -\frac{2C_{12}}{C_{11}} \quad (2.6-2)$$

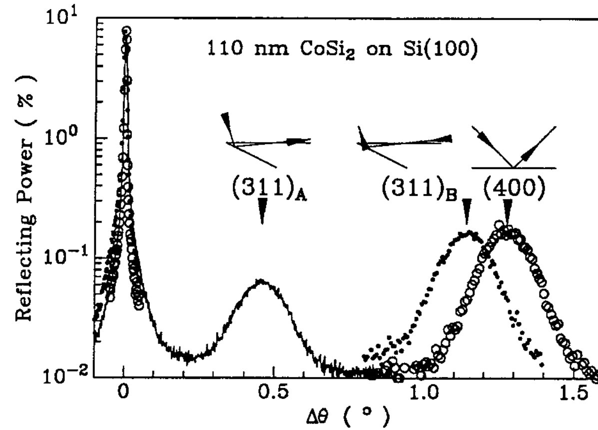

FIG. 2.6-1. Fe K_{α_1} x-ray ($\lambda = 0.1932$ nm) rocking curves of symmetrical (400) and asymmetrical (311) diffractions from a mesotaxial $CoSi_2$/Si(100) sample. The diffraction geometry and direction of x-ray incidence are shown in the inset above the corresponding Bragg peaks from the $CoSi_2$ film.

Table 2.6-I. Lattice distortion of $CoSi_2$ films on (100) and (111) oriented Si substrates. Data for Si/$CoSi_2$/Si samples are from Ref. 49 and that for B-type sample is from Ref. 7.

$f = -1.22\%$	$CoSi_2$/Si(100)	Si/$CoSi_2$ /Si(100)	$CoSi_2$/Si(111)	Si/$CoSi_2$ /Si(111)	B-$CoSi_2$/Si(111)
$\epsilon^{\perp}$ (%)	-2.18	-2.14	-1.69	-1.74	-1.61
$\epsilon^{\parallel}$ (%)	-0.62	-0.66	-0.72	-0.66	-0.80
$\Delta L/L$ (%)	0.7	0.7	0.5	0.6	0.4
$\Delta V/V$ (%)	0.2	0.2	0.5	0.6	0.5

Table 2.6-II. Ratios and elastic constants (in units of GPa) of cubic $CoSi_2$ from strain and curvature measurements. Data for Si are from Ref. 51 and are listed for comparison.

	$\nu_{(100)}$	$\nu_{(111)}$	C_{12}/C_{11}	C_{44}/C_{11}	C_{11}	C_{12}	C_{44}
$CoSi_2$	0.44	0.32	0.80	0.36	277	222	100
Si	0.28	0.18	0.39	0.48	166	64	80

holds in the linear elasticity theory. From the measured strain (Table 2.6-I) and Eqs. (2.6-1)&(2.6-2), the ratio C_{12}/C_{11} is obtained (Table 2.6-II). This value (0.80) is about twice that of silicon (0.39).[50] For later convenience, we define a Poisson ratio, ν, for thin films under biaxial stress, according to

$$\frac{e^{\perp}}{e^{\parallel}} \equiv \frac{-2\nu}{1-\nu}. \qquad (2.6-3)$$

This yields $\nu_{(100)} = 0.44$ for the $CoSi_2$ film on Si(100) substrate (Table 2.6-II).

Similarly, symmetrical (111) and asymmetrical (311) x-ray rocking curves were also recorded for the $CoSi_2$/Si(111) sample. The perpendicular and parallel strain were extracted from the Bragg peak separations. The results are given in Table 2.6-I, which again agrees well with those for buried $CoSi_2$ films ($\epsilon^{\perp} = -1.74\%$ and $\epsilon^{\parallel} = -0.66\%$).[49] Furthermore, they are also about the same as those for MBE-deposited B-type $CoSi_2$ films on Si(111) substrates ($\epsilon^{\perp} = -1.61\%$ and $\epsilon^{\parallel} = -0.80\%$).[7] This shows that the strain state of thick ($> 10nm$) epitaxial $CoSi_2$ films on Si(111) substrates is independent of the process by which the silicide films are formed, and whether the films are type-A or type-B. Burger's vector of the misfit dislocations is $\mathbf{b} = 1/6 < 11\bar{2} >$ for both type-A $CoSi_2$ formed by ^{59}Co implantation[49] and type-B films by MBE[4] on Si(111) substrates. The average misfit dislocation spacing is therefore $p = 31\ nm$, obtained from Table 2.6-I. This is the same as that on Si(100), implying that the dislocation spacing is independent of substrate orientation.

The areal density ρ of imperfections such as threading dislocations in epitaxial $CoSi_2$ films can be estimated from the measured x-ray peak broadening W_θ using Equation (2.2-7),

$$\rho = \frac{{W_\theta}^2 - {W_S}^2}{9b^2}. \qquad (2.6-4)$$

The size broadening W_S can be obtained from the Scherrer Equation (2.2-6). The imperfection density estimated from Eq. (2.6-4) varies from $\sim 2 \times 10^9/\text{cm}^2$ for the (100) and (111) $CoSi_2$ films formed by ^{59}Co implantation (see the peak broadening in Fig. 2.6-1), to $< 10^6/\text{cm}^2$ for the best MBE-grown B-type $CoSi_2$ film on Si(111) that we have measured (see Fig. 2.2-2). However, the average misfit dislocation spacing is about the same ($\sim$ 30 nm) for all samples. This means that the strain relaxation and the imperfections in the film are unrelated, suggesting that the misfit dislocations nucleate at interfacial defects such as atomic steps rather than on the surface. We therefore speculate that specular Si surfaces free of any surface defects such as atomic steps are needed to grow metastable pseudormorphic $CoSi_2$ films ($> 10\ nm$). The inference then is that high dose ^{59}Co-implantation will not produce metastable pseudormorphic $CoSi_2$ layers because defects like atomic steps are always present at the silicide/silicon interface in this case. This is unlike the

relaxation of epitaxial GeSi films on Si, where the strain relaxation necessarily yields to threading dislocations in the film because misfit dislocations nucleate at the surface and glide down to the interface.[52]

In summary, all these observations suggest that the strain relaxation of thick ($> 10\ nm$) epitaxial $CoSi_2$ films is intrinsic to the silicide, and insensitive to the type of the film (A or B), the silicide formation process (high dose implantation or vacuum deposition), the orientation of the substrate, the imperfections in the film, and the thickness of the films.[8] This is in contrast with epitaxial GeSi films grown on Si substrates, where the misfit dislocation spacing is very sensitive to the growth temperature and film thickness for a fixed lattice mismatch.[53]

The perpendicular strain $\epsilon^{\perp}$ of the $CoSi_2$ film is distinctly smaller on Si(111) than on Si(100) (Table 2.6-I), showing that single-crystalline $CoSi_2$ films are elastically anisotropic. This means that the bond strength between (111) planes is stronger than that between (100) planes. This result is similar to that of silicon where the covalent bond along $< 111 >$ direction gives rise to the strongest bond between $\{111\}$ planes. On Si(111), the relative volume expansion of the $CoSi_2$ film is $\sim 0.5\%$, the same as the average linear dilatation ($\sim 0.5\%$, Table 2.6-I).

To extract the second ratio C_{14}/C_{11} from the measurements on the (111) sample, the procedure outlined for the (100) case was repeated with Eq. (2.6-1) and a suitably modified Eq. (2.6-2),[51]

$$\frac{e^{\perp}}{e^{\parallel}} = \frac{C_{44} - (C_{11} + 2C_{12})/2}{C_{44} + (C_{11} + 2C_{12})/4}. \qquad (2.6-5)$$

The result is given in Table 2.6-II. This ratio (0.36) is less than that of silicon (0.48).[51] The Poisson ratio is $\nu_{(111)} = 0.32$, obtained from Eqs. (2.6-1)&(2.6-3) and Table 2.6-I. It is the same as that for MBE-grown B-type $CoSi_2$ films on Si(111) substrates ($\sim 1/3$).[7]

C. Stress and Sample Bending

To obtain the absolute values of the elastic constants, the biaxial tensile stress in the $CoSi_2$ film, σ_f, was estimated by measuring the bending of the $CoSi_2$/Si(100) sample. The stress is related to the tensile strain in the plane according to Hooke's law in the linear elasticity,

$$\sigma_f = B_f e^{\parallel} = B_f(\epsilon^{\parallel} - f), \qquad (2.6-6)$$

where B_f is the biaxial elastic constant of the film. The stress causes the sample to bend with a concave radius of curvature, R. In the case where the thickness of the substrate, t_s, is much larger than that of the film t_f and is smaller than the lateral dimension of the sample, the following relationship holds,[54]

$$\sigma_f = \frac{B_s t_s^2}{6Rt_f}, \qquad (2.6-7)$$

where B_s is the biaxial elastic constant of the substrate. Combining Eqs. (2.6-6) and (2.6-7), one has

$$\frac{B_f}{B_s} = \frac{t_s^2}{6Rt_f} \cdot \frac{1}{\epsilon^{\parallel} - f}. \qquad (2.6-8)$$

The radius R was obtained by measuring the angular difference of the (400) Bragg peaks diffracted from the substrate at two different spots of the sample separated by 4 mm, using a double crystal diffractometer equipped with a translational stage. Substituting appropriate parameters for the aforementioned $CoSi_2$/Si(100) sample, we obtain the ratio $B_f/B_s = 0.8$ from Eq. (2.6-8). Knowing B_s = 180 GPa for Si(100),[51] we obtain B_f = 144 GPa for $CoSi_2$(100). This value agrees well with that extracted from thermal stress measurement by van Ommen et al. (140 GPa).[55] It is slightly larger than the measured biaxial elastic constants of several transition-metal disilicide films (Ti, Ta, Mo, W) on Si(100) substrates ($\sim$ 110 GPa[56]). The biaxial elastic constant of (100) oriented films equals[51]

$$B = C_{11}(1 + \frac{C_{12}}{C_{11}} - 2(\frac{C_{12}}{C_{11}})^2). \qquad (2.6-9)$$

From the the measured values of B and C_{12}/C_{11} for the $CoSi_2$(100) film, the absolute value of C_{11} can be obtained from Eq. (2.6-9). We thus have all three elastic constants of single crystalline $CoSi_2$ (Table 2.6-II). Lambrecht et al.[57] studied theoretically the electronic band structure of $CoSi_2$, using the linear muffin-tin orbital method and calculated the bulk modulus of $CoSi_2$ to be 190 GPa. In comparison, we used the elastic constants in Table 2.6-II and obtained the bulk modulus of 240 GPa, about 25% larger than this theoretical estimate.

D. Dislocation Locking and Thermal Stress

To extract the linear thermal expansion coefficient of $CoSi_2$ and to study the thermal stress, we measured the parallel and perpendicular strains between $CoSi_2$ films and Si substrates up to 500°C. The lattice mismatch f between stress-free $CoSi_2$ and Si equals

$$f = (\frac{1-\nu}{1+\nu})\epsilon^{\perp} + (\frac{2\nu}{1+\nu})\epsilon^{\parallel}$$

from Eqs. (2.6-1) and (2.6-3) (also from Eq. (2.5-2)). Assuming that the Poisson ratio ν does not change with temperature, f can then be extracted from the ν obtained at room temperature (Table 2.6-II) and the measured $\epsilon^{\perp}$ and $\epsilon^{\parallel}$ at various temperatures (Fig. 2.6-2). f decreases linearly with rising temperature up to 500°C (open and filled circles in Fig. 2.6-2). The slope yields the difference between the linear thermal expansion coefficients of $CoSi_2$ and Si. The slope has the same value, within the experimental error, for both the (100) and (111) samples (Fig. 2.6-2(a) and (b)), which averages $(6.5 \pm 0.6) \times 10^{-6}$/°C. This result shows that the thermal expansion coefficient of

$CoSi_2$ is isotropic, in accord with the fact that the unit cell of stress-free $CoSi_2$ is cubic. The linear thermal expansion coefficient of bulk Si is known to be $2.9 \times 10^{-6}/°C$ between 23°C and 500°C.[39] The coefficient for $CoSi_2$ films is therefore $9.4 \times 10^{-6}/°C$, in good agreement with that reported for bulk $CoSi_2$ polycrystalline samples ($9.4 \times 10^{-6}/°C$).[1] It is smaller than the linear thermal expansion coefficients of several transition-metal disilicides (Ti, Ta, Mo, W) ($\sim 15 \times 10^{-6}/°C$[56]).

The parallel strain $\epsilon^{\parallel}$ of $CoSi_2$ films on both Si(100) and Si(111) substrates does not change up to 500°C (open and filled triangles in Fig. 2.6-2(a) and (b)). This means that the misfit dislocations do not glide up to 500°C. By extrapolating $\epsilon^{\parallel}$ and $\epsilon^{\perp}$ to higher temperatures, we found that they meet (and consequently f also) at 825°C, for both (100) and (111) samples (Fig. 2.6-2(a) and (b)). This indicates that the $CoSi_2$ film is fully relaxed at $\sim$ 800°C.

E. Synthesis and Model

Given the above results, we propose the following model: (1) the strain in epitaxial $CoSi_2$ films on Si substrates reaches the equilibrium value at a relaxation temperature, T_R; (2) the misfit dislocations do not shear below T_R. According to Matthews and Blakeslee's strain relaxation model,[38] the equilibrium critical thickness t_{cr} for a pseudomorphic layer is

$$t_{cr} = \frac{b}{8\pi(1+\nu)|f|}(\ln\frac{t_{cr}}{b}+1).$$

For a layer of thickness t_f larger than t_{cr}, the equilibrium parallel strain $\epsilon^{\parallel}{}_{eq}$ equals[38]

$$\epsilon^{\parallel}{}_{eq} = f(1 - \frac{t_{cr}}{t_f}\cdot\frac{\ln t_f/b+1}{\ln t_{cr}/b+1}). \qquad (2.6-10)$$

We apply these predictions to a 110 nm thick $CoSi_2$ film on a Si(111) substrate. Assuming $T_R =$ 700°C, the lattice mismatch equals $f = -0.78\%$ at this relaxation temperature (Fig. 2.6-3), and hence the equilibrium critical thickness is 3 nm ($b=1/6 < 11\bar{2} >$ and $\nu = 1/3$). This value agrees well with the measured critical thickness of B-type $CoSi_2$ grown on Si(111) by MBE at $\sim$ 650°C (~ 3 *nm*).[6] For that same 110 nm thick $CoSi_2$ at $T_R = 700°C$, the equilibrium parallel strain equals $\epsilon^{\parallel}{}_{eq} = 0.95f = -0.74\%$ from Eq. (2.6-10), and the perpendicular one equals $\epsilon^{\perp}{}_{eq} = -0.82\%$ (Fig. 2.6-3). Above T_R, misfit dislocations are generated by either nucleation or multiplication, or both, to minimize the strain energy so that the equilibrium state maintains (Fig. 2.6-3). Below T_R, the misfit dislocations are locked in and $\epsilon^{\parallel}$ remains constant (Fig. 2.6-3). Thermal strain and stress are generated by the different thermal expansions between the film and the substrate. At room temperature, $\epsilon^{\parallel}$ remains the same (-0.74%) and $\epsilon^{\perp}$ decreases to -1.70% (Fig. 2.6-3). These

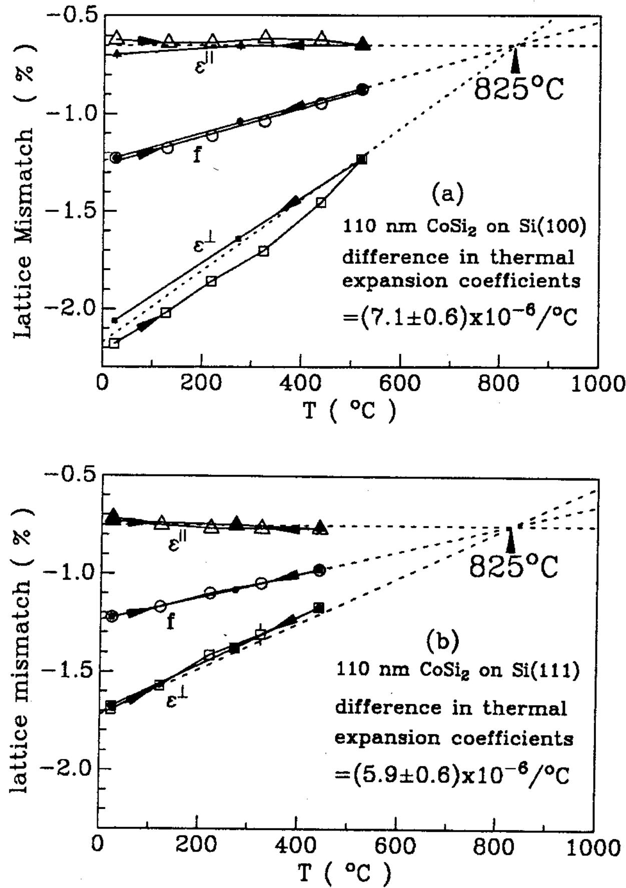

FIG. 2.6-2. The lattice mismatch, $\epsilon^{\perp}$ (square), $\epsilon^{\|}$ (triangle), and f (circle), as a function of the measurement temperature for both (a) the $CoSi_2$/Si(100) and (b) the $CoSi_2$/Si(111) mesotaxial samples. Open (filled) symbols are for the measurements when the temperature was raised (lowered).

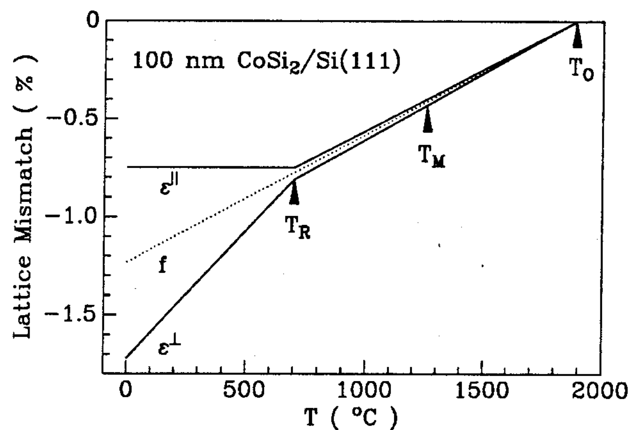

FIG. 2.6-3. Schematics of the proposed model showing how an epitaxial $CoSi_2$ film relaxes to an equilibrium strain state at T_R and above, and that misfit dislocations are locked-in below T_R. T_M is the melting temperature of $CoSi_2$, and T_O is the hypothetical temperature at which the lattice mismatch between $CoSi_2$ and Si becomes zero.

estimates agree well with experimental observations (Table 2.6-I). The exact value of $\epsilon^{\parallel}$ at room temperature depends on the relaxation temperature T_R. An increase of T_R from 600°C to 800°C causes a corresponding increase of f from −0.84% to −0.71%. This change raises $\epsilon^{\parallel}$ from −0.80% to −0.67% according to Eq. (2.6-10). This shows that the lateral lattice mismatch is not sensitive to the change in T_R and explains the observed apparent universal $\epsilon^{\parallel}$ at room temperature (Table 2.6-I).

The relaxation temperature T_R depends on many factors such as the formation process of the silicides. It varies from ~ 600°C for MBE-grown $CoSi_2$ on Si at ~ 600°C to ~ 800°C for the sample formed by high dose ^{59}Co implantation followed by 1000°C vacuum annealing for 30 min. Fig. 2.6-2(a) also shows that the thermal strain in the layer relaxes slightly after heating in ambient air at ~ 500°C for ~ 2 hrs, even if the sample had been annealed in vacuum at 1000°C for 30 min. This suggests that thermal annealing in ambient air lowers the relaxation temperature T_R. This phenomenon is similar to what we observed for MBE-grown B-type $CoSi_2$ layers on Si(111) substrates. There the thermal stress also relaxes slightly after thermal annealing in ambient air at ~ 600°C for ~ 2 hrs, but remains unchanged after vacuum annealing at ~ 800°C for 1 hr.[7] These observations indicate that atomic transport at the silicide/silicon interface lowers the relaxation temperature T_R (see also discussion in Ch. 2.5).

F. Conclusion

We obtained three elastic constants of cubic $CoSi_2$ (C_{11}=277, C_{12}=222, C_{44}=100 GPa) by measuring the strain and stress in $CoSi_2$ films on Si substrates at room temperature using DCD. X-ray rocking curves were also used to measure the lattice mismatch between the film and substrate at elevated temperatures up to 500°C. A linear thermal expansion coefficient of 9.4×10^{-6}/°C was derived for $CoSi_2$. The parallel strain at room temperature is about the same (~ −0.7%) for all the samples, regardless of the silicide formation process and the substrate orientation. It does not change with temperature up to 500°C. The universal $\epsilon^{\parallel}$ was explained by the model that $CoSi_2$ films reach an equilibrium strain state at a relaxation temperature T_R (~ 600–800°C) by generation of misfit dislocations, and the dislocations are locked-in below T_R. We proposed that atomic flux across the silicide/silicon interface lowers T_R. We also speculate that perfectly flat Si surfaces free of defects such as atomic steps are needed for the growth of metastable pseudomorphic $CoSi_2$ films (> 10 nm).

References

1 M-A.Nicolet, S.S.Lau, in *VLSI Electronics, Vol.6*, edited by N.G. Einspruch and G.B. Larrabee (Academic Press, New York, 1983), p. 330.

2. S.P. Murarka, *Silicides for VLSI Applications*, Academic, New York, 1983.

3. G.J. Van Gurp and C. Langereis, J. Appl Phys. 46, 4301 (1975).

4. R.T. Tung, J.C. Bean, J.M. Gibson, J.M. Poate, and D.C. Jacobson, Appl. Phys. Lett. 40, 684 (1982).

5. J.M. Gibson, J.C. Bean, J.M. Poate, and R.T. Tung, Appl. Phys. Lett. 41, 818 (1982).

6. J.M. Phillips, J.L. Batstone, J.C. Hensel, and M. Cerullo, Appl. Phys. Lett. 51, 1895 (1987).

7. G. Bai, M-A. Nicolet, T. Vreeland, Jr., Q. Ye, and K.L. Wang, Appl. Phys. Lett. 55, 1874 (1989).

8. G. Bai, M-A. Nicolet, T. Vreeland Jr., J. Appl. Phys., May 1, 1991.

9. G.Bai, D.N.Jamieson, T.Vreeland Jr., and M-A.Nicolet, Mat. Res. Soc. Symp. Proc. 102, 259 (1988).

10. H. von Känel, J. Henz, M. Ospelt, J. Hugi, E. Müller, N. Onda, and A. Gruhle, Thin Solid Films 184, 295 (1990).

11. R.T. Tung and J.L. Batstone, Appl. Phys. Lett. 52, 648 (1988).

12. T.L. Lin, R.W. Fathauer, P.J. Grunthaner, and C. d'Anterroches, Appl. Phys. Lett. 52, 804 (1988).

13. R.T. Tung, F. Schrey, and S.M. Yalisove, Appl. Phys. Lett. 55, 2005 (1989).

14. A.E. White, K.T. Short, R.C. Dynes, J.P. Garno, and J.M. Gibson, Appl. Phys. Lett. 50, 95 (1987).

15. J.C. Hensel, R.T. Tung, J.M. Poate, and F.C. Unterwald, Appl. Phys. Lett. 44, 913 (1984).

16. C.W.T. Bulle-Lieuwma, A.H. van Ommen, and L.J. van IJzendoorn, Appl. Phys. Lett. 54, 244 (1989).

17. R.T. Tung, Phys. Rev. Lett. 52, 461 (1984).

18. J.C. Hensel, A.F.J. Levi, R.T. Tung, and J.M. Gibson, Appl. Phys. Lett. 47, 151 (1985).

19. L.F. Mattheiss and D.R. Hamann, Phys. Rev. B37, 10623 (1988).

20 Y.C.Kao, K.L.Wang, E de Fresart, R.Hull, G.Bai, D.N.Jamieson, and M-A. Nicolet, J. Vac. Sci. Technol. B6, 745 (1987).

21. A.Y. Cho and J.R. Arthur, in *Progress in Solid State Chemistry*, Vol. 10, eds. G. Somorjai and

J. McCaldin (Pergammon, New York, 1975), p. 157.

22. A. Ishizaka, K. Nakagawa, and Y. Shiraki, in *Proc. of Conf. on Molecular Beam Epitaxy and Clean Surface Techniques*, (Japanese Society of Applied Physics, Tokyo, 1982) p. 183.

23. Q.Ye, T.W. Kang, K.L. Wang, G. Bai, and M-A. Nicolet, Thin Solid Films 184, 269 (1990).

24. D.N. Jamieson, G. Bai, Y.C. Kao, C.W. Nieh, M-A. Nicolet, and K.L. Wang, Mat. Res. Soc. Symp. Proc. 91, 479 (1987).

25. W.K. Chu, J.W. Mayer, and M-A. Nicolet, *Backscattering Spectrometry*, Academic, New York, 1978.

26. J. Hornstra and W.J. Bartels, J. Cryst. Growth 44, 513 (1978).

27. P. Hirsch, A. Howie, R.B. Nicholson, and M.J. Whelan, *Electron Microscopy of Thin Crystals*, Krieger Publishing Inc., Malarbar, Florida, 1977.

28. L.C. Feldman, J.W. Mayer, and S.T. Picraux, *Materials Analysis by Ion Channeling*, Academic, New York, 1982.

29. G. Bai, M-A. Nicolet, J.E. Mahan, and K.M. Geib, Phys. Rev. B 41, 8603 (1990).

30. G. Bai and M-A. Nicolet, unpublished.

31. B.E. Warren, *X-ray Diffraction* (Dover, New York, 1990), p. 253.

32. P. Gay, P.B. Hirsch, and A. Kelly, Acta Metal. 1, 315 (1953).

33. D. Cherns, in *Analytical Techniques for Thin Films*, eds. K.N. Tu and R. Rosenberg (Academic, San Diego, 1988), p. 297.

34. N.C. Bartelt, E.D. Williams, R.J. Phaneuf, Y. Yang, and S. Das Sarma, J. Vac. Sci. Technol. A7, 1898 (1989).

35. G. Bai and M-A. Nicolet, unpublished.

36. R.T. Tung and F. Schrey, Phys. Rev. Lett. 63, 1277 (1989).

37. H. Nagai, J. Appl. Phys. 45, 3789 (1974).

38. J.W. Matthews and A.E. Blakeslee, J. Cryst. Growth 27, 118 (1974).

39. H.F. Wolf, *Silicon Semiconductor Data*, (Pergamon Press, New York, 1969) p. 101.

40. H.Lucas, H.Zabel, H.Morkoc and H.Unlu, Appl. Phys. Lett. 52, 2117 (1988).

41. K.Nakajima, S.Yamazaki,S.Komiya, and K.Akita, J. Appl. Phys., 52, 4575 (1981).

42. G.A.Rozgonyi, P.M.Petroff, and M.B.Panish, J. Appl. Phys., 64, 1173 (1988).

43. C.M. Comrie and J.M. Egan, J. Appl. Phys. 64, 1173 (1988); C.M. Comrie, J.C. Liu, L.S. Huang and J.W. Mayer, J. Appl. Phys. 63, 2403 (1988).

44. D.G. Deppe and N. Holonyak, J. Appl. Phys., 64, 1293(1988) and references therein.

45. S.M.Prokes, W.F.Tseng, and A.Christou, Appl. Phys. Lett. 53, 2483 (1988).

46. R.T.Tung, J.M.Gibson, and J.M.Poate, Appl. Phys. Lett. 42, 888 (1983).

47. S.S.Iyer, J.C.Tsang, M.W.Copel, P.R.Pukite, and R.M.Tromp, Appl. Phys. Lett. 54, 219 (1989).

48. M. Bartur and M-A. Nicolet, Appl. Phys. A29, 69 (1982).

49. J.M. Vandenberg, A.E. White, R. Hull, K.T. Short, and S.M. Yalisove, J. Appl. Phys. 67, 787 (1990).

50. S.M. Yalisove, R.T. Tung, and D. Loretto, J. Vac. Sci. Technol. A7, 1472 (1989).

51. W.A. Brantley, J. Appl. Phys. 44, 534 (1973).

52. R. Hull, J.C. Bean, D.J. Werder, and R.E. Leibenguth, Appl. Phys. Lett. 52, 1605 (1988).

53. J.C. Bean, L.C. Feldman, A.T. Fiory, S. Nakahara, and I.K. Robinson, J. Vac. Sci. Technol. A2, 436 (1984).

54. R.F.S. Hearmon, *An Introduction to Applied Anisotropic Elasticity* (Oxford University, London, 1961), Chap. VII.

55. A.H. van Ommen, C.W.T. Bulle-Lieuwma, and C. Langereis, J. Appl. Phys. 64, 2706 (1988).

56. T.F. Retajczyk, Jr. and A.K. Sinha, Thin Solid Films, 70, 241 (1980).

57. W.R.L. Lambrecht, N.E. Christensen, and P. Blöchl, Phys. Rev. B36, 2493 (1987).

Chapter 3 Epitaxial $ReSi_2$ Films on Si

3.1 Semiconducting silicides

Several metal silicides have been identified to be semiconductors.[1] These semiconducting silicides have potential applications as infrared light sources and detectors in Si-based microelectronics. Some optical and electrical properties of such silicides such as $FeSi_2$,[2,3] $CrSi_2$,[4,5] and $ReSi_2$[6,7] have been characterized. The compatibility of silicides with Si process makes semiconducting silicides the ideal materials for novel Si-based optoelectronic integrated circuits, equalled in their simplicity only by GeSi and SiC.

The epitaxial growth of $FeSi_2$,[8–10] $CrSi_2$,[11–13] and $ReSi_2$[14,15] films on clean Si substrates in ultrahigh vacuum have been investigated. Iron silicides of Fe_3Si, FeSi, and $FeSi_2$ (both α- and β-phases) can be formed by solid-state reaction of iron films on silicon substrates at 200-1100°C.[16,17] β-$FeSi_2$ is thermodynamically stable at $< 900°C$(α-$FeSi_2$ at $> 900°C$). It is a direct gap (0.87 eV) semiconductor.[2] A thin film of β-$FeSi_2$ formed by vacuum deposition without intentional doping is extrinsic at room temperature with p-type conduction. Resisitivity, hole concentration and mobility, are $\sim 2\ \Omega$cm, $\sim 10^{18}/cm^3$ and $\sim 3\ cm^2/Vs$.[2,3] β-$FeSi_2$ is orthorhombic with lattice constants of a=0.986 nm, b=0.779 nm, c=0.783 nm, and has a structure like that of $CoSi_2$.[1] The epitaxial growth of β-$FeSi_2$ films on clean Si(100) and Si(111) substrates in ultrahigh vacuum has been analyzed by reflection high energy electron diffraction, Auger electron microscopy, transmission electron microscopy, x-ray diffraction, and backscattering spectrometry.[8–10] On Si(111), two epitaxial relationships were observed:[8] (I) β-$FeSi_2$(101)//Si(111) and (II) β-$FeSi_2$(110)//Si(111). Furthermore, Si(111) has threefold symmetry, while the β-$FeSi_2$ matching plane has only twofold symmetry. Therefore, three equivalent and equiprobable azimuthal orientations are expected and were observed.[8] The azimuthal relationship is β-$FeSi_2$[010](or [001])//Si$< 0\bar{1}1 >$. On Si(100), epitaxial relationship is β-$FeSi_2$(100)//Si(100).[9,10] However, two competing, inequivalent azimuthal orientations which differ by a rotation of 45° were observed.[10] Type-A orientation has $FeSi_2$[010]//Si$< 011 >$ and predominates at 300-550°C.[9] Type-B orientation has $FeSi_2$[010]//Si$< 001 >$ and occurs at lower (200-300°C) or higher (550-700°C) temperatures.[10]

$CrSi_2$ has an indirect gap of 0.35 eV.[5] Unintentionally doped $CrSi_2$ is a degenerate p-type semicondcutor at room temperature.[4,5] Resisitivity, hole concentration and mobility, are $\sim 0.01\ \Omega$cm, $\sim 4 \times 10^{19}/cm^3$ and $\sim 15\ cm^2/Vs$.[4,5] $CrSi_2$ has a hexagonal structure with a=0.443 nm and c=0.636 nm.[1] Epitaxial $CrSi_2$ films were grown on Si(111) in ultrahigh vacuum.[11–13] The matching face

relationship is $CrSi_2(0001)/Si(111)$.[11-13] Two competing, inequivalent azimuthal orientations were observed: type-A with $CrSi_2[10\bar{1}0]//Si[10\bar{1}]$ and type-B with $CrSi_2[11\bar{2}0]//Si[10\bar{1}]$.[11] Type-B is obtained by a rotation of 30° of type-A about the [111] axis. Recently, the growth of purely type-A epitaxial layers was demonstrated by means of chromium and silicon codeposition onto Si(111) at 450°C.[12]

$ReSi_2$ has an indirect bandgap of 0.12 eV, and is a p-type semiconductor without intentional doping.[6,7] The electrical resistivity, hole concentration and mobility at room temperature are $\sim 0.02\ \Omega cm$, $\sim 4\times 10^{19}/cm^3$ and $\sim 10\ cm^2/Vs$.[6] $ReSi_2$ has a body-centered orthorhombic lattice with lattice constants of a=0.313 nm, b=0.314 nm, c=0.768 nm, and closely resembles the tetragonal $MoSi_2$ structure type.[18] Localized epitaxy of $ReSi_2$ was observed upon vacuum annealing of evaporated rhenium films on Si(111) and (100) substrates at $\sim$ 1000°C.[19] Recently, highly epitaxial $ReSi_2$ films 150 nm thick were grown on Si(100) by rhenium deposition onto a hot substrate at 650°C.[14,15] The next section focuses on the growth and characterization of such films.

3.2 Growth and characterization of $ReSi_2$ on Si(100)

Thin films of $ReSi_2$ were grown on Si(100) substrates at Colorado State University.[14,15] The Si surface was cleaned by etching a Si wafer for 30s in buffered HF solution, and the wafer was then loaded into an ultrahigh vacuum chamber (base pressure 10^{-11} Torr).[14] A "silicon beam clean"[20] was then applied to remove the residual oxide, which amounts to exposure of the surface to a silicon flux corresponding to a deposition rate of 1 nm/min for 4min at 700°C. Rhenium (Pure Tech, Inc., 99.99%) from an electron beam evaporation source was deposited onto a hot silicon substrate at 400-1000°C at a pressure in the mid-10^{-9} Torr range ("reactive deposition epitaxy," or RDE).[14]

The atomic composition and thickness of the formed silicide films were characterized by MeV backscattering spectrometry (see Ch. 2.2). All films ($\sim$65–530 nm thick) are of uniform composition through their entire depth and have the correct Re:Si$\approx$1:2 stoichiometry. The epitaxial quality of films was analyzed by channeling spectrometry (see Ch. 2.2).[21] The minimum channeling yields for both the silicon and rhenium signals of $ReSi_2$ films as a function of the deposition temperature are plotted in Fig. 3.2-1, which shows that highly epitaxial $ReSi_2$ films can be grown on Si(100) at 600-700°C. The data at 650°C are for films of three different thicknesses, 65, 150, and 530 nm. The 150 nm thick $ReSi_2$ film grown at the optimum deposition temperature of 650°C has a minimum channeling yield of 2% for rhenium (Fig. 3.2-1). This yield is comparable with that of the best epitaxial silicide films (see Ch. 2.2) and means that the film is in perfect alignment with the

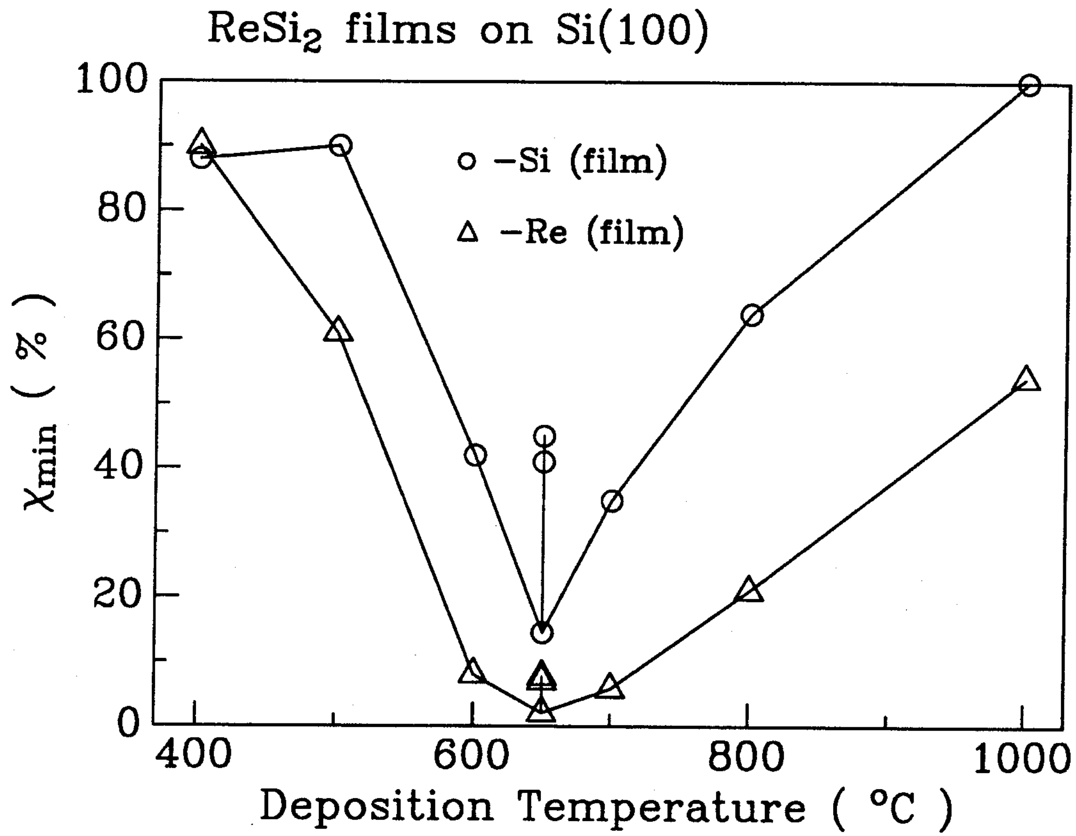

FIG. 3.2-1 2 MeV ^{4}He minimum channeling yields of Re and Si for $ReSi_2$ films grown on Si(100) by reactive deposition epitaxy as a function of substrate temperature during deposition.

substrate. We also noted that the minimum channeling yield of silicon is always larger than that of rhenium for the same sample. This does not mean that the silicon sublattice is less ordered than that of rhenium, but is a feature of ion channeling in a polyatomic crystal.[22] We discuss this phenomenon in the next section.

Bragg-Brentano x-ray diffraction of $ReSi_2$ films grown at 650°C shows only the (020) peak from $ReSi_2$, meaning that the film is highly oriented, with a matching face of $ReSi_2$(010)//Si(100).[15] The same matching relationship was observed for epitaxial tetragonal $MoSi_2$ films grown on Si(100) at 650°C by RDE in ultrahigh vacuum.[23] For films grown at higher temperature, other matching faces, such as $ReSi_2$(011), appear.[15]

The Si(100) plane has 4-fold symmetry, while that of $ReSi_2$(010) is only 2-fold. Two distinct but equivalent azimuthal alignments are therefore equally probable, so that an epitaxial $ReSi_2$ film is expected to have twins that differ by a rotation of 90 degrees about the $ReSi_2$[010] axis. Fig. 3.2-2(a) is an electron diffraction pattern of the $ReSi_2$[010] zone.[15] It has 4-fold symmetry, although the reciprocal lattice of the $ReSi_2$[010] zone has only 2-fold symmetry. This clearly verifies the presence of a twin structure. The relationship between the patterns of $ReSi_2$ and Si shows that the azimuthal alignment is $ReSi_2$[001]//Si[$0\bar{1}1$] or [011].[15] The twinning and azimuthal relationship observed here are again identical to those of tetragonal $MoSi_2$ on Si(100).[23] Twinning is inherent in the epitaxial growth of $ReSi_2$ on Si(100) because substrate surface has a higher symmetry than that of the $ReSi_2$ matching face. One way to overcome this symmetry mismatch may be to use a vicinal Si(100) to lower the symmetry of the substrate surface.

Given above results, Mahan et al.[15] proposed a common unit mesh for the $ReSi_2$/Si(100) heterostructure shown in Fig. 3.2-2(b). The lattice match at room temperature is excellent along the c-axis (−0.04%), and fair along the a-axis (1.8%). The mismatch along the a-axis is better than that along the b-axis (2.3%), which probably is the reason that the matching face is $ReSi_2$(010), not (100).[15] All these three lattice mismatches become positive and worsen at the growth temperature, because of the larger thermal expansion coefficient of $ReSi_2$ ($6.6\times10^{-6}/°C^1$) than that of Si ($2.9\times10^{-6}/°C$).

Transmission electron microscopy (TEM) was used to characterize the microstructure of the $ReSi_2$ films grown at 650°C. Fig. 3.2-3(a) is a plan-view TEM dark-field image, which reveals domains with an average size of 10 nm. Cross-sectional TEM (Fig. 3.2-3(b)) shows that the $ReSi_2$ film consists of tall columns of $\sim$ 10 nm in diameter.

Reflection high energy electron diffraction patterns indicate that the $ReSi_2$ films grown by RDE

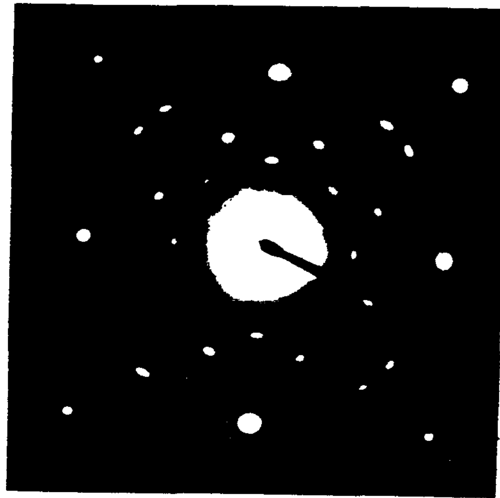

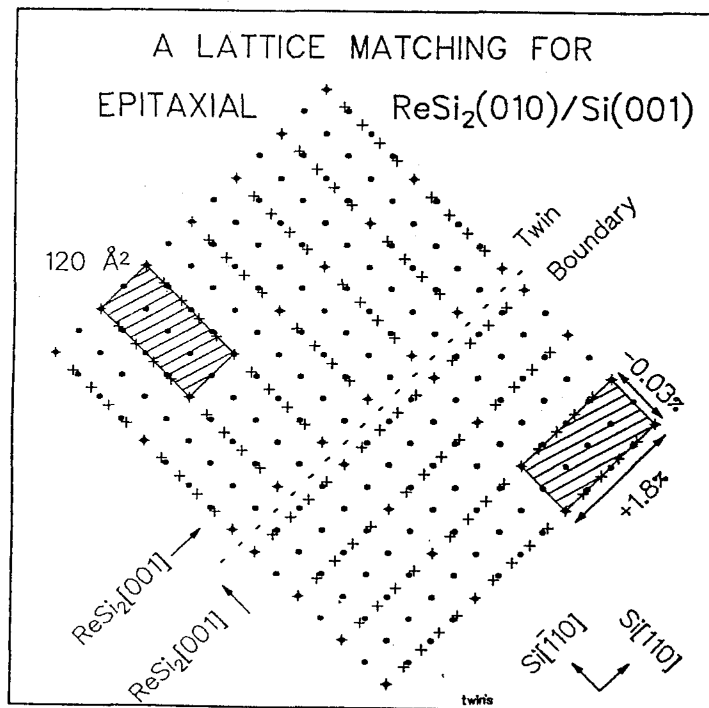

FIG. 3.2-2 Epitaxial relationship between a $ReSi_2$ film and a Si(100) substrate: (a) Transmission electron diffraction pattern of the Si[100] zone and the $ReSi_2$[010] zone (from Ref. 14). The bright spots are Si diffractions. The faint spots are $ReSi_2$ diffractions (note their fourfold symmetry). (b) Schematical drawing of two equivalent common unit meshes (from Ref. 15). The dots are Si atoms in the substrate. The crosses are Re atoms in the film. The actual atomic positions are unknown and assumed.

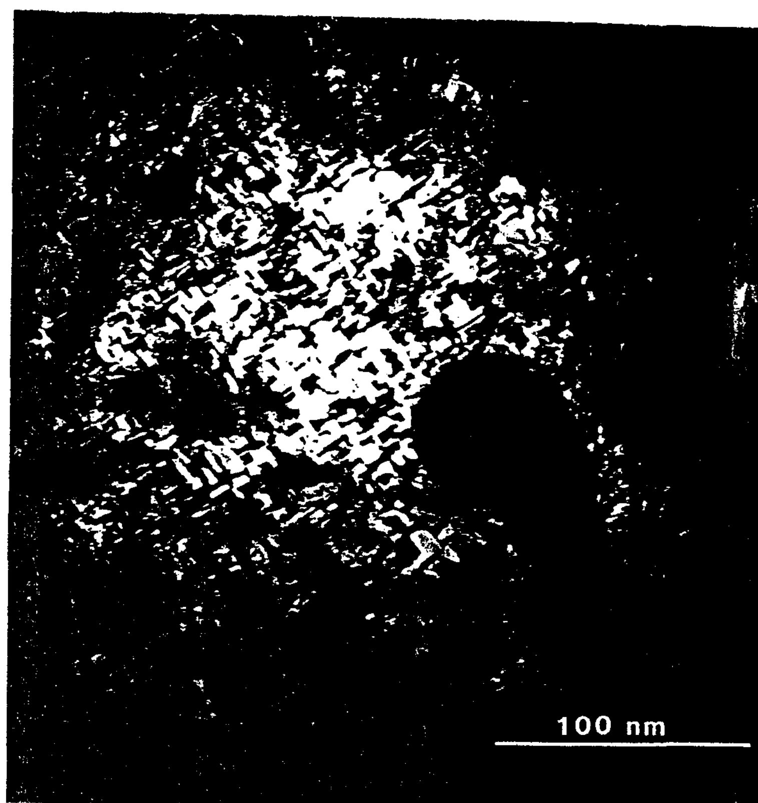

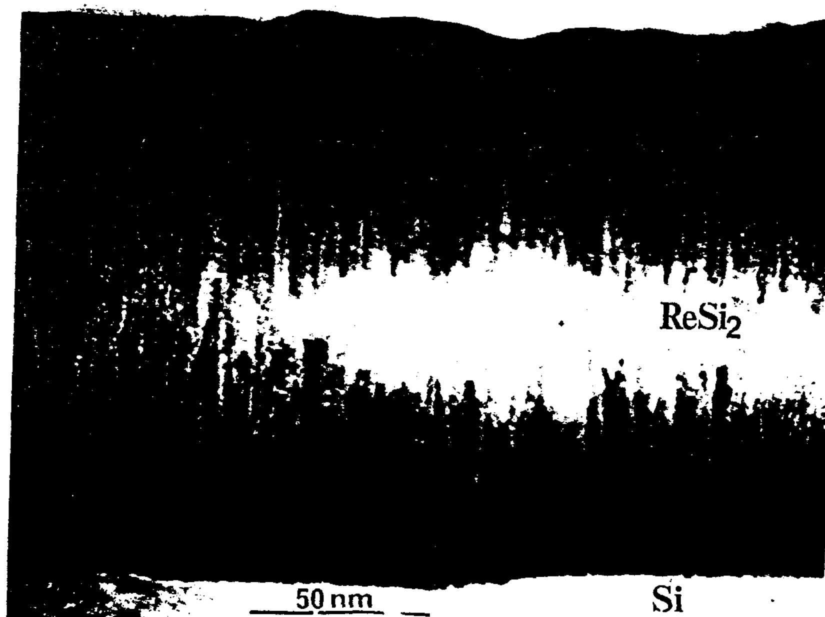

FIG. 3.2-3 Transmission electron micrograph of a 150 nm thick $ReSi_2$ film grown on Si(100) at 650°C (from Ref. 15): (a) plane-view dark-field image with a beam diffraction vector of $ReSi_2(002)$; (b) cross-sectional bright-field image with a beam incident along Si[022].

have rough surfaces.[15] The surface morpholgy might be improved by using more sophisticated growth procedures involving "template" and codeposition. Another possible technique to fabricate $ReSi_2$ films is by high dose implantation of Re into Si substrate and thermal annealing.

3.3 Channeling of MeV ions in polyatomic crystals

Channeling phenomena of MeV ions in crystals and their applications to materials characterization have been extensively reviewed.[21,24] Most experimental results on channeling can be understood in the framework of the continuum model established by Lindhard.[25] Two fundamental channeling parameters, the critical angle, ψ_c, and the minimum yield, χ_{min}, have been throughly studied for various ions (e.g., He and H) over a wide energy range (0.1–10 MeV) in numerous monoatomic crystals. For example, in diamond-type crystals, Picraux et al[26] found that the experimental half angle (measured from angular scan), $\psi_{1/2}$, has the same functional dependence on parameters such as ion energy and atomic number as the critical angle ψ_c of the continuum model. Except for a few perfect crystals such as Si and Ge,[26] the measured minimum yields are usually larger than the predicted ones because of the existence of imperfections. The sensitivity of χ_{min} to the defects in crystals makes it a good indicator of crystal perfection.

Channeling in polyatomic crystals has distinctive characteristics owing to the existence of distinct sublattices. The differences in channeling behavior from different sublattices are pronounced when the atoms occupying the sublattices have very different atomic numbers.[24,26] While these phenomena are of fundamental interest, for practical reasons, there have been relatively few experimental investigations of channeling in polyatomic crystals. For example, for bulk single crystals, it is difficult with backscattering analysis alone to detect the signal from light elements in the presence of heavy ones. One remedy is to measure the close encounter probability of an incident beam with the light element by detecting the characteristic x-ray production or nuclear reaction products from the light element in the channeling mode, while measuring the backscattered beam from the heavy element.[27–30] Another remedy is to use high quality epitaxial thin films so that the signals from light and heavy elements do not overlap. We report here on a comprehensive and revealing experimental study of this type.

We have channeled a ^{4}He beam of 1.4–2.7 MeV into an epitaxial $ReSi_2$ film 150 nm thick grown on a Si(100) substrate at 650°C by RDE.[14] Since the difference between the a- and b-axes of $ReSi_2$ is only $\sim 0.5\%$, we will hereafter assume for convenience that $ReSi_2$ is tetragonal with a=0.313 nm. For a sufficiently thin film, the backscattering signal of the heavy (Re) element does not overlap

in energy with that of the light (Si) element, which enables us to separate clearly the Si signal from the Re signal in the backscattering spectrum. Thus the half angles and the minimum yields of both elements can be obtained from the backscattering measurements alone. This allows us to compare directly the channeling characteristics of different components of a polyatomic crystal. The experimental results are discussed in the framework of the continuum model, suitably extended for polyatomic crystals. The agreement is found to be good for the critical angles but only fair for the predicted minimum yields.

The channeling measurements were performed at room temperature with an x-y rotation and x-y translation goniometer. The vertical y rotation axis is fixed in space and is perpendicular to the horizontal ^{4}He beam. The x rotation axis lies in a horizontal plane and moves with the y rotation. The x-y translation directions are parallel to the corresponding rotation axes. First, the MeV ^{4}He beam was aligned with the [100] axial channel of $ReSi_2$ by finding the minimum backscattering yield in a spectral window extending from beneath the surface peak of the Re signal to the energy corresponding to $\sim$ 100 nm in depth. The same [100] axial channel was found when the window was placed in the Si signal of the silicide or of the Si substrate instead of in the Re signal. This concurrence means that the [100] directions of the Si substrate and the $ReSi_2$ film are exactly aligned. Once the [100] channel had been identified, a channeling spectrum was then taken by translating the sample to a virgin spot (beam size $\sim 0.4 \times 0.4cm^2$, sample size $\sim 2 \times 2cm^2$) to minimize the effect of radiation damage.[31] Figure 3.3-1 shows the [100] axial channeling spectrum for a 1.4 MeV ^{4}He beam. One sees that in the $ReSi_2$ film, the minimum yield of Si much exceeds that of Re. The factor is seven—14% vs. 2%. Channeling spectra were taken with several energies (1.4, 2.0, 2.4, 2.7 MeV) and the minimum yields are the same. This result is consistent with the continuum model, which predicts that the minimum yield is independent of beam energy and is only a property of the host crystal.

The half angles of the Re and the Si in the film and the Si in the substrate were obtained from angular scan measurements, which were performed by tilting the sample about either the x or y rotation axis and recording the backscattering yields within a spectral window corresponding to a thickness of $\sim$ 100 nm placed in the proper region. The half angles measured with a single channel just beneath the surface peak are the same as those measured with a spectral window, to within experimental error. To minimize the effect of radiation damage, we used a spectral window instead of a single channel for the angular scan measurements, and we started each measurement on a virgin sample spot. The half angles obtained by either x or y rotation are the same. Figure 3.3-2 shows

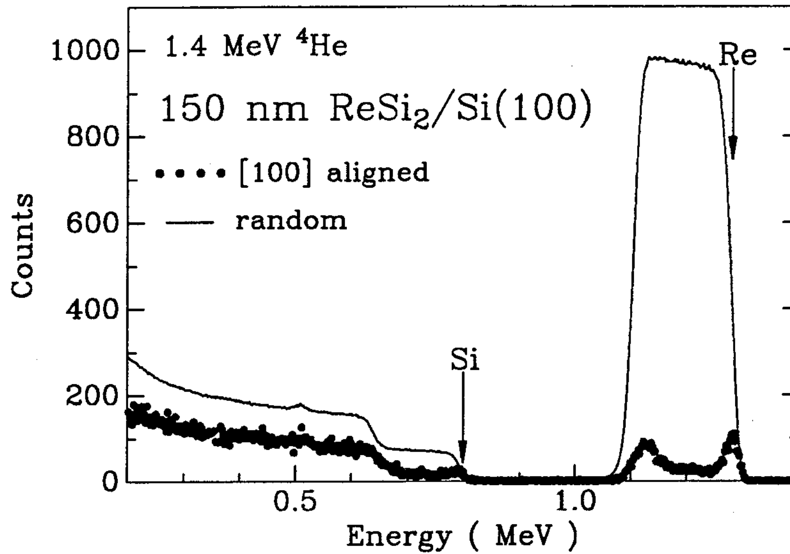

FIG. 3.3-1 Backscattering spectra of 1.4 MeV ^{4}He incident along a random direction (solid line) and a [100]-aligned axial direction (dotted line).

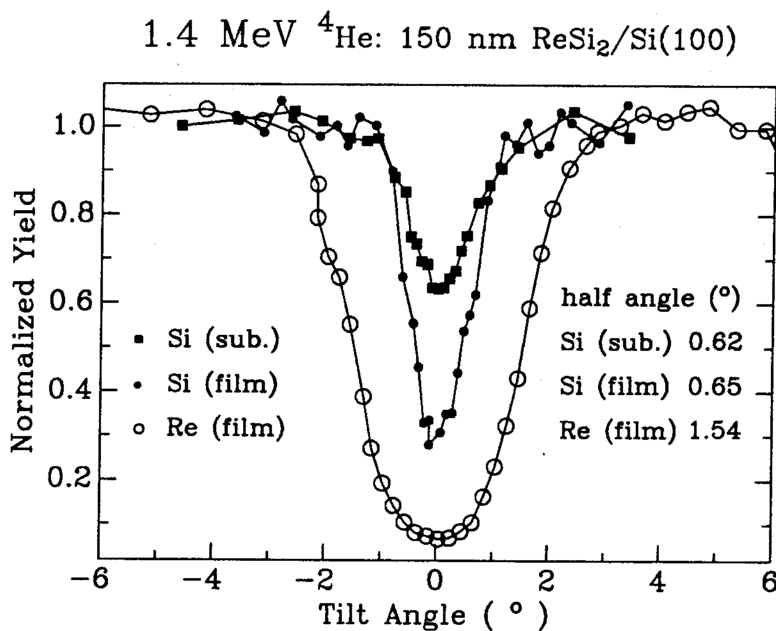

FIG. 3.3-2 A plot of normalized backscattering yield versus tilt angle. The normalization is performed with respect to the backscattering yield of a random incident beam. The half angle is the half of the full width of the angular dip.

the [100] angular scans for a 1.4 MeV ^{4}He beam. Two results immediately follow: (1) the half angle of Re is $\sim$ 2.3 times larger than that of Si in $ReSi_2$; (2) the half angles of Si in the film and in the substrate are about the same. The half angles were measured for several beam energies (1.4, 2.0, 2.7 MeV) and the same conclusions were derived. Furthermore, all half angles decrease with increasing energy, proportionally to $1/\sqrt{E}$, as predicted by the continuum model.

The continuum model of axial channeling by Lindhard[25] represents the atomic chains along the channel of an elemental host crystal as continuous columns of radius r_{min} and electrostatic potential U(r), where r is the distance from the axis of the column. r_{min} is the minimum distance a channeled ion may approach for the continuum model still to validly describe the gentle interaction between the ion and host crystal that keeps the ion channeled. There are two characteristic lengths: (1) the Thomas-Fermi screening distance, a_{TF}; and (2) the thermal vibrational amplitude of the host crystal, ρ. Both are of the order of 0.01 nm in a typical channeling experiment. Lindhard has taken ${r_{min}}^2$ to be the sum of ${a_{TF}}^2$ and ρ^2.

The meaning of r_{min} is that an ion of the incident beam aligned with a channel will be dechanneled if it impinges on the ends of the columns at the surface. Therefore, the minimum yield χ_{min} measured immediately beneath the surface peak for a perfect crystal is just a fraction of the surface area occupied by the columns,

$$\chi_{min} = \sigma\pi {r_{min}}^2, \qquad (3.3-1)$$

where σ is the areal density of surface atoms.

The existence of r_{min} also implies that there is a critical angle ψ_c between an ion's trajectory and a channel above which the ion will be dechanneled,[25]

$$\psi_c = \alpha(\frac{r_{min}}{a_{TF}}) \cdot \psi_1, \qquad (3.3-2)$$

where the numerical coefficient α has a typical value between 0.6 and 1.6[26]. The characteristic angle, ψ_1, equals

$$\psi_1 \equiv \sqrt{\frac{2Z_1Z_2e^2}{Ed}}, \qquad (3.3-3)$$

where Z_1 and Z_2 are the atomic numbers of the ion and the host atom, E is the ion energy and d is the atomic spacing in the channel direction.

In general, axial channeling in a diatomic crystal is complex because more than one type of columns exist. However, there are special directions where channeling is simple. The simplest channeling direction has only one type of column, which consists of both elements (e.g., the [001] channel in $ReSi_2$ for which we have no data). Channeling can then be viewed as being equivalent to

that in a monoatomic crystal with an average atomic number and spacing.[26] The minimum yields and the critical angles of the two elements are then the same. The next simplest channeling direction has two types of columns such as the [100] channel in $ReSi_2$ which we discuss in detail and for which we do present data.

The [100] channel consists of two types of columns (Fig. 3.3-3); one type contains only Si atoms (Si columns) and another only Re atoms (Re columns). We assign a minimum distance of approach for each type of column, r_{min}^{Si} and r_{min}^{Re}, which is determined by the characteristics of each corresponding column. This is the single column potential approximation.

For quantitative evaluations of minimum yields and critical angles, it is necessary to estimate the values of r_{min} in terms of channeling parameters of the ion and the host crystal. In general, r_{min} may depend on both the Thomas-Fermi screening distance[32]

$$a_{TF} = 0.047(\sqrt{Z_1} + \sqrt{Z_2})^{-\frac{2}{3}} \qquad nm, \tag{3.3-4}$$

and the thermal vibrational amplitudes of the host crystal. For an incident He ($Z_1 = 2$) ion scattered by Si ($Z_2 = 14$) and Re ($Z_2 = 75$) atoms, the screening distances are 0.016 nm and 0.011 nm respectively. For elemental Si and Re crystals, the known Debye temperatures ${\Theta_D}^{Si} = 550K$ and ${\Theta_D}^{Re} = 300K$[33] yield thermal vibrational amplitudes of 0.011 nm and 0.008 nm, respectively, at room temperature, in the Debye approximation. These numbers are close to the values of the screening distances. To our knowledge, there are no reliable data on the thermal vibrational amplitudes in $ReSi_2$. Therefore, we shall approximate r_{min} by a_{TF} in computing the critical angles and the minimum yields.

In our single column potential approximation with $r_{min} = a_{TF}$, the critical angles can be directly calculated from eq. (3.3-2). The numerical coefficient α equals 0.8 for both Re and Si columns using the "standard potential."[21] The ratio of the critical angle of the Re columns, ${\psi_c}^{Re}$, to the critical angle of the Si columns, ${\psi_c}^{Si}$, thus becomes

$${\psi_c}^{Re}/{\psi_c}^{Si} = \psi_1^{Re}/\psi_1^{Si} = \sqrt{Z_{Re}/Z_{Si}} = 2.3, \tag{3.3-5}$$

which agrees with the experimental data (see Fig. 3.3-2). Table 3.3-1 lists the values of the characteristic angle ψ_1, the calculated critical angle ψ_c and the measured half angle $\psi_{1/2}$ for Si and Re in the $ReSi_2$ film. The measured half angles agree well with the critical angles.

The minimum yield describes the fraction of an aligned incident beam that is dechanneled by atomic columns. An aligned beam impinging on $ReSi_2$ in the [100] direction will be scattered by

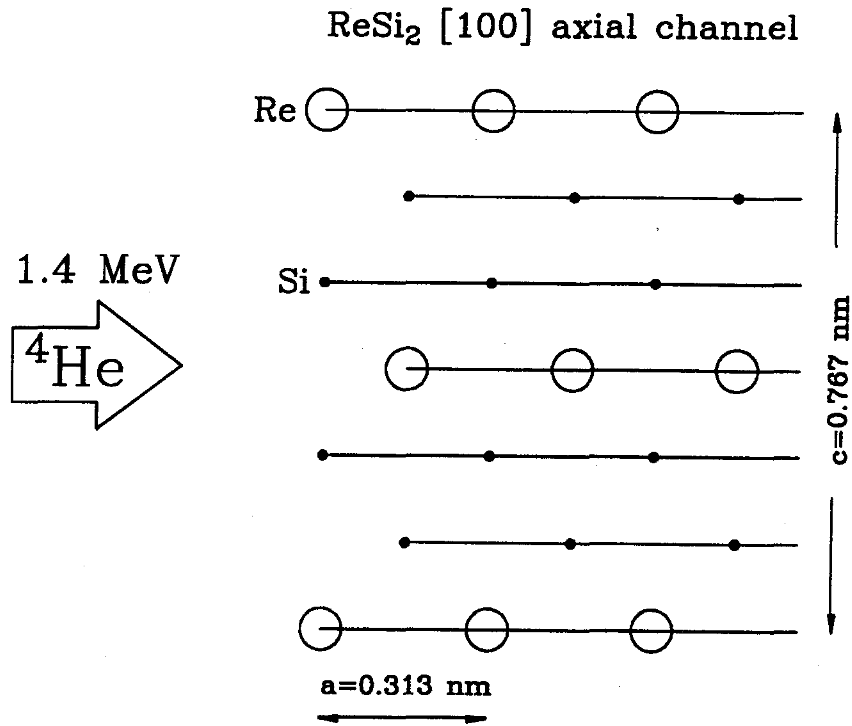

FIG. 3.3-3 A cross-sectional schematic diagram showing the [100] axial channel of $ReSi_2$.

Table 3.3-I Calculated values of the characteristic and critical angles, measured values of half angles, and the calculated and measured minimum yields, for the [100] axial channeling of 1.4 MeV ^{4}He beam in an epitaxial $ReSi_2$ film.

	$\psi_1(^o)$	$\psi_c(^o)$	$\psi_{1/2}^{exp.}(^o)$	$\chi_{min,1}(\%)$	$\chi_{min,2}(\%)$	$\chi_{min}(\%)$	$\chi_{min}^{exp.}(\%)$
Si	0.78	0.65	0.65	3	10	13	14
Re	1.81	1.52	1.54	1	0	1	2

both Si and Re columns. The incident ion will be channeled by both Si and Re columns if the scattering angle, ψ, is less than the critical angles of both the Si columns and the Re columns. For the incident ion that is close to a Si column, the ion will be dechanneled by the Si columns but will still be channeled by the Re columns if the scattering angle ψ is greater than the critical angle of the Si columns ${\psi_c}^{Si}$ but is still less than the critical angle of the Re columns ${\psi_c}^{Re}$. That dechanneling process thus does not contribute to the minimum yield of Re. Conversely, an incident ion that is close to a Re column will be channeled by Re columns but not by the Si columns if the scattering angle ψ is between the critical angles of the Si columns and the Re columns (i.e., ${\psi_c}^{Re} > \psi > {\psi_c}^{Si}$). That channeling process thus contributes to the minimum yield of Si. The minimum yield of the Si columns is therefore larger than that of the Re columns.

According to the previous reasoning, the minimum yield of Re columns, χ_{min}^{Re}, consists of two contributions, backscattering from Re atoms originating from the dechanneling when incident ions impinge on Re columns, $\chi_{min,1}^{Re}$, and backscattering from Re atoms originating from the dechanneling when incident ions impinge on Si columns, $\chi_{min,2}^{Re}$

$$\chi_{min}^{Re} = \chi_{min,1}^{Re} + \chi_{min,2}^{Re}. \qquad (3.3-6)$$

The values of these minimum yields can be estimated from appropriate modification of Eq. (3.3-1). Experimental results of channeling in elemental crystals indicate that Eq. (3.3-1) underestimates the value of the minimum yields.[21] Furthermore, Monte Carlo simulation of channeling phenomena by Barrett[34] indicates that the minimum yield extracted from computer simulation is about 3 times greater than that estimated from Eq. (3.3-1) and is in good agreement with the experiemntal data for perfect crystals such as Si and Ge.[21] We therefore modify Eq. (3.3-1) by a multiplying factor of 3 in order to get a better numerical estimation of the minimum yields. $\chi_{min,1}^{Re}$ thus can be estimated by

$$\chi_{min,1}^{Re} = 3\sigma_{Re}\pi {r_{min,Re}}^2, \qquad (3.3-7)$$

where $r_{min,Re}$ is the minimum distance of approach to Re columns. To get $\chi_{min,2}^{Re}$, we need to know the approaching distance of the incident ion to the Si columns, r_{Si}, when the scattering angle ψ equals the critical angle of the Re columns,

$$\psi(r_{Si}) = {\psi_c}^{Re}. \qquad (3.3-8)$$

Knowing r_{Si}, we obtain

$$\chi_{min,2}^{Re} = 3\sigma_{Si}\pi r_{Si}^2. \qquad (3.3-9)$$

The approaching distance r_{Si} obtained from Eq. (3.3-8) with the "standard potential"[21] is much smaller than $r_{min,Re}$ ($\sim 10^{-5}$ nm vs. $\sim 10^{-2}$ nm), and hence $\chi^{Re}_{min,2}$ is negligible compared to $\chi^{Re}_{min,1}$ (see Table 3.3-I). Therefore, one has

$$\chi^{Re}_{min} \approx \chi^{Re}_{min,1} \approx 3\sigma_{Re}\pi {a_{TF}}^2_{,Re} \approx 1\%. \qquad (3.3-10)$$

This predicted value of χ^{Re}_{min} is only about half of the measured value. One explanation is that the $ReSi_2$ sample contains imperfections. It is not a single crystalline film. Another is that the approximation of r_{min} by a_{TF} is inaccurate.

Similarly, the minimum yield of the Si columns, χ^{Si}_{min}, can be obtained,

$$\chi^{Si}_{min} = \chi^{Si}_{min,1} + \chi^{Si}_{min,2} = 3\sigma_{Si}\pi {r_{min}}^2_{,Si} + 3\sigma_{Re}\pi r^2_{Re}. \qquad (3.3-11)$$

However, here the r_{Re} obtained from the equation

$$\psi_{(}r_{Re}) = {\psi_c}^{Si}, \qquad (3.3-12)$$

is larger than $r_{min,Si}$ so $\chi^{Si}_{min,2}$ is the major contribution to the minimum yield of the Si columns. Table 3.3-I lists the calculated and the measured values of the minimum yields for both Si and Re columns. Compared to the Re column, the relatively good agreement between the measured value and the estimated value of the minimum yield for the Si column is probably due to its relative high value and hence its relative insensitivity to the imperfections in the film. This suggests that one should use only the minimum yield for the heavy (Re) element as an indicator of crystalline perfection, in particular, in the case of low defects density.

The continuum model, as extended here to polyatomic crystals, is able to explain the channeling phenomena that took place along directions for which there are more than one type of column as we have observed in $ReSi_2$. The critical angle of each column is determined only by the parameters of that column. The minimum yields are determined by the parameters of all columns, but are dominated by the dechanneling from the column with the largest average atomic number. These findings are readily generalized to channeling in polyatomic crystals with a number of different types of elemental columns, and from there to columns with different average atomic numbers and spacings. From the point of view of applying channelling to characterize the crystalline perfection of a polyatomic crystal, an important corollary is that high crystalline quality is not synonymous with a low minimum yield for the light element. In particular, a high value of the minimum yield for the light element does not necessarily mean that the sublattice of the light element is disordered.

References

1. M-A. Nicolet and S. S. Lau, in *VLSI Electronics: Microstructure Science* vol. 6, eds. N. Einspruch and G. Larrabee (Academic, New York, 1983), p. 391.
2. M.C. Bost and J.E. Mahan, J. Appl. Phys. 58, 2696 (1985).
3. K. Lefki, P. Muret, N. Cherief, and R.C. Cinti, J. Appl. Phys. 69, 352 (1991).
4. D. Shinoda, S. Asanabe, and Y. Sasaki, J. Phys. Soc. Jpn. 19, 269 (1964).
5. M.C. Bost and J.E. Mahan, J. Appl. Phys. 63, 839 (1987).
6. C. Krontiras, L. Gronbero, I. Suni, F.M. D'Heurle, T. Tersoff, I. Engstrom, B. Karlsson, C.S. Petersson, Thin Solid Films 69, 119 (1988).
7. R.G. Long, M.C. Bost, and J.E. Mahan, Thin Solid Films 162, 29 (1988).
8. N. Cherief, C.D'Anterroches, R.C. Cinti, T.A. Nguyen Tan, and J. Derrien, Appl. Phys. Lett. 55, 1671 (1989).
9. J.E. Mahan, K.M. Geib, G.Y. Robinson, R.G. Long, X.H. Yan, G. Bai, M-A. Nicolet, M. Nathan, Appl. Phys. Lett. 56, 2126 (1990).
10. K.M. Geib, J.E. Mahan, R.G. Long, M. Nathan, G. Bai, and M-A. Nicolet, J. Appl. Phys. (in press).
11. R.W. Fathauer, P.J. Grunthaner, T.L. Lin, K.T. Chang, J.H. Mazur, D.N. Jamieson, J. Vac. Sci. Technol. B6, 708 (1988).
12. L. Haderbache, P. Wetzel, C. Pirri, J.C. Peruchetti, P. Bolmont, and G. Gewinner, Surf. Sci. 209, L139 (1989).
13. J. Mahan, K.M. Geib, G.Y. Robinson, G. Bai, M-A. Nicolet, and M. Nathan, J. Vac. Sci. Technol. B (in press).
14. J.E. Mahan, K.M. Geib, G.Y. Robinson, R.G. Long, X.H. Yan, G. Bai, M-A. Nicolet, M. Nathan, Appl. Phys. Lett. 56, 2439 (1990).
15. J.E. Mahan, G. Bai, M-A. Nicolet, R.G. Long, and K.M. Geib (unpublished).
16. S.S. Lau, J.S-Y. Feng, J.O. Olowolafe, and M-A. Nicolet, Thin Solid Films 25, 415 (1975).
17. H.C. Cheng, T.R. Yew, and L.J. Chen, J. Appl. Phys. 57, 5246 (1985).
18. T. Siegrist, F. Hulliger, and G. Travaglini, J. Less-Comm. Metals 92, 119 (1983).
19. J.J. Chu, L.J. Chen and K.N. Tu, J. Appl. Phys, 62, 461 (1987).
20. M. Tabe, Jpn. J. Appl. Phys. 21, 534 (1982).
21. L.C. Feldman, J.W. Mayer, S.T. Picraux, *Materials Analysis by Ion Channeling*, Academic Press, New York, 1982.

22. G. Bai, M-A. Nicolet, John E. Mahan and Kent M. Geib, Phys. Rev. B 41, 8603 (1990).

23. A. Perio, J. Torres, G. Bomchil, F. Arnaud d'Avitaya, and R. Pantel, Appl. Phys. Lett. 45, 857 (1984).

24. D.S. Gemmell, Rev. Mod. Phys. 46, 129 (1974)

25. J. Lindhard, Dansk. Vid. Selsk. Mat. Fys. Medd., 34, 14 (1965).

26. S.T. Picraux, J.A. Davies, L. Eriksson, N.G.E. Johansson, and J.W. Mayer, Phys. Rev., 180, 873 (1969).

27. D.S. Gemmell and R.C. Mikkelson, Phys. Rev. B6, 1613 (1972).

28. L. Eriksson and J.A. Davies, Ark. Fys. 39, 439 (1972).

29. F.W. Clinard Jr. and W.M. Sanders, J. Appl. Pyhs. 43, 4937 (1972).

30. O. Meyer, Nucl. Instr. Meth. 149, 377 (1978).

31. G. Bai, M-A. Nicolet, J.E. Mahan, K.M. Geib, and G.Y. Robinson, Appl. Phys. Lett. 57, 1657 (1990).

32. O.B. Firsov, Soviet Phys. JETP 6, 534 (1957).

33. *International Tables for X-ray Crystallographs*, Vol. II (Kynoch Press, Birmingham, England, 1959), pp. 234, 239.

34. J.H. Barrett, Phys. Rev., 3, 1527 (1971).

Chapter 4 GeSi Films on Si(100)

4.1 Introduction

Silicon and germanium both have a diamond cubic structure, and form a solid solution over the entire composition. The lattice mismatch is 4.2% at room temperature.[1] The difference between the thermal expansion coefficient of Ge and Si is $\sim 3 \times 10^{-6}/^{o}$C.[1] The lattice mismatch at 550°C (a typical growth temperature) is therefore 4.4%, not much different from the value at room temperature (4.2%). High quality epitaxial GeSi films over the entire Ge composition range were successfully grown on Si(100) substrates at $\sim$ 550°C by MBE in 1984.[2] The films are metastable-strained, meaning that (1) the measured critical thickness for pseudomorphic films is larger than that predicted by Matthews and Blakeslee's equlibrium model,[3] or (2) the strain relaxation in a film thicker than the measured critical thickness is smaller than that predicted by the model. This is due to the fact that generation of misfit dislocations is a thermally activated process.[4] The strain state in a film is determined by kinetics, not by thermodynamics.[3] This also suggests that by lowering the growth temperature (e.g., from 550°C to 300°C), the critical thickness can be increased.[5,6]

The strain in a GeSi film influences its bandgap[7] and its band alignment with the Si substrate.[8] By controlling the strain state of a heterostructure, one could engineer the band gap and band offset to make novel heterostructure devices.[9] One example is a graded SiGe-base heterojunction bipolar transistor, the fastest transistors achieved to date in Si technology with a unity-current gain cutoff frequency of 75 GHz.[10]

Defects such as dislocations in a relaxed film degrade device performance. An understanding of the mechanisms of dislocation generation upon postthermal processing in metastable heterostructures is therefore important to implement novel device structures successfully. In the following section, we first summarize our results for GeSi films grown on both Si(100)[11] and vicinal Si(100)[12] at 550°C. We then investigate the kinetics of strain relaxation of highly metastable films grown at 300°C.[6] Some properties of misfit dislocations and their effects will also be discussed.[13]

4.2 Properties of GeSi films grown at 550°C

In this section, we focus on characterization of epitaxial GeSi films on Si(100) by BS/channeling and DCD. The structural, elastic, and thermal properties will be discussed.

A. Sample Preparation

The silicon wafer surface was cleaned by the procedure described in Ch. 2.2. The GeSi alloy film was grown on Si(100) at 550°C with a rate of ~ 0.2 nm/s by codeposition of silicon and germanium in ultrahigh vacuum at UCLA. The Ge composition of films ranges from 0.05 to 1, and the thickness from 30 nm to 7 μm.

B. Lattice Mismatch and Vegard's Law

The lattice mismatch between GeSi alloy and Si, f, can be estimated according to Vegard's law, which states that the lattice constant of an alloy varies in proportion to the composition of the alloy linearly between the lattice constants of the constituent elements. Knowing that the lattice mismatch between Si and Ge is 4.2%, one obtains

$$f = 4.2\% x, \qquad (4.2-1)$$

where x is the Ge composition. To verify the validity of Vegard's law in the case of thin film GeSi, we independently measured the Ge composition and the lattice mismatch of the samples by BS and DCD, and compared the data with the prediction.

The lattice mismatch between a GeSi film and a Si substrate was extracted from the x-ray rocking curve measurements. Perpendicular and parallel strains, $\epsilon^{\perp}$ and $\epsilon^{\parallel}$, were obtained from the peak separations of the rocking curves diffracted from (400) symmetrical and (311) asymmetrical planes of the sample (see Ch. 2.2). The lattice mismatch equals

$$f = (\frac{1-\nu}{1+\nu})\epsilon^{\perp} + \frac{2\nu}{1+\nu}\epsilon^{\parallel}.$$

The Poisson ratio of the film, ν, is extracted from the Poisson ratio for Si (0.28) and Ge (0.27)[14] using linear interpolation. The result is plotted in Fig. 4.2-1, showing that Vegard's law is applicable to epitaxial GeSi films.

C. Critical Thickness

For a given lattice mismatch of a heteroepitaxial structure such as GeSi/Si, there is an equilibrium critical thickness below which an epitaxial film that is in perfect registry with a substrate has a minimum energy. For GeSi on Si(100), the equilibrium critical thickness from Matthews and Blakeslee's model[3] is plotted as a function of Ge composition in Fig. 4.2-2 (dotted line). The measured critical thickness of GeSi films grown at 550°C by Bean et al.[2] is larger than that predicted by equilibrium model (Δ in Fig. 4.2-2). The results from the DCD and BS measurements of our samples are summarized in the same composition-thickness plot ($\bullet$ in Fig. 4.2-2), where the number associated with each datum point is the normalized parallel strain, $\epsilon^{\parallel}/f$, which equals 0 (1) for a pseudomorphic (decoupled) film. Our data are consistent with those of Bean et al.[2] These results indicate that metastable-strained pseudomorphic films can be grown at low temperature.

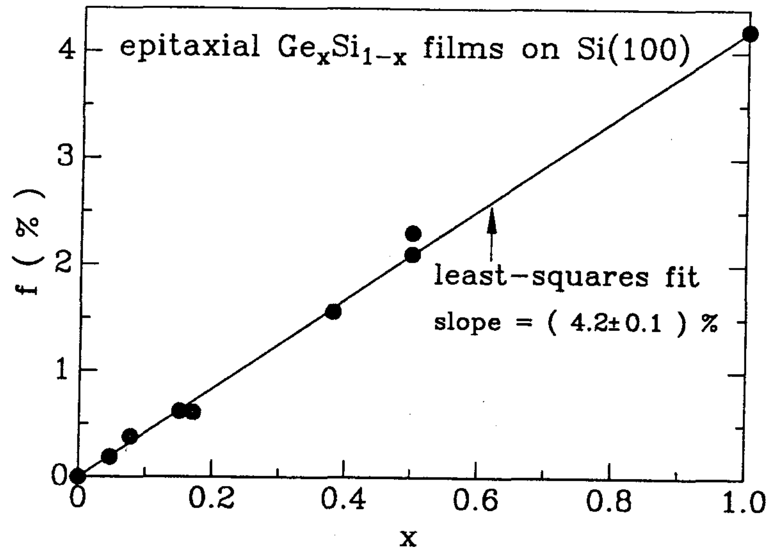

FIG. 4.2-1 The lattice mismatch between epitaxial Ge_xSi_{1-x} alloy and Si, f, as a function of Ge composition. The data agree well with the Vegard law over the entire composition range ($0 \leq x \leq 1$).

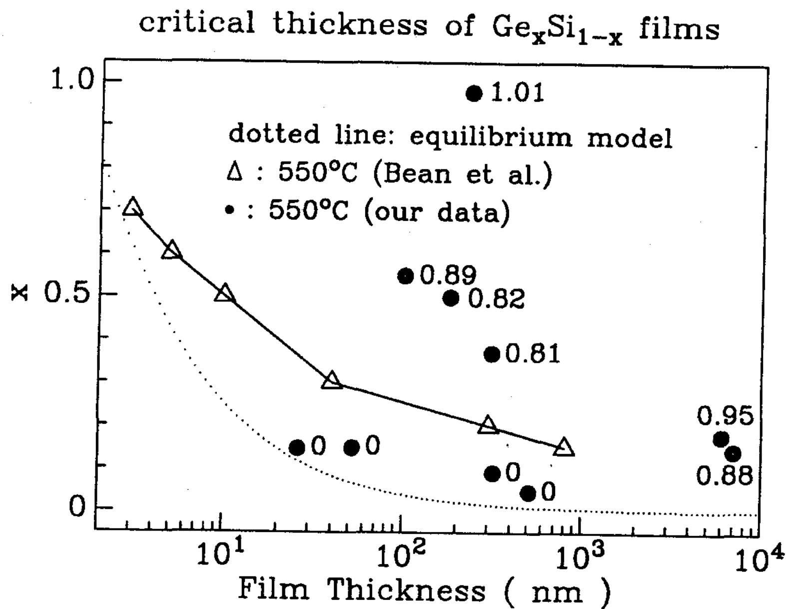

FIG. 4.2-2 Ge composition—film thickness plot of epitaxial Ge_xSi_{1-x} films on Si(100): dotted line is the equilibrium critical thickness from Matthews and Blakeslee's model; △ is the measured critical thickness of films grown at ~ 550°C by Bean et al., and • is from our work. The number associated with each datum point is the normalized parallel strain $\epsilon^{\|}/f$.

It is known that the measured critical thickness differs when different analytical tools are used because of different resolution of dislocation detection.[15] The common techniques (DCD, channeling, TEM) which were used in both Bean et al.'s and our results have a resolution of about 10^{-4}, corresponding to a dislocation spacing of $\sim 1\mu m$. A heterostructure with a dislocation spacing $>\sim 1\mu m$ is therefore regarded as pseudomorphic in this context and subsequent discussion. Techniques capable of resolving a single dislocation in a wafer (e.g., etch pits) reveal that the measured critical thickness of the samples grown at 550°C is smaller than that obtained by the common methods, but is still larger than the equilibrium one.[16]

D. Dislocations and Strain Relxation

Strain in the film thicker than the measured critical thickness (samples in the upper right of the solid line in Fig. 4.2-2) relax via generation of misfit dislocations. The amount of the measured relaxation (number associated with each point in Fig. 4.2-2) is less than that predicted by Matthews and Blakeslee's equilibrium model.[3]

TEM analysis shows that the dominant extended defects in a relaxed GeSi/Si(100) heterostructure are threading dislocations in the epitaxial film and misfit dislocations at the interface.[17] The misfit dislocations are aligned with $< 011 >$ direction with Burger's vector $\mathbf{b}= 1/2 < 110 >$.[17] Both 60°-mixed and 90°-edge type are observed.[17] The spacing between misfit dislocations, p, can be estimated from the parallel strain from

$$p = \frac{b_m}{\epsilon^{\parallel}},$$

where $b_m \sim 0.1\ nm$ is the edge component of Burger's vector on the interfacial plane.

The x-ray diffraction peak from a relaxed film is broader than that caused by the finite film thickness, because of the threading dislocations in the film. This additional peak broadening, W_D, can be used to estimate the threading dislocation density, ρ_t (see Ch 2.2),

$$\rho_t = \frac{W_D^2}{9b^2}.$$

Our results show that the larger the parallel strain $\epsilon^{\parallel}$ is, the broader the x-ray diffraction peak from the film becomes. This suggests that the generation of misfit dislocations also produces threading dislocations.

While channeling spectrum of a pseudomorphic GeSi/Si structure shows no dechanneling at the interface, that of a relaxed one has a measurable interfacial dechanneling caused by misfit dislocations. The dechanneling probability, P_D, is proportional to the misfit dislocation density at

the interface, ρ_m,

$$P_D = \sigma_D \rho_m, \qquad (4.2-2)$$

where σ_D is the dechanneling cross section.[18] The linear misfit dislocation density ρ_m is defined as the total length of misfit dislocations per unit area at the interface, and equals

$$\rho_m = \frac{2}{p} = \frac{2\epsilon^{\|}}{b_m}.$$

The above relationships show that the dechanneling probability P_D across the interface is proportional to the parallel strain $\epsilon^{\|}$,

$$P_D = \frac{2\sigma_D}{b_m}\epsilon^{\|}. \qquad (4.2-3)$$

P_D can be extracted from channeling measurements (see Ch. 7.2 for detailed discussion), and increases linearly with $\epsilon^{\|}$ with a slope of 20 (Fig. 4.2-3(a)). This observation agrees with Eq. (4.2-3) and results in the dechanneling cross section of $\sigma_D = 2$ nm. This value is qualitatively consistent with that from the theoretical estimates ($\sim 1-5$ nm).[18]

The minimum channeling yield of a pseudomorphic film is about 4% for both the Ge and Si signal, and is about the value for a perfect single crystal. It becomes large for a relaxed film, indicating a dislocated crystal. The difference, $\Delta\chi_{min}$, is proportional to the threading dislocation density ρ_t in the film,[18]

$$\Delta\chi_{min} \propto \rho_t \propto W_D^2. \qquad (4.2-4)$$

This relationship agrees with our experimental results, where the measured minimum channeling yield increases as the x-ray diffraction peak for the film broadens (Fig. 4.2-3(b)).

E. Thermal Strain

The thermal expansion coefficient of Ge ($6 \times 10^{-6}/°C$) is greater than that of Si ($3 \times 10^{-6}/°C$), which generates a thermal mismatch of $\sim 0.2\%$ between room temperature and 550°C.[1] This magnitude is insignificant compared to the lattice mismatch of 4.2%, and suggests that thermal strain in a Ge/Si structure is not important, unlike in $CoSi_2$/Si (see Ch 2.5). DCD measurements of epitaxial Ge films on Si(100) at 20-500°C confirm that thermal strain is small, and also indicate that the interface does not shear below about 500°C. For a GeSi alloy, the lattice mismatch is determined by Vegard's law. If we assume that the thermal expansion coefficient can also be estimated by linear interpolation, thermal strain in an alloy film is also negligible compared to the lattice mismatch. Fig. 4.2-4(a) shows the evolution of the lattice mismatch and strain with temperature for a metastable coherent GeSi film on Si(100). The small slope means that the thermal strain is very small. The

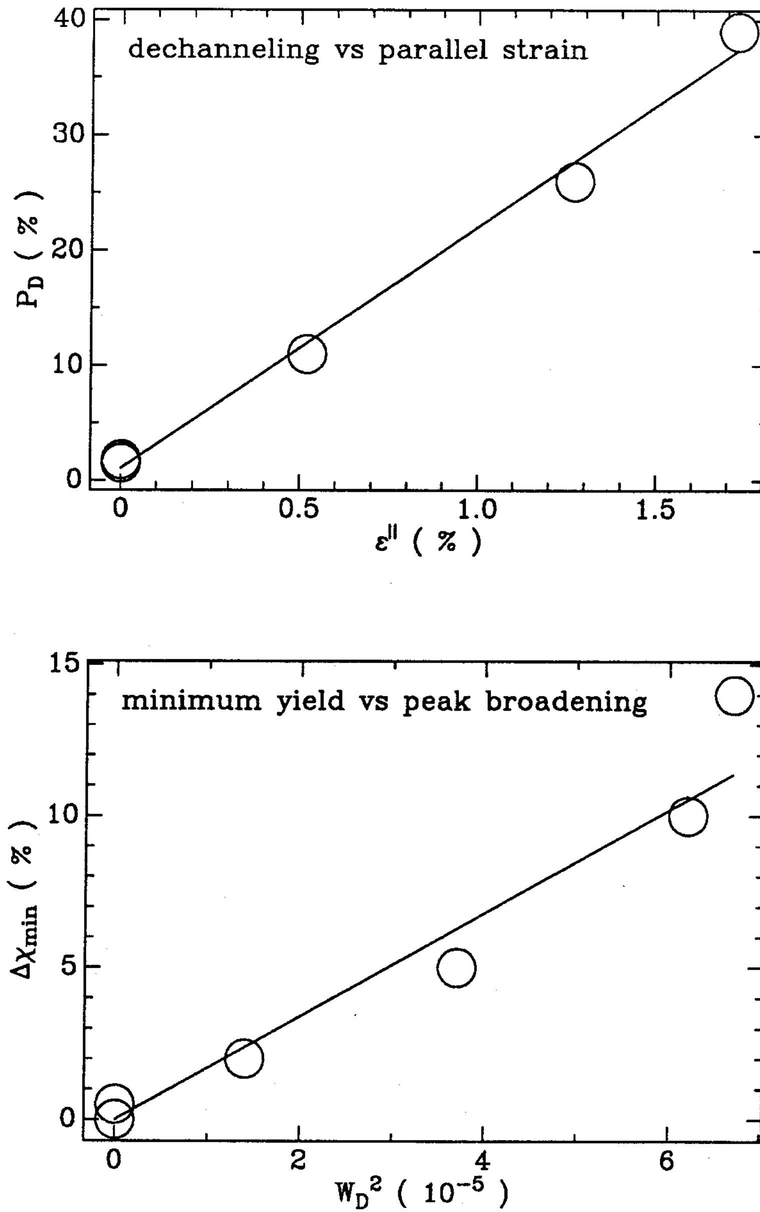

FIG. 4.2-3 Channeling characteristics vs x-ray diffraction of epitaxial GeSi films grown on Si(100) at 550°C: (a) dechanneling probability of an aligned MeV ^{4}He beam across the interface as a function of parallel strain $\epsilon^{\parallel}$ of the film; (b) the difference of the minimum channeling yield between a relaxed and a coherent GeSi film as function of the square of the x-ray peak broadening caused by threading dislocations in the film.

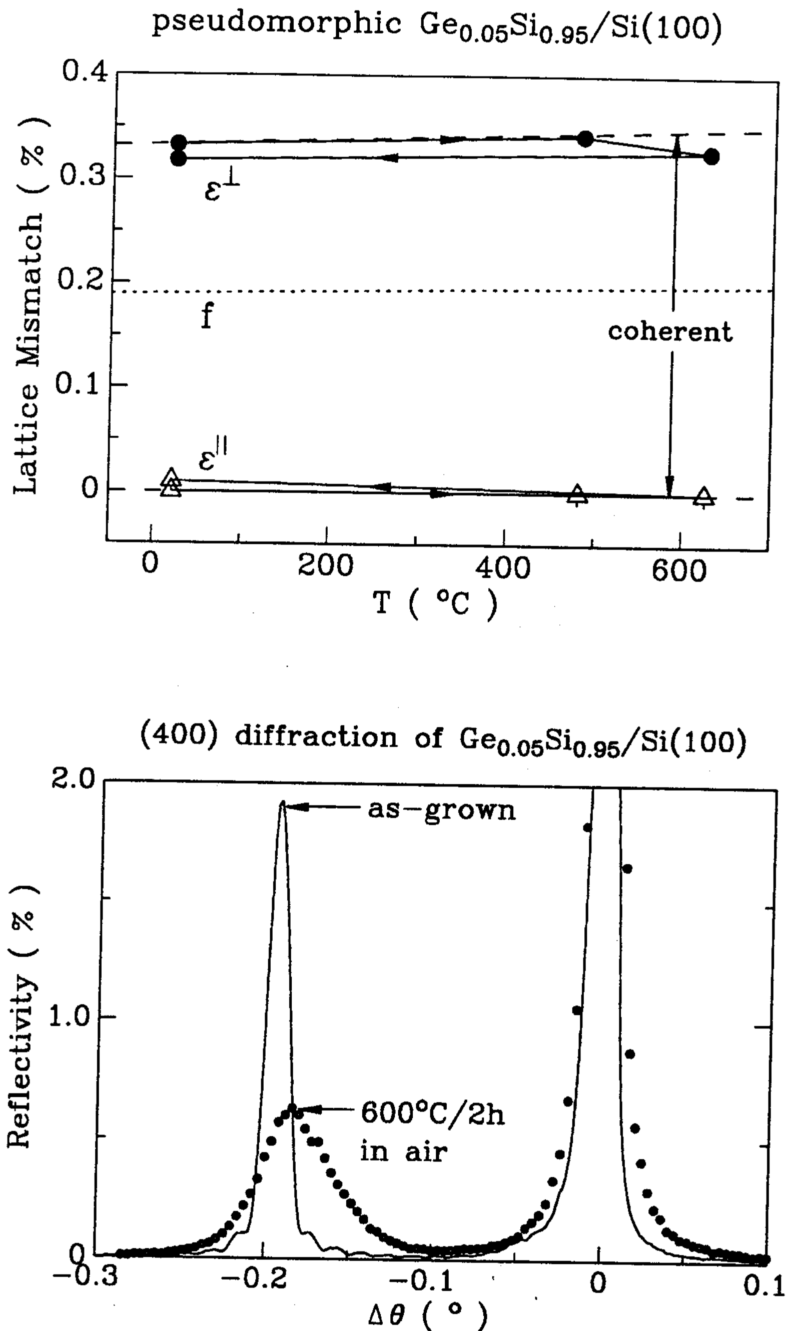

FIG. 4.2-4 Thermal properties of a metastable coherent Ge_xSi_{1-x} film grown on Si(100) at 550°C: (a) the lattice mismatch (dotted line) and the strains (solid lines) as a function of temperature; dashed line is for a film with rigid interface; (b) Fe K_{α_1} x-ray rocking curves diffracted from (400) planes of of sample before (solid line) and after (dotted line) thermal annealing at 630°C for 2h in ambient air.

figure also indicates that there is a small amount of strain relaxation after heating at 630°C in air for 2h. The rocking curve of the annealed sample (dotted line Fig. 4.2-4(b)) has a broader peak compared to that of the as-grown one (solid line Fig. 4.2-4(b)), indicating a degraded film. On the other hand, the sample annealed in vacuum at 630°C for 2 h shows no detectable change. This means that the strain relaxation is induced by the sample interaction with the ambient. GeSi films of low Ge content are known to react with oxygen by selectively oxidizing Si. We hence conclude that interactions promote strain relaxation of metastable GeSi film. A similar effect is observed for epitaxial $CoSi_2$ films on Si(111) (see Ch. 2-5). The phenomenon is quite probably a very general one.

4.3 Pseudomorphic GeSi films and superlattices on vicinal Si(100)

Some properties of GeSi films on vicinal Si(100) substrates are discussed in this section. The substrates used in this study are vicinal Si(100) wafers, with their parallel front and back surface normals tilted from [100] towards $[0\overline{1}\overline{1}]$ by an offset angle ϕ_s of 3.1° and 6°. GeSi films 100 nm thick with Ge composition from 0.06 to 0.16, and a 30 period superlattice of $Ge_{0.2}Si_{0.8}$(8.4 nm)/Si(15.6 nm) were grown at 550°C by MBE at UCLA. Film thicknesses and compositions were determined by BS, and epitaxial quality by channeling measurements. The strain in the films was characterized by DCD.

A. Single Layer GeSi Films

All films are in the lower-left side of Bean et al.'s critical thickness curve in the thickness-composition plot of Fig. 4.2-2, and are therefore pseudomorphic. In the following, we describe in detail the methods we have used to determine the strain state in the $Ge_{0.06}Si_{0.94}$ 100 nm thick film on a vicinal Si(100) substrate with an offset angle of 3.1° (as determined by the back-reflection Laue pattern) by DCD.

First, a series of x-ray rocking curves diffracted from symmetrical (400) planes of the sample in various azimuthal configuration were recorded (see Ch 2.3). The substrate peak position, θ_P, and the difference between the film and the substrate peak position, $\Delta\theta_P$, were plotted as a function of the azimuthal angle in Fig. 4.3-1(a) and (b). That both θ_P and $\Delta\theta_P$ have the same azimuthal dependence means that the [100] directions of the substrate and of the film are misoriented against the surface normal in the same direction, and that the [100] direction of the film is farther away from the surface normal than that of the substrate (Fig. 4.3-1(c)). The solid lines are the least-squares fit of a cos function to the data (see Eq. (2.3-1) and related discussion in Ch 2.3). Fig. 4.3-1(b)

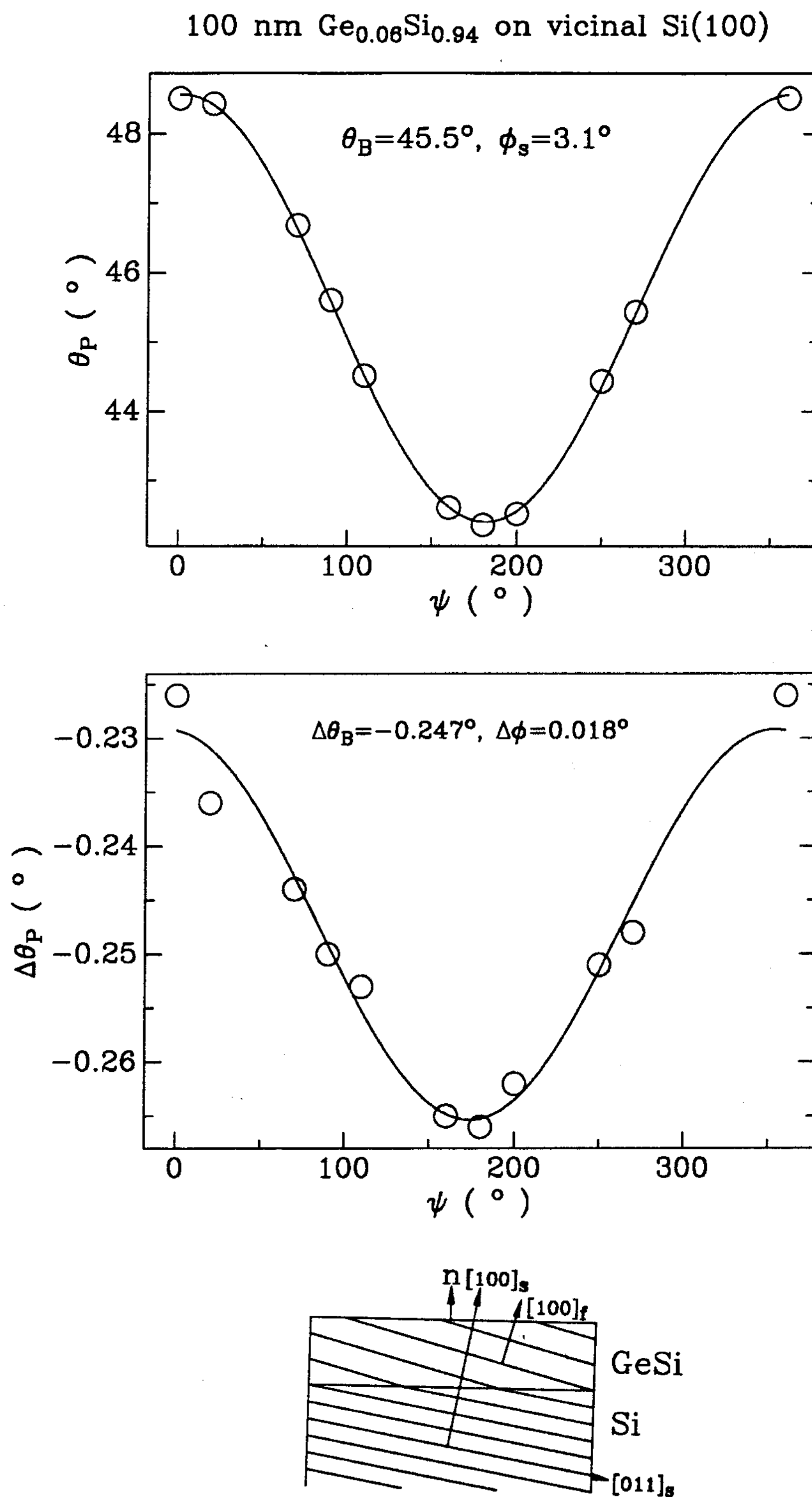

FIG. 4.3-1 (a) the angular position of the (400) peak diffracted from the substrate and (b) the difference of the peaks from the film and the substrate versus the azimuthal angle of the sample configuration. (c) schematics of the results from analysis of the x-ray rocking curve data (a) and (b).

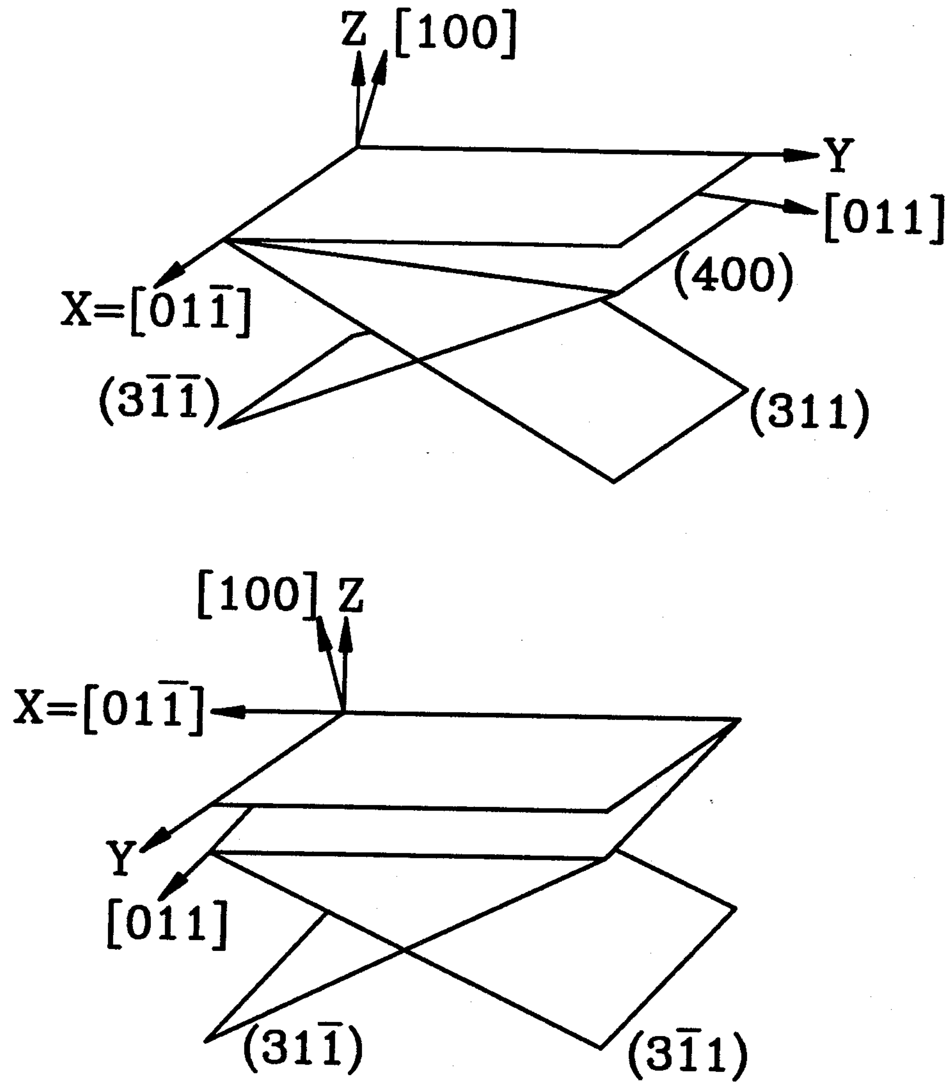

FIG. 4.3-2 Schematics of one symmetrical (400) and four asymmetrical {311} diffracting planes of vicinal samples. The surface normal is taken as Z-axis.

shows that for the (400) plane, the misorientation angle, $\Delta\phi$, is 0.018°, and the interplanar spacing mismatch, ϵ_ϕ, is 0.43%, where ϕ is the angle between the surface normal and the substrate diffracting plane.

Unlike symmetrical diffraction from the (400) plane, there are four sets of asymmetrical diffraction planes such as (311), $(3\bar{1}\bar{1})$, $(3\bar{1}1)$, and $(31\bar{1})$ (see Fig. 4.3-2). X-ray rocking curves diffracted from all four such aymmetrical planes of the sample were also recorded. Both the misorientation angles $\Delta\phi$ and the strains ϵ_ϕ for each set of planes were extracted.

To simplify the analysis, we made two assumptions: (1) the film is under biaxial stress in the x-y plane (parallel to the surface), and the principal axes of stress are therefore along x-, y-, z-directions; (2) the film is elastically isotropic; the principal axes of the strain tensor hence coincide with those of the stress tensor. If the principal strains are ϵ^{XX}, ϵ^{YY}, ϵ^{ZZ}, the strain along the direction in the y-z plane (Fig. 4.3-2(a)) is[19]

$$\epsilon_\phi = \epsilon^{ZZ}\cos^2\phi + \epsilon^{YY}\sin^2\phi = \epsilon^{ZZ} - (\epsilon^{ZZ} - \epsilon^{YY})\sin^2\phi, \qquad (4.3-1)$$

and the misorientation angle is

$$\Delta\phi = (\epsilon^{ZZ} - \epsilon^{YY})\cos\phi\sin\phi = \frac{\epsilon^{ZZ} - \epsilon^{YY}}{2}\sin 2\phi. \qquad (4.3-2)$$

We hence plot the strain ϵ_ϕ obtained from DCD measurements of the diffracting planes (e.g., those shown in Fig. 4.3-2(a)) as a function of $\sin^2\phi$ in Fig. 4.3-3(a). The solid line is the least-squares fit of Eq. (4.3-1) to the data (○). The principal perpendicular and parallel strain extracted from the fitting are $\epsilon^{ZZ} = 0.42 \pm 0.02\%$ and $\epsilon^{YY} = 0 \pm 0.02\%$ (see Table 4.3-I). Similarly, we plot the misorientation angle as a function of $\sin 2\phi$ in Fig. 4.3-4(b). The solid line is obtained from Eq. (4.3-2) using previously determined ϵ^{ZZ} and ϵ^{YY}. The good agreement obtained in Fig. 4.3-4(b) between the data (○) and the predicted value means that the misorientation observed here can be explained by the biaxial stress model and results from the deviation of the diffracting plane from the principal strain axes.

This present misorientation model differs from the misorientation model based on geometrical matching at the interface, developed in Ch. 2.3 for $CoSi_2$ on vicinal Si(111). The misorientation angle predicted from Eq. (4.3-2) for the $CoSi_2$ films on vicinal Si(111) discussed in Ch. 2.3 ($\epsilon^{ZZ} \approx -1.7\%$ and $\epsilon^{YY} \approx -0.8\%$) is

$$\Delta\phi \approx -0.9\% \sin\phi\cos\phi \approx -0.9\%\phi$$

for small ϕ. This prediction does not agree with the experimental data: $\Delta\phi \approx -1.7\%\phi$. In particular,

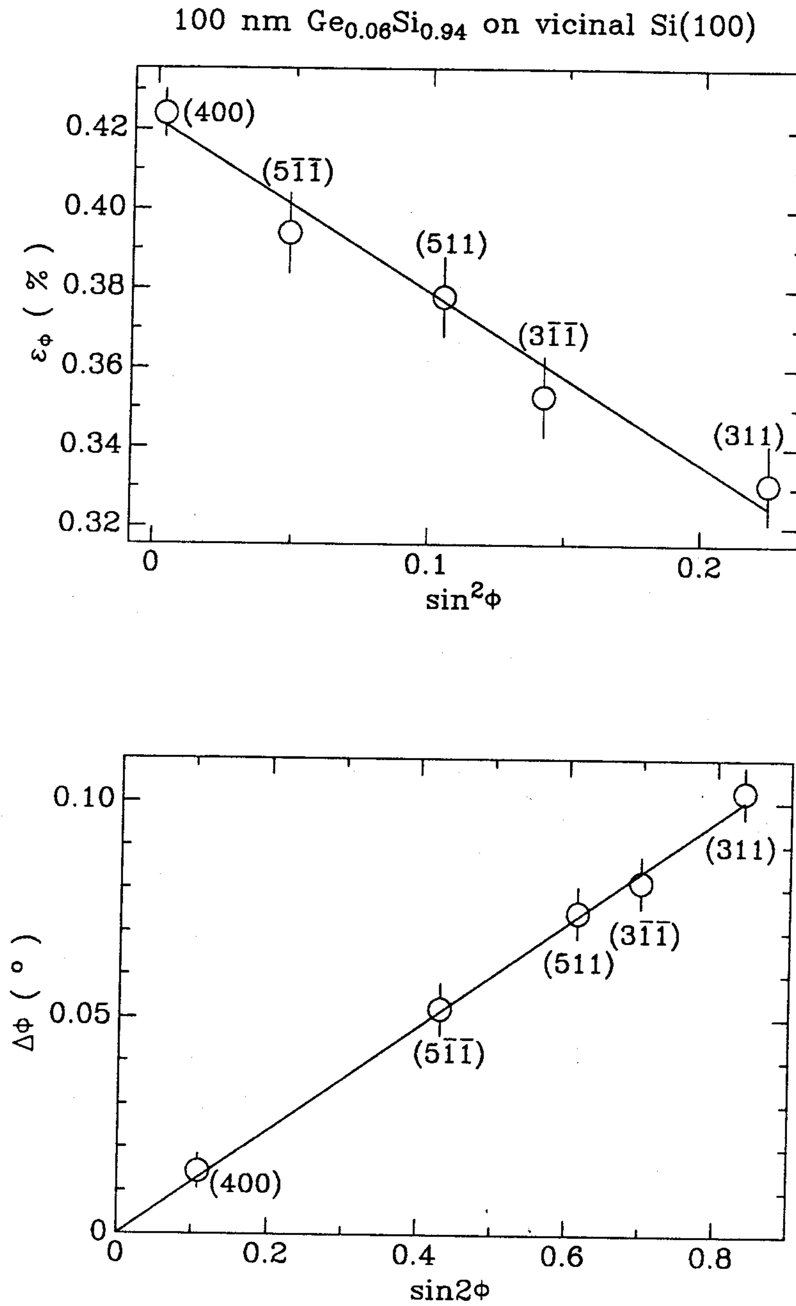

FIG. 4.3-3 (a) The mismatch in interplanar spacing and (b) the misorientation angle as a function of diffracting planes of a $Ge_{0.05}Si_{0.95}$ film 100 nm thick on a vicinal Si(100). The solid line is the prediction of the biaxial stress model with $\epsilon^{XX} = \epsilon^{YY} = 0$, $\epsilon^{ZZ} = 0.52\%$, and $\phi_s = 3.1°$.

for a stress-free film, $\epsilon^{ZZ}=\epsilon^{YY}=0$, the present biaxial stress model yields $\Delta\phi = 0$, in contrast with the experimental observation for $CoSi_2$ (Ch 2.3). This means that the biaxial stress model cannot explain the misorientation in the case of $CoSi_2$ on vicinal Si(111).

The results obtained by analyzing the rocking curves diffracted from asymmetrical planes such as $(3\bar{1}1)$ and $(31\bar{1})$ (see Fig. 4.3-2(b)) yield the strain along the direction in the z-x plane. A similar analysis shows that ϵ^{XX} also equals 0 (Table 4.3-I). We therefore conclude that the film is pseudomorphic within the experimental resolution, and that the strain is isotropic in x-y plane ($\epsilon^{XX}=\epsilon^{YY}=0$).

Other samples with different Ge composition and offset angles were analyzed in the same framework. The results are summarized in Table 4.3-I. All the films are pseudomorphic, and the misorientation between diffracting planes of the film and the substrate can be explained by the biaxial stress model.

B. GeSi/Si Strained-Layer Superlattice

A superlattice 720 nm thick was grown on a vicinal Si(100) with an offset angle of 3.1°. Channeling spectrometry shows that the film is highly epitaxial with a minimum yield of ~ 3%, and pseudomorphic without detectable dechanneling at the interface. X-ray rocking curves from symmetrical (400) diffraction planes of the sample are shown in Fig. 4.3-4. The solid (∘) line in Fig. 4.3-4(b) corresponds to the diffraction geometry I (II) in Fig. 4.3-4(a).

The overall elastical properties of a superlattice are equivalent to those of a uniform alloy with an average composition.[19] The 0th order superlattice peak of two rocking curves are at different angular positions, meaning that the [100] axis of the superlattice is misoriented against that of the substrate. The average strain and misorientation angle can be extracted from the peak separations betweem the 0th order superlattice peak and the substrate peak, $\Delta\theta_I$ and $\Delta\theta_{II}$, according to the previous analysis for a single layer film.[19] The results are summarized in Table 4.3-I, which shows that the superlattice is pseudomorphic and that the misorientation angle can be explained by the biaxial stress model.

The angular oscillation periodicity, $\delta\theta_I$, of the superlattice rocking curve for the diffraction geometry I also differs from that for the geometry II, $\delta\theta_{II}$. This effect is due to the different outgoing angle, θ_o, for the two x-ray paths. For a superlattice whose period has a thickness, t_p, the angular periodicity equals[19]

$$\delta\theta = \frac{\lambda \sin\theta_o}{t_p \sin 2\theta_B}. \qquad (4.3-3)$$

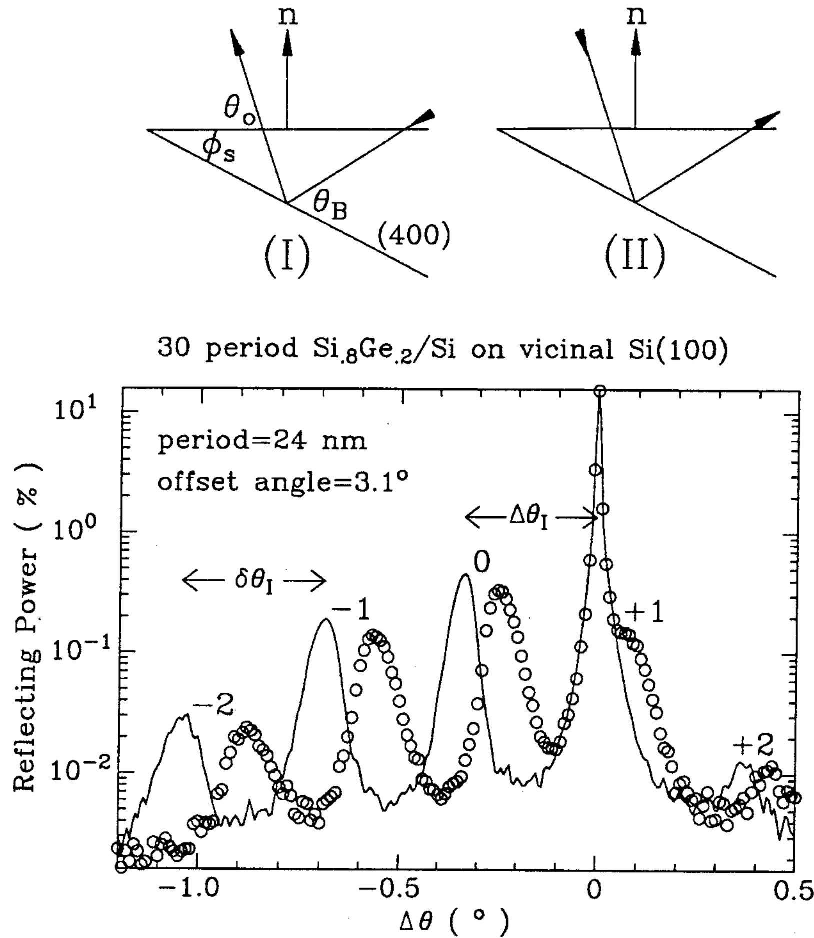

FIG. 4.3-4 Fe K_{α_1} (λ = 0.1932 nm) x-ray rocking curves diffracted from the (400) symmetrical planes of the GeSi superlattice on vicinal Si(100): (a) two diffraction geometries corresponding to a rotation of 180° of the incident x-ray about the surface normal; (b) the corresponding diffraction spectra.

Table 4.3-I The strain obtained from rocking curve analyses and the biaxial stress model of the single layer Ge_xSi_{1-x} films and the superlattice with the average Ge composition of 0.07 grown on vicinal Si(100) substrates at 550°C.

Sample	t (nm)	x	ϕ_s	ϵ^{XX}(%)	ϵ^{YY}(%)	ϵ^{ZZ}(%)
single layer	100	0.06	3.1	0	0	0.42
single layer	100	0.14	3.1	0	0	1.07
single layer	100	0.16	6.0	0	0	1.22
superlattice	720	0.07	3.1	0	0	0.53

For (400) symetrical diffraction and samll offset angle, $\phi_s \ll 1$, we obtain

$$\delta\theta_p \equiv \frac{\delta\theta_I + \delta\theta_{II}}{2} = \frac{\lambda}{2t_p \cos\theta_B}, \tag{4.3-4a}$$

and

$$\frac{\delta\theta_I - \delta\theta_{II}}{2} = (\delta\theta_p \cot\theta_B)\phi_s. \tag{4.3-4b}$$

From the measured periodicity $\delta\theta_I$ and $\delta\theta_{II}$, one has the superlattice period $t_p = 24$ nm from Eq. (4.3-4a) and the offset angle $\phi_s = 3^o$ from Eq. (4.3-4b). These results agree well with those obtained by other techniques, confirming that the apparent different angular periodicity $\delta\theta_I$ and $\delta\theta_{II}$ is caused by the inclination of the diffracting plane from the surface.

4.4 Strain relaxation of pseudomorphic GeSi films grown at 300°C

The growth and stability of coherently strained epitaxial GeSi layers on Si substrates are key issues for the fabrication and operation of Si/GeSi/Si heterojunction bipolar transistors. It is known that the strain state of epitaxial GeSi layers on Si substrates depends critically on the layer thickness, the lattice mismatch, and the growth temperature.[1,2] In the case of growth by molecular beam epitaxy at low temperature ($\leq$ half of the melting point), a metastable structure is usually obtained.[2,5,6] The metastability comes from the kinetic barriers that hinder the generation of misfit dislocations to relax the elastic strain.[4] Such a structure relaxes upon subsequent thermal processing at higher temperatures.[5,6] Dodson and Tsao[4] modeled the kinetics of strain relaxation in terms of dislocation nucleation and multiplication driven by the excess stress in the metastable structure. This model agrees well with experimental results on the strain relaxation of GeSi/Si heterostructures, and provides a framework to interpret data. There exist a handful of detailed quantitative experimetal investigations on strain relaxation.[5,6,20–24] However, a full data set covering a wide range of layer metastability and relaxation temperature is still lacking.

We present here some quantitative results on strain relaxation of metastable pseudomorphic $Ge_{0.3}Si_{0.7}$ layers 570 nm thick on Si(100). The layers were grown at 300°C at a rate of ~0.1 nm/s by co-deposition of silicon and germanium in an ultrahigh vacuum of a base pressure $\sim 10^{-10}$ Torr.

Double crystal x-ray diffractometry and MeV ^{4}He channeling spectrometry were used to characterize the strain and the crystalline quality of the epitaxial layer. The composition and the thickness of the layer were confirmed by MeV ^{4}He backscattering spectrometry. [100] axial channeling of the sample shows that the layer is of high quality with a minimum yield of $\sim$ 5% for both Ge and Si. The interface between the layer and the substrate has no detectable dechanneling centers.

The x-ray rocking curve from (400) symmetrical diffraction shows a sharp, intense diffraction peak from the layer. The full-width at half-maximum of the peak, W_θ, is only $\sim 3 \times 10^{-4}$ radian. It equals the value expected for the peak broadening that is due to the finite thickness (570 nm) of the layer, W_S. This means that the layer is of high crystalline perfection without measurable defects. The peak separations between the layer and substrate for both (400) symmetrical and (311) asymmetrical diffractions show that the layer is pseudomorphic with a non-measurable parallel strain, $\epsilon^{\|} < 0.01\%$, and a perpendicular strain, $\epsilon^{\perp}$, of 2.1%. According to Vegard's law, the lattice mismatch, f, between a stress-free $Ge_{0.3}Si_{0.7}$ layer and Si substrate is 1.2%. In linear elasticity theory, the parallel and perpendicular strains are related to the lattice mismatch by

$$\epsilon^{\perp} = \frac{1+\nu}{1-\nu} f - \frac{2\nu}{1-\nu}\epsilon^{\|}, \qquad (4.4-1)$$

where ν is the Poisson ratio. Using $\nu = 0.273$,[14] the perpendicular strain for pseudomorphic ($\epsilon^{\|}=0$) $Ge_{0.3}Si_{0.7}$ layers on Si ($f = 1.2\%$) is $\epsilon^{\perp} = 2.1\%$, in excellent agreement with the experimental results.

Houghton et al.[16] used an etching technique to map the onset of dislocations in epitaxial GeSi layers grown on Si(100) substrates and showed that the equilibrium critical thickness of the layer agrees with that predicted by Matthews and Blakeslee's model.[3] According to this model, the equilibrium critical thickness of epitaxial $Ge_{0.3}Si_{0.7}$ layers on Si(100) is only 8 nm (see Fig. 4.2-2), and the equilibrium strain state of 570 nm thick layers is almost decoupled, with $\epsilon^{\|} \approx \epsilon^{\perp} \approx f = 1.2\%$. This means that 570 nm pseudomorphic $Ge_{0.3}Si_{0.7}$ layers on Si(100) are highly metastable. We also note that the experimentally measured critical thickness of $Ge_{0.3}Si_{0.7}$ layers grown on Si(100) at 550°C by molecular beam epitaxy is 40 nm (see Fig. 4.2-2), more than 10 times smaller than that of the layers grown at 300°C. This shows that a low growth temperature can greatly enhance the critical thickness of epitaxial GeSi layers.

The strain relaxation of GeSi layers proceeds by nucleation[17,25,26] and multiplication[27,28] of misfit dislocations. We monitored by x-ray rocking curves taken at room temperature the strain relaxation of 570 nm thick pseudomorphic $Ge_{0.3}Si_{0.7}$ layers upon thermal annealing in a vacuum (5×10^{-7} torr). The number of misfit dislocations per unit length at the interface, ρ_m, is proportional to the parallel strain $\epsilon^{\|}$,

$$\rho_m = \frac{\epsilon^{\|}}{b_m}, \qquad (4.4-2)$$

where $b_m = 0.2$ nm is the edge component of Burger's vector in the interfacial plane. We obtained $\epsilon^{\perp}$ from (400) diffractions for all the samples and then extracted $\epsilon^{\|}$ according to Eq. (4.4-1) with known $\nu = 0.273$ and $f = 1.2\%$. The parallel strain $\epsilon^{\|}$ was also measured directly from combined (311) and (400) diffractions for selected samples. The result agrees with that extracted from

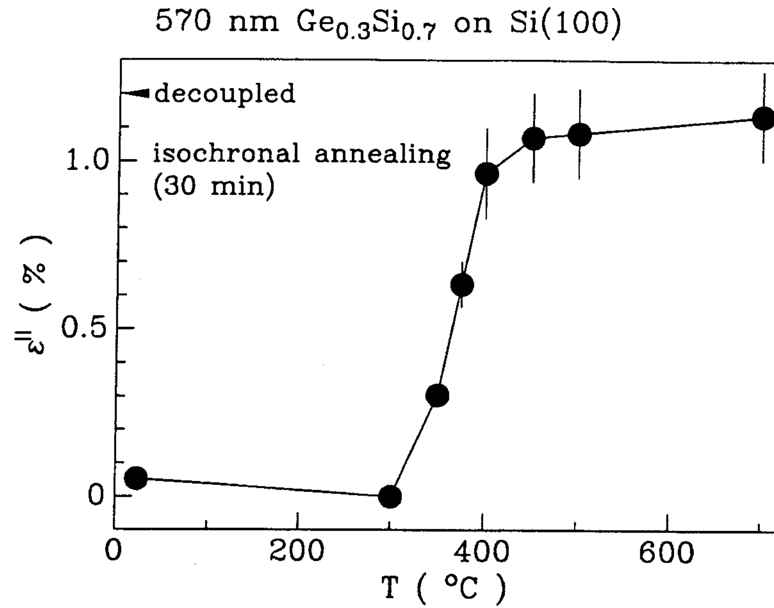

FIG. 4.4-1 The strain relaxation of a highly metastable GeSi strained layer grown on Si(100) at $\sim 300°C$ as a function of temperature upon isochronal annealing for 30 min in vacuum. The strain relaxes sharply at $375 \pm 25°C$.

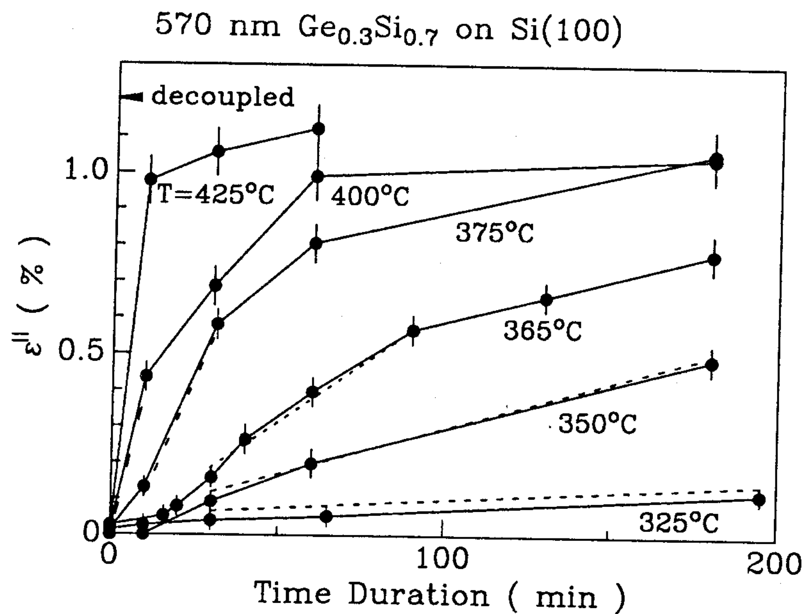

FIG. 4.4-2 Parallel strain $\epsilon^{\parallel}$ of 570 nm thick epitaxial $Ge_{0.3}Si_{0.7}$ layers grown on Si(100) at $\sim 300°C$ obtained from (400) diffraction x-ray rocking curve measurements vs duration of *ex situ* thermal annealing in vacuum ($\sim 5 \times 10^{-7}$ Torr) at various temperatures.

Eq. (4.4-1). As the metastable $Ge_{0.3}Si_{0.7}$ layer relaxes upon annealing, $\epsilon^{\|}$ increases from $< 0.01\%$ for coherent layers to $\sim 1.2\%$ for relaxed ones (see Fig. 4.4-1). The misfit dislocation density ρ_m thus obtained from Eq. (4.4-2) increases correspondingly from $< 1/\mu m$ to $\sim 50/\mu m$. The transition occurs sharply at $375 \pm 25°$C. At 300°C, little relaxation is detectable for annealing lasting up to 180 min. At 500°C, the strain reaches the equilibrium value in less than 10 min. Figure 4.4-2 shows that the parallel strain increases slowly at a low relaxation level ($\epsilon^{\|} < 0.1\%$; see in particular data of $T \leq 365°$C, where this initial phase is well resolved), then increases roughly linearly at a modestly relaxed level ($0.1\% < \epsilon^{\|} < 0.6\%$), and gradually saturates towards nearly complete relaxation ($\epsilon^{\|} > 0.6\%$). On the basis of this observation, we envision the following strain relaxation process: The initial sluggish relaxation is likely associated with a nucleation barrier and low density of misfit dislocations; the approximately linear relaxation at modest level is dominated by multiplication; and the final gradual saturation is related to the dislocation interaction, which impedes their motion, and to a decrease of excess stress, which reduces the driving force for strain relaxation.

We extracted the strain relaxation rate at a modest relaxation level from Fig. 4.4-2 by fitting a linear increase to $\epsilon^{\|}$ in the range of 0.1% to 0.6% (see dashed line in Fig. 4.4-2). Figure 4.4-3 plots that rate as a function of the inverse annealing temperature. The data clearly show an Arrhenius dependence and the slope gives an activation energy of 2.1 ± 0.2 eV. This demonstrates that the strain relaxation of metastable GeSi layers at modest relaxation levels (between the pseudomorphic and the equilibrium strain state) is a thermally activated process.

Dodson and Tsao[4] modeled the strain relaxation by plastic flow, which can be described by a non-linear differential equation, written here in a slightly different form,

$$\frac{d\epsilon^{\|}}{dt} = \frac{(\epsilon^{\|} - \epsilon^{\|}_{eq.})^2(\epsilon^{\|} + \epsilon^{\|}_{o})}{\tau}, \tag{4.4-3}$$

where $\epsilon^{\|}_{eq.}$ is the equilibrium parallel strain and τ is a time constant. The parameter $\epsilon^{\|}_{o}$ is used to simulate the "background" dislocation density or dislocation nucleation, which is very small ($< 0.1\%$) for initially pseudomorphic layers. The time constant τ determines how fast the relaxation proceeds and has an exponential temperature dependence, $\tau \propto exp(E_a/kT)$. The activation energy, E_a, is related to the kinetic barriers of dislocation glide. When the parallel strain is taken at a fixed value corresponding to a modest relaxation level, as was done for Fig. 4.4-3, the relaxation rate of Eq. (4.4-3) becomes

$$rate = \frac{d\epsilon^{\|}}{dt} \propto \frac{1}{\tau} \propto exp(-\frac{E_a}{kT}). \tag{4.4-4}$$

Therefore, the activation energy of 2.1 ± 0.2 eV from Fig. 4.4-3 for the rate of strain relaxation is the same as that for dislocation glide in Dodson and Tsao's model (E_a). This value is the same as that

for dislocation glide in bulk $Ge_{0.3}Si_{0.7}$, ~ 2 eV, obtained by linearly interpolating those of Ge (~ 1.6 eV) and Si (~ 2.2 eV).[29] It also agress reasonably well with that of Tuppen and Gibbings[23] and Houghton [24] (~ 2.2 eV), and Timbrell et al.[22] (~ 1.9 eV), but is about twice that of Hull et al.[20,21] (~ 1.1 eV). Dodson and Tsao[30] suggest that the excess stress in the layer reduces the activation energy for dislocation glide. Our data show that this reduction is not important in our 570 nm thick epitaxial $Ge_{0.3}Si_{0.7}$ strained layers.

The broadening of the x-ray diffraction peak is a measure of crystalline imperfection. The dominant imperfection in epitaxial GeSi layers grown on Si is threading dislocations, which cause a peak broadening, W_D. The areal density of threading dislocations, ρ_t, in the epitaxial layer, can be estimated (see Ch 2.2) by

$$\rho_t = \frac{{W_D}^2}{9b^2}, \qquad (4.4-5)$$

where $b = 0.4$ nm is Burger's vector of threading dislocations. We found that the x-ray (400) diffraction peak from the $Ge_{0.3}Si_{0.7}$ layer broadens as the strain relaxes upon thermal annealing of the sample. Assuming that both the finite layer thickness and the threading dislocations produce a Gaussian broadening of the x-ray peak, one has ${W_D}^2 = {W_\theta}^2 - {W_S}^2$ (W_θ and W_S are defined in Ch. 2.2). The areal density ρ_t thus obtained from Eq. (4.4-5) increases from $< 10^6/\text{cm}^2$ for pseudomorphic layers to $\sim 3 \times 10^9/\text{cm}^2$ for relaxed ones.

Furthermore, Fig. 4.4-4 shows that W_D increases linearly as $\epsilon^{\|}$ increases. We recall that ρ_m and ρ_t are proportional to $\epsilon^{\|}$ and W_D, respectively, according to Eqs. (4.4-2) and (4.4-5). The areal density of threading dislocations in $Ge_{0.3}Si_{0.7}$ layers is therefore proportional to the linear density of misfit dislocations at the interface. This means that threading and misfit dislocations arise together, as is the case if they are different segments of one dislocation.

In that case, the number of misfit dislocations per unit length ρ_m at the interface is proportional to the areal density of threading dislocations ρ_t in the layer,

$$\rho_m = \frac{L}{4}\rho_t, \qquad (4.4-6)$$

where L is the average length of misfit dislocation in the interfacial plane. Combining Eqs. (4.4-6), (4.4-2) and (4.4-5), one obtains

$$L = \frac{4\rho_m}{\rho_t} = \frac{36b^2}{b_m} \cdot \frac{\epsilon^{\|}}{W_D^2} = 4.6 \pm 0.5\mu m$$

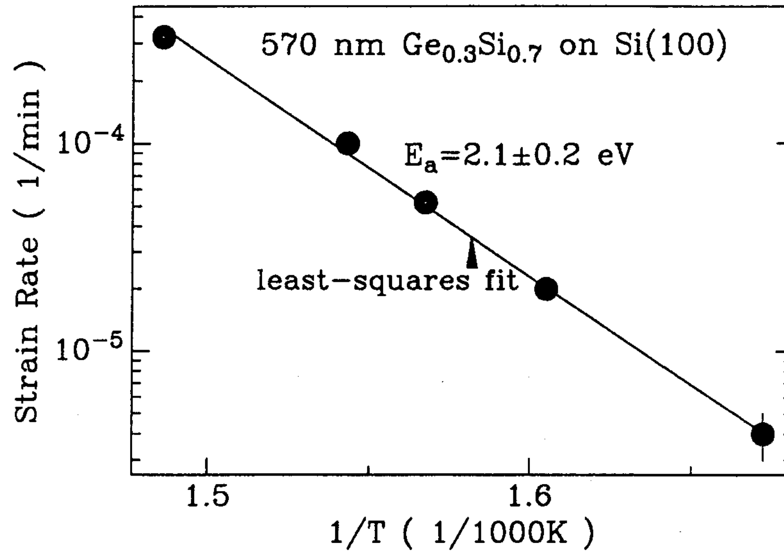

FIG. 4.4-3 Relaxation rate measured by the rate of increasing parallel strain with increasing time at modest relaxation level vs the inverse of the temperature at which the relaxation proceeds (see Fig. 4.4-2). The data follow an Arrhenius behavior with a slope of 2.1 ± 0.2 eV.

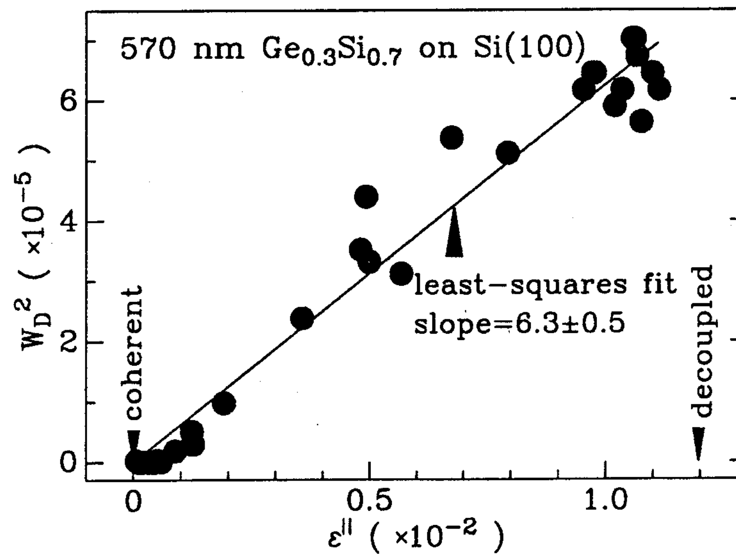

FIG. 4.4-4 X-ray peak broadening of (400) diffraction from 570 nm thick epitaxial $Ge_{0.3}Si_{0.7}$ layers grown at $\sim 300°C$ that is due to imperfections in the layers versus the strain relaxation.

according to Fig. 4.4-4. This value agrees roughly with what Hull et al.[20] obtained from transmission electron microscopy. The well-behaved linear relationship between ρ_t and ρ_m (Fig. 4.4-4) means that the average length of misfit dislocations remains a constant ($\sim$ 4.6 μm) during the strain relaxation. The results suggest that the dislocations are nucleated at the surface and glide down to the interface in slip planes. The strain relaxation at the interface therefore necessarily results in the existence of threading dislocations in the layer. Equation (4.4-6) also shows that increasing the length L of misfit dislocations in the interfacial plane reduces the threading dislocation density ρ_t in the layer for a given strain relaxation level ρ_m.

We also monitored the strain relaxation of pseudomorphic $Ge_{0.3}Si_{0.7}$ layers by MeV ^4He [100] axial channeling spectrometry. As the strain relaxes upon thermal annealing, dechanneling at the interface occurs, confirming that misfit dislocations are generated. At the same time, the minimum yield of the layer for [100] axial channeling increases from $\sim$ 5% for pseudomorphic layers to $\sim$ 12% for relaxed ones. This means that imperfections are also generated within the layer as it relaxes, and supports the previous assertion that relaxation produces threading dislocations.

In summary, the strain in the pseudomorphic $Ge_{0.3}Si_{0.7}$ layers 570 nm thick grown on Si(100) at 300°C relaxes sharply at (375 ± 25)°C, and reaches the thermal equilibrium value after 60 min at 400°C. The rate of strain relaxation and misfit dislocation generation as a function of inverse temperature follows an Arrhenius behavior with an activation energy of 2.1 ± 0.2 eV. As the strain relaxes, the defect density in the layer increases proportionally. This fact suggests that the generation of misfit dislocations necessarily results in the occurrence of threading dislocations.

4.5 Asymmetrical tilt boundary in GeSi/Si(001) heterostructures

In a relaxed heterostructure with a non-zero $\epsilon^{\|}$, there exist misfit dislocations at the hetero-interface to relieve the lattice mismatch between the film and the substrate (Fig. 4.5-1). These interfacial dislocations could also produce a misorientation, ϑ, between the corresponding low index plane of the film and the substrate (Fig. 4.5-1), if the Burger vector of the dislocations has a component along the direction of the surface normal.[31]

To analyze the effect of an interfacial dislocation array, we first summarize the results of simple ones shown in Fig. 4.5-2. The case (I) corresponds to the common misfit dislocation arrays, where the Burger vector is perpendicular to the surface normal. They generate a non-zero parallel strain but a zero misorientation angle. The case (II) is a symmetrical low angle tilt boundary,[31] where the Burger vector is parallel to the surface normal. In case (III), the Burger vector has components

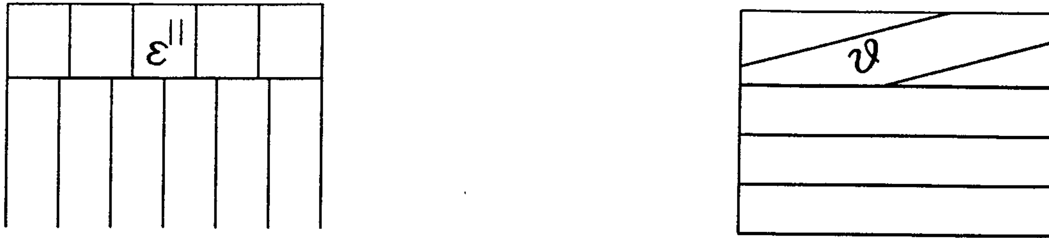

FIG. 4.5-1 Schematic representation of parallel strain and misorientation in a heterostructure.

(I) Misfit Dislocations

$\varepsilon^{||} = b/p, \quad \vartheta = 0$

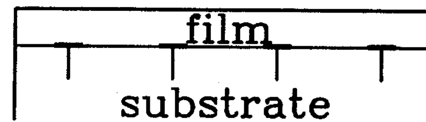

(II) Tilt Boundary

$\varepsilon^{||} = 0, \quad \vartheta = b/p$

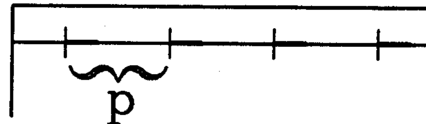

(III) Mixed Dislocations

$\varepsilon^{||} = b^{||}/p, \quad \vartheta = 0$

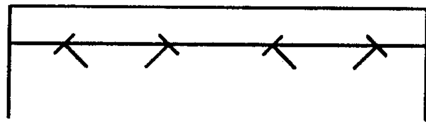

(IV) Mixed Dislocations

$\varepsilon^{||} = b^{||}/p, \quad \vartheta = b^{\perp}/p$

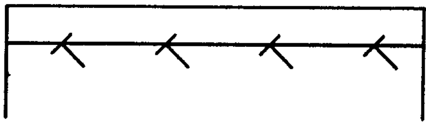

FIG. 4.5-2 Four different types of dislocation arrangements at heterointerfaces: (I) mismatch relieving dislocations; (II) asymmetrical low angle tilt boundary; (III) mixed dislocations with a non-zero parallel strain and a zero misorientation angle; (IV) mixed dislocations with both non-zero net mismatch relieving and tilt components.

both perpendicular and parallel to the surface normal, but the net sum of the Burger vector of the dislocation arrays parallel to the surface normal is zero; the net effect of such dislocation arrays is thus similar to case (I). In case (IV), the dislocation is in fully aligned arrangement; both components of the Burger vector of each dislocation parallel and perpendicular to the surface normal simply add up, producing a non-zero parallel strain and misorientation angle.

In a GeSi/Si(001) structure, the interfacial dislocations consist of square arrays running along $< 110 >$ directions with both 60°-mixed and 90°-edge type characters.[17] The 60°-mixed dislocations can be nucleated at the surface in the $\{111\}$ slip plane and glide down to the interface to relieve the elastic strain.[6,26,28] The 90° edge dislocations relieve the elastic strain most efficiently and move by glide and climb.[17] At low temperature ($\leq 600°C$), the climb motion is very difficult; one therefore expects that the interfacial dislocations are predominantly of 60°-mixed type.[17,26,28] The Burger vector of the 60°-mixed dislocation can be decomposed into screw and edge components (Fig. 4.5-3). The interfacial dislocations of square arrays with a net screw component form a twist boundary,[31] which produces a rotation of the film about the surface normal with respect to the substrate. The edge component resembles the mixed dislocation shown in cases (III) and (IV) of Fig. 4.5-2. It can be further decomposed into the components parallel and perpendicular to the surface normal (see Fig. 4.5-3). The parallel component relieves the elastic strain in the film. The perpendicular component produces a misorientation between the film and the substrate. In this section, we will focus on the misorientation effect by interfacial dislocations.[13]

A set of $Ge_{0.3}Si_{0.7}$ films $\sim$ 570 nm thick were grown on Si(001) at $\sim 300 - 500°C$ by MBE at UCLA. About 30-40 samples were made by various deposition-temperature sequences with varying growth pressure from high 10^{-10} Torr to low 10^{-8} Torr. The critical thickness, stability, and strain relaxation upon thermal processing of such samples have been discussed in a previous section. We investigate here the misorientation between the film and the substrate of such samples (both as-grown and after annealing). To simplify the analysis, we will assume in the following discussion that all the interfacial dislocations are of the 60°-mixed type.

DCD was used to extract the parallel strain $\epsilon^{\|}$ and the misorientation angle ϑ of each sample. The experiemntal results are summarized in Fig. 4.5-4. The thick solid line labeled A in the figure represents the data from the majority of the samples analyzed. Some samples in this set are initially pseudomorphic with $\epsilon^{\|}=0$. Upon thermal annealing in the vacuum, the structures relax and develop a non-zero $\epsilon^{\|}$. The parallel strain increases with more interfacial dislocations being generated to relieve the elastic strain till it reaches the equilibrium value. Other samples in this set are initially

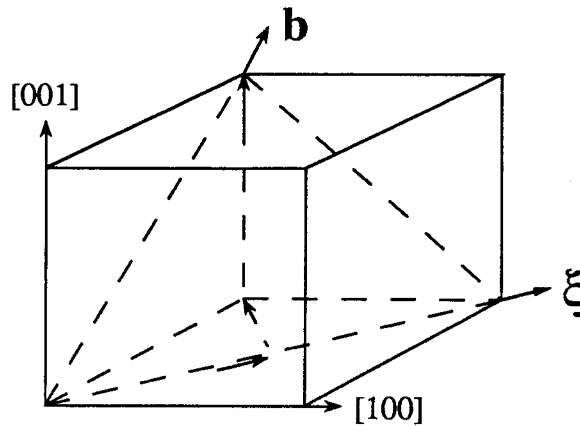

FIG. 4.5-3 Schematic representation of a 60°-mixed dislocation in a GeSi/Si(001) structure.

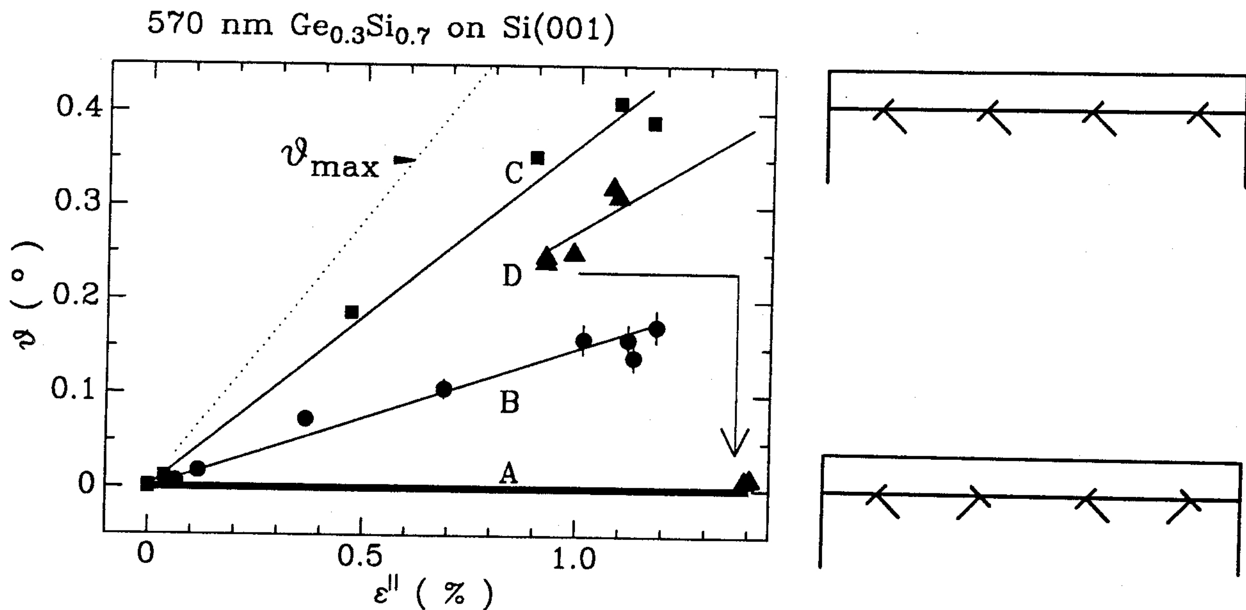

FIG. 4.5-4 Misorientation angle vs parallel strain of ~ 570 nm thick $Ge_{0.3}Si_{0.7}$ films grown on Si(001) substrates at 300-500°C. Most samples (A) analyzed have zero misorientation angles regardless of the value of the parallel strain. Samples B and C are initially pseudomorphic and have zero misorientation angle. They relax upon thermal annealing and develop finite misorientation angles. Sample D is relaxed initially and has a non-zero misorientation angle. It relaxes further upon annealing. After amorphization of the entire film and solid phase epitaxial regrowth, the misorientation becomes zero.

partially relaxed with a non-zero $\epsilon^{\|}$. The common feature of the samples in this set is that there is no misorientation between the film and the substrate. This indicates that the arrangement of the interfacial dislocations in this set of samples corresponds to case (III) of Fig. 4.5-2. The sample B in the figure is initially pseudomorphic with both $\epsilon^{\|}$ and ϑ equal to zero. Upon thermal annealing (300-700°C for 30 min), $\epsilon^{\|}$ increases. At the same time, ϑ increases proportionally. The sample C is similar to the sample B except that the slope is different. The sample D is initially partially relaxed, and has a non-zero $\epsilon^{\|}$ and ϑ. Upon annealing, it relaxes further and the misorientation also increases further, correspondingly. In addition, the as-grown sample D was implanted with 380 keV 10^{15} $^{28}Si/cm^2$ at room temperature and the entire film was completely amorphized.[32] Solid phase epitaxy was then initiated by vacuum annealing at 600 and 700°C for 30 min. The parallel strain of the regrown film equals the value of the equilibrium strain state. The misorientation angle becomes zero. This result clearly shows that the misorientation is caused by the aligned arrangement of the interfacial dislocations, not by the surface morphology of the substrate like that discussed in Ch. 4.3. The misorientation angle of all the samples studied here is smaller than the maximum value expected for an arrangement where all the dislocations are exactly aligned (dotted line in Fig. 4.5-4).

For a given number of interfacial dislocations, N, the parallel strain is the same. The misorientation can vary from zero of case (III) to a maximum of case (IV), depending on the particular arrangement. There is an elastic energy associated with a finite misorientation angle. This suggests that the arrangement giving a zero misorientation angle has minimum energy. This could explain the fact that most samples have a zero misorientation angle. However, it is known that kinetics determines the process of the dislocation generation and strain relaxation. The dislocation generation proceeds by initial nucleation and then multiplication. The orientation of initially nucleated dislocations is equally probable among possible orientations, since these initially nucleated dislocations are far apart so that interaction energy among them is negligible. The further relaxation proceeds by the multiplication of these dislocations. The misorientation angle increases proportionally. The slope of the misorientation angle versus parallel strain is hence determined by the arrangement of very few initially nucleated dislocations. As the initial arrangement is governed by probability, the misorientation angle for any given parallel strain is hence also determined by probability The probabilty for the arrangement of the zero misorientation angle is the highest. Therefore, most samples have a zero misorientation angle. Furthermore, there is finite probability for the arrangement where the misorientation angle is not zero. This explains the misorientation observed for some samples.

References

1. E. Kasper and H.-J. Herzog, Thin Solid Films 44, 357 (1977).
2. J.C. Bean, L.C. Feldman, A.T. Fiory, S. Nakahara, and I.K. Robinson, J. Vac. Sci. Technol. A2, 436 (1984).
3. J.W. Matthews and A.E. Blakeslee, J. Cryst. Growth 27, 118 (1974).
4. B.W. Dodson and J.Y. Tsao, Appl. Phys. Lett. 51, 1325 (1987).
5. R.J. Hauenstein, R.H. Miles, E.T. Croke, and T.C. McGill, Thin Solid Films 183, 79 (1989).
6. G. Bai, M-A. Nicolet, C.H. Chern, and K.L. Wang, unpublished.
7. C.G. Van de Walle and R.M. Martin, J. Vac. Sci. Technol. B3, 1256 (1985).
8. D.V. Lang, R. People, J.C. Bean, and A.M. Sergent, Appl. Phys. Lett. 47, 1333 (1985).
9. See, e.g., R. People, IEEE QE-22, 1696 (1986).
10. G.L. Patton, J.H. Comfort, B.S. Meyerson, E.F. Crabbé, G.J. Scilla, E.D. Frésart, J.M.C. Stork, J.Y.-C. Sun, D.L. Harame, J.N. Burghartz, IEEE Electron Device Lett. 4, 171 (1990).
11. G. Bai and M-A. Nicolet, unpublished.
12. G. Bai, M-A. Nicolet, C.H. Chern, and K.L. Wang, unpublished.
13. G. Bai, M-A. Nicolet, C.H. Chern, and K.L. Wang, unpublished.
14. W.A. Brantley, J. Appl. Phys. 44, 534 (1973).
15. I.J. Fritz, Appl. Phys. Lett. 51, 1080 (1987).
16. D.C. Houghton, C.J. Gibbings, C.G. Tuppen, M.H. Lyons, and M.A.G. Halliwell, Appl. Phys. Lett. 56, 460 (1990).
17. R. Hull and J.C. Bean, J. Vac. Sci. Technol. A7, 2580 (1989).
18. L.C. Feldman, J.W. Mayer, S.T. Picraux, *Materials Analysis by Ion Channeling*, Academic, New York, 1982.
19. V.S. Speriosu and T. Vreeland, Jr., J. Appl. Phys. 56, 1591 (1984).
20. R. Hull, J.C. Bean, D.J. Werder, and R.E. Leibenguth, Phys. Rev. B40, 1681 (1989).
21. R. Hull, J.C. Bean, and C. Buescher, J. Appl. Phys. 66, 5837 (1989).
22. P.Y. Timbrell, J.-M. Baribeau, D.J. Lockwood, and J.P. McCaffrey, J. Appl. Phys. 67, 6292 (1990).
23. C.G. Tuppen and C.J. Gibbings, J. Appl. Phys. 68, 1526 (1990).
24. D.C. Houghton, Appl. Phys. Lett. 57, 2124 (1990).
25. C.J. Gibbings, C.G. Tuppen, and M. Hockly, Appl. Phys. Lett. 54, 148 (1989).

26. D.J. Eaglesham, E.P. Kvam, D.M. Maher, C.J. Humphreys, and J.C. Bean, Philos. Mag. A59, 1059 (1989).

27. W. Hagen and H. Strunk. Appl. Phys. 17, 85 (1978).

28. K. Rajan and M. Denhoff, J. Appl. Phys. 62, 1710 (1987).

29. H. Alexander and P. Hassen, Solid State Phys. 22, 27 (1968).

30. B.W. Dodson and J.Y. Tsao, Appl. Phys. Lett. 53, 2498 (1988).

31. D. Hull and D.J. Bacon, *Introduction to Dislocations*, 3rd Edition, Pergamon, Oxford, 1984.

32. G. Bai and M-A. Nicolet, unpublished.

Chapter 5 Porous Si and Its Properties

5.1 Introduction

Porous Si technology has potential applications in dielectric isolation of integrated circuits,[1] and in epitaxial growth of heterostructures on Si substrates.[2] Recent work has demonstrated efficient visible light emission from porous Si pumped with a green light,[3] which could open the door to Si-based optoelectronics. Since the formation of porous Si by anodic dissolution of single crystalline Si in a concentrated HF solution was first reported by Uhlir[4] and Turner,[5] various properties of porous Si have been extensively studied.

Porous Si has a very large surface area (surface here means the physical boundary between solid and external ambient) and a complex surface morphology. One therefore anticipates that many properties of porous Si are dominated by surface effects. The morphology and the microstrcuture, such as porosity, specific surface area, and pore size, have been carefully characterized by gas adsorption isotherms[6] and transmission electron microscopy.[7] X-ray diffraction was used to characterize the strain and the elastic properties of porous Si.[8,9] Barla et al.[8] reported that as-prepared porous Si has a larger lattice constant than that of bulk Si substrate in the direction normal to the surface , and is less stiff. Young et al.[9] attributed the lattice expansion to the formation of the native oxide layer on the pore surface. Thermal annealing behavior of porous Si has also been investigated.[10–12] The composition of porous Si was measured by ion beam analysis, Auger electron spectroscopy, and x-ray photoelectron spectroscopy.[13,14] High concentration of light impurity atoms of H, O, C, F were detected (up to a few tens %).[13,14]

The study described in the following sections was undetaken to further clarify the nature of strain in porous Si and to explain the experimental findings on the influences of temperature and ambient gases on the strain in porous Si.[15,16] What resulted from this investigation is a model for porous Si, where the large internal surface is the primary feature of this material.[15] We will discuss briefly heteroepitaxial films of $CoSi_2$ (Ref. 2) and GeSi alloy[17] grown on porous Si substrates and the effects of such capping layers on the strain change in porous Si.[16]

5.2 Strain and stress in porous Si(100)

In this section, we study the strain in porous Si formed by anodization of Si(100) wafers, and the change of that strain in various environments.[15,16]

A. Formation of Porous Si Layers

Single crystalline p^+-Si(100) wafers of 2-in diameter with a resistivity of ~ 0.01 Ωcm were used for the formation of porous Si layers. Si wafers were first cleaned by repeatedly etching in boiling nitric acid and dipping in HF solution. Porous Si layers of $\sim 2\mu m$ were then formed by anodization of the p^+-Si wafers in a 30% HF electrolyte. The porosity of the porous Si layers thus formed is about 30%. After the formation of porous Si, the samples were kept at room temperature in air.

B. Experimental Results

Double crystal x-ray diffractometry was used to measure the strain of porous Si (the relative difference between the lattice constants of the layer and the substrate). The perpendicular strain, $\epsilon^{\perp}$, was extracted from the x-ray rocking curves diffracted from (400) planes. The parallel strain, $\epsilon^{\parallel}$, was extracted from (311) asymmetrical diffraction planes. The strain measured several days after the porous Si was made is $\epsilon^{\perp} \approx 0.1\%$ and $\epsilon^{\parallel} < 0.01\%$. When porous Si is kept at room temperature in air, the perpendicular strain $\epsilon^{\perp}$ increases from $\sim 0.1\%$ to $\sim 0.3\%$ in ~ 18 months, and the parallel strain $\epsilon^{\parallel}$ remains zero. Since it is unlikely that the microstructure of porous Si changes at room temperature, the increase of strain must be caused by other sources, such as absorption of gas from air.

Figure 5.2-1(a) shows the 2 MeV ^{4}He backscattering and [100] axial channeling spectra of as-prepared porous Si and bulk Si. The backscattering yield from Si atoms in porous Si is $\sim 25\%$ smaller than that from bulk Si. This indicates that porous Si contains a high concentration of light impurities. The backscattering yield rises by $\sim 10\%$ at ~ 0.7 MeV in Fig. 5.2-1(a). This can be attributed to the backscattering from O atoms in porous Si. The ratio of the yields from Si to that from O gives a relative concentration of Si to O of about 1:0.3. The minimum yield of porous Si ($\sim 30\%$) is much larger than that of bulk crystalline Si ($\sim 3\%$), and increases rapidly as the aligned beam penetrates into the porous Si. This means that porous Si contains a high concentration of dechanneling scattering centers. However, x-ray rocking curves indicate that the Si lattices in porous Si layers are highly ordered. The large minimum yield may therefore be caused by the surface dechanneling of an aligned incident beam, since porous Si has a very large specific surface area (~ 200 m^2/cm^3; see, e.g., Ref. 6). Furthermore, the spectra of the samples kept in air

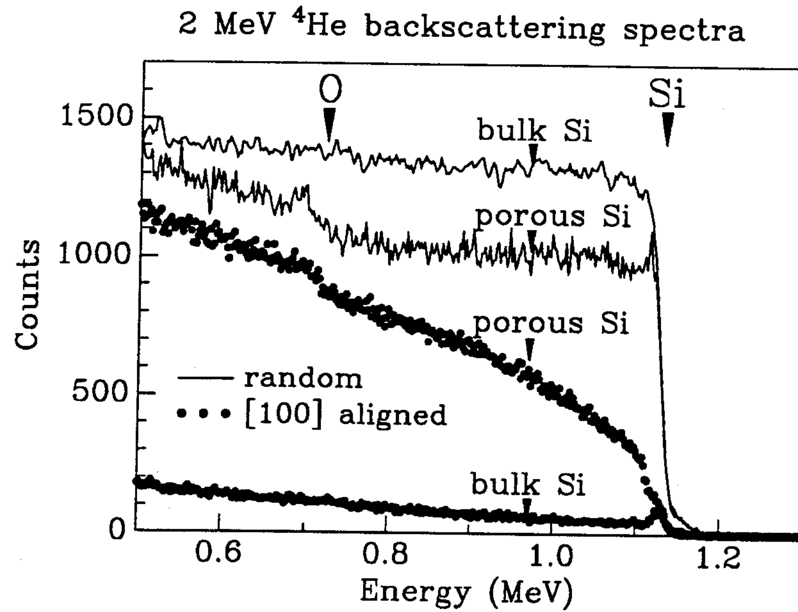

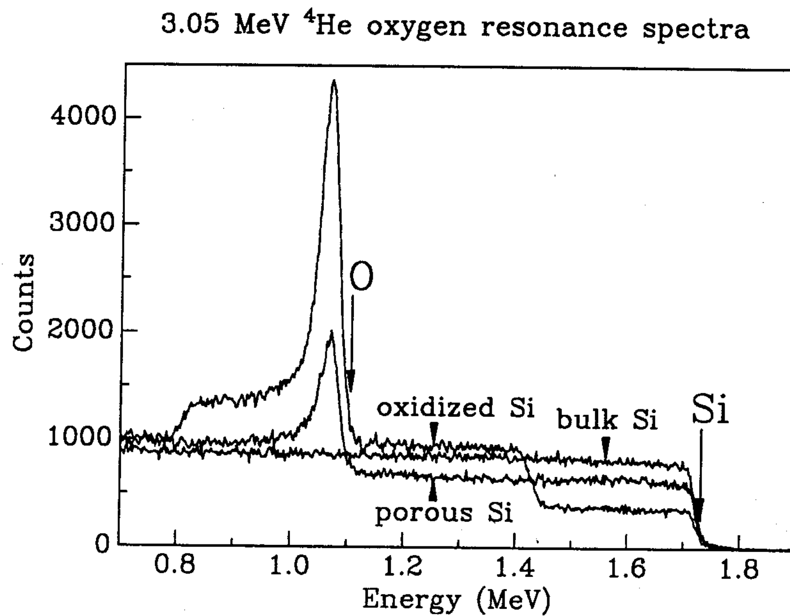

FIG. 5.2-1 Backscattering spectra of porous Si and bulk Si: (a) a 2 MeV ^{4}He beam incident along a near-normal random direction (solid lines) and along the [100]-aligned direction (dotted lines); (b) 3.05 MeV oxygen resonance of a bulk Si, of a porous Si after storage of 18 months in air at 23°C, and of a thermally oxidized Si wafer ($\sim 1\ \mu m$ SiO_2/Si).

at room temperature for $\sim$ 18 months are the same as those shown in Fig. 5.2-1(a) for the as-prepared one. This implies that the overall structure of porous Si changes little upon storage in air at room temperature.

We also used the 3.05 MeV $^{16}O(\alpha,\alpha)^{16}O$ resonance backscattering[18] to measure the oxygen concentration in porous Si samples that had been kept at room temperature in air for $\sim$ 18 months (Fig. 5.2-1(b)). By comparing the oxygen resonance peaks from porous Si and from thermally grown SiO_2, we estimat the oxygen concentration of porous Si to be Si:O $\approx$1:0.3, the same as the value obtained before. By tuning the incident ^4He ion energy so that the resonance scattering occurs at a different depth, an oxygen depth profile was obtained. The oxygen composition is roughly the same throughout the porous Si layer, indicating that there exists a substantial fraction of oxidized Si over the entire porous Si layer. The oxygen fraction of $\sim$ 23 *at.*% is consistent with the assumption that the pores of the porous Si with a specific surface area of $\sim$ 200 m^2/cm^3 and a porosity of $\sim$ 30% are covered by a native oxide layer of $\sim$ 1 nm thick.

Auger electron spectroscopy (AES) equipped with Ar^+ ion sputtering was used for measuring the elemental depth profile of porous Si. The detection limit of AES is typically $\sim$ 0.1% of volume concentration and the depth resolution is about $1nm$. The detailed shape of the $Si_{L_{2,3}VV}$ Auger line was recorded to monitor the chemical state of Si in the porous layer. Figure 5.2-2 shows the AES depth profiles for porous Si stored at room temperature in air for $\sim$ 18 months. The oxygen concentration is nearly constant throughout the porous layer and equals about 22 to 25 *at.*%, calculated from the empirical equation[19]

$$C_O = \frac{I_O/S_O}{I_O/S_O + I_{Si}/S_{Si}}.$$

S_O and S_{Si} are the inverse Auger sensitivity factors of oxygen and silicon, respectively, determined from the ratio of the peak-to-peak height of the O_{KLL} and the Si_{LVV} signal from a standard SiO_2 sample. I_O and I_{Si} are the peak-to-peak amplitude of the oxygen and silicon Auger spectrum in the derivative mode. The oxygen concentration obtained from the Auger spectrum agrees well with that obtained from $^{16}O(\alpha,\alpha)^{16}O$ resonance. The detailed line shape of the $Si_{L_{2,3}VV}$ derivative Auger spectrum shows that the bonding state of the Si orbitals in the porous layer is mainly mixed sp^3 and Si-O instead of pure Si-O bonding. This is consistent with the idea that only the specific surface of the pores are covered with a native oxide.

To better understand the possible causes for the observed strain change in the porous Si layer, we conducted a set of experiments to monitor the influence on the strain of external variables such as temperature and ambient gas.

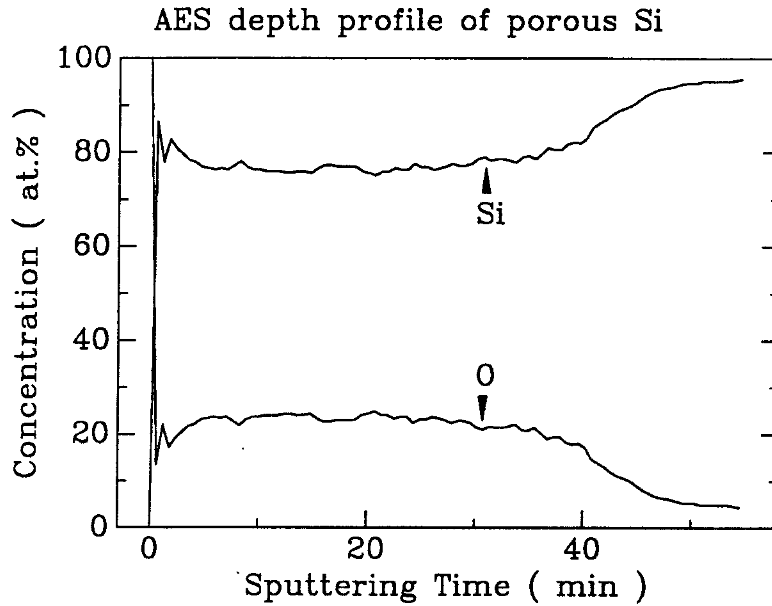

FIG. 5.2-2 Auger electron spectroscopy depth profile of oxygen and silicon in porous Si of the sample that had been stored in air at room temperature for ~ 18 months after the formation of porous Si.

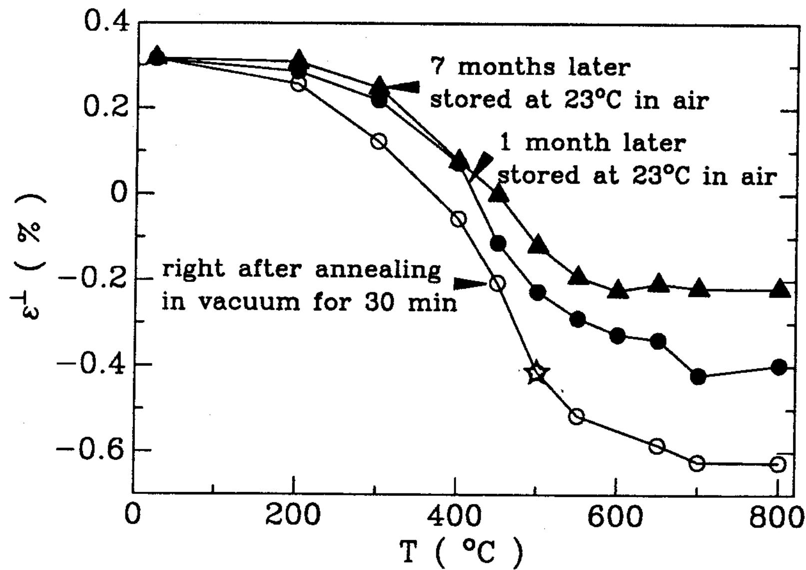

FIG. 5.2-3 Perpendicular strain $\epsilon^{\perp}$ of porous Si aged for 18 months in air at 23°C and then annealed in vacuum for 30 min, measured immediately after annealing (○), after storage in air at room temperature for about 1 month (●) and 7 months (filled triangle).

Samples that had been stored for $\sim$ 18 months in air were annealed in vacuum ($\sim 5 \times 10^{-7}$ torr) between 200°C and 800°C for 30 min. X-ray rocking curves were taken at room temperature in air immediately after the annealing was completed. The measured perpendicular strain $\epsilon^{\perp}$ decreases monotonically from $\sim$ 0.3% with increasing annealing temperature (o in Fig. 5.2-3) and saturates at $\sim -0.6\%$ above 600°C. The measured parallel strain $\epsilon^{\parallel}$ remains zero in all cases. These results suggest that the decrease of strain is caused by desorption of gas from porous Si during vacuum annealing.

To reveal kinetics and energetics of gas desorption from porous Si, we monitored the decreases of $\epsilon^{\perp}$ as a function of annealing duration in vacuum at 300°C, 400°C and 600°C (Fig. 5.2-4(a)). The time dependence of $\epsilon^{\perp}$ is characteristic to thermally activated desorption.[20] The strain decreases exponentially with a time constant, τ, which decreases with increasing annealing temperature from about $\sim$ 9 min at 300°C to $\sim$ 4 min at 600°C. Figure 5.2-4(b) is an Arrhenius plot of τ as a function of inverse temperature, $1/T$. The slope yields the activation energy, $E_d \approx 0.1$ eV, of desorption of molecules from porous Si. It is about the same as the typical binding energy of physisorbed molecules on solid surfaces.[21] This fact convincingly shows that the decrease of strain upon thermal annealing is caused by the desorption of physisorbed molecules from porous Si.

When the annealed porous Si samples are stored at room temperature in air, the perpendicular strain increases again. Figure 5.2-3 also shows the perpendicular strain of the annealed porous Si after storage at room temperature for $\sim$ 1 month (•) and for $\sim$ 7 months (filled triangle). These facts suggest that the increase of strain in the porous Si stored in ambient air is caused by the adsorption of impurity atoms (molecules) from air.

To identify the molecular species that alter the strain, we annealed samples at 400°C in vacuum for 30 min and then kept them in different ambient gases (vacuum, forming gas, O_2, air, moisture) at room temperature. The perpendicular strain $\epsilon^{\perp}$ increases with time approximately as a complementary exponential (Fig. 5.2-5). Little change of strain was detected for the sample kept in vacuum. The observed change is attributable to air exposure during the measurements. The strain changed most for the sample kept in moisture (water-saturated air). This shows that the observed increase of strain at room temperature is caused mainly by the absorption of water molecules.

The non-resonant backscattering and channeling spectra for all of the samples discussed above are indistinguishable within experimental uncertainty. This indicates that thermal annealing up to 800°C in vacuum does not cause significant structural or compositional change in porous Si. The sensitive 3.05 MeV oxygen resonance backscattering confirms that the oxygen concentration

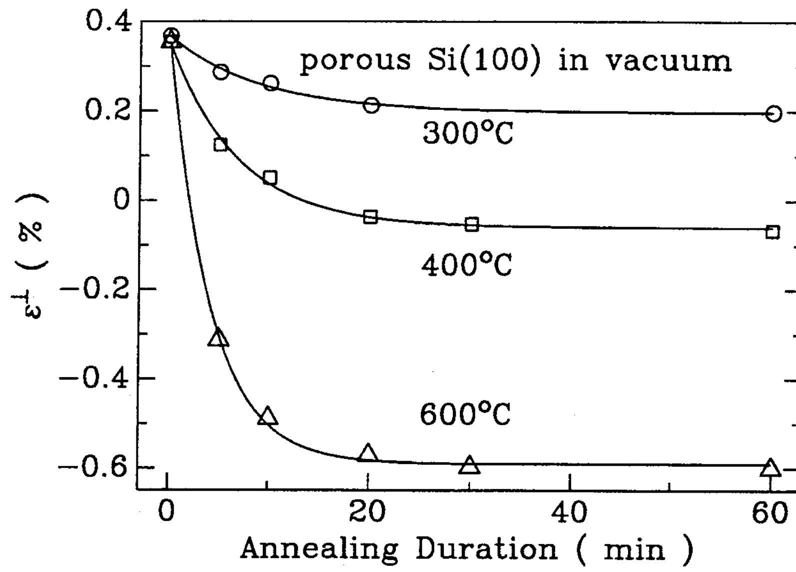

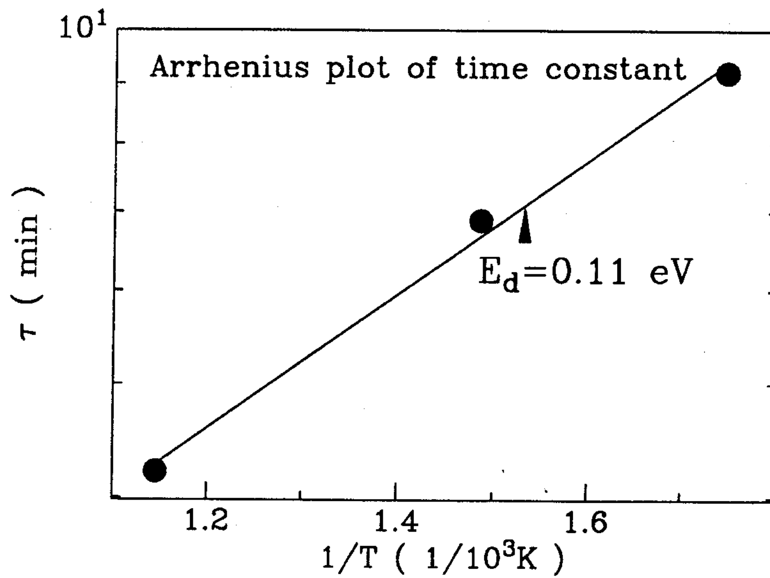

FIG. 5.2-4 Decreasing rate of perpendicular strain in porous Si upon vacuum annealing: (a) $\epsilon^{\perp}$ versus annealing duration at 300, 400, and 600°C; (b) Arrhenius plot of the time constant τ of the decrease of the perpendicular strain.

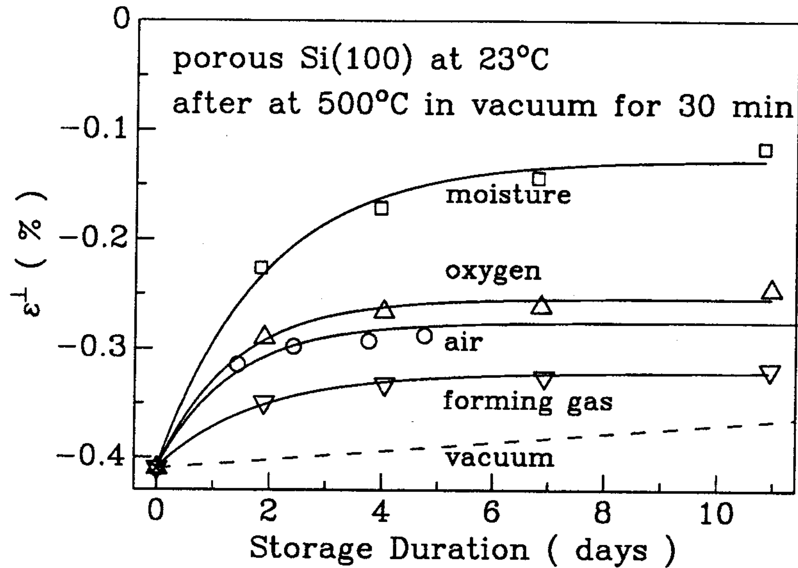

FIG. 5.2-5 Time evolution of the perpendicular strain $\epsilon^{\perp}$ of the porous Si stored at room temperature in different ambient gases after being annealed in vacuum at 500°C for 30 min (see the point marked by star in Fig. 5.2-3).

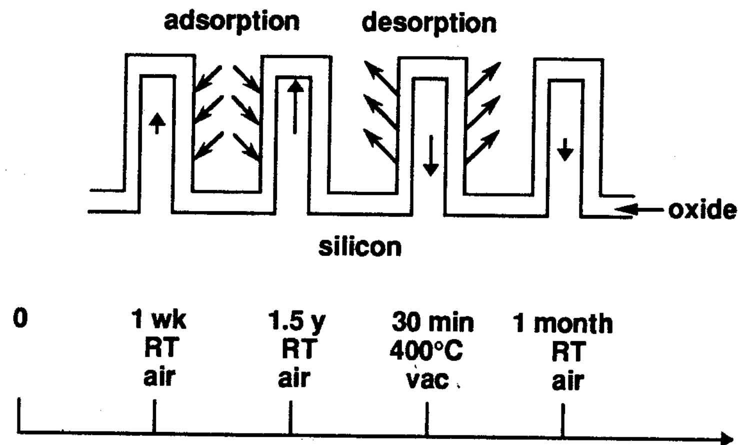

FIG. 5.2-6 Schematic representation of porous Si and of the evolution of the perpendicular strain as a function of the sample history given on the abscissa. The upwards (downwards) arrows in the silicon rods indicate the positive (negative) perpendicular strain; their length suggests the magnitude of the strain. The perpendicular strain evolves as a result of absorption by and their desorption from the native oxide.

decreases by only a small fraction ($<\sim 10\%$) of its original value after thermal annealing in vacuum. The native oxide thus remains present in porous Si after annealing in vacuum up to 800°C.

C. Discussion

The increase of strain in porous Si at room temperature in ambient air has been discussed by Young et al.[9] who observed that the strain of porous Si increases at room temperature when stored in ambient air for a few weeks after the formation of the porous Si. They attribute the increase to slow thickening of the native oxide layer. This model is inconsistent with our observations where we also find the increase of strain of the porous Si stored in air at room temperature, but the oxygen content in the porous Si remains constant.

Decreases of strain in porous Si upon thermal annealing have been discussed by others.[11,12] Labunov et al.[11] observed that the perpendicular strain of porous Si layer decreases from $\sim 4 \times 10^{-4}$ to $\sim -1 \times 10^{-4}$ upon thermal annealing in H_2 at $\sim$ 1000°C and they attributed it to the collapse of porous structure to form closed cavities. The change we observe upon annealing in vacuum is about 20 times greater ($\sim -1\%$ vs $\sim -0.05\%$), and occurs at lower temperature (600°C vs 1000°C) where the porous Si structure is known not to change significantly.[10] It is therefore clear that the decrease of strain at low temperature (e.g., $<$ 800°C) is not related to the overall structural change of porous Si. Sugiyama and Nittono[12] also found that the perpendicular strain decreases from $\sim 4 \times 10^{-4}$ to $\sim -2 \times 10^{-3}$ upon annealing at $\sim$ 450°C in vacuum. At the same time, H_2 concentration also decreases. These authors therefore proposed that the decrease of strain is related to the formation of a clean pore surface by desorption of chemisorped H_2 at an elevated temperature. This interpretation is inconsistent with our experimental findings where we observe a similar decrease of strain, but the oxide layer covering the pore surface remains. To better clarify the influence of H_2 on strain in a porous Si layer, we annealed a sample at 400°C for 30 minutes in pressurized H_2 ($\sim$ 45 psi) gas. The strain decreases, as it does in vacuum. For comparison, we also heated a sample at 400°C for 30 minutes in air. The strain increases by a small amount. These results clearly demonstrate that H_2 is not the major cause for the change of strain.

D. Model

On the basis of the above experimental results, we propose the following model for the strain in porous Si (see Fig. 5.2-6 for illustration). In simplified terms, a porous Si layer may be modeled as consisting of many long Si rods of a small average diameter d ($\sim$ 10 nm), standing on the bulk Si substrate. The surface tension between the rods and the ambient gas, γ, tends to reduce the surface

area by decreasing the size of the Si rods. An equilibrium state is reached when the surface tension is balanced by the volume strain such that the total energy of surface and volume is minimized. The resultant compressive strain is $\sim -\gamma/\mu d$ (μ is elastic modulus). It has a value of $\sim -10^{-3}$, using typical values of $\gamma \sim 10^3$ erg/cm^2 and $\mu \sim 10^{12}$ dyn/cm^2. On the other hand, the formation of a native oxide of thickness d_{ox} ($\sim$ 1 nm) on the pore surface produces a compressive stress of σ_{ox} ($\sim -10^{10}$ dyn/cm^2) in the oxide layer.[22] This gives rise to a tensile stress of $\sigma \sim -\sigma_{ox} d_{ox}/d \sim 10^9$ dyn/cm^2 in the Si rods, inducing a tensile strain of $\sim \sigma/\mu \sim 10^{-3}$. The compressive strain from surface tension and the tensile strain from oxidation compensate each other. The constraint imposed by the substrate on the porous Si layer confines the parallel strain in the layer to be zero. The perpendicular strain thus estimated is consistent with the measured values of $\sim 10^{-4}$–10^{-3} (see also data in Refs 8,9,11,12). If the sample is kept in air, the oxide layer in porous Si will absorb gas molecules such as H_2O from air. This causes its volume to expand,[23] inducing a tensile strain in the Si rods. When the sample is heated in vacuum, the absorbed gas molecules such as H_2O will escape from the oxide layer. This causes volume contraction in the native oxide, inducing a compressive strain in the Si rods. This model qualitatively explains observations made here and in the literature. A quantitative estimation is, however, obscured by the complexity of the microstructure of porous Si and of the native oxide.

E. Summary

The perpendicular strain in the as-formed porous Si layer is $\sim 10^{-3}$. The parallel strain is not measurable ($< 10^{-4}$). Upon annealing in vacuum at an elevated temperature, the perpendicular strain decreases, while the parallel strain remains zero. The perpendicular strain of the annealed sample increases with time at room temperature by amounts that depend on the ambient gas (vacuum, forming gas, O_2, air, moisture). The pores in the porous Si are covered by a native oxide layer. The observed changes of strain in porous Si layers are caused mainly by modification of stress in the oxide layer that is due to desorption and absorption of gas. The measured strain in porous Si is the net result of stress induced by surface tension, oxide formation, and exchange of gas between the oxide and the ambient gas.

5.3 Epitaxial films of GeSi and $CoSi_2$ on porous Si

Luryi and Suhir[24] studied the elastic system of a heteroepitaxial film grown on a patterned substrate of small seed pads with a lateral dimension, l (Fig. 5.3-1). They showed that for a given lattice mismatch between the film and the substrate, f, the entire elastic stress in the film can be accommodated without dislocations when the lateral dimension l is sufficiently small, $l \leq l_{min}(f)$. For example, in the case of a Ge film on Si ($f = 4\%$), l_{min} is $\sim 10\ nm$.[24] Porous Si provides a possible candidate for such a substrate.

A. Properties of films grown on porous Si

We have analyzed epitaxial GeSi alloy and $CoSi_2$ films grown on porous Si substrates by MBE at UCLA,[2,17] and have compared the properties of these films with those grown on regular Si substrates.

GeSi on porous Si(100)

Epitaxial GeSi alloy films 8 to 200 nm thick with Ge compositions of 20%, 50%, and 100% grown on both porous and regular Si(100) substrates were characterized by backscattering spectrometry (BS), x-ray double crystal diffractometry (DCD), and transmission electron microscopy (TEM).[17] Channeling spectra of films on porous and regular substrates are the same, meaning that the films on porous Si are also highly epitaxial. The strain in the films on porous and regular substrates is also the same, meaning that there is no reduction of misfit dislocations in the film on porous Si, in contrast to what one would expect. However, the x-ray diffraction peak from the film on the porous substrate is broader than that from the corresponding film on the regular one, suggesting that the strain distribution in a film grown on a porous substrate is very inhomogeneous. Plane view TEM confirmed that the average dislocation spacing in films on porous and regular Si is the same, and that the strain in films on porous Si is inhomogeneous.[17,25]

The apparent discrepancy between Luryi and Suhir's model and the experimental observations may be due to the fact that seed pads in the model are isolated while the rods in porous Si are interconnected (Fig. 5.3-2)[25]

$CoSi_2$ on porous Si(111)

Epitaxial $CoSi_2$ films of various thickness grown on regular and porous Si(111) substrates were also analyzed by BS, DCD, and TEM.[2] The same results as those discussed previously for GeSi films were obtained. The room temperature strain in a $CoSi_2$ film on porous Si is again caused by the difference of thermal expansion coefficient between the film and the substrate (see also Ch. 2.5 and 2.6).

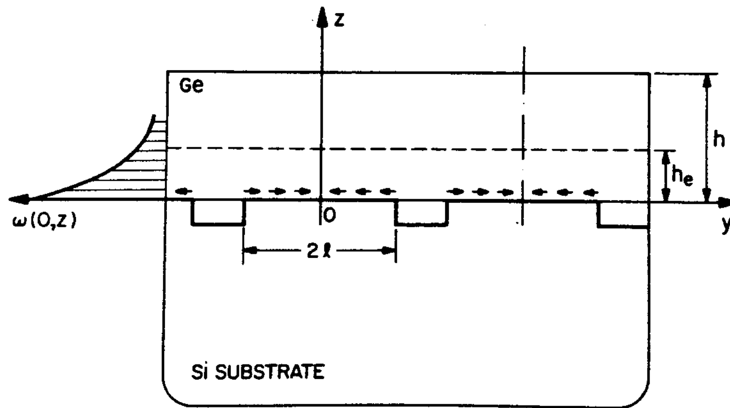

FIG. 5.3-1 Illustration of a heteroepitaxial Ge film on a Si substrate of seed pads with lateral dimension l. The strain energy profile, $\omega(0, z)$, for the pad mid-cross section is shown on the left (from Ref. 24).

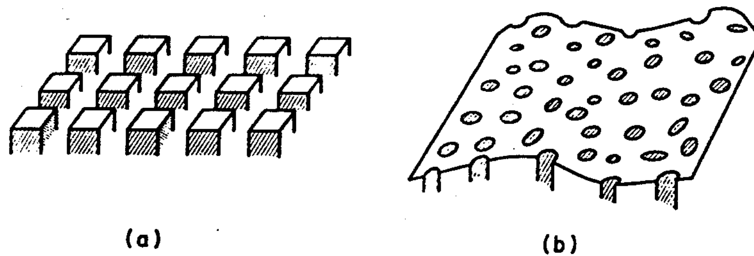

FIG. 5.3-2 Schematic drawings of (a) a patterned substrate as used in Luryi and Suhir's model (Fig. 5.3-1), and (b) a porous Si substrate (from Ref. 26).

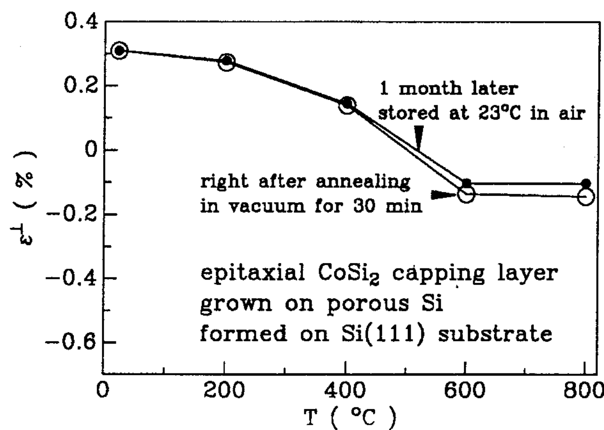

Fig. 5.3-3 Perpendicular strain $\epsilon^{\perp}$ of $CoSi_2$-capped porous Si(111) aged for 18 months in air and then annealed in vacuum for 30 min, measured immediately after annealing (∘), and after storage in air at room temperature for 1 month (•). The figure has identical scales as those of Fig. 5.2-3 for comparison.

In summary, we conclude that heteroepitaxial growths on porous Si are similar to those on regular Si.

B. Properties of porous Si with caps

To confirm our model[15] that the exchange of gaseous species between porous Si and the ambient gas causes the observed strain changes (see Ch. 5.2), we analyzed the strain change in porous Si with caps.[16]

GeSi cap/porous Si/Si(100)

The perpendicular strain of porous Si(100) immediately after the GeSi films were grown by MBE is $\sim -0.1\%$. This decrease of strain from that of the as-grown porous Si ($\sim 0.1\%$, see Chp. 5.2) was caused by desorption of impurity atoms from porous Si when the sample was heated to $\sim 600°C$ in the MBE system prior to film growth. The perpendicular strain does not change at room temperature in ambient air in ~ 18 months, regardless of the different Ge composition and cap thickness. Furthermore, the perpendicular strain remains unchanged upon thermal annealing at 600°C for 30 min in vacuum. These facts show that epitaxial GeSi films are perfect seals that prevent any exchange of molecules between the porous Si and the ambient gas. The result verifies that the change of strain in uncapped porous Si is caused by gas desorption and adsorption.

$CoSi_2$ cap/porous Si/Si(111)

The perpendicular strain of the porous Si(111) increases from $\sim 0.2\%$ to $\sim 0.3\%$ at room temperature in ambient air in ~ 18 months. We attribute this change to the presence of pinholes in $CoSi_2$ films (pinhole density $\sim 10^8/cm^2$, Ref. 2). The perpendicular strain of the porous Si(111) with a different cap thickness is the same within experimental uncertainty. Upon thermal annealing in vacuum, the perpendicular strain decreases monotonically with increasing temperature and saturates at $\sim 600°C$ (○ in Fig. 5.3-3). When stored in air at room temperature, the perpendicular strain of the annealed porous Si increases a little in 1 month (• in Fig. 5.3-3). These results show that the epitaxial $CoSi_2$ caps do not fully prevent the exchange of gas molecules between the porous Si and the ambient gas. The result also suggests that one could measure the strain change of capped porous Si to probe for the presence of pinholes in the capping layer.

References

1. K. Imai and H. Unno, IEEE Transactions on Electron Devices, ED-31, 297 (1984).
2. See, e.g., Y. C. Kao, K. L. Wang, B.J. Wu, T.L. Lin, C.W. Nieh, D. Jamieson and G. Bai, Appl. Phys. Lett. 51, 1809 (1987).
3. L.T. Canham, Appl. Phys. Lett. 57, 1046 (1990).
4. A. Uhlir, Bell. Syst. Tech. J. 35, 333 (1956).
5. D. R. Turner, J. Electrochem. Soc. 105, 402 (1958).
6. R. Herino, G. Bomchil, K. Barla, C. Bertrand and J. L. Ginoux, J. Electrochem. Soc. 134, 1994 (1987).
7. M.I.J. Beale, N.G. Chew, M.J. Uren, A.G. Cullis, and J.D. Benjamin, Appl. Phys. Lett., 46, 86 (1985).
8. K. Barla, R. Herino, G. Bomchil, J. C. Pfister and A. Freund, J. Cryst. Growth, 68, 727 (1984).
9. I. M. Young, M. I. J. Beale and J. D. Benjamin, Appl. Phys. Lett. 46, 1133 (1985).
10. R. Herino, A. Perio, K. Barla and G. Bomchil, Mater. Lett., 2, 519 (1984).
11. V. Labunov, V. Bondarenko, L. Gurenko, A. Dorofeev and L. Tabulina, Thin Solid Films, 137, 123 (1986).
12. H. Sugiyama and O. Nittono, Jpn. J. Appl. Phys. 28, L2013 (1989).
13. L.G. Earwaker, J.P.G. Farr, P.E. Grzeszczyk, I. Sturland and J.M. Keen, Nucl. Instr. and Meth., B9, 317 (1985).
14. R.W. Hardeman, M.I.J. Beale, D.B. Gasson, J.M. Keen, C. Pickering and D.J. Robbins, Surface Sci., 152, 1051 (1985).
15. G. Bai, Kun Ho Kim and M-A. Nicolet, Appl. Phys. Lett. 57, (1990).
16. K.H. Kim, G. Bai, and M-A. Nicolet, J. Appl. Phys. 69, 2201 (1991).
17. C.H. Chern, Y.C. Kao, C.W. Nieh, G. Bai, K.L. Wang, and M-A. Nicolet, in *2nd Int. Symp. on Si-MBE*, (Honolulu, Hawaii, 1987).
18. W. K. Chu, J. W. Mayer and M-A. Nicolet, *Backscattering Spectrometry* (Academic Press, New York, 1978), p. 210.
19. C. C. Chang, *Characterization of Solid Surfaces*, Plenum, New York, 1974.
20. A. V. Kiselov, *Surface Chemistry of Oxides*, Discussions of the Faraday Society, No. **52** (Faraday Society, London, 1971), p. 14.
21. H. J. Krenzer and Z. W. Gortel, *Physisorption Kinetics* (Springer Verlag, Berlin, 1985), p. 8.
22. E.P. EerNisse, Appl. Phys. Lett. 35, 8 (1979).

23. I. Blech and U. Cohen, J. Appl. Phys. 53, 4202(1982).

24. S. Luryi and E. Suhir, Appl. Phys. Lett. 49, 140 (1986).

25. Y.H. Xie and J.C. Bean, J. Vac. Sci. Technol. B8, 227 (1990).

Part II

Ion Implantation in Si and Heterostructures

Chapter 6 Ion-Solid Interaction

When an energetic ion penetrates into a solid, it transfers energy to the target atoms, slows down and finally stops inside the solid. This transient process takes place in $\sim 10^{-11} - 10^{-13}$s. The energy loss can be seperated into two parts, electronic and nuclear stopping. On the basis of the pioneer works by Bohr, Bethe and Bloch, Fermi and Teller, and others on the interaction between incident ions and target atoms, Lindhard, Scharff, and Schiott (LSS theory) developed a unified approach to calculate the stopping of low energy (10 keV-1 MeV) ions and their range in solids.[1] The theoretical prediction agrees excellently with experimental results (within $\sim$ 5%). A target nucleus that acquires energy exceeding the displacement threshold energy ($\sim$ 15 eV) leaves its lattice site, and generates secondary collision. A collision cascade is thus formed in a solid. One effect of the cascade is sputtering—removal of target atoms from the surface of a solid.[2] The cascade also generates defects in the solid, such as interstitials and vacancies. Kinchin and Pease[3] developed a simple model to estimate the amount of such Frenkel pairs. However, the model applies only to the case of light (low atomic number) ion implantation at low temperature where individual defects are well seperated and are not mobile. In the case of heavy (high atomic number) ion implantation, high energy density is deposited around the track of incident ions, and a spike may form.[4] Winterbon, Sigmund, and Sanders (WSS theory),[5] established a model to calculate the cascade energy density. Dense cascade (or spike) causes enhanced production of defects compared to that predicted by the Kinchin-Pease model.[6] Recently, Cheng et al.[7] applied the fractal concepts to the collision cascade and proposed "space filling" as a criterion of thermal spike formation. In the case of ion implantation at an elevated temperature, individual defects are mobile, and damage production becomes a dynamic process where defects interact, cluster, and recombine. This process results in complex defect structures. In both cases, the final microstructure and concentration of defects produced by ion implantation are almost impossible to predict.

One key application of ion implantation technology is semiconductor doping in integrated circuit fabrication, because of precise controllability and high reproducibility of implanted dopant profiles. Associated with the introduction of dopants is the damage produced in a target. The annealing of damage and the recovery of crystalline perfection of the target is critical to activating dopants and achieving the desired electrical properties. There are many books and reviews on damage production and annealing in ion implanted Si.[8,9] Defects produced by ion implantation also act as dilatational centers, which induce strain.[10] In most semiconductors such as Si, Ge, and GaAs, the strain is positive, meaning that the damage causes volume expansion.[11] One known exception is

MeV ion-implanted InP, where the negative strain is induced.[12] Ion implantation can also produce an amorphous phase, and provides an excellent vehicle for studying thermodynamics and kinetics of phase transformation among crystalline, amorphous, and liquid Si. An amorphous Si layer on a crystalline Si substrate recrystallizes by solid phase epitaxy upon thermal annealing.[13] The rate of regrowth follows an Arrehnius behavior with an activation energy of 2.7 eV.[14] Solid phase epitaxy can also be induced by a deeply penetrating ion beam, with lower activation energy.[15]

In recent years, ion implantation technology has been extended to other fields of materials research. One example is the formation of mesotaxial silicides such as $CoSi_2$[16] and $CrSi_2$[17] by high dose implantation followed by thermal annealing. Formation of epitaxial GeSi alloy layers by high dose Ge implantation into Si substrates and solid phase epitaxy was also demonstrated.[18] This technique has the potential of being used to make heterostructures that are difficult to grow by vacuum deposition. Another application is the fabrication of amorphous-crystalline superlattices from epitaxial ones by using ion implantation to induce selective amorphization.[19]

In the next two chapters, we will discuss some aspects of ion-solid interaction. The damage and induced strain in the implanted layers are emphasized. Chapter 7 focuses on damage production and annealing in bulk Si crystals, while Chapter 8 concentrates on the effects of ion implantation into silicides/Si and GeSi/Si heterostructures.

References

1. J. Lindhard, M.E. Scharff, and H.E. Schiott, Kgl. Dan. Vid. Selsk. Mat. Fys. Medd. 13, 14 (1963).
2. P. Sigmund, Appl. Phys. Lett. 14, 114 (1969).
3. G.H. Kinchin and R.S. Pease, Rep. Prog. Phys. 18, 1 (1955).
4. P. Sigmund, Appl. Phys. Lett. 25, 169 (1974).
5. K.B. Winterbon, P. Sigmund, and J.B. Sanders, Kgl. Dan. Vid. Selsk. Mat. Fys. Medd. 37, 14 (1970).
6. D.A. Thompson and R.S. Walker, Rad. Effects 36, 91 (1978).
7. Y.-T. Cheng, M-A. Nicolet, and W.L. Johnson, Phys. Rev. Lett. 58, 2083 (1987).
8. J.F. Gibbons, Proc. IEEE 60, 1062 (1972).
9. J.W. Mayer, L. Eriksson, and J.A. Davies, *Ion Implantation in Semiconductors*, Academic, New York, 1970.
10. G. Bai and M-A. Nicolet, J. Appl. Phys., July 15, 1991.
11. V.S. Speriosu, B.M. Paine, M-A. Nicolet, and H.L. Glass, Appl. Phys. Lett. 40, 604 (1982).
12. C.R. Wie, T. Jones, T.A. Tombrello, T. Vreeland, Jr., F.L. Xiong, Z. Zhou, G. Burns, and F.H. Dacol, Mat. Res. Soc. Symp. Proc. 74, 517 (1987).
13. L. Cespregi, E.F. Kennedy, S.S. Lau, J.W. Mayer, and T.W. Sigmon, Appl. Phys. Lett. 29, 645 (1976).
14. G.L. Olson, Mat. Res. Soc. Symp. Proc. 35, 25 (1985).
15. J. Linnors and G. Holmen, Phys. Rev. B32, 2770 (1985).
16. A.E. White, K.T. Short, R.C. Dynes, J.P. Garno, and J.M. Gibson, Appl. Phys. Lett. 50, 95 (1987).
17. A.E. White, K.T. Short, and D.J. Eaglesham, Appl. Phys. Lett. 56, 1260 (1990).
18. D.C. Paine, D.J. Howard, N.G. Stoffel, J.A. Horton, J. Mater. Res. 5, 1023 (1990).
19. D.J. Eaglesham, J.M. Poate, D.C. Jacobson, M. Cerullo, L.N. Pfeiffer, and K. West, Appl. Phys. Lett. 58, 523 (1991).

Chapter 7 Damage Production and Annealing in Si(100)

7.1 Introduction

Radiation damage in semiconductors produced by energetic electrons or neutrons attracted much attension in the 60's.[1] A great amount of information about the nature of simple defects and their annealing characteristics has been assembled with techniques such as electron paramagnetic resonance[2] and infrared optical absorption.[3] Since the 70's, ion implantation and ion-solid interaction became the focus of investigation because of their technological importance.[4] Unlike electron-produced damage, which consists mainly of isolated interstitials and vacancies, defects produced by ion implantation are complex.[5] Additional techniques such as channeling spectrometry[6], transmission electron microscopy[7], optical reflection spectroscopy[8], and double crystal diffractometry[9], have been used to reveal various aspects of the defect structures of ion-implanted semiconductors and of Si in particular.[10] However, a detailed picture of the nature of defect production and their stability is still lacking. In recent years, ion implantation technology has found new applications in areas such as ion-beam-induced epitaxial growth[11] and the synthesis of buried heterostructure.[12] The critical role of point defects produced by ion implantation in enhanced diffusion of dopants upon thermal annealing has been recognized.[13] An improved understanding of ion-induced defect production and annealing promises deepened insights into these phenomena.

In the following sections, we employ both x-ray double crystal diffractometry and MeV ^{4}He channeling spectrometry to analyze quantitatively the damage in a Si(100) crystal produced by implantation of 200−600 keV ions at both room and liquid nitrogen temperature. Some perspectives on the nature of defects produced by the implantation, and their stability and annealing characteristics are discussed in the light of the experimental results.

7.2 Damage by self-implantation at room temperature

Recognizing the important role that defects play in an implanted material, we undertook a careful analysis of damage produced by implantation of 230 keV ^{28}Si in a Si(100) crystal at room temperature. Double crystal diffractometry and channeling spectrometry were used to characterize the strain and the defect concentration.

A. Sample preparation

The samples were prepared by implantating 230 keV ^{28}Si ions into $\sim 1\ \Omega$cm n-type Si(100) wafers at room temperature in high vacumm ($\sim 10^{-7}$ Torr). The wafers were chemically cleaned before loaded into the implanter. The surface normal was misoriented by 7^0 from the incidence line of the beam to avoid channeling. The beam current was limited to be small ($\sim 0.2\ \mu A/\text{cm}^2$) to minimize beam heating. The implantation dose ranges from $10^{14}/\text{cm}^2$ to $10^{15}/\text{cm}^2$.

B. Double crystal diffractometry

Double crystal diffractometry was used to monitor the strain in the implanted layer. X-ray rocking curves of both symmetrical (400) and asymmetrical (311) diffractions were taken at room temperature in air 1 hour after implantation and 6 months later. The strain profile as a function of depth is extracted by simulating the experimental rocking curve using the dynamical x-ray diffraction theory.[14] The parallel strain, $\epsilon^{\|}$, of all samples considered here is zero within experimental sensitivity ($\sim 10^{-4}$), meaning that the lateral lattice spacing in the implanted layer is constrained to be equal to that in the substrate. The perpendicular strain, $\epsilon^{\perp}$, is positive and increases with dose, meaning that the perpendicular lattice spacing in the implanted layer is larger than that of the substrate and increases with the damage in the layer. The expansion of the lattice in the implanted layer implies that the strain contribution is dominated by the interstitial-like defects.[15] The magnitude of the perpendicular strain relaxes linearly with the logarithm of time at room temperature. The defects are almost stabilized at room temperature in less than 1 hr after implantation. Subsequently to that, relaxation proceeds very slowly. We shall neglect this subsequent time dependence thereafter because it is minute ($\sim$ 0.02% in 6 months).

Figure 7.2-1 shows a set of selected x-ray rocking curves from symmtrical (400) diffraction. The x-ray diffraction peak intensity from the implanted layer decreases rapidly when the dose increases (notice the ordinate scales). At the same time, the largest angular separation between the diffraction peaks of the implanted layer and the substrate increases. These facts mean that both the damage and the strain rise rapidly as the dose increases (notice the abscissa scales). Figure 7.2-2 is a plot of

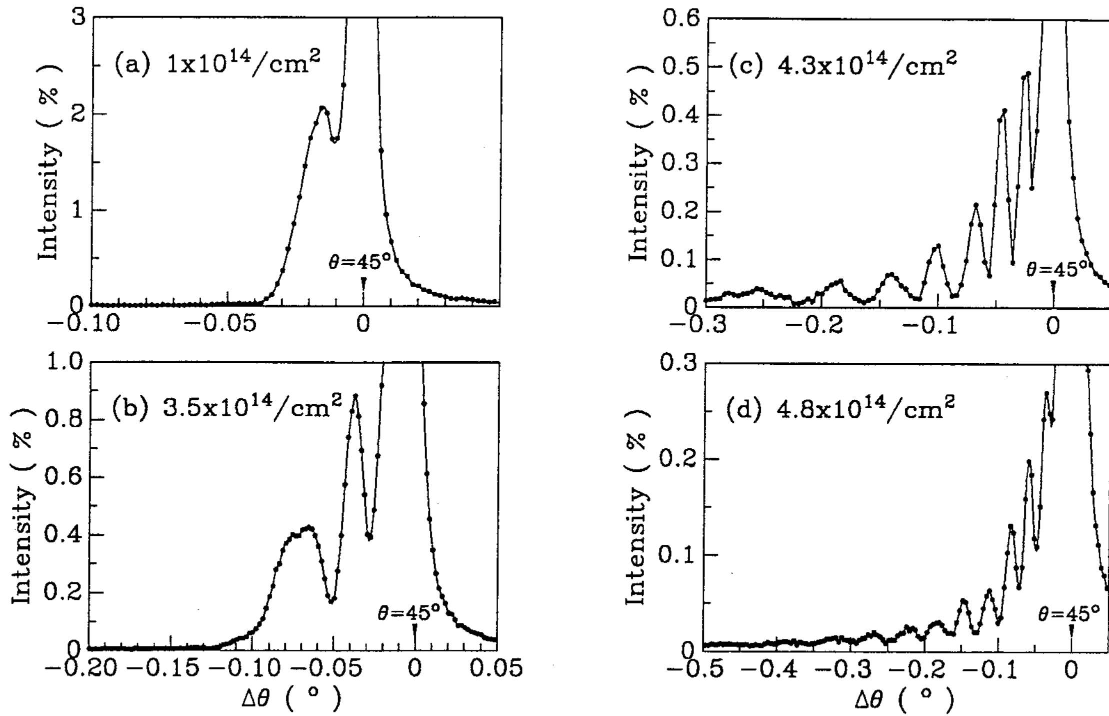

FIG. 7.2-1 Fe K_{α_1} x-ray (wavelength=0.1936 nm) rocking curves diffracted from the symmetrical (400) planes of the Si(100) samples implanted at room temperature by 230 keV ^{28}Si ions to the doses of (a) 1×, (b) 3.5×, (c) 4.3×, (d) 4.8 × $10^{14}/cm^2$.

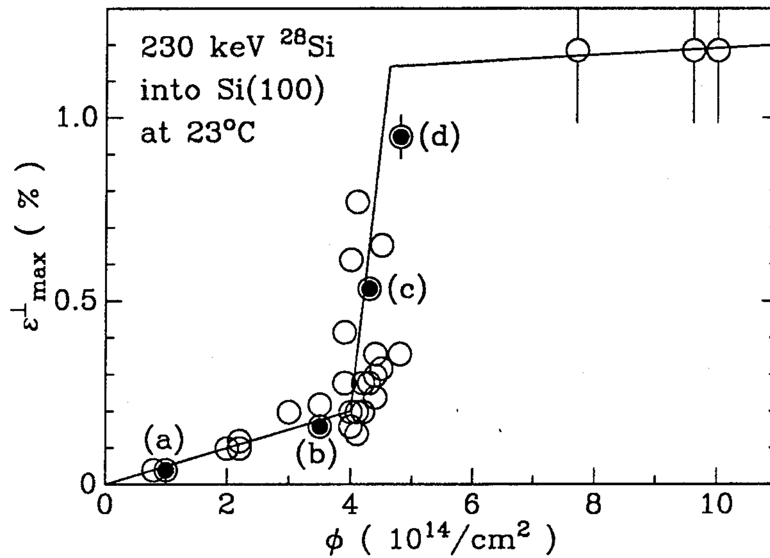

FIG. 7.2-2 The maximum perpendicular strain (○) extracted from dynamical x-ray diffraction simulations of the experimental rocking curves as a function of the Si implantation dose. The solid line is to stress the trend. The filled circles correspond to the samples for which the x-ray rocking curves are shown in Fig. 7.2-1.

the maximum value $\epsilon^{\perp}{}_{max}$ from the perpendicular strain profile as a function of implantation dose. There exist three distinct regimes in this room-temperature implanted Si layer: (I) the strain builds up slowly to a critical dose of $\sim 4 \times 10^{14}/\mathrm{cm}^2$; (II) the strain then rises rapidly within a very narrow dose range, and (III) finally saturates beyond a dose of $\sim 4.5 \times 10^{14}/\mathrm{cm}^2$. Dynamical x-ray diffraction simulation also gives an estimate of the static Debye-Waller factor, $(\delta r)_{rms}$, (the root mean-square of the atomic displacement from the lattice site). At any depth, the static displacement $(\delta r)_{rms}$ is approximately proportional to the perpendicular strain. The maximum displacement is small in regime I ($\sim$ 0.01 nm), increases to $\sim$ 0.06 nm in regime II and saturates at this value in regime III. One can obtain an "equivalent temperature," T_{eq}, corresponding to the atomic displacement of $(\delta r)_{rms}$, by using the Debye-Waller formula,

$$(\delta r)_{rms}{}^2 = \frac{9\hbar^2 T_{eq}}{Mk\Theta^2}, \tag{7.2-1}$$

where M is the mass of silicon atoms and Θ (=645K[16]) is the Debye temperature of crystalline Si. The maximum "equivalent temperature" thus obtained for the implanted Si layer is about 0.2 T_m (T_m = 1685K is the melting temperature) in the low damage regime (I), and reaches about $4T_m$ in regime (III). The very high "equivelent temperature" associated with regime (III) suggests that the heavily damaged state is far from equilibrium and hence is highly metastable.

C. Backscattering and channeling spectrometry

Backscattering and channeling spectrometry were used to measure defect concentration in the implanted layer. Figure 7.2-3 shows 2 MeV ^{4}He [100] axial channeling spectra of selected samples. The defect concentrations were extracted from the channeling spectra according to the following model. The channeling yield, χ_D, of the damaged layer consists of two contributions: normal backscattering from the dechanneled ("random") fraction of an aligned incident beam, χ_R, and direct backscattering of a channeled beam from the defect of concentration, c_D,[17]

$$\chi_D = \chi_R + (1 - \chi_R)c_D. \tag{7.2-2}$$

The dechanneling of an aligned incident beam in the crystal equals

$$\chi_R = P_D + (1 - P_D)\chi_V, \tag{7.2-3}$$

where P_D is the probability that a channeled incident ion is dechanneled by the defect and χ_V is the channeling yield of a virgin crystal. Combining Eqs. (7.2-2) and (7.2-3) gives

$$\gamma_D = c_D + (1 - c_D)P_D, \tag{7.2-4}$$

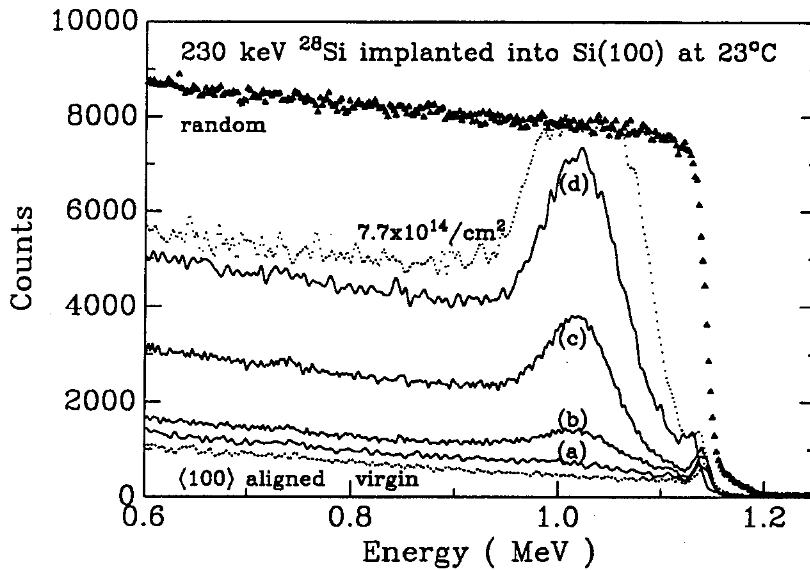

FIG. 7.2-3 2 MeV ^{4}He backscattering (filled triangle) and channeling spectra (solid line) of the set of the samples shown in Fig. 7.2-1. Also plotted are the channeling spectra (dotted line) of a virgin Si sample and a sample implanted 7.7×10^{14} ^{28}Si/cm^2 in which a continuous amorphous layer forms.

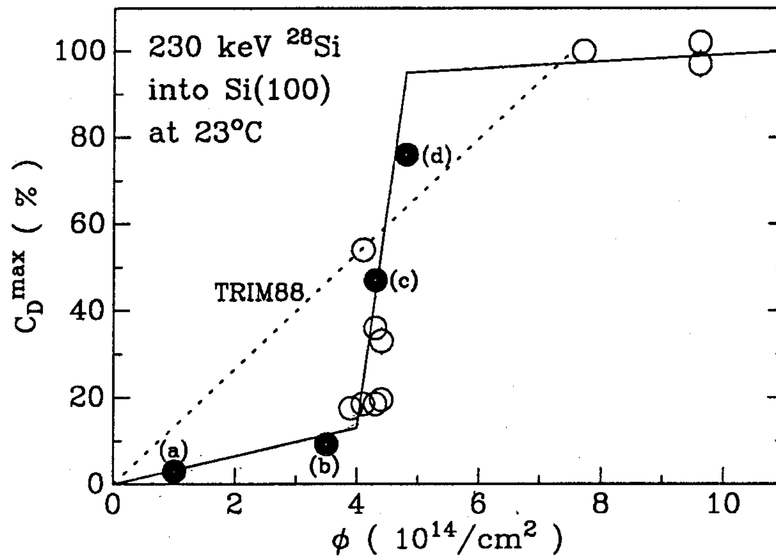

FIG. 7.2-4 The maximum defect concentration extracted from channeling spectra such as those of Fig. 7.2-3 as a function of the Si dose. The solid line is to highlight the trend. The filled circle corresponds to the samples (a-d) shown in Fig. 7.2-3. The dashed line is the maximum value in the concentration profile of the Frenkel pair predicted by the TRIM88 simulation code of 230 keV ^{28}Si implantation in an amorphous Si target.

where the dechanneling parameter, γ_D, is defined by

$$\gamma_D \equiv \frac{\chi_D - \chi_V}{1 - \chi_V} \in [0, 1]. \qquad (7.2-5)$$

γ_D can be obtained directly from the channeling spectra of the virgin and the damaged crystals. To extract the defect concentration c_D from Eq. (7.2-4), one needs to know how the dechanneling probability P_D is related to c_D. In the single scattering approximation, one can define a dechanneling cross section, σ_D, by

$$\frac{dP_D}{dx} = n\sigma_D c_D, \qquad (7.2-6a)$$

or

$$P_D(x) = \int_0^x n\sigma_D c_D(x')dx', \qquad (7.2-6b)$$

where x is the depth from the surface and n is the atomic density of the crystal. From Eqs. (7.2-4) and (7.2-6b), one finally obtains

$$\gamma_D(t) = c_D(t) + (1 - c_D(t)) \int_0^t c_D(t')dt', \qquad (7.2-7)$$

where

$$t \equiv n\sigma_D x \qquad (7.2-8)$$

is a dimensionless depth scale. Eq. (7.2-7) is a nonlinear integral equation for the defect concentration c_D. The dechanneling parameter $\gamma_D(t)$ can be extracted from channeling measurements, the defect concentration $c_D(t)$ is hence obtained by solving Eq. (7.2-7). We solved Eq. (7.2-7) numerically by adjusting the parameter σ_D to satisfy the boundary condition that P_D equals γ_D beyond the damaged layer (where $c_D = 0$), and the defect concentration profile c_D(x) was then obtained. The best-fitted dechanneling cross section σ_D obtained according to the above procedure for the samples implanted to various doses is about the same. The average value is $\sim 7 \times 10^{-19}$cm^2. This is significantly smaller than the cross-sectional area of a channel ($\sim 10^{-15}$ cm^2).

The results from channeling measurements are summarized in Fig. 7.2-4, a plot of the maximum value c_D^{max} from the defect concentration profile $c_D(x)$ as a function of dose. Although derived from quite different experimental inputs, the dependence closely resembles that of strain-dose relationship and also exhibits the three distinct damage regimes with the same critical dose ($\sim 4 \times 10^{14}$/cm^2).

To elucidate what the amount of the measured damage means, we computed the maximum Frenkel pair concentrations produced by 230 keV ^{28}Si implantation into an amorphous Si target at 0 K using the TRIM88 simulation program[18] (dashed line in Fig. 7.2-4). We used the binding energy

of 1 eV and the displacement threshold energy of 15 eV as input parameters in the simulation. One sees that the measured damage in the low dose regime (I) is only $\sim$ 0.2 of that predicted. This suggests that the majority of initially created defects anneals out at room temperature. That result is consistent with the observation that single vacancies and interstitials are mobile at room temperature.[19] We thus conclude that the majority of initially created defects in regime I are in the form of simple Frenkel pairs, which are mobile and readily recombine at room temperature. The measured stable defects are therefore di-vacancies, di-interstials, and their clusters, formed during the migration of the point defects.[19]

In regime II, the damage increases with dose much faster ($\sim$ 8 times) than the production of Frenkel pairs calculated from TRIM88. This indicates that the defect production in the predamaged crystal is more efficient than that in a virgin crystal, suggesting that the newly produced defects can destabilize the predamaged crystal and cause the formation of disordered zones of increased size. Such a process produces about 8 times more displacements than can be directly generated by nuclear collisions (see Fig. 7.2-4). In other words, in a predamaged crystal with a defect concentration $> 15\%$, the effective threshold energy of atomic displacement is reduced from $\sim 15\ eV$[5] in the virgin crystal to $\sim 2\ eV$, which is approximately the formation energy of point defects in a solid by thermal activation.[5] Stated differently, the damage production depends on the interaction with existing defects beyond the critical defect concentration ($\sim$ 15%). The effect of dose is no longer simply additive. Guided by our observation of the accelerated growth of damage, we model the damage build-up phenomologically by assuming that the production rate of stable defects is proportional to the concentration of existing defects. We also take into account the fact that the defects produced within already existing damaged regions do not increase defect concentration. Combining these two factors, we obtain the net rate of the production of stable defects,

$$\frac{dc_D}{d\phi} = \frac{c_D + c_o}{\phi_o} \cdot (1 - c_D), \tag{7.2-9}$$

where c_o and ϕ_o are fitting parameters. The solution is obtainable by direct integration and gives the growth of defect concentration as a function of dose. The best fit with experimental data ($\circ$) gives $c_o \approx 2 \times 10^{-6}$ and $\phi_o \approx 3 \times 10^{13}/\text{cm}^2$ (solid line in Fig. 7.2-5). The small value of c_o reflects the difficulty in producing stable defects in a virgin crystal. This simple model fits the data reasonably well. Thompson and Walker[20] also observed that the effective threshold energy for atomic displacement decreases as the energy density deposited in the nuclear collision increases. They attribute the enhancement to the thermal spike phenomenon. That phenomenon differs from what we observe in that the thermal spike also occurs in a virgin crystal. The enhancement seen

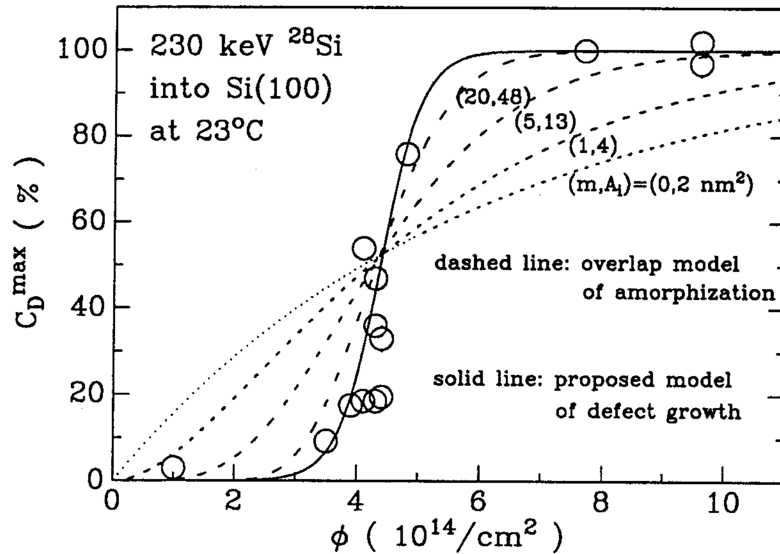

FIG. 7.2-5 The measured maximum defect concentration as a function of dose (o of Fig. 7.2-4) is compared with that predicted from the phenomenological model of the accelerated damage growth in a predamaged crystal (solid line, see text). The dashed lines are the fraction of the amorphous zones calculated from Gibbson's overlap model with various (m,A_i) parameters.

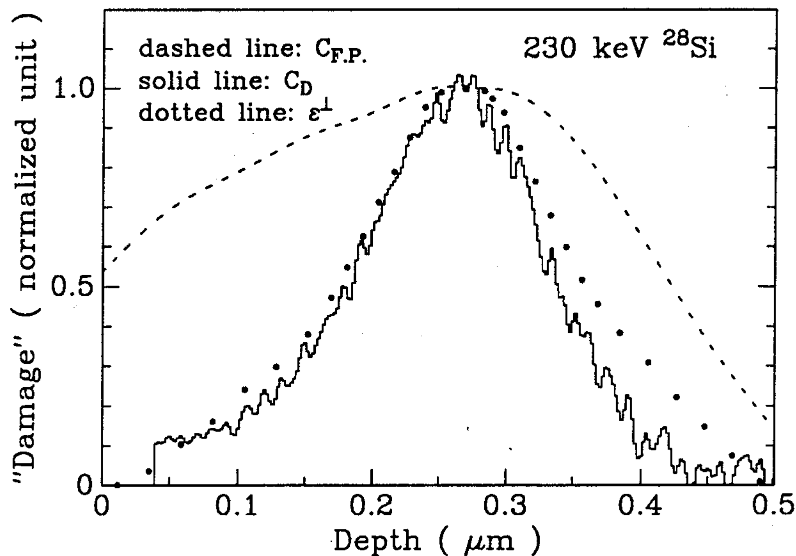

FIG. 7.2-6 The depth profile of the Frenkel pair concentration from TRIM88 simulation (dashed line), the defect concentration from the channeling measurements of the sample (c) (solid line), and the perpendicular strain from the dynamical x-ray diffraction simulation of the rocking curve (dotted line). The vertical scale is in an arbitrarily normalized unit.

here is caused by the existence of predamage, not the dense casade produced by an incident ion.

In regime III, a continuous amorphous layer is known to form at the maximum damage location when the yield for channeled beam incidence becomes the same as that for random beam incidence.[6] The dose for the onset of the formation of a continouous amorphous layer is $\sim 5 \times 10^{14}/\text{cm}^2$ (see Fig. 7.2-4), which from TRIM88 simulation corresponds to a maximum energy density deposited in nuclear collision of $\sim 10^{24}$ eV/cm^3. This value agrees with the prediction of critical energy density criterion for amorphization ($\sim 10^{24}$ eV/cm^3).[5] Further implantation only causes the widening of the amorphous layer. To gain some insight into the mechanism of amorphization, we apply Gibbons' overlap model[5] to fit the measured maximum defect concentration (dashed line in Fig. 7.2-5). Assuming that each incident ion creats a cylindrical zone of damage of cross section A_i and the formation of an amorphous region is caused by the m-tuple overlap of damage zones, the fraction of the amorphous regions, f_A, is given by[5]

$$f_A = 1 - \left(\sum_{j=0}^{m} \frac{(A_i\phi)^j}{j!}\right) e^{-A_i\phi}. \qquad (7.2-10)$$

Figure 7.2-5 shows several f_A curves with various parameters of (m, A_i). It is evident that the fitting improves as the m parameter increases (A_i increases correspondingly). This strongly suggests that the direct impact amorphization[21] by implanted ions does not occur in self-implanted Si at room temperature and that amorphous zones are formed because of the overlap of defected regions.[22] Futhermore, it is necessary to invoke very many overlaps ($m > 20$) to fit the rapid growth of damage. We thus hypothesize that amorphization may occur spontaneously as a result of collaps of heavily defected crystal.

D. Depth profile of "damage"

The depth profiles of the Frenkel pair concentration ($c_{F.P.}$, dashed line) calculated from TRIM88 simulations is compared with the defect concentration (c_D, solid line) extracted from channeling measurements of the sample (c) in Fig. 7.2-3. To reveal the difference in the shapes of the damage-depth profiles, each profile is plotted by normalizing its peak value to unity. The measured profile is steeper than the calculated one, indicating that defects associated with smaller Frenkel pair concentration anneal out at room temperature, consistent with the previous discussion. In particular, the measured defect concentration near the surface is much depleted compared to the simulated one, indicating that the surface is a very efficient sink for defects. Figure 7.2-6 also shows the depth profile of the perpendicular strain extracted from the simulation of x-ray rocking curves ($\epsilon^{\perp}$, dotted line),

which closely follows that of the measured defect concentration c_D. The strain and the defect concentration are seen to be proportional to each other.

Figure 7.2-7 shows the measured maximum strain in the implanted Si layer versus the measured maximum defect concentration. The two quantities are linearly related,

$$\epsilon^{\perp}{}_{max} = B c_D^{max}, \tag{7.2-11}$$

with a slope of $B \sim 0.013$. This slope is a constant, valid over the entire range of strain and damage (regimes I, II, III).

E. Relationship between strain and defect concentration

We apply continuum elasticity theory to estimate the order of the magnitude of the ratio between the strain and defect concentration. For simplicity of book-keeping, we treat the material as an elastically isotropic medium, although crystalline Si is anisotropic. The lattice expansion can be extracted from the strain according to linear elasticity,

$$\frac{\Delta a}{a} = \frac{1-\nu}{1+\nu}\epsilon^{\perp} + \frac{2\nu}{1+\nu}\epsilon^{\|},$$

where ν is the Poisson ratio. Using the measured value of $\epsilon^{\|}=0$ and $\nu = 0.28$ of bulk Si, we obtain the relationship between the lattice expansion and the defect concentration,

$$(\frac{\Delta a}{a}) = 0.56\ \epsilon^{\perp} = 0.007 c_D. \tag{7.2-12}$$

The last relation is derived from Fig. 7.2-7.

Eshelby[23] showed that the lattice dilatation induced by point dilatation centers of concentration c, and "strength" k, equals

$$\frac{\Delta a}{a} = k \cdot c. \tag{7.2-13}$$

The "strength" of a dilatation center of radius, R, is given by[23]

$$k = \frac{4\pi(1-\nu)}{1+\nu} \cdot R^2 \delta n, \tag{7.2-14}$$

where δ is the the lattice displacement at R, and n is the atomic density.

In fcc metals such as Cu, $k_v \sim -0.2$ for single vacancies and $k_i \sim 1.5$ for interstitials.[15,24] For a crystal containing an equal number of single vacancies and interstitials, the "strength" becomes $k \sim 1.5 - 0.2 = 1.3$. This number is more than 100 times larger than the coefficient in Eq. (7.2-12). The smallness of the "strength" in Si could be due to the open structure of the diamond

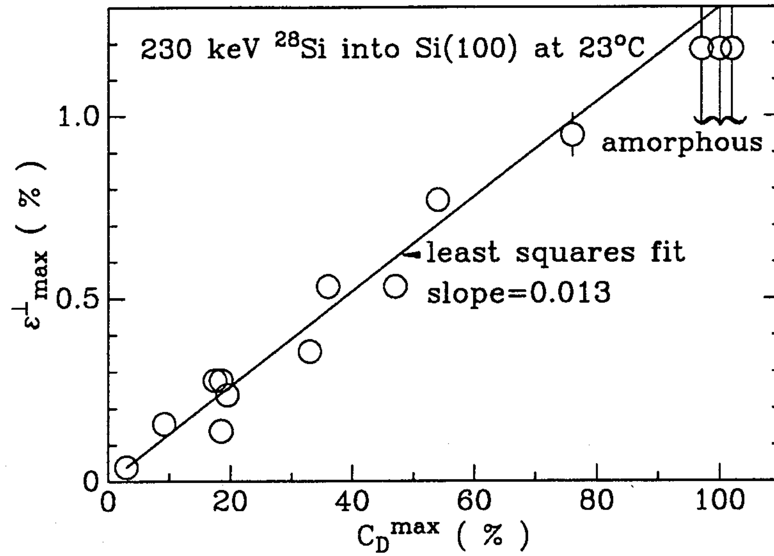

FIG. 7.2-7 The relationship between the maximum values of the perpendicular strain from x-ray diffraction measurements and the defect concentration from 2 MeV ^{4}He channeling measurements. The solid line is the least-squares fit of the data (o) to a linear function.

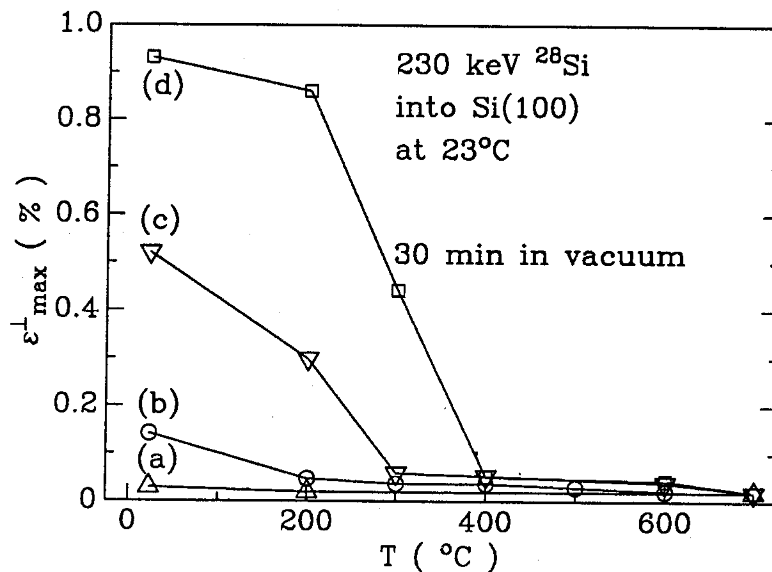

FIG. 7.2-8 The isochronal annealing characteristics of the perpendicular strain in the implanted layers as a function of the annealing temperature. All annealings were performed in a vacuum of $\sim 7 \times 10^{-7}$ Torr for a duration of 30 min. The data are from the four samples for which the x-ray rocking curves are shown in Fig. 7.2-1 and the channeling spectra in Fig. 7.2-3.

lattice compared to the closed-packed fcc lattice.[25] However, it is unlikely that this can explain the difference of more than two orders of magnitude.

Another explanation is that the defect in the room-temperature-implanted Si is in the form of aggregates of vacancies and interstitials. To simplify the analysis, we will assume that the defect is in the form of vacancy and interstial clusters containing an average of p lattice sites. We treat each cluster as an individual dilatation center of "strength" k_p. The lattice dilatation induced by the clusters of concentration c_p is

$$\frac{\Delta a}{a} = k_p \cdot c_p. \qquad (7.2-15)$$

The "strength" k_p for the cluster can be obtained from Eq. (7.2-14),

$$k_p = \frac{4\pi(1-\nu)}{1+\nu} \cdot R_p^2 \delta_p n = p^{2/3} \left(\frac{4\pi(1-\nu)}{1+\nu} \cdot R_1^2 \delta_1 n\right) = p^{2/3} \cdot k_1, \qquad (7.2-16)$$

because $R_p = p^{1/3} R_1$, and the displacement δ of a dilatation center is not sensitive to the size ($\delta_p \approx \delta_1$[26]). For a given defect concentration of c_D, the cluster concentration is

$$c_p = p^{-1} \cdot c_D. \qquad (7.2-17)$$

Substituting Eqs. (7.2-16) and (7.2-17) into Eq. (7.2-15) gives

$$\frac{\Delta a}{a} = p^{-1/3} \cdot k_1 \cdot c_D. \qquad (7.2-18)$$

Using the typical value of $k_1 \sim 1$ for a single vacancy-interstitial pair in a fcc crystal,[27] we have

$$\frac{\Delta a}{a} \sim p^{-1/3} \cdot c_D. \qquad (7.2-19)$$

The coefficient in Eq. (7.2-19) becomes ~ 0.007 if the cluster contains $p \sim 3 \times 10^6$ lattice sites. The diameter, D, of such a cluster is about 50 nm. It is 10 times larger than that in a similarly implanted Si observed by transmission electron microscopy.[28,29] Using the value from transmission electron microscopy, $D \sim 5$ nm, Eq. (7.2-18) becomes

$$\frac{\Delta a}{a} \sim 0.07 k_1 \cdot c_D. \qquad (7.2-20)$$

The coefficient in Eq. (7.2-20) becomes 0.007 if the "strength" of a single vacancy-interstitial pair k_1 in Si equals 0.1. This is about 10 times less than that in fcc metals.

This oversimplified model demonstrates that the observed smallness of the coefficient can be attributed to the combined effect of defect clustering ($p > 1$) and the small single vacancy-interstitial "strength" ($k_1 < 1$). This is consistent with the fact that single vacancies and interstitials are

mobile[19] at room temperature, and Si has an open structure. The above analysis can be readily generalized to a more realistic defect structure than that discussed here, where a distribution of different sizes of clusters exists.

F. Thermal annealing and damage recovery

To further reveal the nature of the defect in self-implanted Si, we conducted experiments to investigate the effect of thermal annealing on the strain in implanted Si. It is known that single interstitials and vacancies anneal out at temperatures much less than room temperature,[19] di-interstitials anneal at $\sim 150°C$,[30] di-vacancies anneal at $\sim 100-250°C$,[31], small damage clusters (< 10 nm) anneal between 100°C and 400°C,[32] and a continuous amorphous layer starts to regrow by solid phase epitaxy with an appreciable rate at $\sim 550°C$.[6] Isochronal annealings of the samples of Figs. 7.2-1 and 7.2-3 with different damage levels were performed in high vacuum (5×10^{-7} Torr) for 30 min at temperatures from 200°C to 700°C. The parallel strain remains zero after annealing. The annealing behavior of the perpendicular strain is shown in Fig. 7.2-8. The temperature for significant recovery increases as the damage increases, indicating that different damage levels have different defect structures. Regime (I) with low damage (samples (a) and (b)) consists of relatively simple defects such as di-interstitials and di-vacancies. The intermediate damage regime (II) (samples (c) and (d)) contains more complex defects such as clusters or small disordered zones. As the damage increases further, a continuous amorphous layer forms because of the overlap of the damaged regions. This picture differs from Vook and Stein's[33] where there are only two distinct annealing stages at $\sim 250°C$ and $\sim 550°C$, which they associate with the annealing of di-vacancies and epitaxial regrowth of an amorphous layer, respectively. They accordingly proposed that amorphization is controlled by di-vacancy annealing.[33,34] Our results are based on data taken with fine increments of the dose near the amorphization threshold (Fig. 7.2-2 and 7.2-4) and reveal a complex defect hierarchy.

G. Conclusion

In the light of the above experimental results and discussion, we propose the following model for the damage build-up and amorphization of self-implanted Si at room temperature. Initially, the majority of defects produced by incident ions in a virgin crystal are Frenkel pairs, which are mobile at room temperature. The migration of these interstitials and vacancies results in recombination and clustering to form stable defects such as di-interstitials and di-vacancies. Only a small fraction of initially created defects remains at room temperature. They generate perpendicular strain. As the damage rises to the critical value ($\sim 10-20\%$), a large amount of energy is stored in the damaged

layer. Additionally created defects cause the collapse of the damaged region into large disordered zones. This mechanism produces more damage than that generated directly in a virgin crystal by nuclear displacements, giving rise to an enhanced production of damage and strain. The larger the damage, the more complex the defect structure becomes. Amorphization occurs spontaneously as a cooperative process because of the overlap of heavily defected crystalline regions.

7.3 Damage by ^{19}F, ^{40}Ar, and ^{131}Xe implantation at room temperature

In this section, we extend the investigation of defects production and their stability in room temperature implanted Si(100) to ions of vastly different nuclear charges and masses.[35]

A. Experimental procedures

Ions of either 230 keV ^{19}F, 250 keV ^{40}Ar, or 570 keV ^{131}Xe were implanted into Si(100) at room temperature in high vacuum ($\sim 10^{-7}$ Torr). The beam flux was limited to $\leq 0.5\ \mu A/\mathrm{cm}^2$ to minimize the sample heating. The ranges of implanted ions in Si(100), calculated from TRIM simulation,[18] vary from $\sim 0.2\ \mu m$ for 570 keV ^{131}Xe to $\sim 0.4\ \mu m$ for 230 keV ^{19}F. The doses were chosen to produce a spectrum that covers the entire range of damage, from a lightly damaged crystal to one with a buried continuous amorphous layer.

2 MeV ^{4}He channeling measurements were used to extract the defect concentration in the implanted layer, according to the procedures described in the previous section.[36] The strain induced by the damage was obtained by fitting the measured x-ray rocking curves to the calculated one from the dynamical diffraction model.[14]

B. Results of 230 keV ^{19}F implantation

Channeling spectra of 230 keV ^{19}F implanted Si(100) samples resemble those of 230 keV ^{28}Si implanted ones shown in Fig. 7.2-3. Implantation to a dose of 5×10^{14} ^{19}F/cm^2 produces a marginally detectable dechanneling yield above the background yield of a virgin sample (labeled by virgin in Fig. 7.2-3), while implantation to a dose of 2×10^{15} ^{19}F/cm^2 produces a region in the channeling spectrum where the channeling yield equals the random one (similar to the dotted line spectrum labeled by 7.7×10^{14}/cm^2 in Fig. 7.2-3). We will refer to the corresponding region in the sample as a continous amorphous layer for the rest of this chapter. The depth profile of defect concentration $c_D(x)$ is also similar to that obtained before for ^{28}Si (Fig. 7.2-6). The defect concentration near the surface is again depleted compared to that predicted from TRIM88 simulation. The maximum

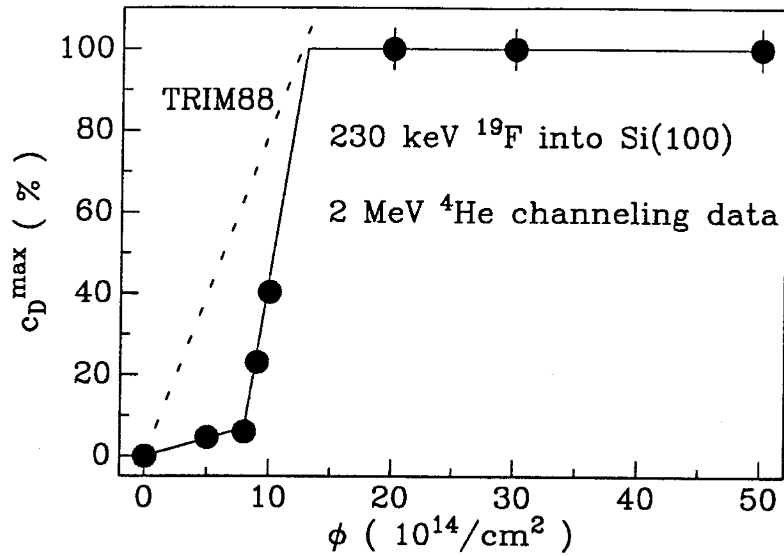

FIG. 7.3-1 The maximum defect concentration extracted from channeling spectra similar to those of Fig. 7.2-3 as a function of the ^{19}F dose. The solid line is to highlight the trend. The dashed line is the maximum value in the depth profile of the Frenkel pair concentration predicted by the TRIM88 simulation of 230 keV ^{19}F implantation into an amorphous Si target.

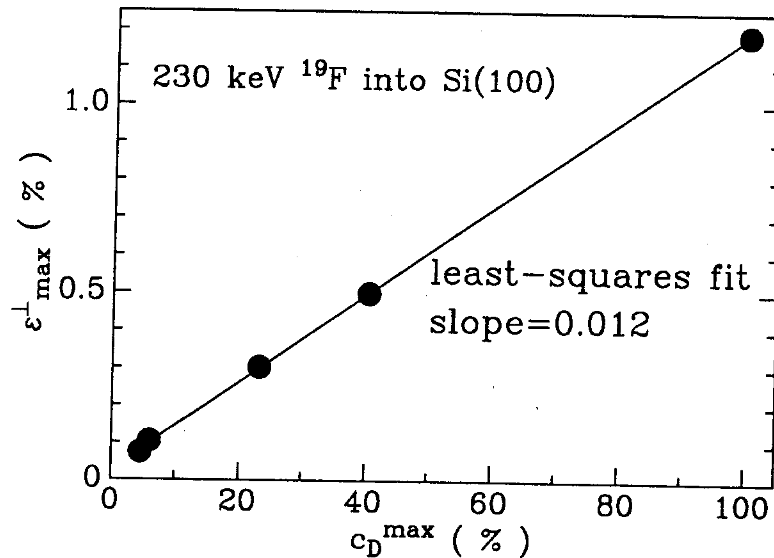

FIG. 7.3-2 The relationship between the maximum values of the perpendicular strain from x-ray diffraction measurements and the defect concentration from 2 MeV ^4He channeling measurements. The solid line is the least-squares fit to the data (•) of a linear function.

value of the defect concentration profile is plotted as a function of the ^{19}F dose in Fig. 7.3-1. It is clear that the dependence is highly nonlinear and similar to that observed in the ^{28}Si implanted Si(100) (see Fig. 7.2-4). The damage here can also be categorized into three regimes I, II, III, corresponding to the lightly damaged, enhanced damage production, and formation of a continuous amorphous layer, respectively.[36] In particular, we notice that the transition from I to II occurs at a defect concentration of $\sim$ 10%, the same damage level as that in the ^{28}Si implanted samples. This suggests that the general character of damage production in Si(100) by room-temperature implantation is insensitive to the implanted ions. The critical dose ($\sim 8 \times 10^{14}/\mathrm{cm}^2$) of the ^{19}F implanted sample is, however, more than twice larger than that of the ^{28}Si implanted one ($\sim 3 \times 10^{14}/\mathrm{cm}^2$). This is partly due to the fact that each ^{19}F ion produces less Frenkel pairs than each ^{28}Si ion does. The dose required to produce the same amount of Frenkel pairs is hence greater for ^{19}F than for ^{28}Si.

The strain profile extracted from x-ray rocking curves has the same shape as the defect profile. This result is again similar to that of the ^{28}Si implanted samples (see Fig. 7.2-6). The maximum value in the perpendicular strain profile rises nonlinearly with the ^{19}F dose.[35] It has the same dependence as that of the defect concentration of Fig. 7.3-1, with the same critical dose, $\sim 8 \times 10^{14}/\mathrm{cm}^2$. The transition from regime I to II occurs at a strain value of $\sim$ 0.2%. All these results are similar to those obtained for the ^{28}Si implanted samples.

Furthermore, we discover that as for the ^{28}Si implanted samples, the strain in the damaged layer of the ^{19}F implanted samples is also proportional to the defect concentration over the whole range of strain and damage (Fig. 7.3-2),

$$\epsilon^{\perp} = 0.012 c_D. \qquad (7.3-1)$$

The coefficient is also the same (compared with Fig. 7.2-7). Thus, we have again that $\epsilon^{\perp} = B c_D$. This relationship between the defect and its induced strain is thus insensitive to the implanted ions, but is an intrinsic property of the Si target.

C. Generalization to any ions

X-ray rocking curve analyses of 250 keV ^{40}Ar and 570 keV ^{131}Xe implanted samples were also performed. The strain profiles all have the similar shape. In particular, the strain near the surface is always depleted in comparison with that predicted by TRIM88.[35] The maximum perpendicular strain as a function of dose is plotted in Fig. 7.3-3 for all ions. Firstly, they all show similarly nonlinear dose dependences. The nonlinearity is strongest for ^{19}F and weakest for ^{131}Xe. This tendency is in accord with our previous proposition that the nonlinearity arises from the

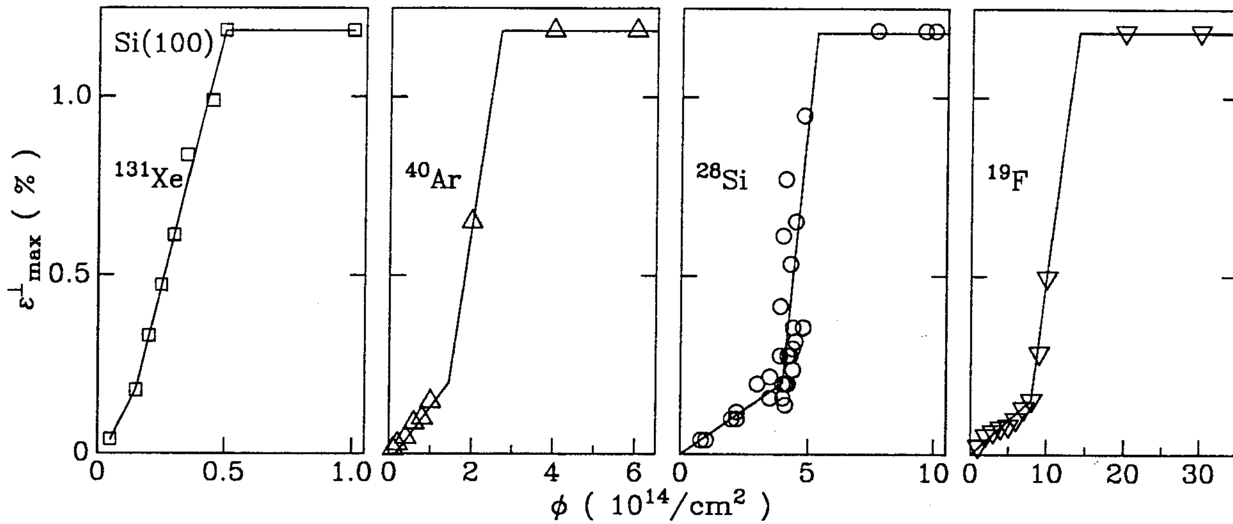

FIG. 7.3-3 The maximum perpendicular strain obtained by fitting the dynamical x-ray diffraction simulations to the experimental rocking curves as a function of the implantation dose for four different ions. The solid line is to stress the trend.

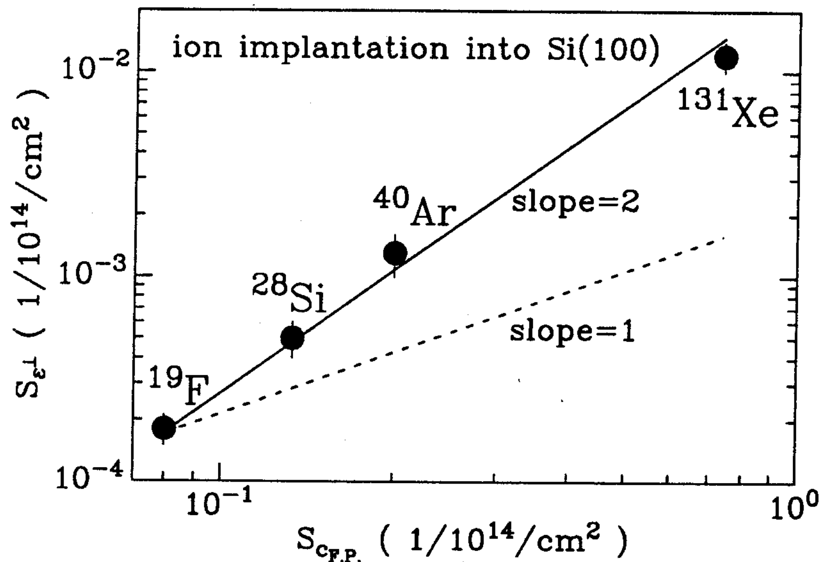

FIG. 7.3-4 The initial (regime I) slope of the maximum perpendicular strain vs dose as a function of the Frenkel pair concentration per unit dose for various incident ions.

recombination of simple vacancy-interstitial defects at room temperature.[36] Light ions produce defects that are sparesly distributed within a large cascade volume and consist mainly of isolated interstitials and vacancies so that few stable complexes are formed and most defects recombine. On the other hand, heavy ions produce defects that distribute densely in a small cascade volume so that defect complexes and clusters that are stable at room temperature are generated. Secondly, the transition from regime I to II occurs at about the same strain value of $\sim 0.1 - 0.2\%$, independent of the ion species, while the critical dose decreases from $\sim 8 \times 10^{14}/\mathrm{cm}^2$ for the light ^{19}F to $\sim 10^{13}/\mathrm{cm}^2$ for the heavy ^{131}Xe.

Given the results on the linear relationship between the strain and the defect concentration obtained in the ^{19}F and ^{28}Si implanted samples (Fig. 7.3-2 and 7.2-7), we assume that this same linear relationship also applies to other ions. The common critical perpendicular strain $\epsilon^{\perp}{}_{cr}$ of Fig. 7.3-3 for various ions thus means that the critical defect concentration is also the same ($\sim 10 - 20\%$) for all ions. Above this damage level, the defected crystal becomes unstable and the damage rises rapidly (regime II) till a continuous amorphous layer forms (regime III).

In the lightly damaged regime I, the strain (and hence defect concentration) increases approximately linearly with dose,

$$\epsilon^{\perp} = S_{\epsilon^{\perp}} \phi, \qquad (7.3-2)$$

where $S_{\epsilon^{\perp}}$ is the slope of $\epsilon^{\perp}{}_{max}$ vs ϕ. $S_{\epsilon^{\perp}}$ increases from $\sim 0.02\%/(10^{14}/\mathrm{cm}^2)$ for ^{19}F to $\sim 1.2\%/(10^{14}/\mathrm{cm}^2)$ for ^{131}Xe.

To put these values into perspective, we computed the maximum of the Frenkel pair concentration per unit dose of incident ions, $S_{c_{F.P.}}$, by TRIM88.[18] $S_{c_{F.P.}}$ measures the amount of displacement produced by each incident ion. For a given implantation dose ϕ, the maximum Frenkel concentration $c_{F.P.}$ equals $S_{c_{F.P.}}$ times the dose ϕ. The heavier an incident ion is, the more damage it produces, and hence the larger $S_{c_{F.P.}}$ becomes. It increases from $\sim 8\%/(10^{14}/\mathrm{cm}^2)$ for ^{19}F to $\sim 74\%/(10^{14}/\mathrm{cm}^2)$ for ^{131}Xe.[36]

Figure 7.3-4 shows the measured slope $S_{\epsilon^{\perp}}$ as a function of the calculated $S_{c_{F.P.}}$ from TRIM88 for four ions (•). The solid line represents a quadratic dependence of the slope on $S_{c_{F.P.}}$, and the dashed line, a linear dependence. It is evident from the figure that the slope $S_{\epsilon^{\perp}}$ has an approximate quadratic dependence on $S_{c_{F.P.}}$,

$$S_{\epsilon^{\perp}} \propto S^2_{c_{F.P.}}. \qquad (7.3-3)$$

We also plot the critical dose as a function of $S_{c_{F.P.}}$ for the four ions, and discover that

$$\phi_{cr} \propto S^{-2}_{c_{F.P.}}. \qquad (7.3-4)$$

Combining these results, we find that the critical strain defined by

$$\epsilon^{\perp}{}_{cr} \equiv S_{\epsilon^{\perp}} \phi_{cr} = 0.17\%, \qquad (7.3-5)$$

is a constant independent of incident ions. This result agrees with that obtained previously from Fig. 7.3-3.

Paine and Speriosu[37] observed that the strain in a lightly damaged GaAs also increases linearly with ion doses. However, the slope of strain versus dose is a linear function of the Frenkel pairs per unit dose of incident ions, rather than a quadratic one.

We already know that the defect concentration c_D in an implanted Si is proportional to the strain $\epsilon^{\perp}$,[36] and have therefore the following relation according to Fig. 7.3-4,

$$S_{c_D} \propto S^2_{c_{F.P.}}, \qquad (7.3-6)$$

where S_{c_D} is the slope of the defect concentration from the channeling analysis of the implanted samples in regime I versus dose. It states that the stable defect concentration rises quadratically as the Frenkel pair concentration per unit ion dose increases. This fact means that the stable defects produced by room-temperature implantation in Si(100) cannot be predicted by the linear cascade model. It supports our previous hypothesis that the simple vacancy-interstitial defects are not stable at room temperature. They recombine or form defect complexes and clusters, and it is these that are stable at room temperature. The fraction of the various microstructural defects depends on the density of the Frenkel pairs initially produced by an incident ion in a cascade volume. A low density in a large volume (for light ion) results in a large fraction of simple defects. While a high density in a small volume (for heavy ion) results in a large fraction of defect complexes and clusters. This could explain qualitatively the nonlinear dependence of S_{c_D} on $S_{c_{F.P.}}$.[35]

7.4 Damage by ion implantation at liquid nitrogen temperature

We report here the results on the damage produced by ion implantation at liquid nitrogen temperature and analyzed at room temperature,[38] and compare them with those obtained by room-temperature implantation.[35]

A. Experimental procedures

Ions of either 230 keV ^{28}Si, 250 keV ^{40}Ar, or 570 keV ^{131}Xe were implanted into Si(100) at $\sim$ 100K in high vacuum ($\sim 10^{-7}$ Torr). The beam flux was kept low to minimize the sample heating during implantation. The samples gradually warmed up to room temperature in $\sim$ 1 hr after the completion of implantation. X-ray rocking curves were taken at room temperature in ambient air immediately afterwards. The samples were then stored in ambient air at room temperature. DCD measurements of selected samples were also made at room temperature after about one day, one week, one month, and one year to monitor the time evolution of the rocking curves.

B. Results of 250 keV ^{40}Ar implantation at 100K

The strain in the damaged layer induced by the implantation of 250 keV ^{40}Ar ions into Si(100) at 100K to doses from $10^{13}/cm^2$ to $10^{14}/cm^2$ was extracted by fitting the experimental rocking curves to the calculated ones based on the dynamical diffraction model.[14] The parallel strain is always zero. The depth profile of the perpendicualr strain has a shape similar to that of the room-temperature implanted samples (see Fig. 7.2-6).[35] The strain decreases to about 90% of the initial value (measured 1 hr after implantation) in about 1 month and is almost constant thereafter. The amount of decrease observed here is smaller than that seen in similarly implanted GaAs(100) samples (where a decrease of $\sim$ 50% is observed).[39] We discuss only the final strain measured after one month or more in the rest of this section.

The maximum perpendicular strain as a function of the ^{40}Ar dose is shown in Fig. 7.4-1 (∇). It is evident that for a given dose, the final strain produced by implantation at 100K is greater than that generated at 300K. This means that implantation at low temperature followed by room temperature annealing is not eqiuvalent to that at room temperature. This dissimilarity is a well-known fact to the Si implantation community and applies also to other semiconductors. This fact shows that the interaction of defects and the dynamical annealing during the implantation are a crucial mechanisim in determining the final defect microstructure and damage level. On the other hand, the dose dependence of the strain is similar to that of the room-temperature-implanted samples (Δ in Fig. 7.4-1). One can again identify three distinct regimes of damage production.[36] The strain

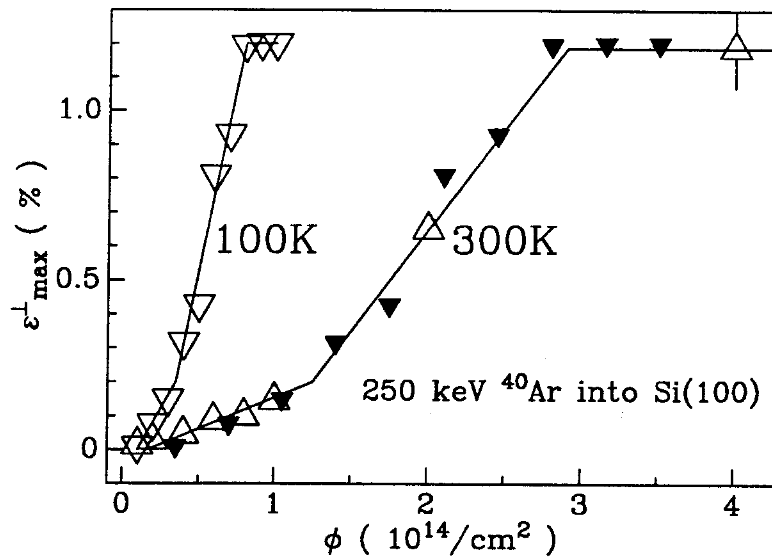

FIG. 7.4-1 The maximum perpendicular strain extracted from the dynamical x-ray diffraction simulations of experimental rocking curves as a function of the 250 keV ^{40}Ar dose of implantations at 100K ($\triangledown$) and at 300K ($\triangle$) into Si(100). The solid line is to stress the trend. The modified data points (filled inverse triangle) are obtained by multiplying the dose of the data o by a factor of 3.5.

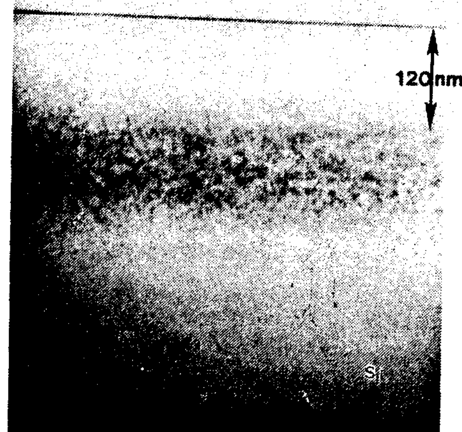

Fig. 7.4-2 The cross-sectional TEM (from Ref. 40) of the sample implanted by 250 keV 5×10^{13} ^{40}Ar/cm^2 into Si(100) at 100K ($\epsilon^{\perp}_{max} \sim 0.4\%$, see Fig. 7.4-1). A heavily damaged layer is located from a depth of 120 nm to 240 nm.

rises approximately linearly with dose in regime I, then rapidly increases in regime II, and finally saturates in regime III (see discussion in Ch. 7.2). Furthermore, by multiplying the dose of each data point corresponding to the 100K-implanted sample ($\bigtriangledown$ in Fig. 7.4-1) by 3.5, one obtains a modified set of data points (filled inverse triangle in Fig. 7.4-1) that are the same as those of the 300K-implanted samples ($\triangle$ in Fig. 7.4-1). The damage produced by 250 keV ^{40}Ar implantation at 100K to a dose ϕ followed by room temperature annealing is thus the same as that by implantation at 300K to a dose 3.5ϕ.[38] This result can be explained by assuming that the relationship between $\epsilon^{\perp}$ and c_D is invariant with temperature (i.e., B is constant), but that the production of stable defects rises with falling temperature.

Fig. 7.4-2 shows a cross-sectional TEM micrograph[40] of the sample implanted at 100K to a dose of 5×10^{13} ^{40}Ar/cm^2 ($\epsilon^{\perp}{}_{max} \sim 0.4\%$, see Fig. 7.4-1). There is a heavily damaged layer near the depth at which the maximum Frenkel pair concentration predicted by TRIM simulation[18] occurs. The damage consists of clusters. The average size of each cluster is about 5 nm.[41] This is the same size as that observed in room-temperature implanted Si samples (see Ch. 7.2).[28,29] Since the strain induced by the defects is determined by their microstrcuture, and their size in particular (see Ch 7.2), the same cluster size in the liquid-nitrogen- and room-temperature implanted Si explains why the relationship between the strain and defect concentration obtained previously for the room-temperature implanted samples[36] also applies to low-temperature implanted samples, i.e.,

$$\epsilon^{\perp} = Bc_D \approx 0.01c_D. \qquad (7.4-1)$$

C. Generalization to any low temperature of implantation

The strain in the samples implanted at 100K by 230 keV ^{28}Si or 570 keV ^{131}Xe ions was also obtained from the rocking curve analysis.[38] The parallel strain is again zero. The perpendicular strain also decreases to about 90% of the initial value in about one month and saturates afterwards. The strain rises nonlinearly with dose for all ions. The transition occurs at a strain value of about $\sim 0.1 - 0.2\%$, the same as that of the room-temperature implanted samples. This means that the transition is not sensitive to the implantation ions and temperature, but is determined by the intrinsic damage level in the implanted layer. For a given dose, the final damage produced by implantation at 100K is always larger than that at 300K, for all ions. Furthermore, as for the 250 keV ^{40}Ar implanted samples discussed above, the strain or defect concentration produced by implantation at 300K can be obtained from that at 100K by a scaling of dose for all ions,[38]

$$230\ keV\ ^{28}Si: \quad \epsilon^{\perp}(100K,\phi) = \epsilon^{\perp}(300K, 5.5\phi) \quad or \quad c_D(100K,\phi) = c_D(300K, 5.5\phi);$$

$$250\ keV\ ^{40}Ar: \quad \epsilon^{\perp}(100K, \phi) = \epsilon^{\perp}(300K, 3.5\phi) \quad or \quad c_D(100K, \phi) = c_D(300K, 3.5\phi);$$

$$570\ keV\ ^{131}Xe: \quad \epsilon^{\perp}(100K, \phi) = \epsilon^{\perp}(300K, 2.7\phi) \quad or \quad c_D(100K, \phi) = c_D(300K, 2.7\phi).$$

The scaling factor decreases from 5.5 for ^{28}Si ions to 2.7 for ^{131}Xe ions, meaning that the difference of the measured damage between implantation at room and low temperature is most pronounced for light ^{28}Si ions and least pronouced for heavy ^{131}Xe ions. This again supports the notion that the measured damage at room temperature is related to the stability of defects produced during ion implantation.[36] The light ^{28}Si ions produce some simple vacancy-interstitial defects that are unstable and mostly recombine. The heavy ^{131}Xe ions produce more defect complexes and clusters that are stable.

Given the above results, we propose the following generalization of (i) the linear relationship between $\epsilon^{\perp}$ and c_D,

$$\epsilon^{\perp}(T, \phi) = Bc_D(T, \phi), \qquad (7.4-2)$$

where B is a constant for a given target (~ 0.01 for Si); and (ii) the scaling behavior,

$$\epsilon^{\perp}(T, \phi) = \epsilon^{\perp}(T_o, \lambda\phi) \qquad or \qquad c_D(T, \phi) = c_D(T_o, \lambda\phi), \qquad (7.4-3)$$

where λ is a dimensionless parameter that depends on two temperatures T and T_o. This enables one to compute the damage produced by implantation to a dose of ϕ at temperature T and measured at an elevated temperature T_o from the results obtained by implantation at T_o, if one knows the scaling parameter λ. We further assume that λ scales as the ratio of two temperatures based on the dimensional arguments,

$$\lambda(T, T_o) \propto (\frac{T}{T_o})^{-\beta}, \qquad (7.4-4)$$

where β is the "critical exponent," which depends on the incident ions. From the above results for ^{28}Si, ^{40}Ar, and ^{131}Xe ions, we see that β has a value close to 1. By investigating implantation damage at various low temperatures (< 300K), one could test the proposed scaling behavior and extract the β parameter.

References

1. F.L. Vook, ed. *Radiation Effects in Semiconductors*, Plenum Press, New York, 1968.
2. G.D. Watkins, J. Phys. Soc. Japan 18, Suppl. II, 22 (1963).
3. L.J. Cheng, J.C. Corelli, J. W. Corbett, and G.D. Watkins, Phys. Rev. 152, 761 (1966).
4. L. Chadderton and F. Eisen, eds. *Proc. 1st Int. Conf. on Ion implantation*, Gordon and Breach, New York, 1971.
5. J.F. Gibbons, Proc. IEEE, Vol. 60, 1062 (1972).
6. J.W. Mayer, L. Eriksson, S.T. Picraux, and J.A. Davis, Can. J. Phys. 46, 663 (1968).
7. M.L. Swanson, J.R. Parsons, and C.W. Hoelke, *Radiation Effects in Semiconductors*, eds. J.W. Corbett and G.D. Watkins (Gordon and Breach, New York, 1971), p. 359.
8. S. Kurtin, G.A. Shifrin, and T.C. McGill, Appl. Phys. Lett. 14, 223 (1969).
9. V.S. Speriosu, B.M. Paine, M-A. Nicolet, and H.L. Glass, Appl. Phys. Lett. 40, 604 (1982).
10. E.Glaser, G. Götz, N. Sobolev, and W. Wesch, Phys. Stat. Sol. A69, 603 (1982).
11. J.S. Williams, R.G. Elliman, W.L. Brown, and T.E. Seidel, Phys. Rev. Lett. 55, 1482 (1985).
12. A.E. White, K.T. Short, R.C. Dynes, J.P. Garno, and J.M. Gibson, Appl. Phys. Lett. 50, 95 (1987).
13. P.A. Packan and J.D. Plummer, Appl. Phys. Lett. 56, 1787 (1990).
14. C.R.Wie, T.A. Tombrello, and T. Vreeland, Jr., J. Appl. Phys. 59, 3743 (1986).
15. L. Tewordt, Phys. Rev. 109, 61 (1958).
16. C. Kittel, *Introduction to Solid State Physics*, 5th ed. (John Wiley & Sons, New York, 1976) p. 126.
17. E. Bogh, Can. J. Phys. 46, 653 (1968).
18. J.P. Biersack and L.G. Haggmark, Nucl. Instr. and Meth. 174, 257 (1980).
19. J.W. Corbett, J.P. Karins, T.Y. Tan, Nucl. Instr. and Meth. 182/183, 457 (1981).
20. D.A. Thompson and R.S. Walker, Nucl. Instr. and Meth. 132, 281 (1976).
21. F.F. Morehead, Jr. and B.L. Crowder, Rad. Eff. 6, 27 (1970).
22. J.R. Dennis and E.B. Hale, J. Appl. Phys. 49, 1119 (1978).
23. J.D. Eshelby, *Solid State Physics*, F. Seitz and D. Turnbull, eds. (Academic Press, New York, 1956) p. 79.
24. H.G. Haubold and D. Martinsen, J. Nucl. Mater. 69/70, 644 (1978).
25. F.L. Vook, Phys. Rev. 125, 855 (1962).

26. M.W. Thompson, *Defects and Radiation Damage in Metals* (University Press, Cambridge, 1969), p. 16.

27. R.O. Simmons and R.W. Balluffi, J. Appl. Phys. 30, 1249 (1959).

28. D.J. Mazey, R.S. Nelson, and R.S. Barnes, Phil. Mag. 17, 1145 (1968).

29. M.O. Ruault, J. Chaumont, and H. Bernas, Nucl. Instr. and Meth. 209/210, 351 (1983).

30. W. Jung and G.S. Newell, Phys. Rev. 132, 648 (1963).

31. H.J. Stein, F.L. Vook, and J.A. Borders, Appl. Phys. Lett. 14, 328 (1969).

32. L.M. Howe, M.H. Rainville, H.K. Haugen, and D.A. Thompson, Nucl. Instr. and Meth. 170, 419 (1980).

33. F.L. Vook and H.J. Stein, Rad. Eff. 2, 23 (1969).

34. O.W. Holland, S.J. Pennycook, and G.L. Albert, Appl. Phys. Lett. 55, 2503 (1989).

35. G. Bai and M-A. Nicolet, submitted to J. Appl. Phys.

36. G. Bai and M-A. Nicolet, J. Appl. Phys., July 1, 1991.

37. B.M. Paine and V.S. Speriosu, J. Appl. Phys. 62, 1704 (1987).

38. G. Bai and M-A. Nicolet, unpublished.

39. G. Bai, D.N. Jamieson, M-A. Nicolet, T. Vreeland, Jr., Mat. Res. Soc. Symp. Proc. 93, 67 (1987).

40. C.J. Tsai, A. Dommann, M-A. Nicolet, and T. Vreeland, Jr., J. Appl. Phys. 69, 2076 (1991).

41. C.J. Tsai, private communication.

Chapter 8 Ion Implantation in Heterostructures

8.1 Introduction

Epitaxial heterostructures are the building blocks of novel electronic and photonic devices. Some effects of ion beams on these structures have been actively explored in the past decade from the viewpoints of both fundamental materials research and potential applications.[1-22] Most earlier studies focused on III-V compound semiconductor superlattices.[1-5] Many interesting phenomena pertaining to interaction of ion beams with superlattices were observed, such as compositional disordering and mixing of AlAs/GaAs superlattices by ion implantation and subsequent annealing,[1] superposition of strain induced by damage and built-in (intrinsic) strain in AlGaAs/GaAs[2] and GaAsP/GaP[3] superlattices, and selective amorphization of AlAs/GaAs heterostructures and superlattices.[4,5] Ion implantation can also induce the generation of misfit dislocations and strain relaxation in strained-layer superlattices.[6] Radiation damage in some silicides was also explored in the past decade.[7-17] Epitaxial $NiSi_2$ and $CoSi_2$ films on Si can be amorphized by ion implantation, and solid phase epitaxial regrowth proceeds in a layer-by-layer manner.[8-12] The resistivity of these metallic silicides increases upon implantation.[13,14] Compared to metallic silicides, semiconducting silicides such as $ReSi_2$ are more susceptible to radiation damage,[15,16] and the resistvity of semiconducting $ReSi_2$[16] and $CrSi_2$[17] decreases upon ion implantation, which is opposite to what metallic silicides do. Recently, there has been a surge of interest in GeSi/Si heterostructures, because of the successful demonstration of high-speed heterojunction bipolar transistors. Some properties of GeSi/Si heterostructures under ion beams, such as amorphization of GeSi by implantation and solid phase epitaxial regrowth,[18,19] selective damage production and amorphization in GeSi/Si heterostructures and superlattices,[5,20] enhanced strain relaxation of implanted GeSi/Si,[21] and strain modification in ion-assisted grown GeSi layers,[22] have been studied.

In the following sections, we describe some of our results on the response of epitaxial $CoSi_2$,[23] $ReSi_2$,[15,16] and GeSi[24] films to ion implantation. Properties related to damage production and annealing, stability of strained layers under implantation and subsequent annealing, and strain induced by defects, are the focus of our investigation.

8.2 Damage production and annealing in ^{28}Si implanted $CoSi_2$ films

Transistion-metal silicides have applications as contacting layers in Si-MOSFET integrated circuits. Compared to Si, the metallic silicides are highly resistive to radiation damage.[7-12] Most previous studies focused on the amorphization of the silicides by implantation and recrystallization by subsequent thermal annealing.[8-12] The amorphized $CoSi_2$ layer on a crystalline seed recrystallize in a layer-by-layer manner by solid phase epitaxy.[9-12] Hensel et al.[13] studied the effect of ion implantation on carrier transport of $CoSi_2$ films and found that the resistivity increases with dose. In this section, we report some studies on defects production in room-temperature ^{28}Si implanted $CoSi_2$ films on Si(111), and concentrate on the strain and its relationship with the defects in the implanted films.[23] Damage recovery upon vacuum annealing is also investigated.

A. Experimental Procedures

An epitaxial $CoSi_2$ film 50 nm thick was grown on Si(111) at $\sim$ 600°C by MBE at UCLA (Ch. 2.2). The samples were implanted at room temperature in vacuum ($\sim 10^{-7}$ Torr) by 150 keV ^{28}Si ions to doses from $5 \times 10^{13}/cm^2$ to $3 \times 10^{15}/cm^2$. The maximum damage locates inside the Si substrate at a depth of $\sim$ 150 nm beneath the interface, according to TRIM88 simulation.[25] The damage in the implanted layers was characterized by 2 MeV ^4He ion channeling, Fe K_{α_1} x-ray (wavelength $\lambda = 0.1936$ nm) double crystal diffraction, and electrical resistivity measurements.

The implanted samples were annealed afterwards in vacuum ($\sim 5 \times 10^{-7}$ Torr) at 250-800°C for 60 min, and the damage recovery was monitored.

B. Results and Discussion

(i) damage production

2 MeV ^4He [111] axial channeling with a glancing exit angle (82°) was used to measure the damage in the implanted layers. The spectra of the implanted samples show that the channeling yields of both the film and the substrate rise with the dose (Fig. 8.2-1). For a given dose, the damage level in the $CoSi_2$ film is much smaller than that in the Si substrate, meaning that $CoSi_2$ is more radiation resistant than Si. The high radiation resistance of $CoSi_2$ agrees with the results of room temperature implanted Pd_2Si, $NiSi_2$,[7,8] and is consistent with the metallic nature of these silicides.

The damage build-up in the Si substrate as a function of the dose is very similar to that observed in the self-implanted Si samples (see Ch. 7.2). The damage rises slowly as the dose increases from $5 \times 10^{13}/cm^2$ to $2 \times 10^{14}/cm^2$. It then rapidly rises to the level of an amorphous Si at $5 \times 10^{14}/cm^2$.

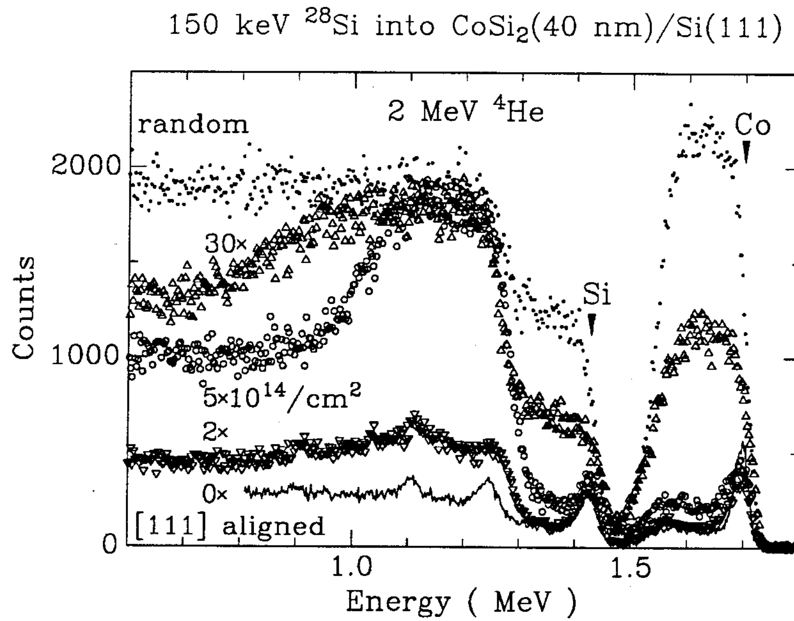

FIG. 8.2-1 2 MeV ^{4}He backscattering spectra with a beam incident along a random (•) and a [111] axial channel orientation of the as-grown $CoSi_2$(50 nm)/Si(111) (solid line); and the samples implanted at room temperature by 150 keV ^{28}Si to doses of 2× (▽), 5× (○), 30 × 10^{14}/cm^2 (△). The detected ^{4}He particles exit at an angle of 82° from the line of the incident beam.

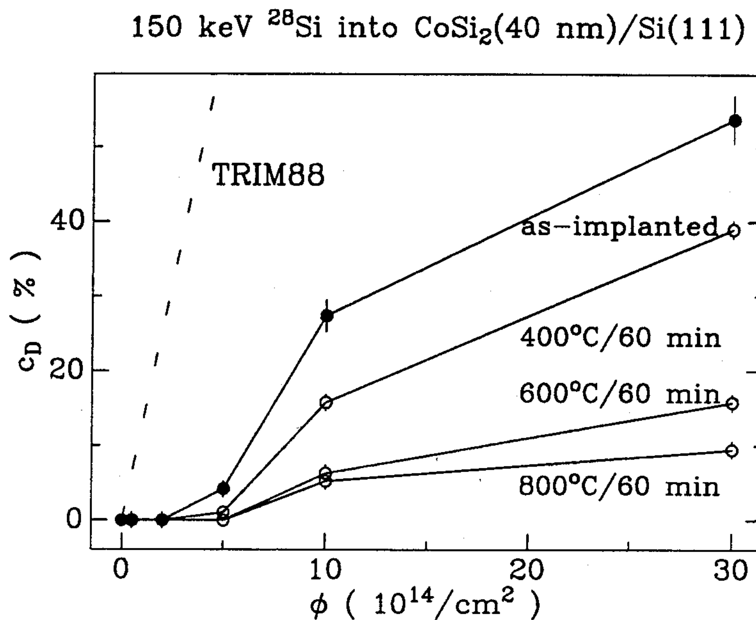

FIG. 8.2-2 The defect concentration in the $CoSi_2$ films extracted from the channeling yields of Fig. 8.2-1 vs the ^{28}Si dose, for the as-implanted samples (•), and those annealed for 60 min at 400°C (○), 600°C (△), 800°C (square). The Frenkel pair concentration as a function of dose, predicted from TRIM88, is also shown (dashed line).

As the dose increases further, the maximum damage level saturates, and the damage region widens.

On the other hand, the damage build-up in the $CoSi_2$ film has very different dose dependence. The channeling yield in the film implanted to $\leq 2 \times 10^{14}/\text{cm}^2$ is the same as that of the as-grown one ($\sim 5\%$, Fig. 8.2-1). It increases to $\sim 9\%$ at $5 \times 10^{14}/\text{cm}^2$, and rises to $\sim 56\%$ at $3 \times 10^{15}/\text{cm}^2$. Maex et al.[12] also found that the channeling yield of $CoSi_2$ films implanted at room temperature by 200 keV ^{28}Si to $2 \times 10^{15}/\text{cm}^2$ is $\sim 50\%$, in good agreement with our results. They also observed that the damage in $CoSi_2$ is sensitive to the implantation temperature, as is in Si.[26] Hewett et al.[9] demonstrated that $CoSi_2$ can be amorphized by 40-200 keV ^{28}Si implantation to $\sim 2 \times 10^{15}/\text{cm}^2$ at liquid nitrogen temperature.[9-12]

We apply the procedure outlined in Ch. 7.2 to estimate the defect concentration c_D in the $CoSi_2$ film from the channeling yield. To simplify the analysis, we assume that the fraction of displaced Si atoms in the film is the same as that of displaced Co atoms. The dechanneling factor γ_D (defined in terms of channeling yields, see Ch. 7.2), then equals[27]

$$\gamma_D = c_D + P_D(1 - c_D). \qquad (8.2-1)$$

TRIM88 simulation shows that the damage is roughly a constant through the entire film. The channeling spectra of Fig. 8.2-1 suggest the same conclusion. We therefore assume that c_D is depth-independent, so that the dechanneling probability P_D at depth x_o becomes

$$P_D = \int_0^{x_o} n\sigma_D c_D dx = (n\sigma_D x_o)c_D, \qquad (8.2-2)$$

where n is the atomic density of $CoSi_2$, and σ_D is the average dechanneling cross section of Si and Co atoms. We compute γ_D from the minimum channeling yield of the Co signal at the energy immediately beneath the surface peak (~ 1.65 MeV in Fig. 8.2-1). The corresponding depth is $x_o \approx$ 10 nm. Substituting the appropriate numbers into Eq. (8.2-2), and assuming that $\sigma_D < 10^{-18}/\text{cm}^2$ (see Ch. 7.2), one obtains

$$P_D < 0.05c_D.$$

P_D is small compared to c_D, and we therefore neglect the second term in Eq. (8.2-1) and have

$$c_D \approx \gamma_D. \qquad (8.2-3)$$

The extracted defect concentration in the $CoSi_2$ films is plotted as a function of the implantation dose in Fig. 8.2-2 (•). It is undetectable ($\leq 1\%$) after the implantation to $2 \times 10^{14}/\text{cm}^2$ and increases monotonically with the dose.

In comparison, we also computed the Frenkel pair concentration in a 150 keV ^{28}Si implanted $CoSi_2$(50 nm)/Si amorphous matrix by TRIM88 simulation (dashed line in Fig. 8.2-2). A displacement threshold energy of 15 eV and a binding energy of 1 eV were assumed. It is evident that the measured damage is only a small fraction of that directly produced by collision cascade, which suggests that the majority of the defects produced anneal out at room temperature during and after implantation. This observation leads us to hypothesize that the higher radiation resistance of $CoSi_2$ than that of Si at room temperature is due to its higher defect recombination rate, probably resulting from the higher mobility of defects in $CoSi_2$.

A heterostructure differs from a bulk crystal in that there exists intrinsic strain in an as-grown heterostructures. Implantation produces defects, which induce additional strain in the heteroepitaxial film. We use x-ray double crystal diffraction to monitor the strain change in the $CoSi_2$ film as a result of the implantation. Figure 8.2-3 shows a set of x-ray rocking curves diffracted from the (111) symmetrical plane of the $CoSi_2$/Si(111) samples implanted to a dose of (a) 0×, (b) 0.5×, (c) 1×, (d) 2×, (e) $5 \times 10^{14}/\text{cm}^2$.

On the basis of previous studies on implantation in Si(100) (see Ch. 7), we expect that the damage in the Si substrate induces positive strain, and that additional diffraction peaks will appear on the lower angle side of the bulk Si peak at $\theta_B = 18^o$ in Fig 8.2-3. Implantation to $\leq 2 \times 10^{14}/\text{cm}^2$ produces low damage in the Si substrate and induces small perpendicular strain of $\leq 0.1\%$ (see Ch. 7.2). The corresponding shift in the position for the (111) diffraction peak of the implanted layer is $\leq 0.02^o$, which lies within the main peak and hence is undetectable (see Fig. 8.2-3). Implantation to $\geq 5 \times 10^{14}/\text{cm}^2$ produces a heavily damaged or continuous amorphous layer (see Ch. 7.2); the corresponding diffraction peak then becomes weak and remains buried in the background intensity of $\sim 0.003\%$ (Fig. 8.2-1).

The peak intensity of x-ray diffracted from the $CoSi_2$ (111) planes decreases with increasing dose (Fig. 8.2-3). After implantation to a dose of $2 \times 10^{14}/\text{cm}^2$, the intensity drops to $\sim 1/4$ of that of the as-grown film, unlike the channeling yield, which is the same as that of the as-grown sample (Fig. 8.2-1&2). This fact demonstrates that x-ray diffraction is much more sensitive to low defect concentrations than channeling. The x-ray intensity from the $CoSi_2$ layer of the sample implanted to a dose of $\geq 10^{15}/\text{cm}^2$ drops below the background ($\sim 0.003\%$) and hence becomes unmeasurable. The defect concentration extracted from the channeling yield of that same sample is only about 27%. A comparison of the channeling spectra (Fig. 8.2-1) and x-ray rocking curves (Fig. 8.2-3) of the implanted $CoSi_2$ films clearly illustrates that channeling is insensitive to very low damage

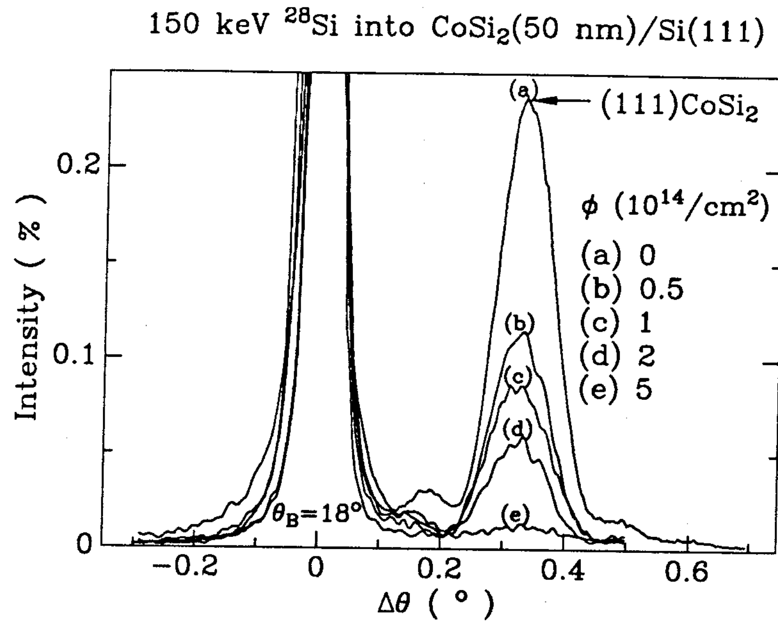

FIG. 8.2-3 Fe K_{α_1} x-ray rocking curves diffracted from the symmetrical (111) planes of (a) as-grown $CoSi_2/Si(111)$; and the samples implanted to doses of (b) 0.5×, (c) 1×, (d) 2×, (e) $5 \times 10^{14}/cm^2$. Bragg peak from the bulk Si substrate is $\theta_B = 18°$.

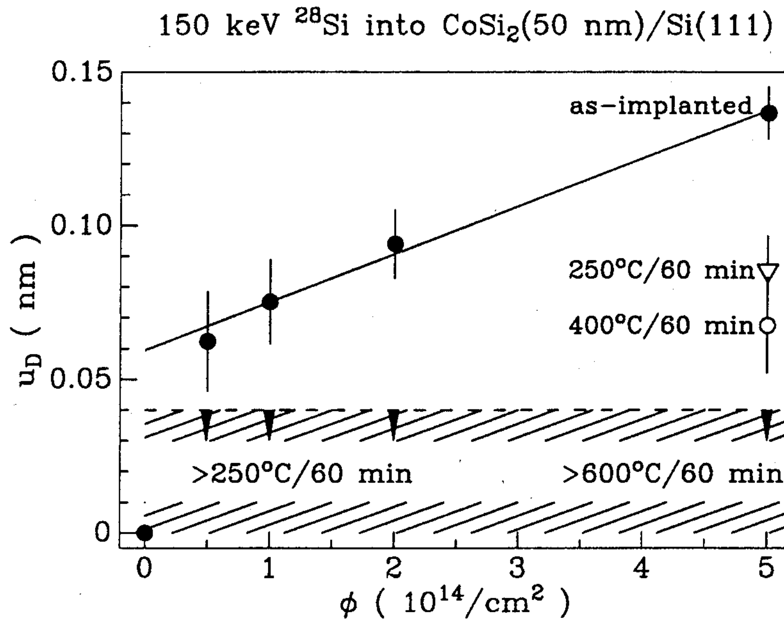

FIG. 8.2-4 The static atomic displacement induced by the defects in the $CoSi_2$ films vs the ^{28}Si dose, for the as-implanted sample (•), and for those annealed in vacuum for 60 min at 250°C (▽) and 400°C (○). The shaded area represents the error in estimating the displacement of a perfect $CoSi_2$ film.

($c_D \leq 1\%$), while the x-ray diffraction from the highly damaged films ($c_D \geq 27\%$) becomes unmeasurable. These two techniques are therefore complementary and together provide a good picture of damage production by ion implantation in $CoSi_2$.

In the following, we will analyze quantitatively the x-ray rocking curves diffracted from the $CoSi_2$ films implanted to $\leq 5 \times 10^{14}/cm^2$. The angular position of the (111) diffraction peak does not change with the dose ($\sim 0.33^\circ$, Fig. 8.2-3). This means that the perpendicular strain $\epsilon^\perp$ in the films is a roughly constant, $\sim -1.76\%$, within the experimental sensitivity ($\sim 0.08\%$). In other words, the upper limit in the difference of the magnitude of the strain between the implanted and as-grown films, $\Delta\epsilon^\perp$, is $\sim 0.08\%$. The defect concentration c_D in the corresponding films ranges from $\leq 1\%$ to $\sim 4\%$ (• Fig. 8.2-2). The above results imply that in the implanted $CoSi_2$ films, one has

$$|\Delta\epsilon^\perp| \leq 0.02 c_D. \qquad (8.2-4)$$

We were unable to measure the parallel strain in the $CoSi_2$ film, which is B-type (Ch. 2.2). Given the knowledge that the interfacial misfit dislocations do not shear at room temperature (see Ch. 2.5-6), it is reasonable to assume that the parallel strain of the film remains unchanged upon the implantation; i.e., $\Delta\epsilon^\parallel = 0$. From the above results and the relationship between the strain and lattice mismatch (see Ch. 7.2), we obtain the lattice dilatation of the $CoSi_2$ induced by the defects,

$$|\frac{\Delta a}{a}| = (\frac{1-\nu}{1+\nu})|\Delta\epsilon^\perp| \leq 0.01 c_D, \qquad (8.2-5)$$

where a is the lattice constant of the as-grown $CoSi_2$ film, and ν is Poisson's ratio of $CoSi_2$ (=1/3, see Ch. 2.6). The coefficient relating $|\Delta a/a|$ to c_D for $CoSi_2$ is ≤ 0.01, consistent with that for Si (~ 0.007, see Ch. 7.2).

The full-width at half-maximum of all diffraction peaks that are strong enough to be detected (films implanted to $\leq 5 \times 10^{14}/cm^2$) is an invariant, independent of the damage induced by ion implantation (Fig. 8.2-3). The peak broadening of the as-grown film is due to the finite film thickness. This result implies that the x-ray diffraction from the implanted film is highly coherent, and suggests that the damage in the implanted film consists mainly of randomly distributed point-like defects. The x-ray diffraction can therefore be modeled by a static Debye-Waller factor, which does not change the peak width but decreases only the intensity.[28] The ratio of the peak intensity from the implanted film, I_D, to that from the as-grown one, I_V, equals,[28]

$$\frac{I_D}{I_V} = exp(-\frac{16\pi^2}{3} u_D^2 \frac{\sin^2\theta_B}{\lambda^2}), \qquad (8.2-6)$$

where u_D is the mean-square root of the atomic displacement caused by the point-like defects in the implanted film. For Fe K_{α_1} x-ray diffracted from CoSi(111) planes, Eq. (8.2-6) results in

$$u_D = 0.085\sqrt{\ln\frac{I_V}{I_D}}\ (nm). \qquad (8.2-7)$$

The displacement u_D in the implanted $CoSi_2$ film thus extracted from the measured intensities in Fig. 8.2-3 rapidly rises to ~ 0.06 nm after implantation to $5\times10^{13}/cm^2$, and then increases linearly with dose (• in Fig. 8.2-4).

We also measured the resistivity in the implanted film to monitor the defects build-up. Four-point-probe methods were used to measure the sheet resistance of the $CoSi_2$ films. The resistivity of the selected samples was also measured by the van der Pauw method, and agrees with that from four-point-probe measurements. Current-voltage measurements show that the vertical resistance across the silicide-silicon interface is always much greater than the sheet resistance of the silicide film for all samples, implying that the film is practically insulated from the substrate. The measured resistivity of the $CoSi_2$ films increases from $\sim 16\ \mu\Omega cm$ for the as-grown sample to $\sim 300\ \mu\Omega cm$ for the sample implanted to $5\times10^{14}/cm^2$. It flattens off up to $3\times10^{15}/cm^2$.

Resistivity, ρ, in metals can be decomposed into two terms according to Matthiessen's rule,[13]

$$\rho = \rho_L + \rho_D, \qquad (8.2-8)$$

where ρ_L is the lattice (Bloch-Gruneisen) contribution, and ρ_D results from carrier scattering by defects. Hensel et al.[13] measured the resistivity of 2 MeV ^4He bombarded $CoSi_2$ films at 4-300K and found good agreement with Eq. (8.2-8). These authors also established that the resistivity of the samples implanted to different doses has a similar temperature dependence, meaning that the lattice contribution ρ_L is the same regardless of the damage (so long as the film is not amorphized to cause localization of carriers). The difference of ρ between the bombarded and the as-grown films, $\Delta\rho$, hence equals $\Delta\rho_D$, the resistivity contribution from radiation-induced defects. Hensel et al.[13] discovered that $\Delta\rho_D$ rises approximately linearly with dose till $\sim 100\ \mu\Omega$cm and then flattens off with further dose increase. The resistivity jumps abruptly to $\sim 1000\ \mu\Omega$cm once the $CoSi_2$ is amorphized, and remains constant thereafter.

We used the van der Pauw method to measure the resistivity of the $CoSi_2$ film for selected samples at 130-300K. The temperature dependence of the resistivity agrees with the prediction of Eq. (8.2-8), and that reported by Hensel.[13] We assume in the following that the resistivity difference $\Delta\rho$ between the implanted and the as-grown $CoSi_2$ films equals that induced by the implantation

$\Delta\rho_D$ for all our samples. $\Delta\rho_D$ increases with dose to $\sim 280\ \mu\Omega$cm at $5 \times 10^{14}/\text{cm}^2$ and flattens off up to $3 \times 10^{15}/\text{cm}^2$ (• in Fig. 8.2-5).

The resistivity from carrier scattering by point-like defects is proportional to the density of scatterers. The initial rise of $\Delta\rho_D$ ($\phi \leq 5 \times 10^{14}$) suggests that the implantation produces point-like defects, which build up with increasing dose.[13] This conclusion is very similar to that drawn from x-ray diffraction results (see previous discussion). Figure 8.2-6 plots the resistivity caused by defects as a function of the atomic displacement induced by defects in the $CoSi_2$ film implanted to a dose of $\leq 5 \times 10^{14}/\text{cm}^2$. The plot shows a good correlation between these two indicators of the defect concentration in the $CoSi_2$ films. From $5 \times 10^{14}/\text{cm}^2$ to $3 \times 10^{15}/\text{cm}^2$, $\Delta\rho_D$ is roughly a constant ($\sim 280\ \mu\Omega$cm, Fig. 8.2-5), while the defect concentration c_D extracted from the channeling yields increases from $\sim 4\%$ to $\sim 54\%$ (• in Fig. 8.2-2). This suggests that the flat $\Delta\rho_D$ is probably indicative of some agglomeration of defects.[13]

(ii) damage annealing

2 MeV ^{4}He axial channeling was also used to monitor the change of the channeling yield as a function of the annealing temperature. The annealing characteristics of the damaged Si substrate is the same as that of implanted bulk Si.[27] At low damage level ($\phi \leq 2 \times 10^{14}/\text{cm}^2$, Fig. 8.2-1), the channeling yield decreases as the annealing temperature rises. The dominant process is probably the recombination of point-like defects. At high damage levels near the amorphization threshold ($\phi = 5 \times 10^{14}/\text{cm}^2$, Fig. 8.2-1), the channeling spectrum does not change after 60 min isochronal annealing at 250°C. The channeling yield decreases after 400°C annealing, and becomes the same as that of the as-grown sample after 600°C annealing. The channeling spectrum of the amorphized samples ($\phi \geq 10^{15}/\text{cm}^2$, Fig. 8.2-1) does not change after 400°C annealing. In that case, appreciable solid-phase epitaxial growth occurs after annealing at 600°C. However, the channeling yield is very high ($\sim 50\%$) and remains that high after 800°C annealing. A high density of extended defects (e.g., dislocation loops, microtwins) is probably present.

The qualitative annealing features of the $CoSi_2$ films are simpler than those of the Si substrate, since the film is not amorphized after implantation to the highest dose of $3 \times 10^{15}/\text{cm}^2$ (see Fig. 8.2-1). The channeling yields of the implanted films decrease with increasing annealing temperature. The defect concentration in the film after annealing at various temperatures, extracted from the channeling yield according to Eq. (8.2-3), is shown in Fig. 8.2-2. The films implanted to a dose of $\leq 5 \times 10^{14}/\text{cm}^2$ completely recover, while those implanted to doses $\geq 10^{15}/\text{cm}^2$ do not. We believe that the non-zero c_D ($\sim 10\%$, Fig. 8.2-2) after annealing is more indicative of the presence of

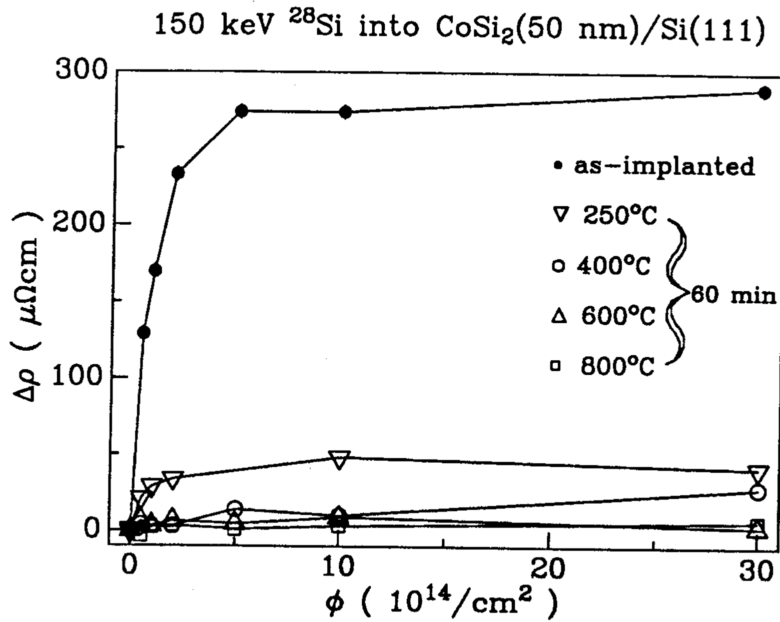

FIG. 8.2-5 The resistivity difference between the implanted and as-grown $CoSi_2$ films vs the dose, for the as-implanted sample (•), and for those annealed in vacuum for 60 min at 250°C (▽), 400°C (∘), 600°C (△), 800°C (square).

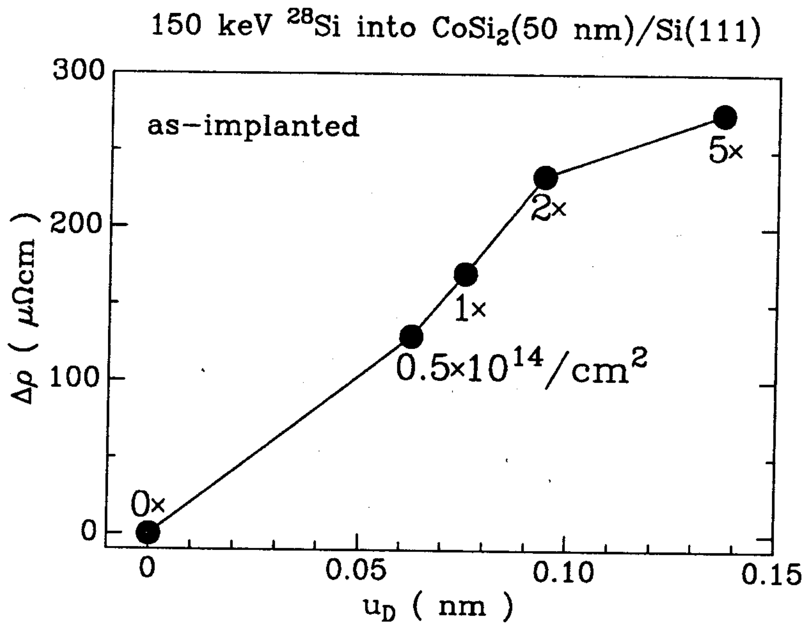

FIG. 8.2-6 The resistivity difference vs the static displacement of the lightly damaged $CoSi_2$ films ($c_D \leq 4\%$ or $\phi \leq 5 \times 10^{14}/\mathrm{cm}^2$). The approximately linear relationship indicates a good correlation between the concentration of the carrier scatterers and the structural defects in such films.

extended defects than of a measure of the point-like defect concentration. The imcomplete recovery of the film coincides with that of the Si substrate.

Upon thermal annealing, both the angular position and width of the x-ray diffraction peak from the lightly damaged $CoSi_2$ films ($c_D \leq 4\%$) remanin unchanged. This means that the strain of the $CoSi_2$ films does not change, and indicates that the presence of a small defect concentration in the film does not enhance the strain relaxation upon thermal annealing. The x-ray peak intensity rises with increasing temperature. For the films implanted up to $2 \times 10^{14}/\text{cm}^2$, the intensity after 250°C is the same as that of the as-grown film within the experimental uncertainty ($\sim 20\%$). The uncertainty in the intensity measurements causes a corrsponding uncentainty in the estimation of the atomic displacement extracted according to Eq. (8.2-7),

$$\frac{(\delta u_D/u_D)}{\sqrt{(\delta I_D/I_D)^2 + (\delta I_V/I_V)^2}} = \frac{0.5}{\ln(I_V/I_D)}. \qquad (8.2-9)$$

This relationship shows that u_D of the film with the intensity close to that of I_V has a large percentage error. For a percentage error of the x-ray intensity of $\sim 20\%$, the error of u_D is about 0.04 nm, which means that measured displacements of 0-0.04 nm all correspond to a perfect $CoSi_2$ film. The displacement extracted for the films implanted to $\leq 2 \times 10^{14}/\text{cm}^2$ after all annealings is ≤ 0.04 nm (Fig. 8.2-4). This suggests that these films recover completely after all annealings. The displacement of the film implanted to $5 \times 10^{14}/\text{cm}^2$ decreases with increasing annealing temperature, and becomes indistinguishable from that of the as-grown film after 600°C annealing (Fig. 8.2-4).

The heavily damaged $CoSi_2$ films ($\phi \geq 10^{15}/\text{cm}^2$) have very different annealing characterisitics. Upon thermal annealing, the x-ray peak intensity rises above the background ($\sim 0.003\%$) and becomes measurable. The peak position is about the same as that of the as-grown film, meaning that the strain of the heavily damaged films does not change after annealing. However, the peak is much broader and weaker than that of the as-grown film, even after 800°C. This result signifies that the strain in the annealed films is very inhomogeneous, and indicates the presence of extended defects. The above results correlate well with those obtained from channeling measurements.

The resistivity of the $CoSi_2$ films of all samples decreases drastically after 250°C (∇ in Fig. 8.2-5), and becomes about the same as that of the as-grown sample after 600°C ($\triangle$ in Fig. 8.2-5). The decrease of the resistivity of the low damaged films ($\phi \leq 5 \times 10^{14}/\text{cm}^2$) after annealing correlates well with the recovery of structure defects probed by channeling and x-ray diffraction measurements. For the highly damaged films ($\phi \geq 10^{15}/\text{cm}^2$), the structural recovery after annealing is incomplete, with a channeling yield of $\sim 10\%$ (greater than that of the as-implanted films to a dose $\leq 5 \times 10^{14}/\text{cm}^2$), and x-ray diffraction suggests that there exist extended defects in these annealed films. Yet the

resistivity of such films is about the same as those of the structurally perfect ones, much less than that of the as-implanted films of any dose. Apparently the extended defects that still exist in the highly damaged films after annealing are ineffective scattering centers for the carrier transport.

In summary, we discovered that MeV ion channeling is well suited to characterize heavily damaged $CoSi_2$ films ($c_D > 1\%$), while x-ray diffraction is for lighly damaged ones. Resistivity is a valid indicator of the damage over the entire range. A linear relationship exists between the structural and electrical defects in lightly damaged films. Such a relationship is absent in heavily damaged ones, where the resistivity flattens but the defect concentration further increases with dose. The lightly damaged films recover completely upon thermal annealing, whereas the heavily damaged ones do not. The residual defects after annealing are of the type of extended defects such as dislocation loops and microtwins, and are ineffective for carrier scattering.

8.3 Radiation damage in $ReSi_2$ by an MeV ^4He beam

Backscattering and channeling spectrometry are extensively used to probe compositional and structural properties of materials within submicron depths below the surface.[29,30] They have become routine analytical tools to characterize electronic materials. The effect of an analysis beam (of MeV ^4He or ^1H ions) on the materials studied is therefore important both from a practical point of view for the correct interpretation of experimental data, and from a fundamental point of view for the understanding of MeV ion–solid interactions.

In the past two decades, there have been about a dozen studies explicitly concerned with the radiation damage in solids by MeV ^4He and ^1H beams.[31–41] Alkali halides are the most extensively studied class of materials[31–34], where the ionization of target atoms by incident ions is the main mechanism for damage production. In Si and Ge, the damage is mainly produced by elastic nuclear collisions.[35–37] In GaP, both inelastic electronic ionization and elastic nuclear collisions contribute to the damage.[38] Extensive radiation damage has also been observed in some oxides ($BaTiO_3$[39], NbO[40], Al_2O_3[41]). Little work has been done on the radiation damage in transition-metal silicides by MeV ^4He and ^1H ions, in spite of the widespread utilization of the backscattering and channeling technique in the characterization of these thin films. J.C. Hensel et al.[13] studied the effect of 2 MeV ^4He irradiation on the resistivity of $CoSi_2$ and $NiSi_2$ thin films. H. Ishiwara et al.[7] used MeV ^4He ion beam to analyze the radiation damage produced by 100 keV ^{40}Ar ions in epitaxial Pd_2Si and $NiSi_2$ thin films grown on Si substrates.

We present here some experimental results on the damage induced by MeV ^4He ion irradiation

in epitaxial $ReSi_2$ thin films grown on Si(100) substrates. Both the minimum yield of [100] axial channeling and the half angle were measured as a function of sample exposure to the ^{4}He analysis beam. The damages induced at room temperature by beams incident along a random direction and an axial [100] direction are compared. We will show that the damage is produced by elastic nuclear collisions. The measured amount of damage produced by a random incident beam agrees with that computed from TRIM[25]. This agreement indicates that the total amount of damage produced by elastic nuclear collisions is preserved at room temperature.

The epitaxial $ReSi_2$ film of $\sim$ 150 nm thick was grown on a hot Si(100) substrate ($\sim$ 650°C) by "reactive deposition epitaxy" in ultrahigh vacuum ($\sim 10^{-9}$ Torr) at Colorado State University.[42] Details of the growth procedure and the characterization of the epitaxial $ReSi_2$/Si(100) structure were described in Ch. 3.2. The fundamental parameters of channeling, the minimum yield, χ_{min}, and the critical angle, $\psi_{1/2}$, of as-grown $ReSi_2$/Si(100) sample were discussed in Ch. 3.3.[43] Radiation damage produced by the analysis beam is the focus here.

Experiments were performed at room temperature, using an MeV ^{4}He beam as both an irradiation source and analysis probe, with the $ReSi_2$/Si(100) sample mounted on a goniometer with x-y translations and with two axes of rotation. To eliminate the effect of irradiation during the process of aligning the [100] channel with the incident beam, the channeling spectra were taken according to the following procedure: we first used the two rotation axes to find the [100] axial channel at one corner of the sample (beam size $\sim 0.2 \times 0.2$ cm^2, sample size $\sim 1 \times 1$ cm^2) and then translated the sample so that a virgin region of the sample was exposed to the irradiation beam for analysis. Figure 8.3-1 shows the backscattering spectra of the sample for a beam with random incidence (solid line) and for a beam incident along the [100] axial channel at three different damage stages, (a) as-grown (the dose during the channeling measurement of the as-grown sample is less than $\sim 10^{14}$/cm^2 and the damage induced is negligible), after irradiation by a 1.4 MeV $\sim 10^{17}$/cm^2 ^{4}He ion beam incident (b) along the [100] axial direction or (c) along a random direction. Three facts are evident from the spectra: (1) the as-grown $ReSi_2$ sample is highly epitaxial with a Re minimum yield χ_{min} of $\sim$ 2% (the fraction of counts below the surface peak of the aligned spectrum normalized with respect to that of a random spectrum); (2) substantial doses of the analysis beam produce damage in the $ReSi_2$ film, which results in noticeable increases of the minimum yield; and (3) the amount of damage produced by irradiation with an aligned beam is much smaller than that with a beam of random incidence. This last fact suggests that the damage is produced predominantly by elastic collisions among nuclei.

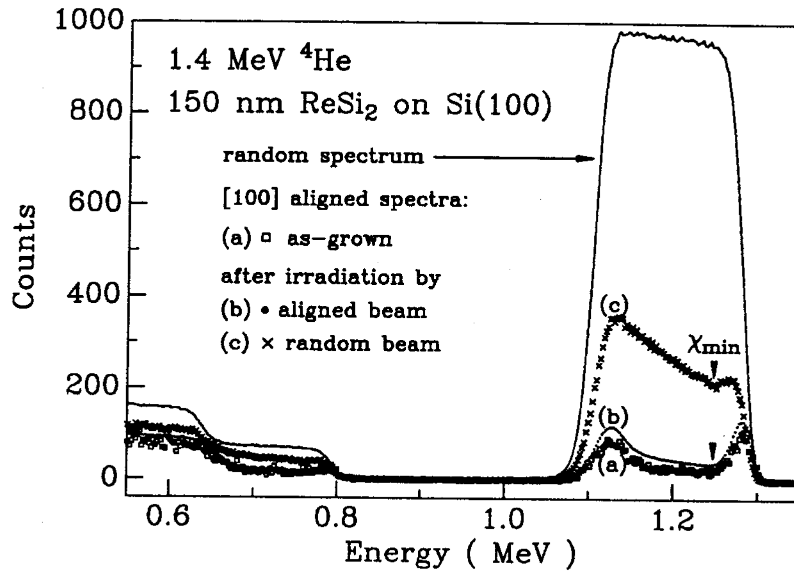

FIG. 8.3-1 1.4 MeV ^{4}He backscattering and channeling spectra of a 150 nm thick epitaxial $ReSi_2$ layer grown on a Si(100) substrate. All four spectra were taken at room temperature and are plotted by normalizing incident doses to a common value. The solid line is the spectrum for random incidence. The three [100] channeling spectra are for samples irradiated at room temperature with doses of (a) $\sim 10^{14}/cm^2$, $\sim 10^{17}/cm^2$ (b) in a [100] aligned direction and (c) in a random direction.

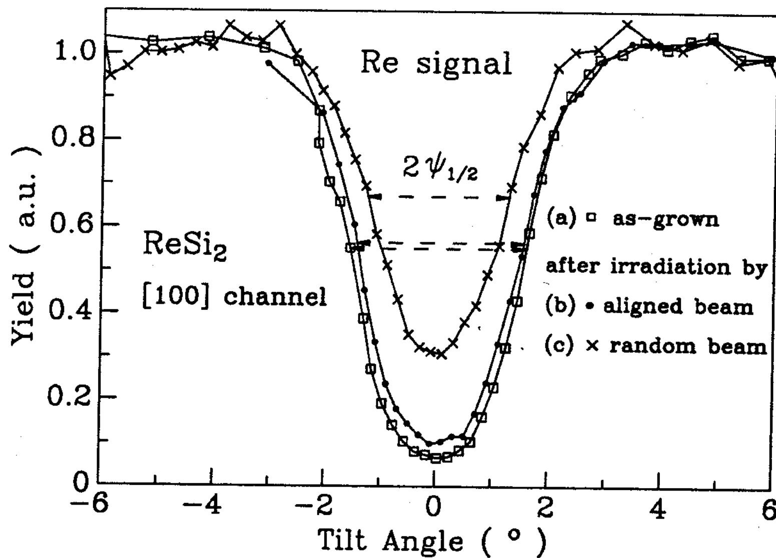

FIG. 8.3-2 The normalized backscattering yield of the Re signal versus angle of tilt between the incident beam and the [100] direction of the sample for the three damage stages of Fig. 8.3-1.

To further probe the damage structure of $ReSi_2$ by an MeV ^4He beam, we also measured the critical angles for the [100] axial channel before and after irradiation. In this channeling orientation, the atomic columns of the $ReSi_2$ lattice consist of only Si or only Re atoms (see Fig. 3.3-3). There are therefore two critical angles, one for Si columns and one for Re columns (see Fig. 3.3-2).[43] The angular scan and the critical angle of Re at the three damage stages discussed above (Fig. 8.3-1) are shown in Fig. 8.3-2 For the virgin sample, the critical angle for Re (as well as Si) agrees with Lindhard's prediction.[30] The critical angle decreases as the minimum yield (or damage) increases. It is known that disorder in the form of amorphous regions[44] or a mosaic structure[45,46] increases both the minimum yield and the critical angle. On the other hand, a spatially correlated disorder similar to that produced by lattice vibrations increases the minimum yield and decreases the critical angle.[36] The angular scan measurements on irradiated $ReSi_2$ (Fig. 8.3-2) therefore suggest a defect structure of correlated displacements for MeV ^4He irradiated $ReSi_2$. The same conclusion about the defect structure was obtained from the angular scans of the Si signal.

The damage induced by 1.4 MeV ^4He irradiation was quantified by monitoring the minimum yields of the [100] axial channeling spectra as a function of the total dose of exposure. To measure damage by a beam incident along a random direction, the sample was repetitively irradiated and then oriented in the [100] direction to take a channeling spectrum at increasing dose levels. Since a channeled beam generates little damage compared to that generated by the random beam (see Fig. 8.3-1), the channeling yield may be measured without significantly increasing the state of damage. Figure 8.3-3 shows the dependence of the minimum yield χ_{min} versus dose of random irradiation. The minimum yield χ_{min} of Si (and of Re as well, $\triangle$ and $\circ$ in Fig. 8.3-3) initially increases rapidly (starting value: 14% and 2% respectively) up to a dose of $\sim 2 \times 10^{15}/cm^2$ and then with a slower rate ($\sim 2.5\%/10^{16}/cm^2$ for Si and $\sim 1.9\%/10^{16}/cm^2$ for Re).

The fact that the minimum yield for Si is always larger than that for Re is peculiar to channeling of MeV ions in a diatomic crystal,[43] not an indication of higher initial or subsequent defect concentration for the Si sublattice (see Ch. 3.3). The reason is that the minimum yield of the element with low atomic number (Si) is enhanced and dominated by the ions deflected from the columns with the element of high atomic number (Re), while the minimum yield of Re is affected little by the deflection of He from Si columns.[43] We therefore use the minimum yield χ_{min} of Re as a measure of irradiation damage in $ReSi_2$.

To obtain the dose dependence of irradiation damage by an aligned beam, we first oriented the sample in the [100] direction and then monitored the damage build-up by recording channeling

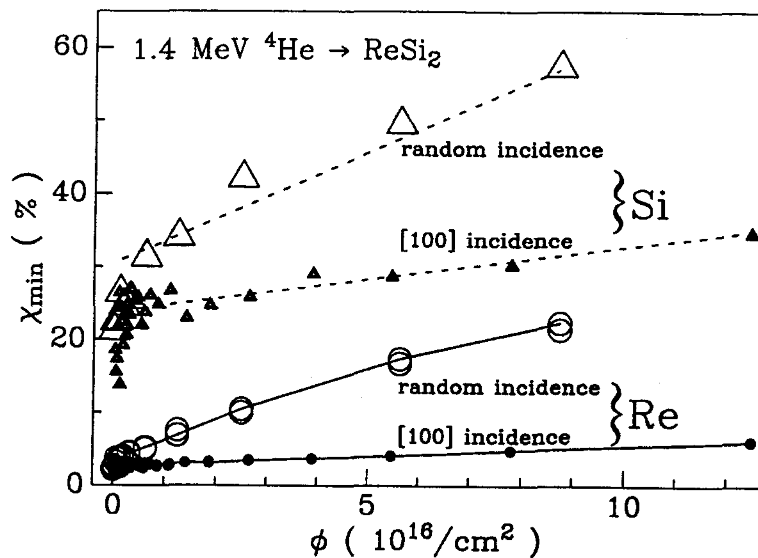

FIG. 8.3-3 The minimum channeling yields of the Si and Re signals for an epitaxial $ReSi_2$ film as a function of the 1.4 MeV ^4He irradiation dose for both a random and a [100] aligned incidence.

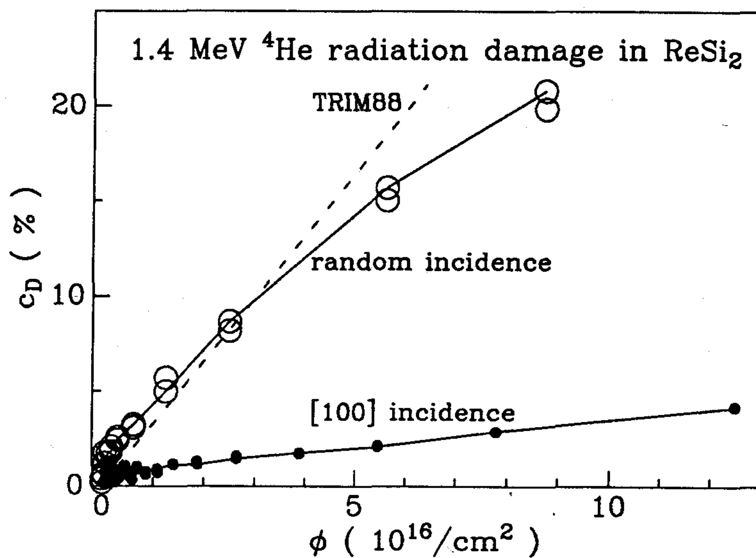

FIG. 8.3-4 Comparison of the measured defect concentration versus irradiation dose in $ReSi_2$ produced by 1.4 MeV ^4He ion beams of random (∘) and [100] aligned (•) incidence at 300K, and one calculated (dashed line) by a TRIM88 computer simulation of a beam of random incidence at 0K.

spectra at increasing dose levels during irradiation. The minimum yield $\chi_{min}(\phi)$ of the sample after irradiation of dose, ϕ, is defined as

$$\chi_{min}(\phi) \equiv \frac{dN_A(\phi)}{d\phi} / \frac{dN_R(\phi)}{d\phi}, \qquad (8.3-1)$$

where $N_A(\phi)$ and $N_R(\phi)$ are the total backscattering counts resulting from a dose ϕ of a [100] aligned and randomly incident beam, respectively. $\frac{dN_A(\phi)}{d\phi}$ was obtained from channeling measurements by numerical differentiation. $\frac{dN_R(\phi)}{d\phi}$ is a dose-independent normalization constant, obtained from a random backscattering spectrum. Figure 8.3-3 shows the dependence of the minimum yield χ_{min} versus irradiation dose for a [100] aligned beam. Again, the minimum yield χ_{min} of Si (and of Re as well, filled triangle and • in Fig. 8.3-3) initially increases rapidly up to a dose of $\sim 2 \times 10^{15}/\mathrm{cm}^2$ and then with a slower rate ($\sim 0.9\%/10^{16}/\mathrm{cm}^2$ for Si and $\sim 0.3\%/10^{16}/\mathrm{cm}^2$ for Re). The rapid initial rise, although clearly present in all four plots of Fig. 8.3-3, is difficult to grasp experimentally because of the poor statistics involved and will not be discussed further.

Energetic ions lose energy to target atoms in two processes: electronic and nuclear stopping. According to TRIM88 simulation, almost all the energy of an MeV ^{4}He ion generates electronic excitation in $ReSi_2$, and only a very small fraction of the energy ($\sim 0.3\%$) goes to the target nuclei to produce displacements. In the regime of high energy and light incident ions, the persistent damage resulting from these displacements consists mainly of isolated interstitial–vacancy pairs,[47] although some small defect clusters may also be produced. We used the TRIM88 program to simulate damage production. The simulation assumes an amorphous 150 nm thick $ReSi_2$ film on an amorphous Si substrate and computes the concentration (defect density/atomic density of $ReSi_2$) of displaced atoms as a function of depth in the linear cascade approximation.[25] A typical value for displacement threshold energy of 15 eV and binding energy of 1 eV was chosen. The maximum defect concentration in the simulation locates at a depth of $\sim 4\ \mu m$, well into the Si substrate where the majority of stopped ^{4}He ions also reside. In the $ReSi_2$ film, the defect concentration is very small and is roughly uniform in depth through the entire film. This defect concentration from the TRIM simulation is plotted versus dose in Fig. 8.3-4 (dashed line).

Experimentally, the defect concentration in a damaged crystal can be estimated from channeling measurements. When the defect concentration at depth z is $c_D(z)$ and the probability that an aligned incident beam is dechanneled by the defects over the region from the surface to the depth z is $P_D(z)$, we have[27]

$$c_D(z) + (1 - c_D(z))P_D(z) = \frac{\chi_D(z) - \chi_V(z)}{1 - \chi_V(z)}, \qquad (8.3-2)$$

where $\chi_V(z)$ and $\chi_D(z)$ are the normalized channeling yields at depth z for virgin and damaged crystals, respectively. In the near-surface region, the dechanneling probability P_D is small compared to the defect concentration c_D. Equation (8.3-2) therefore becomes

$$c_D = \frac{\chi_{min,D} - \chi_{min,V}}{1 - \chi_{min,V}}, \qquad (8.3-3)$$

where $\chi_{min,V}$ and $\chi_{min,D}$ are the minimum yields. When the minimum yield of Re is used in Eq. (8.3-3), one obtains the defect concentration in $ReSi_2$ shown in Fig. 8.3-4. An aligned beam produces only about 1/7 the number of defects produced by a random beam. This is in accord with the observation that the close encounter probability between the incident ion and the target nuclei for an aligned beam is about one order of magnitude smaller than that for a random beam[30] and our assertion above that the defects are produced by elastic collisions among nuclei.

Figure 8.3-4 shows that the measured defect concentration produced by a random beam approximately equals that computed from TRIM88. If a value for the threshold energy E_d other than 15 eV were chosen, the slope of the TRIM88 result would change inversely with E_d. However, within the range of acceptable threshold values, the qualitative agreement between the simulation and the experiment would still hold. We therefore conclude that the defects are stable at room temperature. This result is in contrast with that obtained for other silicides such as $CoSi_2$ (Ch. 8.2) and other semiconductors such as Si,[27] where the measured damage produced by light energetic ions (no dense cascade) at room temperature is much less than that predicted by TRIM88. The stability of defects may be explained by the semiconductor character and the relatively large cohesive energy of $ReSi_2$. Semiconductors are more sensitive to irradiation than metals because the strong chemical bonding in semiconductors gives a higher activation energy for vacancy-interstitial pairs to recombine. Defects are therefore more stable in semiconducting $ReSi_2$ than in metallic silicides such as $CoSi_2$. In addition, $ReSi_2$ has a cohesive energy of 8.0 $eV/atom$ (obtained from the cohesive energy[48] of elemental Re and Si and the heat of formation[49] of $ReSi_2$) compared with 4.6 $eV/atom$[48] for Si. This gives rise to a larger energy barrier for the migration of point defects in $ReSi_2$ than in Si. Defects in $ReSi_2$ are therefore more stable than those in Si. The sublinear rise of the measured defect concentration in Fig. 8.3-4 suggests that defects formed late in the irradiation are increasingly likely to be annihilated,[47] a process that results in a gradual saturation of the defect concentration as the damage increases.

In summary, epitaxial $ReSi_2$ thin films grown on Si(100) substrates were analyzed at room temperature by MeV ^{4}He backscattering and channeling spectrometry. The minimum yield of [100] axial channeling increases with increasing exposure of the $ReSi_2$ sample to the analyzing He beam. This means that $ReSi_2$ suffers irradiation damage induced by an MeV ^{4}He beam at room temperature. The damage in the film induced by a beam incident along a random direction is about one order of magnitude larger than that induced by a beam with an aligned incidence, indicating that the damage is mainly generated by elastic collisions of nuclei. The experimentally measured defect concentration produced at 300 K by a beam of random incidence is compared with the theoretically estimated one produced at 0 K in an amorphous target. The agreement is fairly good, suggesting that the defects produced by elastic nuclear collisions are stable at room temperature.

8.4 Amorphization and recrystallization of epitaxial $ReSi_2$ films

Transition-metal silicides have attracted much attention in the last decade because of their importance in Si-based microelectronics.[49,50] Some silicides, such as $ReSi_2$ and $CrSi_2$, are semiconductors with narrow bandgaps.[49,51] In the previous section, we showed that epitaxial $ReSi_2$ films suffer irradiation damage by an MeV ^{4}He beam.[15] We report here the results of the effect of 300 keV ^{28}Si and 380 keV ^{40}Ar ion implantation on some structural properties of epitaxial $ReSi_2$ films and of the damage recovery by thermal annealing.[16]

Epitaxial $ReSi_2$ films 150 nm thick were grown on phosphorous-doped ($\rho \sim 50\Omega{\cdot}$cm) n-type 3-in Si(100) wafers in ultrahigh vacuum ($\sim 10^{-9}$ Torr) at $\sim 650°$C by reactive deposition epitaxy (see Ch. 3.2).[42] The thickness and composition of the as-grown films were confirmed by 2 MeV ^{4}He backscattering spectrometry. Channeling measurements give a minimum yield of $\sim 2\%$ for Re, showing that the films are highly epitaxial. Furthermore, θ–2θ x-ray diffractometry shows only the $ReSi_2$ (200) peak in the 2θ angular scan from 20° to 170° (the relevant section is shown in Fig. 8.4-1 a), indicating that the films are epitaxially oriented with respect to the Si (100) substrate.

Film-substrate current-voltage (I-V) measurements on $ReSi_2$ films grown on both p- and n-type Si substrates were performed. While the film on the p-type Si substrate shows ohmic behavior, the sample on the n-type Si substrate has the characteristics of a rectifying junction (junction resistance ~ 2 kΩ at $\sim +10$ V and ~ 1 MΩ at ~ -10 V, sample size $\sim 1cm \times 1cm$). This means that the $ReSi_2$ film is electrically isolated to a degree from the n-type Si substrate. The van der Pauw method was used for Hall and resistivity measurements on the $ReSi_2$ film grown on the n-type Si substrate and showed that the $ReSi_2$ film is p-type. The resistivity of the $ReSi_2$ film was also measured from 90 K

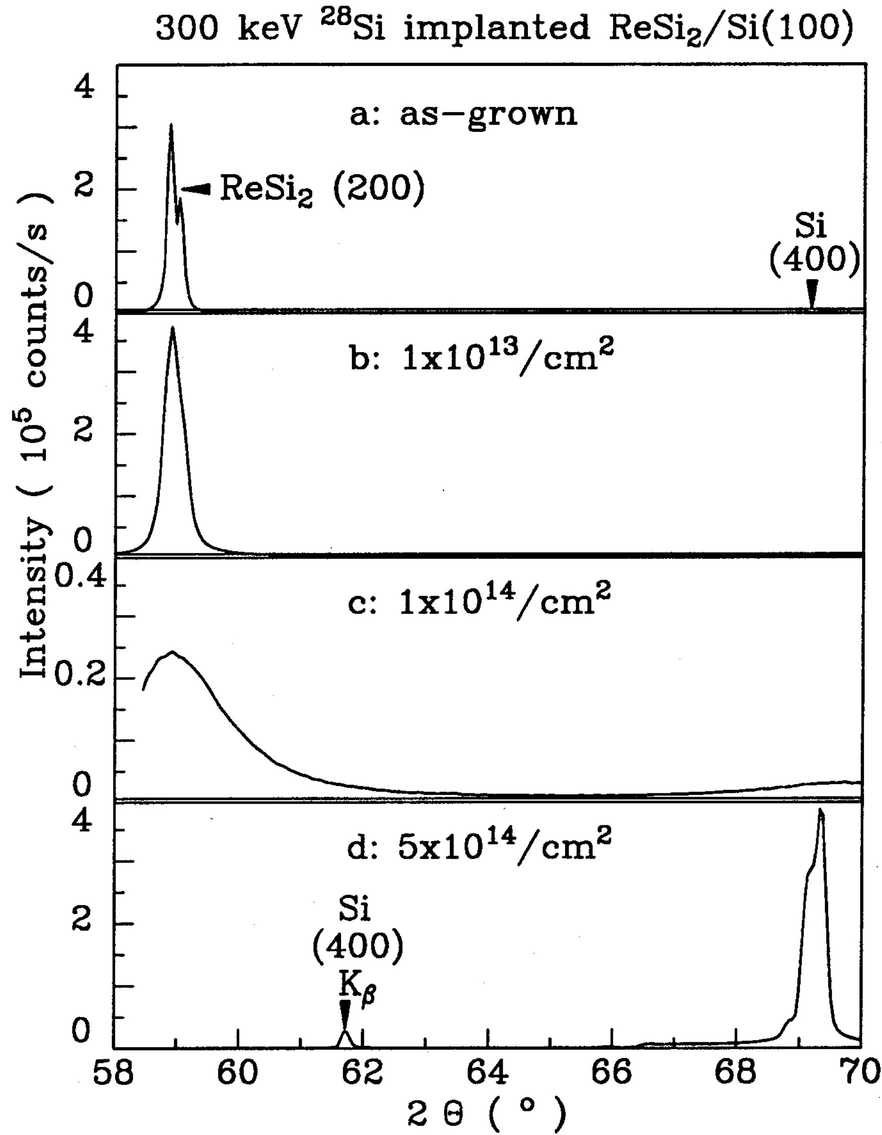

FIG. 8.4-1 X-ray diffraction spectra of epitaxial $ReSi_2$/Si(100) samples: (a) as-grown; and implanted by 300 keV ^{28}Si to doses of (b) $10^{13}/cm^2$, (c) $10^{14}/cm^2$, and (d) $5 \times 10^{14}/cm^2$. A Cu x-ray source and θ–2θ geometry were used.

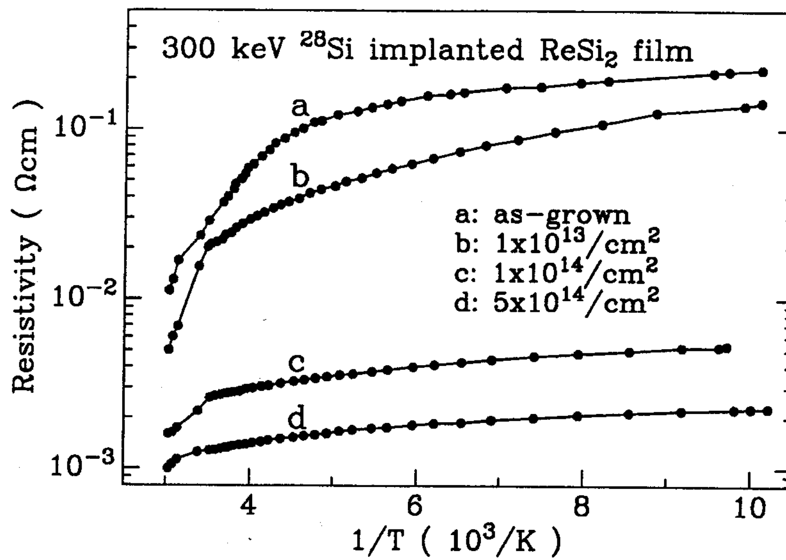

FIG. 8.4-2 Resistivity of the samples shown in Fig. 8.4-1, measured at temperatures ranging from 90K to 330K in the dark.

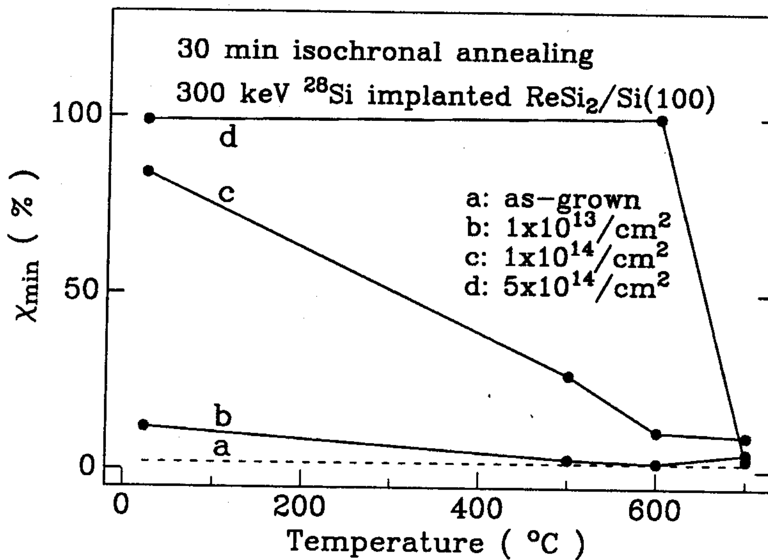

FIG. 8.4-3 Changes of the minimum yield for Re upon thermal annealing in vacuum at 500°C, 600°C and 700°C for 30 min for the samples shown in Fig 8.4-1.

to 330 K (Fig. 8.4-2 curve a). It equals $\sim$ 23 mΩcm at room temperature, nearly the same as those reported for polycrystalline films ($\sim$ 20 mΩcm).[52,53] All electrical measurements were carried out in the dark.

To investigate the effect of implantation damage and of chemical species on the structural and electrical properties of the $ReSi_2$ films, either 300 keV ^{28}Si or 380 keV ^{40}Ar ions were implanted into selected samples at room temperature with doses ranging from $10^{13}/cm^2$ to $10^{15}/cm^2$. At the implantation energies chosen, the damage peaks before the film-substrate interface.

2 MeV ^{4}He backscattering and channeling spectrometry were used to monitor the damage build-up in the $ReSi_2$ film. Because the minimum yield from only the element with the largest atomic number indicates the epitaxial quality in a polyatomic crystal,[43] we use the minimum yield for Re as an indicator of damage in the $ReSi_2$ film. The minimum yield for Re increases monotonically with increasing implantation dose from $\sim$ 2% for the as-grown sample to 100% for the 5×10^{14} $^{28}Si/cm^2$ implanted sample. This suggests that the $ReSi_2$ is amorphized at room temperature by the 300 keV 5×10^{14} $^{28}Si/cm^2$ implantation. The channeling spectrum of the sample implanted to $5 \times 10^{14}/cm^2$ also shows that the Si substrate is not amorphized. Similar results on damage build-up were found for the ^{40}Ar implanted samples. The epitaxial $ReSi_2$ film is amorphized at room temperature by implantation of 380 keV 10^{14} $^{40}Ar/cm^2$.

The damage induced in semiconducting $ReSi_2$ by room temperature implantation is significantly larger than that found in metallic silicides. $NiSi_2$ is amorphized at room temperature only after implantation of 100 keV 3×10^{15} $^{40}Ar/cm^2$,[7] which is about 30 times the dose for amorphization of semiconducting $ReSi_2$. $CoSi_2$ is not amorphized by room-temperature implantation of 150 keV ^{28}Si to a dose of $3 \times 10^{15}/cm^2$[23] and Pd_2Si by 100 keV ^{40}Ar to $10^{17}/cm^2$.[7] On the other hand, the critical dose for amorphization of $ReSi_2$ is about the same as that for bare Si.[27] The radiation sensitivity of $ReSi_2$ is typical of the covalent bonding of semiconductors rather than of metallic bonding. This result is also consistent with the high susceptibility of $ReSi_2$ to irradiation damage by an MeV ^{4}He beam.[15]

The crystalline quality of the epitaxial $ReSi_2$ film was also evaluated from the intensity and full-width at half-maximum (FWHM) of the x-ray diffraction peak from the film. Fig. 8.4-1 shows the evolution of the x-ray diffraction spectrum as the ^{28}Si ion dose increases from 0 to $5 \times 10^{14}/cm^2$ (Fig. 8.4-1 a to d). A strong $ReSi_2$ (200) peak is detected from the as-grown sample. That the Si (400) peak is weak and observable only in a magnified plot is probably due to the strong diffraction of the incident x-ray by the epitaxial $ReSi_2$ film. As the implantation dose rises, the FWHM of

the $ReSi_2$ (200) diffraction peak increases and the intensity decreases. For the 5×10^{14} $^{28}Si/cm^2$ implanted sample, the $ReSi_2$ (200) peak disappears while the Si (400) peak simultaneously becomes intense, indicating that the film becomes relatively transparent to the incident x-rays. An x-ray diffraction pattern was taken with a Read camera for the 5×10^{14} $^{28}Si/cm^2$ implanted sample. Diffuse rings were detected that are characteristic of amorphous material. We conclude that the $ReSi_2$ film becomes x-ray-amorphous upon 5×10^{14} $^{28}Si/cm^2$ implantation. Again, similar results were obtained for the ^{40}Ar implanted samples.

Figure 8.4-2 shows the resistivity from 90 to 330 K of the as-grown and ^{28}Si implanted $ReSi_2$ films. The resistivity decreases with increasing temperature for all the samples, suggesting that $ReSi_2$ remains a semiconductor upon implantation. The resistivity decreases monotonically with increasing implantation dose at all measurement temperatures. The same behavior was observed for the ^{40}Ar implanted samples. I-V measurements confirmed that the films are still electrically isolated from the substrates up to the highest dose, with about the same forward and reverse resistances as those measured before implantation.

The resistivity decrease of $ReSi_2$ we observed is associated with structural changes produced by implantation, not with the chemical identity of the added impurity. A decrease in resisitivity upon ion implantation was also observed in semiconducting $CrSi_2$.[9,17] This is opposite to the response of metallic transition-metal silicides to implantation damage.[13,14,23] There, the carrier concentration is roughly constant. Implantation produces static disorder, which reduces the carrrier scattering length. The resistivity hence increases. The amount of increase is typically proportional to the density of disorder (see Ch. 8.2).[23] However, the resistivity of the amorphized $ReSi_2$ is about the same as that of the amorphized $CoSi_2$, $\sim 1\ m\Omega cm$.[13] This indicates that the electrical conduction in amorphous materials is governed by the hopping of charge carriers among the localized states[13] and is roughly material-independent.

Upon thermal annealing, the channeling yields through the entire film decrease approximately uniformly, indicative of none layer-by-layer growth. Figure 8.4-3 shows how the minimum yield of the Re signal changes as a function of the temperature for 30 min isochronal annealing in vacuum ($\sim 5 \times 10^{-7}$ Torr). The lightly damaged $ReSi_2$ recovers after 500°C annealing (Fig. 8.4-3, curve b). On the other hand, the minimum yield of fully amorphized $ReSi_2$ remains unchanged upon annealing at 600°C, and drops to $\sim$ 2% after 700°C annealing (Fig. 8.4-3, curve d). Clearly, amorphous $ReSi_2$ recrystallizes completely after 700°C annealing and recreates a highly epitaxial film. The heavily damaged but non-amorphized $ReSi_2$ film (Fig. 8.4-3, curve c) recovers incompletely

after 700°C annealing, as the minimum channeling yield of ~ 10% indicates. Heavily damaged but non-amorphized Si also regrows poorly upon thermal annealing.[54]

The recovery was also monitored by the $ReSi_2$ (200) x-ray diffraction peak intensity and FWHM. The annealing characteristics are similar to those obtained from channeling analysis (Fig. 8.4-3). The diffraction peak of the lightly damaged sample (Fig. 8.4-1, curve b) intensifies and sharpens with increasing annealing temperature, while that of the amorphous sample (Fig. 8.4-1, curve d) changes only after 700°C annealing. The diffraction spectrum becomes the same as that of the as-grown sample (Fig. 8.4-1, curve a). This result suggests that solid phase crystallization of amorphous $ReSi_2$ films could be an alternative technique to grow epitaxial $ReSi_2$ films on Si(100) substrates.

The resistivity of all implanted $ReSi_2$ films also increases with increasing annealing temperature and returns to about the value of the as-grown sample after 700°C annealing.

By both x-ray diffractometry and channeling spectrometry, the ^{40}Ar implanted $ReSi_2$ films that are not amorphized recover similarly to the ^{28}Si implanted films upon thermal annealing. However, unlike the ^{28}Si implanted amorphous film, the ^{40}Ar implanted amorphous one fails to recrystallize epitaxially up to 1000°C annealing for 30 min. For all annealing temperatures, the ^{40}Ar amorphized $ReSi_2$ films retain a channeling yield of 100% and produce no detectable (200) x-ray diffraction peak. The Read camera x-ray diffraction pattern shows that the film after 1000°C annealing is polycrystalline. One possible explanation, based on an assumed analogy with crystallization of ^{40}Ar implanted amorphous Si,[55] is that the implanted ^{40}Ar atoms form bubbles in the matrix that interfere with the epitaxial regrowth of the amorphized $ReSi_2$.

The present results and the analogy with damage production and annealing in Si,[54] suggest the following processes in implanted $ReSi_2$: at low doses, ion implantation at room temperature produces damaged zones dispersed in a crystalline matrix. As the dose increases, the zones overlap and interact until the entire matrix is amorphized. The individual zones, which probably consist of defect clusters or small amorphous regions, reorder at a relatively low temperature (< 600°C). The amorphous film recrystalizes abruptly at a higher temperature (~ 700°C), in contrast to the layer-by-layer growth of amorphous Si on crystalline Si. In that case, a seed exists and recrystallization is limited by the growth. In the present case, no seed is present and recrystallization is presumably nucleation-limited, and is therefore abrupt. The recrystallization temperature is roughly 1/3 of the melting point, similar to that for semiconducting $CrSi_2$ films.[9,56]

In summary, we used 2 MeV ^4He backscattering spectrometry, x-ray diffractometry, and the van der Pauw technique to study how 150 nm epitaxial $ReSi_2$ films on Si(100) change structurally and

electrically upon room-temperature implantation of 300 keV ^{28}Si or 380 keV ^{40}Ar. The as-grown film has a minimum channeling yield of ~ 2% for Re, and a resistivity of ~ 23 mΩcm at room temperature. Ion implantation produces damage in the film, which increases monotonically with dose. At a dose of either 5×10^{14} ^{28}Si/cm^2 or 1×10^{14} ^{40}Ar/cm^2, the entire $ReSi_2$ film becomes both x-ray- and channeling-amorphous. The resistivity of the film decreases monotonically with dose. The amorphous film has a resisitivity of ~ 1.2 mΩcm at room temperature. Upon annealing in vacuum at 700°C for 30 min, the damage anneals out and the amorphous $ReSi_2$ film recrystallizes epitaxially, once again exhibiting a minimum channeling yield of ~ 2% for Re and a resistivity of ~ 23 mΩcm.

8.5 Strain induced by ion implantation in GeSi films

Recent interest in GeSi-base heterojunction bipolar transistors has spurred extensive studies on various properties of GeSi/Si structures, including the effect of ion implantation. The difference in atomic numbers of Ge and Si results in selective damage of GeSi and Si layers, which can induce amorphous-crystalline superlattices.[5,20] Amorphized GeSi layers on crystalline Si recrystallize epitaxially upon thermal processing.[18,19] Defects produced in a metastable strained layer by ion implantation could enhance strain relaxation.[21] In this section, we report some results on the strain and damage induced by 320 keV ^{28}Si implantation into pseudomorphic GeSi layers on Si(100), and the effects of thermal annealing.[57] The stability of ion-implanted strained layers is also discussed.

A. Experimental Procedures

Pseudomorphic metastable Ge_xSi_{1-x} ($x \approx 0.04, 0.09, 0.13$) layers ~ 170 nm thick were grown on Si(100) wafers at ~ 600°C by ultrahigh vacuum chemical vapor deposition at IBM. The samples were sent to Caltech, degreased, and loaded into the implanter. 320 keV ^{28}Si ions were implanted into the samples at room temperature in vacuum (~ 10^{-7} Torr). The damage peaks at ~ 200 nm beneath the interface inside the Si substrate, according to TRIM88 simulation.[25] Doses range from 10^{14}/cm^2 to 2×10^{15}/cm^2, and the flux was kept below 10^{12}/cm^2/s. Double crystal diffractometry and MeV ion channeling were used to analyze the strain and damage induced by implantation.

Samples were also annealed for 30 min at 300-700°C in vacuum (~ 5×10^{-7} Torr). The recovery of damage and the change of strain in the GeSi layers were monitored.

B. Results and Discussion

(i) damage and induced strain

Perpendicular and parallel strain, $\epsilon^{\perp}$ and $\epsilon^{\parallel}$, in GeSi/Si(100) heterostructures were extracted from x-ray rocking curves diffracted from both symmetrical (400) and asymmetrical (311) planes (see Ch. 2.2). All the as-grown samples are pseudomorphic within experimental sensitivity ($\epsilon^{\parallel} \leq 0.01\%$), in agreement with the experimental results of Ch. 4.2. These samples are metastable, meaning that they are all thicker than the equilibrium critical thickness predicted by Matthews-Blakeslee's model (see Fig. 4.2-2). Figure 8.5-1 shows the (400) rocking curves of the as-grown $Ge_{0.09}Si_{0.91}$/Si(100) (solid line) and of the samples implanted to doses of $2\times$ ($\bullet$) and $5 \times 10^{14}/cm^2$ ($\circ$). The rocking curve of the as-grown sample shows clearly visible small-amplitude oscillations, indicating a high crystalline perfection of the GeSi layer. The angular width of the diffraction peak from the layer is due entirely to the finite thickness of the layer. The perpendicular strain of the as-grown sample is $\epsilon^{\perp} = 0.69\%$. After implantation to $2 \times 10^{14}/cm^2$, the diffraction peak from the GeSi layer shifts farther away from the substrate Si peak, meaning that the GeSi layer develops an additional positive strain (see $\bullet$ in Fig. 8.5-1). The peak intensity decreases, while the angular width remains about the same. These facts suggest that defects are produced in the layer, that the layer still diffracts x-ray coherently (see discussion in Ch. 8.2), and that the defects are uniformly distributed in the layer and induce uniform lattice expansion. The perpendicular strain of the implanted sample is $\epsilon^{\perp} = 0.97\%$, while the parallel strain remains zero. The sample is thus still pseudomorphic and becomes more metastable than it was before. The additional perpendicular strain induced by the implantation damage, $\Delta\epsilon^{\perp}$, is 0.28%. One can also see the diffraction peak (at $\sim -0.05^{o}$ near the Si reference peak) from the damaged substrate Si ($\bullet$ in Fig. 8.5-1). The strain induced ($\sim 0.06\%$) is about the same as that in the implanted bulk Si samples, suggesting that the GeSi overlayer has no influence on the implantation damage in the Si substrate. As the dose rises to $5 \times 10^{14}/cm^2$, the diffraction peak from the GeSi layer is buried in the background and becomes undetectable, while that from the damaged Si substrate is still measurable ($\circ$ in Fig. 8.5-1). These findings indicate that the GeSi layer is more severely damaged than the Si substrate. In other words, GeSi alloy is more susceptible to radiation damage than Si is, in agreement with others' results.[5,20] As the dose increases further to $2 \times 10^{15}/cm^2$, the rocking curve from the sample becomes featureless (not shown) because both the layer and the substrate are amorphized.[27]

We also used 2 MeV ^{4}He [100] axial channeling to characterize the damage in the GeSi layer. The defect concentration, c_D, was extracted from the measured channeling yields (see Ch. 8.2 and 8.3). The average defect concentration in the layer is $\sim 14\%$ after $2 \times 10^{14}/cm^2$, rises to $\sim 80\%$ after $5 \times 10^{14}/cm^2$, and becomes 100% after $2 \times 10^{15}/cm^2$ when the layer is amorphized. Combining the

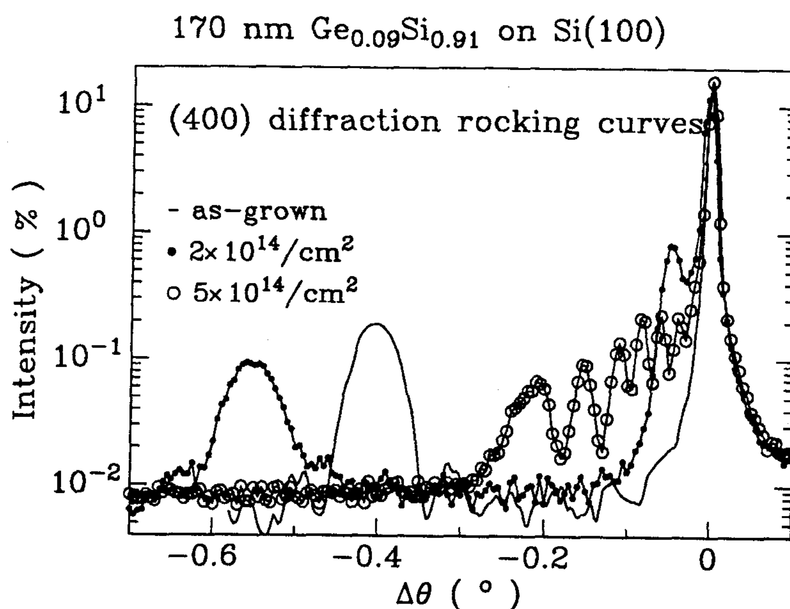

FIG. 8.5-1 X-ray rocking curves diffracted from the (400) symmetrical planes of the as-grown $Ge_{0.09}Si_{0.91}$/Si(100) sample (solid line), and of those implanted at room temperature with 320 keV ^{28}Si to 2× (•), 5 × $10^{14}/cm^2$ (○).

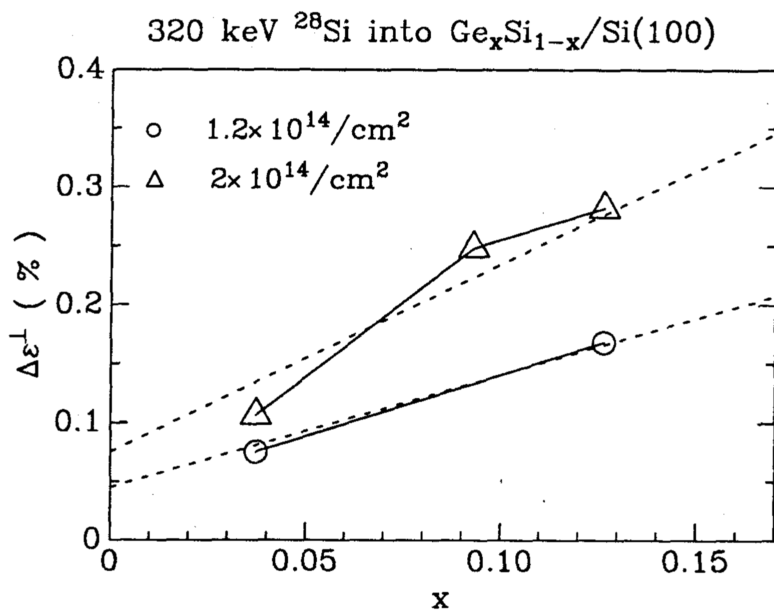

FIG. 8.5-2 The strain induced by 320 keV ^{28}Si implantation into pseudomorphic GeSi layers vs the Ge composition. The dashed lines are the strains predicted from a linear interpolation model of Eq. (8.5-2).

x-ray and channeling results for the $2 \times 10^{14}/\mathrm{cm}^2$ implanted sample, we obtain the following relationship between $\Delta\epsilon^{\perp}$ and c_D,

$$\Delta\epsilon^{\perp} = 0.02c_D. \qquad (8.5-1)$$

We tentatively postulate that this relation applies for this sample implanted to any dose. To verify this hypothesis, additional experiments with fine dose intervals are needed. The coefficient (0.02) is of the same order of magnitude as that for implanted bulk Si (0.012; see Ch. 7.2). We are currently in the process of measuring the coefficient for implanted bulk Ge, and of studying the dependence of the coefficient on the Ge composition.

X-ray rocking curve measurements of other implanted samples with different Ge composition give similar results as those described above. Firstly, the strain in the damaged substrate Si is the same as that in the implanted bulk Si (Ch. 7.2). Secondly, the implantation damage induces additional strain in the GeSi layer besides the intrinsic strain of the heterostructure. The layers remain pseudomorphic. At low damage level ($\phi \leq 2 \times 10^{14}/\mathrm{cm}^2$) where the diffraction peak from the GeSi layers is measurable, the additional strain induced by damage, $\Delta\epsilon^{\perp}$, increases with the implantation dose (Fig. 8.5-2). We know that the strain increases linearly with the Si dose at low damage levels in implanted bulk Si (Ch. 7.2) and Ge (Ref. 58) crystals. The limited data in Fig. 8.5-2 and the analogy with Si and Ge lead us to propose that for any Ge composition, $\Delta\epsilon^{\perp}$ is proportional to the dose at low damage levels. For a given dose, the induced strain in the GeSi alloy increases linearly with the Ge composition (Fig. 8.5-2). The dashed line is that obtained by interpolation between the corresponding strain of implanted Si (Ch. 7.2) and Ge (Ref. 58). For that interpolation, the strain in implanted Si can be found directly from the measurements (Ch. 7.2). The strain for implanted Ge was computed by multiplying the slope of strain versus dose by the corresponding dose ($1.2\times$ or $2 \times 10^{14}/\mathrm{cm}^2$), because this strain cannot be realized physically since the Ge is amorphized beyond $\sim 7 \times 10^{13}$ $^{28}\mathrm{Si/cm}^2$. Figure 8.5-2 shows that the interpolation fits the data reasonably well. This result suggests that the slope, $S_\phi(Ge_xSi_{1-x})$, of the implantation-induced strain $\Delta\epsilon^{\perp}$ vs the dose ϕ for $\mathrm{Ge}_x\mathrm{Si}_{1-x}$ alloy, may be predicted from that of Ge and Si, $S_\phi(Ge)$ and $S_\phi(Si)$ according to

$$S_\phi(Ge_xSi_{1-x}) = xS_\phi(Ge) + (1-x)S_\phi(Si). \qquad (8.5-2)$$

Further experiments are needed to prove or to invalidate this generalization.

(ii) damage annealing and strain change

To investigate the stability of these implanted layers upon thermal processing, we annealed the samples at 300-700°C in vacuum for 30 min and monitored the change of strain. Firstly, we noticed

that the annealing characteristics of the damaged Si substrate are similar to those of implanted bulk Si samples (see Ch. 7.2). The annealing behavior of the GeSi layers can be categorized into three types according to the initial damage levels. For the lightly damaged samples ($\phi \leq 2 \times 10^{14}/\text{cm}^2$), the annealing shifts the diffraction peak from the GeSi layer towards the main peak, and the peak intensity increases. The peak width remains the same. The rocking curve becomes the same as that of the as-grown sample after 700°C. For the heavily damaged samples ($\phi = 5 \times 10^{14}/\text{cm}^2$, ∘ in Fig. 8.5-3) where the peak from the implanted GeSi layer is undetectable, it is still undetectable after 300°C (filled inverse triangle in Fig. 8.5-3), but becomes measurable after 400°C annealing (•), and the samples completely recover after 700°C (solid line in Fig. 8.5-3). Figure 8.5-4 plots the perpendicular strain of three samples studied here as a function of 30 min isochronal annealing temperature. The filled symbols represent the as-grown samples. Two conclusions are evident: (a) the major annealing stage occurs at 23-300°C, and (b) the strain and damage induced by the implantation can be completely healed by a 700°C annealing. Furthermore, no relaxation of the intrinsic strain was observed for any sample after 700°C annealing, meaning that the presence of defects does not significantly enhance the relaxation of the metastable strain. Hull et al.[21] did observe some enhancement of strain relaxation in implanted GeSi/Si structures by transmission electron microscopy. These authors suggested that the defects promote the nucleation of dislocations, but impede their propagation. The x-ray rocking curve technique is not sensitive enough to explore that regime of initial dislocation nucleations because the dislocation density is below the x-ray detection limit. Our results therefore do not contradict those of Hull et al.[21]

We also used x-ray diffraction and MeV ion channeling to study the solid-phase epitaxial regrowth of the amorphized GeSi layers ($\phi = 2 \times 10^{15}/\text{cm}^2$). The regrown layers have larger channeling yields, much weaker and broader x-ray diffraction peaks, than the as-grown ones, indicating the presence of extended defects in the layers. To maintain the crystalline perfection of epitaxial GeSi layers, amorphization transformation should be avoided.

In summary, we found that ion implantation in GeSi layers on Si(100) produces damage. This damage induces additional positive strain in the layers. At a low damage level, the induced strain increases linearly with the dose. The slope of the induced strain vs the dose rises linearly with the Ge composition, and can be predicted by interpolation of the slopes for bulk Ge and Si crystals. Thermal annealing removes damage and eliminates the induced strain. Damaged, but not amorphized, samples fully recover after 700°C annealing for 30 min; amorphized samples recover only partially.

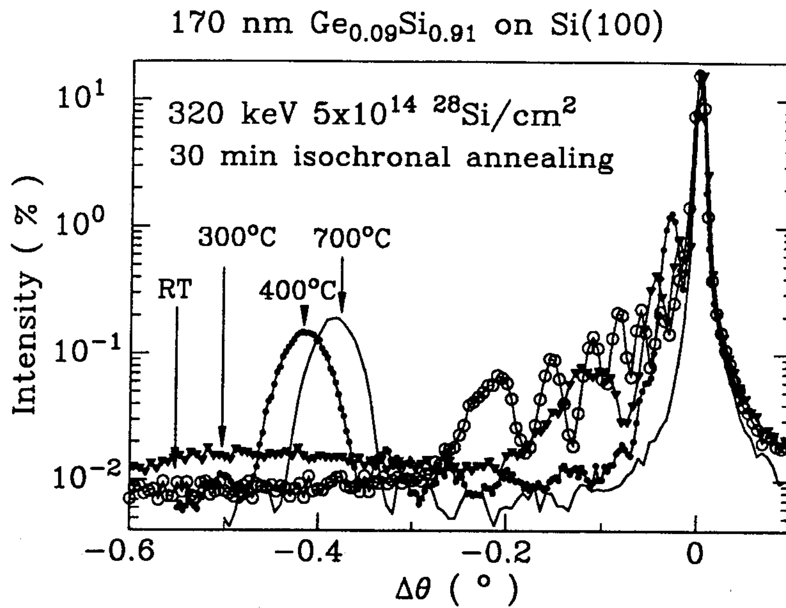

FIG. 8.5-3 (400) x-ray rocking curves of a pseudomorphic $Ge_{0.09}Si_{0.91}$/Si(100) implanted at room temperature (RT) by 320 keV 5×10^{14} $^{28}Si/cm^2$ and annealed for 30 min at various temperatures. The spectrum of the 700°C annealed sample (solid line) is indistinguishable from that of the as-grown sample (Fig. 8.5-1).

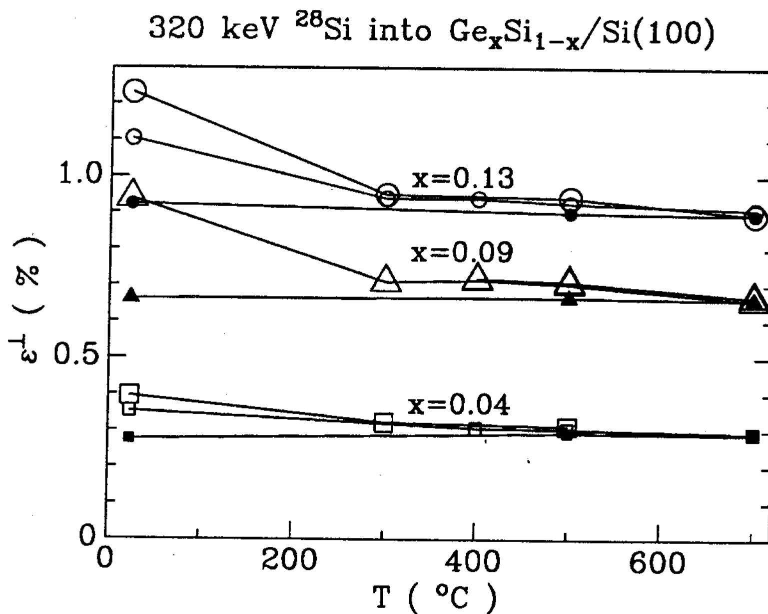

FIG. 8.5-4 The strain in the Ge_xSi_{1-x} layer vs the annealing temperature. The square, triangle, and circle are for the samples with $x = 0.04$, 0.09, and 0.13, respectively. The filled symbols represent the unimplanted samples. The small (big) open symbols represent the samples implanted by 320 keV $1.2\times$ $(2\times)$ 10^{14} $^{28}Si/cm^2$.

References

1. J.J. Coleman, P.D. Dapkus, C.G. Kirkpatrick, M.D. Camras, and N. Holonyale, Jr., Appl. Phys. Lett. 40, 904 (1982).
2. A.H. Hamdi, J.L. Tandon, and M-A. Nicolet, Nucl. Instr. and Meth. B10/11, 588 (1985).
3. D.R. Myers, S.T. Picraux, B.L. Doyle, G.W. Arnold, and R.M. Biefeld, J. Appl. Phys. 60, 3631 (1986).
4. A.G. Cullis, P.W. Smith, D.C. Jacobson, and J.M. Poate, J. Appl. Phys. 69, 1279 (1991).
5. D.J. Eaglesham, J.M. Poate, D.C. Jacobson, M. Cerullo, L.N. Pfeiffer, and K. West, Appl. Phys. Lett. 58, 523 (1991).
6. S. Mantl, D.B. Poker, and K. Reichelt, Nucl. Instr. and Meth. B19/20, 677 (1987).
7. H. Ishiwara, K. Hikosaka, and S. Furukawa, Appl. Phys. Lett. 32, 23 (1978).
8. M. Mäenpää, L.S. Hung, M-A. Nicolet, D.K. Sadana, and S.S. Lau, Thin Solid Films 87, 277 (1982).
9. C. A. Hewett, I. Suni, S. S. Lau, L. S. Hung, and D. M. Scott, Mat. Res. Soc. Symp. Proc. 27, 145 (1984).
10. C.A. Hewett, S.S. Lau, I. Suni, L.S. Hung, J. Appl. Phys. 57, 1089 (1985).
11. M. C. Ridgway, R. G. Elliman, R. P. Thornton, and J. S. Williams, Appl. Phys. Lett. 56, 1992 (1990).
12. K. Maex, A.E. White, K.T. Short, Y.F. Hsieh, R. Hull, J.W. Osenbach, and H.C. Praefcke, J. Appl. Phys. 68, 5641 (1990).
13. J. C. Hensel, R. T. Tung, J. M. Poate, and F. C. Unterwald, Nucl. Instrum. and Meth. B7/8, 409 (1985).
14. B-Y. Tsaur and C. H. Anderson, Jr., J. Appl. Phys. 53, 94 (1982).
15. G. Bai, M-A. Nicolet, J.E. Mahan, and K.M. Geib, Appl. Phys. Lett. 57, 1657 (1990).
16. K.H. Kim, G. Bai, M-A. Nicolet, J.E. Mahan, and K.M. Geib, Appl. Phys. Lett. April 29, 1991.
17. T. C. Banwell, X. A. Zhao, and M-A. Nicolet, J. Appl. Phys. 59, 3077 (1986).
18. B.T. Chilton, B.J. Robinson, D.A. Thompson, T.E. Jackman, and J.-M. Baribeau, Appl. Phys. Lett. 54, 42 (1989).
19. S. Mantl, B. Holländer, W. Jäger, B. Kabins, H.J. Jorke, and E. Kasper, Nucl. Instr. and Meth. B39, 405 (1989).

20. M. Vos, C. Wu, I.V. Mitchell, T.E. Jackman, J.-M. Baribeau, and J. McCaffrey, Appl. Phys. Lett. 58, 951 (1991).

21. R. Hull, J.C. Bean, J.M. Bonar, G.S. Higashi, K.T. Short, H. Temkin, and A.E. White, Appl. Phys. Lett. 56, 2445 (1990).

22. C.J. Tsai, H.A. Atwater, and T. Vreeland, Appl. Phys. Lett. 57, 2305 (1990).

23. G. Bai, M-A. Nicolet, unpublished.

24. G. Bai, M-A. Nicolet, unpublished.

25. J.P. Biersack and L.G. Haggmark, Nucl. Instr. and Meth. 174, 257 (1980).

26. G. Bai and M-A. Nicolet, unpublished.

27. G. Bai and M-A. Nicolet, J. Appl. Phys., July 15, 1991.

28. B.E. Warren, *X-Ray Diffraction*, Dover, New York, 1990.

29. W.K. Chu, J.W. Mayer, M-A. Nicolet, *Backscattering Spectrometry*, Academic Press, New York, 1978.

30. L.C. Feldman, J.W. Mayer, T.C. Picraux, *Materials Analysis by Ion Channeling*, Academic Press, New York, 1982.

31. S. Roth and R. Sizmann, R. Coutelle, and F. Bell, Phys. Lett. 32A, 119 (1970).

32. M.J. Hollis, Phys. Rev. B8, 931 (1973).

33. C.S. Newton, R.B. Alexander, G.J. Clark,, H.J. Hay, P.B. Treacy, Nucl. Instr. and Meth. 132, 213 (1976).

34. P.B. Price and J.C. Kelly, Phys. Rev. B17, 4237 (1978).

35. P. Baruch, F. Abel, C. Cohen, M. Bruneaux, D.W. Palmer, and H. Pabst, Rad. Eff. 9, 211 (1971).

36. S.U. Campisano, G. Foti, F. Grasso, and E. Rimini, Appl. Phys. Lett. 21, 425 (1972).

37. W.H. Kool, H.E. Roosendaal, L.W. Wiggers, and F.W. Saris, Nucl. Instr. and Meth. 132, 285 (1976).

38. G. Dearnaley and D.R. Jordan, Phys. Lett. 55A, 201 (1975).

39. D.S. Gemmel and R.C. Mikkelson, Phys. Rev. B6, 1613 (1972).

40. S. Yamaguchi, M. Koiwa, M. Hirabayashi, Y. Fujino, J. Takahashi, K. Ozawa, and K. Doi, Rad. Eff. 40, 231 (1979).

41. T.F. Luera, J. Appl. Phys. 51, 5792 (1980).

42. J.E. Mahan, K.M. Geib, G.Y. Robinson, R.G. Long, X.H. Yan, G. Bai, M-A. Nicolet, and M. Nathan, Appl. Phys. Lett. 56, 2439 (1990).

43. G. Bai, M-A. Nicolet, J.M. Mahan, and K.M. Geib, Phys. Rev. B41, 8603 (1990).

44. E. Rimini, E. Lugujio, and J.W. Mayer, Phys. Rev. B6, 718 (1972).

45. H. Ishiwara and S. Furakawa, J. Appl. Pyhs. 47, 1686 (1976).

46. N. Cheung, M-A. Nicolet, and J.W. Mayer, *Proceedings of the Symposium on thin film interfaces and interactions*, edited by J.E.E. Baglin and J.M. Poate (The Electrochemical Society Inc., Princeton, 1980), p. 176.

47. M.W. Thompson, *Defects and Radiation Damage in Metals* (Cambridge University Press, 1969), p. 253.

48. C. Kittel, *Introduction to Solid State Physics*, 5th ed. (Wiley, New York, 1976), p. 74.

49. M-A. Nicolet and S. S. Lau, in *VLSI Electronics: Microstructure Science* Vol. 6, ed. by N. Einspruch and G. Larrabee (Academic, New York, 1983), p. 391.

50. S.P. Murarka, in *Silicides for VLSI Application*, Academic, New York, 1983.

51. M. C. Bost and J. E. Mahan, J. Appl. Phys. **58**, 2696 (1985).

52. C. Krontiras, L. Groenberg, I. Suni, F. M. d'Heurle, J. Tersoff, I. Engstroem, B. Karlsson, and C. S. Petersson, Thin Solid Films, **161**, 197 (1988).

53. R. G. Long, M.C. Bost, and John E. Mahan, Thin Solid Films, **162**, 29 (1988).

54. J.F. Gibbons, Proc. IEEE, vol. 6, 1062 (1972).

55. P. Revesz, M. Wittmer, J. Roth, and J.W. Mayer, J. Appl. Phys. 49, 5199 (1978).

56. F. Nava, T. Tien, and K. N. Tu, J. Appl. Phys. **57**, 2018 (1985).

57. G. Bai, M-A. Nicolet, unpublished.

58. V.S. Speriosu, B.M. Paine, M-A. Nicolet, and H.L. Glass, Appl. Phys. Lett. 40, 604 (1982).

Appendix I Some Studies of Compound Semiconductors

Summary

A1. Thermal Strain of Epitaxial $In_uGa_{1-u}As_{1-v}P_v$ Films on InP(100)

— in collaboration with Dr. S.J. Kim at AT&T Bell Laboratories

Single layers of $\sim 0.5\mu m$ thick $In_uGa_{1-u}As_{1-v}P_v$ ($0.52 < u < 0.63$ and $0.03 < v < 0.16$) were grown epitaxially on InP(100) substrates by liquid phase epitaxy at $\sim 630°C$. The compositions of the films were chosen to yield a constant bandgap of ~ 0.8 eV ($\lambda = 1.55\ \mu m$) at room temperature. The lattice mismatch at room temperature between the epitaxial film and the substrate varies from -4×10^{-3} to $+4 \times 10^{-3}$. The strain in the films was characterized in air by x-ray double crystal diffractometry with a controllable heating stage from 23°C to $\sim$ 700°C. All the samples have an almost coherent interface from 23°C to about $\sim$ 330°C with the lattice mismatch accommodated mainly by the tetragonal distortion of the epitaxial films. In this temperature range, the x-ray strain in the growth direction increases linearly with temperature at a rate of $(2.0 \pm 0.4) \times 10^{-6}/°C$, and the strain state of the films is reversible. Once the samples are heated above $\sim$ 330°C, a significant irreversible deterioration of the epitaxial films sets in (publication No. 15).

A2. Damage in GaAs, Si, and Ge by MeV ^{4}He Irradiation at Room Temperature

MeV ^{4}He backscattering spectrometry is routinely used to characterize the composition and thickness of thin films ($< 1\ \mu m$). It is therefore important to know what effects an ^{4}He beam has upon the materials analyzed. X-ray double crystal diffractometry analysis of bulk Si, Ge, and GaAs crystals irradiated at room temperature by 2 MeV $\sim 10^{16}\ {}^4\mathrm{He/cm^2}$ (a typical dose needed to get a channeling spectrum of good statistics) shows that while no measurable strain ($\leq 0.01\%$) is induced in Si and Ge, significant positive strain ($\sim 0.4\%$) is produced in GaAs. The strain in irradiated GaAs decreases to zero upon annealing at 400°C for 15 min, indicating that the damage heals. We conclude that backscattering spectrometry is practically a non-destructive analytical tool for Si and Ge crystals, but not for GaAs. Special care is therefore needed in the analysis of GaAs and AlGaAs/GaAs by MeV ion beams and in the interpretation of experimental results (publication No. 8).

A3. Defects Annealing Near Room Temperature of ^{28}Si implanted GaAs(100)

The annealing behavior near room temperature of the defects in 300keV ^{28}Si implanted GaAs was monitored by using x-ray double crystal diffractometry to measure the strain relaxation as a function of time duration. The maximum strain of the samples stored in ambient air at 23°C and 100°C decreases with time, revealing that the defects are mobile near room temperature and can recombine and reorder. Strain relaxation is exponential in time. At least two time constants of ~ 0.24 hr and ~ 24 hr are needed to fit the experimental data, indicating that two different kinds of defects are responsible for the strain relaxation. Time constants are also obtained for different implantation doses and temperatures (23°C or −194°C), and are insensitive to both these parameters, suggesting that the time constants are intrinsic properties of the defects in GaAs (publication No. 4).

A4. Sequential Nature of Damage Annealing and Dopant Activation in Implanted GaAs

—in collaboration with Dr. J.L. Tandon at McDonnell Douglas Astronautics Company

Rapid thermal processing of implanted GaAs reveals a definitive sequence in damage annealing and electrical activation. Removal of the damage occurs first. At that stage, the GaAs is n-type with a very low carrier concentration ($\sim 10^6/cm^2$) and high electron mobility ($\sim 5000\ cm^2/Vs$), regardless of the implanted species. Electrical activation is achieved next. The GaAs becomes n- or p-type, or remains semi-insulating, depending on the chemical nature of the dopants. Similar experiments were performed in implanted Ge. No such two-step sequence is observed, suggesting that the sequential nature may be unique to compound semiconductors (publication Nos. 9, 12, 14).

Appendix II List of Publications

1. Y.C. Kao, K.L. Wang, E. deFresart, R. Hull, G. Bai, D.N. Jamieson, and M-A. Nicolet, "Study of $CoSi_2/Si$ strained layers grown by molecular beam epitaxy," J. Vac. Sci. Technol. B5, 745 (1987).
2. D.N. Jamieson, G. Bai, Y.C. Kao, C.W. Nieh, M-A. Nicolet, and K.L. Wang, "On the critical layer thickness of strained-layer heteroepitaxial $CoSi_2$ films on (111)Si," Mat. Res. Soc. Symp. Proc., Vol. 91, 479 (1987).
3. Y.C. Kao, D.N. Jamieson, G. Bai, C.W. Nieh, T.L. Lin, B.J. Wu, H.Y. Chen, and K.L. Wang, "Epitaxial $CoSi_2$/porous-Si strained layer structures grown by MBE," Mat. Res. Soc. Symp. Proc., Vol. 91, 473 (1987).
4. G. Bai, D.N. Jamieson, M-A. Nicolet, and T. Vreeland Jr., "Defects annealing of Si implanted GaAs at room temperature and 100 C," Mat. Res. Soc. Symp. Proc., Vol. 93, 67 (1987).
5. Y.C. Kao, K.L. Wang, B.J. Wu, T.L. Lin, C.W. Nieh, D.N. Jamieson, and G. Bai, "Molecular beam epitaxial growth of $CoSi_2$ on porous Si," Appl. Phys. Lett., 51, 1809 (1987).
6. C.H. Chern, Y.C. Kao, C.W. Nieh, G. Bai, K.L. Wang, and M-A. Nicolet, "MBE growth of SiGe on porous Si," J. Electrochem Soc. 134, 543 (1987).
7. G. Bai, D.N. Jamieson, M-A. Nicolet, T. Vreeland Jr., "Misoriented epitaxial growth of $CoSi_2$ on offset (111)Si substrates," Mat. Res. Soc. Symp. Proc., Vol. 102, 259 (1988).
8. G. Bai, C.J. Tsai, A. Dommann, M-A. Nicolet, and T. Vreeland, Jr., "Characterization of semiconductors by MeV He backscattering spectrometry, channeling and double crystal diffraction," presented at TECHCON'88, Oct. 12-14, 1988, Dallas, TX.
9. J. L. Tandon, J.H. Madok, I.S. Leybovich, and G. Bai, "Damage removal and activation in rapid-thermally-annealed Si implanted GaAs," Mat. Res. Soc. Symp. Proc., Vol. 126, 207 (1988).
10. Y.J. Mii, R. Karunasiri, K.L. Wang, G. Bai, "Growth and characterizations of GaAs/AlGaAs multiple quantum well structures on Si substrates for infrared detection," J. Vac. Sci. Technol. B7, 341 (1989).
11. G. Bai, M-A. Nicolet, T. Vreeland, Jr., Q. Ye, Y.C. Kao, K.L. Wang, "Thermal strain measurements in epitaxial $CoSi_2/Si$ by double crystal x-ray diffraction," Mat. Res. Soc. Symp. Proc., Vol. 130, 35 (1989).
12. J.L. Tandon, J.H. Madok, I.S. Leybovich, G. Bai, and M-A. Nicolet, "Sequential nature of

damage annealing and activation in implanted GaAs," Appl. Phys. Lett., 54, 30 (1989).

13. G. Bai, M-A.Nicolet, T.Vreeland, Jr., Q.Ye, and K.L. Wang, "Strain in epitaxial $CoSi_2$ films on Si(111) and inference for pseudomorphic growth," Appl. Phys. Lett. 55, 1874 (1989).
14. J. L. Tandon, I.S. Leybovich, and G. Bai, "Activation analysis of rapid-thermally-annealed Si and Mg implanted GaAs," J. Vac. Sci. Technol. B7, 1090 (1989).
15. G. Bai, S.J. Kim, M-A. Nicolet, R.G. Sobers, J.W. Lee, M. Brelvi, P.M. Thomas, and D.P. Wilt, "Thermal strain and photoluminnescence study of epitaxial InGaAsP films on InP," Mat. Res. Soc. Symp. Proc. Vol. 160, 171 (1990).
16. J.E. Mahan, K.M. Geib, G.Y. Robinson, R.G. Long, X.H. Yan, G. Bai, M-A. Nicolet, and M. Nathan, "Epitaxial tendencies of $ReSi_2$ on (001)Si," Appl. Phys. Lett. 56, 2439 (1990).
17. G. Bai, M-A. Nicolet, J.E. Mahan, K.M. Geib, "Backscattering and channeling study of epitaxial $ReSi_2$/Si(111)," Phys. Rev. B41, 8603 (1990).
18. J.E. Mahan, K.M. Geib, G.Y. Robinson, R.G. Long, X.H. Yan, G. Bai, M-A. Nicolet, and M. Nathan, "Large-area single-crystal films of semiconducting $FeSi_2$," Appl. Phys. Lett. 56, 2126 (1990).
19. Q. Ye, T.W. Kang, K.L. Wang, G. Bai, and M-A. Nicolet, "RHEED study of $CoSi_2$/Si multilayer structures," Thin Solid Films, 184, 269 (1990).
20. G. Bai, M.A. Nicolet, J.E. Mahan, K.M. Geib, "Radiation damage in $ReSi_2$ by a MeV ^4He beam," Appl. Phys. Lett. 57, 1657 (1990).
21. G. Bai, K.H. Kim, M-A. Nicolet, "Strain in porous Si layers formed on p^+-Si(100) substrates," Appl. Phys. Lett. 57, 2247 (1990).
22. K.H. Kim, G. Bai, M-A. Nicolet, and A. Venezia, "Strain in porous Si with and without capping layers," J. Appl. Phys., Feb. 15, 1991.
23. G. Bai, M-A. Nicolet, "Defects production and annealing in self-implanted Si," J. Appl. Phys., July 15, 1991.
24. K.H. Kim, G. Bai, M-A. Nicolet, "Amorphization and recrystallization of ion-implanted epitaxial $ReSi_2$ films on Si(100)," Appl. Phys. Lett., April 29, 1991.
25. J.E. Mahan, K.M. Geib, G.Y. Robinson, G. Bai, and M-A. Nicolet, "RHEED patterns of $CrSi_2$ films on Si(111)," J. Vac. Sci. Technol. B (in press).
26. G. Bai, M-A. Nicolet, T. Vreeland, Jr., "Elastic and thermal properties of $CoSi_2$ layers on Si(100) substrates," J. Appl. Phys. May 1, 1991.
27. K.M. Geib, J.E. Mahan, R.G. Long, G.Y. Robinson, M. Nathan, G. Bai, and M-A. Nicolet,

"Epitaxial orientation and morphology of β–$FeSi_2$ on Si(100)," J. Appl. Phys. (in press).

28. J.E. Mahan, G. Bai, M-A. Nicolet, R.G. Long, and K.M. Geib, "Microstructure and morphology of some epitaxial $ReSi_2$ films on Si(100)," submitted to Thin Solid Films.
29. G. Bai, M-A. Nicolet, "Defects production by ^{19}F, ^{28}Si, ^{40}Ar, and ^{131}Xe implantation into Si(100) at room temperature," submitted to J. Appl. Phys.

Papers in preparation

30. G. Bai. M-A. Nicolet, "Damage in implanted Si(100) at liquid nitrogen temperature."
31. G. Bai, M-A. Nicolet, "Defects production and annealing in Si implanted $CoSi_2$/Si(111)."
32. G. Bai, M-A. Nicolet, C.H. Chern, K.L. Wang, "Some properties of epitaxial GeSi alloys grown on Si(100)."
33. G. Bai, M-A. Nicolet, "Misorientation in heterostructures."
34. G. Bai, M-A. Nicolet, C.H. Chern, K.L. Wang, "Kinetics of strain relaxation of metastable GeSi layers on Si(100)."
35. G. Bai, M-A. Nicolet, C.H. Chern, K.L. Wang, "Asymmetrical tilt boundary in epitaxial GeSi/Si heterostructure."
36. G. Bai, M-A. Nicolet, C.H. Chern, K.L. Wang, "Strain modification and relaxation of GeSi/Si heterostructures by ion implantation and thermal annealing."